MEASUREMENT OF QUANTUM LIGHT PULSES FOR ENHANCED PRECISION SENSING

Alexander Owen Clayton Davis

Keble College, Oxford



Submitted for the degree of Doctor of Philosophy
Trinity Term 2018

Supervised by
Professor Brian Smith

Clarendon Laboratory
University of Oxford
United Kingdom

To my parents, Clive and Angela, and my siblings, Philip, Katy, and Christopher, for encouraging my curiosity and fostering my imagination.

Measurement of quantum light pulses for enhanced precision sensing

Alexander Davis, Keble College, Oxford

Submitted for the degree of Doctor of Philosophy, Trinity Term, 2018

Quantum physics holds promise to revolutionise a number of technologies by enabling performance beyond what is feasible with classical resources, such as secure communications, precision measurement and high-speed simulation and computation. To realise this, quantum information must be encoded into one of the physical degrees of freedom of light. The time-frequency (TF) domain provides a infinite-dimensional space which is naturally compatible with integrated optical platforms. Additionally, future quantum networks will require coherent coupling of quantum systems that do not necessarily exhibit TF mode overlap. The ability to generate, coherently control and measure a variety of TF states of quantum light is therefore a necessary step towards implementing optical quantum technologies. Developing the building blocks for future optical quantum applications calls for an assortment of methods for measuring the properties of TF states of quantum light. Whilst much progress has been made towards this goal recently, deficiencies with existing methods remain. Efficient spectrally-resolved detection away from the telecoms wavelength range and a robust approach to single-photon state characterisation that is sensitive to the spectral phase have so far proven challenging. Additionally, accessing quantum advantages requires measurements that are sensitive to the nonclassical correlations that can exist between separate subsystems. However, until now a flexible approach to determining the full quantum state of systems of multiple time/frequency entangled photons has been lacking. Here we develop a toolbox of techniques for the measurement of TF quantum states of light for few-photon systems, and apply these to the task of precision measurement. Firstly, we propose, construct and demonstrate efficient single-photon spectrometers based on dispersive time-to-frequency mapping, using chirped fibre Bragg gratings to apply the necessary group delay dispersion. We use two such devices operating in coincidence to realise a full phase-sensitive reconstruction of the TF state of a single photon, by spectrally resolving the output of a nonclassical interference process with an external reference. We also demonstrate a complementary, optical reference-free method. This characterisation tool, an implementation of electro-optic spectral shearing interferometry with coincident spectrally-resolved single-photon detection, melds techniques from ultrafast metrology and quantum optics. We proceed to demonstrate the flexibility of this device by reconstructing a wide range of test pulses generated with a pulse shaper. By implementing this technique in conjunction with spectrally-resolved detection of a second photon, we realise complete characterisation of the TF wave function of a spectrally-entangled broadband photon pair. This method is robust to a wide range of inputs and is generalisable to spectrally mixed states and across a wide range of wavelengths, including to spectrally non-degenerate photon pairs. To demonstrate, we generate an entangled photon pair with controllable TF entanglement and perform a full reconstruction. Lastly, we present a new technique for using TF entangled photon pairs to realise quantum-enhanced measurement of a time delay in a quantum channel in the presence of environmental noise. This scheme is based on entanglement-enhanced rejection of background light. A simple experiment demonstrating the feasibility of such a measurement is presented.

Acknowledgements

Despite being obliged to declare this thesis as entirely my own work, I have to come clean: nothing would have been possible without the support of my team-mates in the OQT group, and those who supported me in less direct, but no less important ways.

The first person I must thank is Michał Karpiński. The uneviable task of transforming me from a helpless recent graduate into something worthy of lab space fell to him. It is only with the benefit of hindsight that I realise how much patience it must have taken on his part to deal with my frequent cluelessness- whether on the difference between homodyne and heterodyne detection, or the correct pronunciation of the letter ł. Gradually, I learnt enough to recognise that he was also one of the most resourceful scientists I was ever likely to meet, and that having him as my mentor was the first of several wondrous pieces of good luck my time at Oxford would grant me.

The next of those came in the spring of 2015 with the opportunity to work with Paul Saulnier. Whilst Paul's visit was instrumental in building one of the most important pieces of equipment used throughout this thesis, I will remember it for his kindness and generosity to me, not to mention his excellent taste in cheese.

It is at this point that I will mention Valerian Thiel, in case he tells anyone where we buried those bodies. Whilst his fetishisation of coupling light into fibres certainly eased progress in the lab, his meticulous labelling was what truly saved my DPhil, and after his arrival I not once wasted hours vainly searching the lab for bondage gear and coke bags. Unfortunately, the task of filtering the thermal background of banter from our work proved beyond either of us. Nonetheless, Valerian's diligence in the lab and selfless attitude to teamwork, as well as his extraordinary talent as a scientist, has left me greatly indebted to him over these last two years. I am also very grateful for his intense preoccupation with aesthetics, since nearly every decent-looking plot in this thesis has his hand in it. Of course, he's not the first Frenchman to obsess over a sexy figure.

I've had the privilege of collaborating with some excellent Masters students- Sam Holder, Peru D'Ornellas, Ke Sun and Alistair Smith. Each of them was a pleasure to work with, and they all made valuable contributions to the work presented here. I'm also relieved none of them found the experience so wretched as to deter them from continuing their careers in science. However, Peru's stint deserves a special mention, for his dank rhyming, dependable companionship whenever I craved cheap Thai food, and his introducing me to the world of techno music (from which I swiftly exited). In addition to those I have worked with directly, Laura Wright's legacy to me was a world-class lab available from the outset, and much of what I have accomplished is a continuation of her work. I am also extremely grateful to my funding agency, DSTL. It goes without saying that their contribution was *sine qua non*. Additionally, their personal support throughout has been very valuable to me.

I extend my warmest thanks to my DPhil examiners, Paul Ewart and Andy Weiner. They both generously gifted time from their busy schedules to provide a fair and thorough inspection

of this thesis, which led to a viva that was as much a fascinating discussion of physics as it was a robust examination.

Of course, there is always the last author. As well as establishing our group and collecting all of the above talent, Brian Smith personally took me under his wing, and generously provided his profound scientific insight and a sense of direction - not to mention quite a few pints - at every step. It is entirely thanks to him that I had the opportunity to work with all the first-rate scientists above, himself not least among them. Most importantly, though, he has shown an earnest commitment to my personal and professional development at every point during what was also a period of great change for himself. It has been a true privilege to be his student.

In addition to my OQT colleagues, there are a few people who have provided indispensible support to me throughout my time at Oxford. I'll give a shout out to all the people who have collectively formed my social life during the last four years in Oxford. There are too many individuals to name, but the Abingdon lads, Nikki, and my co-residents at 27 Regent Street spring to mind as deserving special mention for the good times.

At the end of the day, though, nothing that anyone else has done for me over the last four years compares to what my family, especially my parents Clive and Angela, have done over the last twenty-five, and this is reflected in the dedication of this thesis. Every step, at first quite literally, towards pursuing my passion for physics at the frontier of human knowledge was guided by them. I can only hope to scratch the surface of the impossible task of repaying them for their investment in me.

Declaration

I confirm that the thesis I am submitting is wholly my own work. No part of my thesis has been accepted or is currently being submitted for any degree, diploma or certificate or other qualification in this University or elsewhere.

Contents

1 Light reading **1**

1.1 Historical context . . . 2

1.2 The quantum world . . . 3

1.3 The machinery of modern optics . . . 5

1.3.1 Lasers . . . 5

1.3.2 Nonlinear quantum optics . . . 8

1.4 Thesis outline . . . 9

2 An introduction to ultrafast quantum pulse characterisation **11**

2.1 Introduction . . . 12

2.2 Why study ultrafast pulses? . . . 13

2.3 Strategies for ultrafast quantum pulse characterisation . . . 17

2.4 Partial single-mode characterisation methods . . . 19

2.4.1 A note on real measurements of infinite-dimensional spaces . . . 19

2.4.2 Spectrometry . . . 20

2.4.3 Temporal intensity characterisation . . . 22

2.4.4 Purity measurements . . . 24

2.5 Full single-mode characterisation methods . . . 24

2.5.1 Optical gating . . . 25
2.5.2 Linear interferometric approaches . . . 26
2.5.3 Spectral shearing interferometry . . . 28
2.6 Entangled state characterisation . . . 30
2.6.1 Stimulated-emission based measurement . . . 30
2.6.2 Joint intensity measurements . . . 31
2.6.3 Photon pair self-interferometry . . . 32
2.6.4 Two-mode homodyne tomography . . . 32
2.7 Chapter summary . . . 32

3 Time-frequency quantum optics **35**
3.1 Introduction . . . 36
3.2 Spectral-temporal modes in classical electromagnetism . . . 37
3.2.1 Paraxial approximation . . . 39
3.2.2 Modes and mode transformations . . . 41
3.2.3 Temporal representation of modes . . . 43
3.2.4 Hermite-Gauss representation of modes . . . 45
3.2.5 Spectral representation of modes . . . 46
3.2.6 Spectral phase and dispersion . . . 48
3.2.7 Temporal phase operations . . . 52
3.2.8 The chronocyclic Wigner representation . . . 53
3.3 Quantisation of the electromagnetic field . . . 58
3.3.1 A single mode . . . 58
3.3.2 Approaches to quantisation . . . 59
3.3.3 Canonical quantisation . . . 59
3.3.4 The wave function of a single photon . . . 64

3.3.5 Density operators . . . 67
3.3.6 Fidelity of quantum states . . . 69
3.3.7 Photon pairs and multimode entanglement . . . 69
3.3.8 Gaussian states . . . 73
3.3.9 Coherence functions . . . 76
3.4 Chapter summary . . . 81

4 Single-photon spectrometry with dispersive optics 83
4.1 Introduction . . . 84
4.2 Single-photon sources . . . 85
4.3 Time-resolved single-photon spectrometry . . . 88
4.4 Building the spectrometers . . . 89
4.4.1 Device construction . . . 89
4.4.2 Device characteristics . . . 92
4.4.3 Device calibration . . . 93
4.5 Results . . . 95
4.5.1 Spectrum of heralded single photons . . . 95
4.5.2 Joint spectral intensity of a photon pair . . . 97
4.6 Improvements . . . 98
4.7 Chapter summary . . . 99

5 Spectrally-resolved Hong-Ou-Mandel interference 101
5.1 Introduction . . . 101
5.2 Spectrally-resolved HOMI for partially distinguishable modes . . . 103
5.3 Pulse shaping . . . 108
5.4 Attenuated coherent state reference . . . 111
5.5 Twin photon reference . . . 112

5.6 Results . . . 116
5.7 Chapter summary . . . 119

6 Single photon characterisation by electro-optic spectral shearing interferometry 121
6.1 Introduction . . . 122
6.2 Measurement principle . . . 123
6.2.1 Background . . . 123
6.2.2 Phase reconstruction . . . 126
6.3 Experiment . . . 130
6.3.1 Obtaining spectral shear . . . 130
6.3.2 Experimental set-up . . . 135
6.4 Calibrating the interferometer . . . 136
6.5 Results . . . 140
6.5.1 Data acquisition . . . 140
6.5.2 Reconstruction of phase that is polynomial in frequency . . . 141
6.5.3 Arbitrary phase reconstruction . . . 146
6.5.4 Time-frequency distributions . . . 148
6.6 Discussion . . . 149
6.6.1 Characterisation of single-mode fields . . . 149
6.6.2 Mixed state reconstruction . . . 153
6.6.3 Heralding . . . 155
6.6.4 Practical considerations . . . 157
6.7 Chapter summary . . . 159

7 Measuring a spectrally entangled photon pair 161
7.1 Introduction . . . 162
7.2 The two-photon wave function . . . 163

7.2.1 Schmidt decomposition . . . 163
7.2.2 Local and nonlocal phase . . . 164
7.3 Measurement principle . . . 167
7.4 State preparation . . . 168
7.4.1 Photon pair generation . . . 168
7.4.2 Joint temporal distribution . . . 170
7.4.3 Phase reconstruction . . . 172
7.5 Experimental methods . . . 175
7.5.1 Data acquisition and processing . . . 175
7.5.2 Noise and stability . . . 175
7.5.3 Spectral matching . . . 176
7.6 Results . . . 176
7.6.1 Unchirped pump . . . 176
7.6.2 Chirped pump . . . 178
7.6.3 Full complex joint amplitude reconstruction . . . 178
7.7 Mixed state characterisation . . . 182
7.8 Chapter summary . . . 183

8 Entanglement-enhanced noise rejection 185
8.1 Introduction . . . 186
8.2 Quantum metrology . . . 186
8.3 Environmental noise reduction in parameter estimation . . . 189
8.3.1 Environmental noise . . . 189
8.3.2 The quantum Cramer-Rao bound . . . 190
8.4 Demonstration . . . 195
8.4.1 Experimental principle . . . 195

8.4.2 Measurement stage . . . 199
8.4.3 Experimental design . . . 200
8.4.4 Results . . . 202
8.4.5 Discussion . . . 204
8.5 Chapter summary . . . 205

9 Conclusions and outlook **207**
9.1 Summary . . . 207
9.2 Outlook . . . 209
9.2.1 Improvements . . . 209
9.2.2 Implications . . . 211

A Path Integral formulation **213**

B Loss of visibility analysis **215**

“And why beholdest thou the mote that is in thy brother’s eye, but considerest not the beam that is in thine own eye?” (Matthew 7:3)

Jesus foresees the importance of laser safety.

Chapter 1

Light reading

Contents

1.1 Historical context 2

1.2 The quantum world 3

1.3 The machinery of modern optics 5

1.3.1 Lasers 5

1.3.2 Nonlinear quantum optics 8

1.4 Thesis outline 9

LIGHT, or more generally electromagnetic radiation, is one of the most familiar phenomena in all of science. In spite of its obvious prominence in everyday experience, the process of understanding its true nature has taken many centuries and occupies the central position in the history of physics. Both of the fundamental pillars of our current understanding of the world- relativity and quantum mechanics- initially sprung from considering the properties of light.

Besides its place in fundamental science, light also takes up a crucial position in the technologies that enable our modern way of life. Communication and measurement technology as we know it today- such as the Internet, smartphones, self-driving cars, modern maps and surveys, and information storage in media such as compact discs- would be inconceivable without

the major progress in optical technology over the last half-century. As our expertise in controlling and measuring optical systems advances, so do our opportunities to exploit it, both to study the world at a fundamental level and to improve our experience of living in it. This potential has, in its turn, provided the impetus behind the rapid advancements in generating, manipulating and detecting beams of light that has taken place since the mid-twentieth century.

One property of light stands out at having not yet been widely exploited in spite of the enormous potential to do so: its quantum nature. Quantum optical technologies promise more rapid communications, ultra-precise measurements, computers and simulators with unprecedented capabilities, and fundamentally impregnable message encryption. Whilst these prizes have so far been largely inaccessible to us, the techniques that have recently become available to modern science are gradually starting to creak open the door, and progress towards this objective is the subject of this thesis.

1.1 Historical context

The nature of light was a subject of dispute since antiquity, but by the 18th century two views dominated. Isaac Newton and others imagined a ray of light to consist of many small, fast-moving particles or "corpuscles". These corpuscles were believed to travel incredibly quickly, bounce elastically off certain materials, and have a mass that depends on the colour of the light. This intuition explained several optical effects that were already known by Newton's time, such as reflection and refraction, and the corpuscular theory was initially popular among the natural philosophers of the day. It was challenged, however, by the idea that light was instead a wave rippling through all-permeating, otherwise invisible material known as the luminiferous (light-bearing) aether. In the early 19th century, the direct observation of interference effects, most famously in Young's double-slit experiment and the observation of the Arago spot (a bright spot of light that appears at the centre of the shadows of circular objects), apparently settled the

dispute in favour of the wave theory of light. Theoretical work then showed that polarisation, a property that the corpuscular model struggled to explain, was accounted for by a description of light as a transverse wave. It seemed only the nature of the aether needed to be settled.

Meanwhile, the rapidly advancing understanding of electricity and magnetism over the nineteenth century introduced the concept of the electromagnetic field, and early experiments by Michael Faraday and others began to demonstrate its intimate connection with light. In 1873, James Clerk Maxwell completed the theory now known as classical electromagnetism, which predicted waves in the electromagnetic field with the same properties as light. Very quickly, the scientific community put two and two together, and realised that light and these predicted electromagnetic waves were one and the same. This yielded a precise, mathematically consistent description of light as an electromagnetic wave, which came to be universally accepted and is still used today.[1]

1.2 The quantum world

Classical electromagnetism enjoyed several decades as the consensus description of light with strong experimental support. By the turn of the 20th century, however, several experiments were revealing serious inadequacies in the framework. The theory was unable to explain the observed spectrum of thermal radiation from idealised hot objects ("black bodies"), instead nonsensically predicting infinite radiated energy at high frequencies- an apparent paradox dramatically named the Ultraviolet Catastrophe. Meanwhile, an apparent discontinuity in the behaviour of electrons expelled from illuminated metals (the "photoelectric effect") also confounded the theorists. In 1900, Planck showed how the black body radiation spectrum could be reproduced in theory by proposing that light could only exchange energy with matter in discrete amounts proportional

[1] The predicted speed of light as electromagnetic radiation was determined entirely by the universal constants of electricity and magnetism, rather than by speed relative to any aether, in apparent conflict with Galilean relativity. The verification of this prediction of classical electromagnetism by several experiments ultimately sealed the fate the aether theory and the emergence of relativity, the other great pillar of modern physics.

to its frequency. Planck auspiciously named these chunks of energy "quanta". Subsequently, Einstein suggested that this "quantisation" of light was not a merely a detail of its interaction with matter, but was fundamental to its nature, and hence also deduced an explanation of the photoelectric effect. Quanta appeared to be indivisible, much like particles, and came to be attached to the name "photon". Having been buried for nearly a century, the corpuscular theory was suddenly re-animated, but with a ghostly twist: the outcomes of measurements on these particles, such as where they would hit an illuminated screen, was impossible to predict in advance with certainty, but following a probability distribution that behaved as a wave. This allowed the particle theory to be consistent with the earlier observations of Young and Arago. This "wave-particle duality" was the first glimpse into the new world of quantum mechanics.

Subsequent work on the quantum theory of light, known as quantum optics, showed that at this fundamental level light exhibits unfamiliar and exotic properties. The distinction is so marked that all of physics before the quantum revolution is collectively referred to as "classical", as opposed to "quantum" or "nonclassical". The classical understanding of an idealised measurement, in which the measured quantity need not be affected at all by the process of observation, proved to be fundamentally incompatible with the new theory. Instead, measurements could only result in one of a limited number of specific outcomes, occurring probabilistically from a set determined by the observer's choice of measurement basis. Gone was the non-probabilistic view of the "clockwork" Universe, sacrificed in favour of an intrinsically probabilistic theory - one describing a world where, apparently, God plays dice. Full knowledge of the state of a beam of light is only possible up to the ability to assign probabilities to the outcomes of measurements- it is impossible, even in principle, to predict precisely what the outcome of a quantum measurement will be. One consequence of this that will appear prominently in this thesis is that in quantum mechanics, the full state of a physical system cannot be described locally. Two or more physically separated light beams can be "entangled": their physical states cannot be considered independently of one another, and the choice of measurement made on

one must be taken into account to predict the behaviour of the other. This "spooky action at a distance", first explored in 1935 in the famous Einstein-Podolsky-Rosen (EPR) paper [1] and subsequently formalised and tested with the Bell inequalities, is considered by some to be the definitive indicator of quantum behaviour. Even so, there is still heated disagreement over the precise distinction between classical and quantum physics and what effects can be categorised as being comprehensively described by one or the other[2]. Concurrent work on the structure of atoms and the behaviour of free electrons showed that not just light, but ordinary matter also exhibits clearly quantum behaviour.

The basic theoretical groundwork of quantum optics was put on firm footing in the middle of the twentieth century. The new science predicted exotic states of light exhibiting effects that defied the predictions of classical optics. However, the same reasons that these "nonclassical" phenomena had been hidden from science for so long- the extreme difficulty in generating, manipulating and detecting these dim, fragile beams of light- meant that an earnest exploration of these new effects- and an appreciation of their potential usefulness- would have to wait for revolutionary technological advances.

1.3 The machinery of modern optics

1.3.1 Lasers

Ever since Archimedes used focused sunlight to ignite attacking Roman warships, people have sought to actively manipulate light for technological purposes. The need for better telescopes for naval purposes drove early progress in optical technology in the seventeenth century, which was compounded by the realisation that this technology had many more uses in astronomy, mi-

[2]The idea that classical physics can always be recovered from quantum mechanics in a certain limit is known as the *correspondence principle*.

croscopy and visual correction. Ever since then, the development of new techniques to control light has opened up new applications, in turn spurring demand for new technology. The most significant step-change in this progression came in the early 1960s, with the invention of the laser.

The principle behind laser operation is relatively straightforward. Lasers contain a material (known as the gain medium) consisting of particles with three or more possible energy levels, energetically separated by transitions with the energy of an optical-frequency photon. The gain medium is situated in a mirrored cavity and driven by an external energy source, known as the pump, to create a "population inversion", where one of the middle energy levels is less populated than a higher level. This creates the conditions for stimulated emission, where photons in a mode resonant in the cavity stimulate a cascade of more photons from the gain medium emitted into the same mode. The resulting avalanche of photoemission into a single optical mode manifests as a strong, coherent beam of light, consisting of vastly more photons concentrated into a smaller range of modes than had ever been feasible with earlier sources based on spontaneous emission.

Whilst it was originally regarded as little more than a curiosity, the laser soon came to be acknowledged, without exaggeration, as one of the most important inventions in history. Nowadays, a whole menagerie of lasers exists in many shapes and sizes- from quasi-monochromatic lasers emitting continuous waves with long coherence times to ultrafast pulsed lasers operating close to the single-cycle regime; from free-electron X-ray lasers to microwave masers and others spanning the entire electromagnetic spectrum in between; from attenuated lasers that contain very few photons to beams so bright that they are on the cusp of spontaneously generating matter-antimatter pairs. These lasers find a vast number of applications in various fields of academic research as well as industry.

The ability of high-power lasers to deliver large amounts of energy to a remote substrate or target is often first to capture the imagination. Whilst Archimedes would no doubt approve of

lasers used as directed-energy weapons, there remain major challenges with such applications and lasers are much more valuable for more peaceful purposes. Today, the revolution in computer technology rests to a considerable extent on the technique of optical lithography, where highly-focused laser beams are used to deliver the energy needed to write tiny, densely-packed features onto the surfaces of microchips. High-intensity beams of light have found myriad other uses, from welding to brain surgery. Paradoxically, laser light is also capable of cooling and trapping matter, and it is this capability that underlies recent momentous advances in atomic physics. However, it is exploitation of light's ability to transfer *information*, rather than energy, that is of greatest importance to our modern way of life.

Today, approximately 99% of all telecommunication is encoded as laser pulses propagating through optical fibre networks. The development of telecoms switching technology, low-loss fibres and fast photodetectors was also pivotal for this success, and such networks are now indispensible in delivering modern data services. Optical data storage devices are also a familar part of everyday life. As the name implies, Blu-Ray discs contain large amounts of information in surface features that are read by a short-wavelength optical frequency laser (able to resolve a higher density of features than the longer wavelengths used in earlier optical media formats such as DVD). Modern surveying techniques in agriculture, mining, vehicle tracking and architecture employ LIDAR: imaging, detection and ranging using lasers. Modern techniques in biological sciences such as optical fluorescence microscopy are especially dependent on lasers. Laser interferometry as a measurement tool is used across science, such as in the recent observations of gravitational waves by the LIGO collaboration [2].

The new availability of a bright, single-mode source of coherent light also marks the start the story of experimental quantum optics. An important step on this path was the development of the field of nonlinear optics. There are many effects that can modify a beam of light propagating through a material, and whilst some of these effects are linear in the electric field, the strength of others varies with its higher powers. Prior to the invention of the laser, it was not possible

to create beams of light bright enough for these nonlinear effects to be observed. With the discovery of second harmonic generation by Franken in 1961, however, it became possible to utilise such effects [3].

1.3.2 Nonlinear quantum optics

The advent of nonlinear optics opened a new route to experimentally access states of light that manifest nonclassical properties [4]. Over the past thirty years, two nonlinear optical processes- spontaneous parametric down conversion (SPDC)[5] and spontaneous four-wave mixing (SFWM)[6] have been put to use as a mechanism for probabilistic sources of photon pairs, which could in turn be used as a resource for conditionally-prepared single photons. Throughout this thesis, we will employ the first of these processes to provide us with nonclassical light. In contrast to previously-existing single-emitter sources of single photons, SPDC sources can be designed to produce single photons with very broad spectra and very short pulse durations. We will introduce the opportunities provided by this regime in Chapter 2.

Over the same period, considerable advances have made in the equally important sphere of single-photon detector technology [7, 8]. This was in part driven by the burgeoning interest in quantum technologies such as quantum key distribution (QKD) and quantum-enhanced measurements, which place stringent demands on detector performance. The development of solid-state avalanche photodiodes for single-photon detection, such as those used through the experimental parts of this thesis, provided a dependable workhorse for quantum optics experiments working with systems of single photons. At the cutting edge, the development of superconducting nanowire detectors and transition-edge sensors raise are raising hopes that optical quantum-enhanced technologies may become a practical reality in the near future.

At present, quantum optics is one of the liveliest and most promising areas of physics in which to work, with tremendous fresh progress such as loophole-free Bell tests and demonstrations of quantum teleportation. In the technological realm, quantum key distribution is already

close to being a practical means of fundamentally securing communications from eavesdropping, and nonclassical light is being used for ultra-sensitive interferometric measurements such as the gravitational wave detector [2].

1.4 Thesis outline

This thesis is organised into a succession of chapters, each building on those that came before it. Chapter 2 motivates why the physical systems that are the subject of this thesis- ultrashort quantum light pulses- are of scientific and technological interest, and why experimental approaches to characterising them are meritworthy. This then flows into a brief review of the existing technologies used to perform these measurements and their various benefits and limitations, and maps out the space that will be filled by the work described in the subsequent chapters.

Chapter 3 details the theoretical concepts that will be necessary to convey the ideas in this thesis. The first half of the chapter, starting with Maxwell's equations, proceeds to derive the concept of spectral-temporal modes and describes their representations and transformations. The second half derives the quantum mechanical description of electromagnetic fields from the solutions to Maxwell's equations and the imposition of field quantisation. It then introduces the crucial concepts of the single-photon and biphoton wave functions, as well as the density operator representation of incoherent mixtures. It also discusses multimode bipartite entanglement, the Gaussian states, and characterisation of the excitation state of the field through higher-order coherence function measurements.

Chapter 4 marks the beginning of the experimental part of the thesis. It introduces aspects of the experimental set-up that are common to all the work undertaken here, before describing the construction, calibration and characterisation of optical-frequency single-photon spectrometers based on the dispersive Fourier transform concept.

Chapter 5 makes use of two of these devices to realise a phase-sensitive measurement of the

spectral-temporal state of a single photon by nonclassical interference with a reference photon. It also introduces the pulse shaper, a device used to produce a variety of test pulses for such characterisation schemes, which will be used in the next chapter.

Chapter 6 describes a device that also characterises the full state of a single photon, but without the need for an external reference. This feature provides numerous advantages, which are described here. A full description of the contruction, calibration and demonstration of this device are presented, together with a discussion of its limitations.

Chapter 7 reports on work building on these capabilities to realise full characterisation of the wave function of a spectrally entangled photon pair. The experimental preparation of these entangled states is described, and the chapter ends with a presentation of results that demonstrate the effectiveness of this technique by comparing the reconstructions of entangled and separable quantum states.

Chapter 8, the final chapter of the main body, begins by describing theoretically how such entangled states can be used in practice to surpass the limits on precision that apply for certain classes of measurement when one is restricted to using classical probes. An experiment that demonstrates the feasibility of this prescription is then described.

The thesis finally concludes with a summary of what has been accomplished and a commentary on the outlook of this work.

Chapter 2

An introduction to ultrafast quantum pulse characterisation

Contents

2.1 Introduction 12

2.2 Why study ultrafast pulses? 13

2.3 Strategies for ultrafast quantum pulse characterisation 17

2.4 Partial single-mode characterisation methods 19

2.4.1 A note on real measurements of infinite-dimensional spaces 19

2.4.2 Spectrometry 20

2.4.3 Temporal intensity characterisation 22

2.4.4 Purity measurements 24

2.5 Full single-mode characterisation methods 24

2.5.1 Optical gating 25

2.5.2 Linear interferometric approaches 26

2.5.3 Spectral shearing interferometry 28

2.6 Entangled state characterisation 30

2.6.1 Stimulated-emission based measurement 30

2.6.2 Joint intensity measurements 31
2.6.3 Photon pair self-interferometry 32
2.6.4 Two-mode homodyne tomography 32
2.7 Chapter summary 32

2.1 Introduction

Of the various physical domains in which quantum information can be encoded, this thesis will focus on the longitudinal domain of ultrafast pulses - short-duration, spectrally broad flashes of light. The first objective of this chapter is to justify to the reader that it is of both fundamental and practical interest to consider ultrafast pulses as an interesting platform for quantum technologies. We also address how the spectral-temporal degree of freedom of such systems has previously been demonstrated as a platform for quantum information applications.

Once the importance of being able to extract information from such systems is established, we must answer what experimental techniques there are for studying a pulse, and how their suitability varies with its spectral-temporal properties. The second part aims to familiarise the reader with the various approaches to experimental determination of the temporal (spectral) amplitude of light pulses, and introduce how these techniques can be extended to characterisation of pulses with nonclassical properties. In asking this question, we are drawn into the field of pulse characterisation- that is, the study of experimentally retrieving various properties of the time-frequency mode of pulsed states of light.

All optical applications begin with the generation of a pulse of light, end with its detection, and in the interim involve some sort of manipulation or interaction with the light. The techniques involved in all three of these stages depend most heavily on the centre frequency of the pulse, ω_0, and the spectral bandwidth $\Delta\omega$. The latter largely determines the minimum pulse duration and hence the timescales over which the pulse intensity varies. Pulses with widely dis-

similar bandwidths are generated by particular sources, behave very differently under various physical processes, and are best suited to specific detection and characterisation schemes.

The scope of this thesis will focus on the ultrafast regime, considering modes of light with a relatively large bandwidth (typically several THz at optical frequencies) and consequently with pulse envelopes of around a picosecond or less.

This section will be divided into two parts. Firstly, we consider what can be learnt from characterising ultrafast pulses at the single-photon level, and why some form of characterisation is usually a pivotal part of any practical application involving ultrafast pulses. Secondly, we frame the work that follows in this thesis in its context by discussing existing approaches to pulse characterisation (focusing on characterisation at the single-photon level), their respective advantages and drawbacks, and the motivation for the work presented hereafter.

2.2 Why study ultrafast pulses?

The most useful property of light, fundamental to most of its applications, is it ability to carry information. The optical technologies that use light in this way can broadly be divided into three categories: metrology, logical processing, and communications.

Metrology is the general study of measurements. In the context of optics, this relates to protocols that use pulses of light to probe some relevant physical system, where the interaction with the optical field depends on certain parameters in which the experimentalist is interested, and characterise the returned optical probe. Where the dynamics governing the probe/system interaction is understood, it is thus possible to recover the values of the desired quantities. This is a very general concept, with applications ranging from finding one's way around a dark room with a torch to highly sophisticated quantum optical techniques aiming to surpass classical bounds on precision: in the case of quantum optics, non-classical states of light enable performance beyond that possible with classical resources alone in a range of applications [2,

9, 10]. Nonetheless, a common feature is that the characterisation of both the initial probe pulse and the returned signal, as well as an understanding of the processes governing the interaction, are essential to any such realisation.

Light is also increasingly being explored as a physical system for simulating complex problems [11, 12]. In the quantum realm, proposals based on optics are in serious contention as a platform for realising a quantum computer or simulator, such as linear optical quantum computing [13], boson sampling [14] and optical qubit gates mediated by Rydberg atoms [15]. The potential applications of a universal quantum computer are myriad, ranging from modelling complex biologically relevant molecules for medical research, simulating many-body solid state quantum systems, and cryptoanalysis.

Sadly, the comparatively weak interactions of photons with their environment and one another, compared to material quantum system such as trapped ions and solid-state excitations, raises doubts about their suitability for quantum information processing. Fortunately, the same property makes them ideal for encoding "flying" qubits: to act as the medium for coherent communications between physically remote endpoints. Through optical fibre networks, photons can carry quantum information coherently over considerable distances, making optical systems uniquely suitable for applications in communications, which solve problems where two parties need to exchange information remotely. It is therefore widely anticipated that future quantum communications networks will make use of nonclassical states of light for protocols such as quantum key distribution [16, 17] and quantum-enhanced channel capacity [18].

In each field, the ability to encode or extract a greater information capacity in the degrees of freedom of the pulse is desirable, since it allows more precise measurements, higher processing speeds, or faster bit rates and/or greater security in communications. Information can be encoded in any of the degrees of freedom of paraxial pulses (polarisation, spectral-temporal mode or transverse spatial mode). Though the easiest to manipulate, the capacity of polarisation encoding is limited by its finite dimensionality to one qubit per photon. The spectral-temporal and

spatial degrees of freedom, by contrast, are infinite-dimensional, and so information capacity is limited only by the experimentalist's ability to resolve the longitudinal or transverse structure of the pulse or, in the case of communcations, the encoder resolution. The latter domain, however, requires wide multi-mode fibres and spatially-resolved detection, and is vulnerable to wavefront distortion, leading to cross-talk which in many applications proves prohibitive. By comparison, spectral-temporal encoding is naturally compatible with integrated optics and fibres, allowing practical bit rates of many gigahertz for a single-mode fibre, and so this domain is used for the primary encoding in conventional optical telecommunications. Processes that distort the signal, such as dispersion or loss, can be largely circumvented using careful engineering or sophisticated characterisation and cancellation.

With the development of mode-locked lasers [19], ultrashort pulses of light have found numerous applications in both metrology and communications. The underlying reasons for their great utility is their short duration and large spectral bandwidth. When the experimentalist has access to high-resolution spectrometers and pulse-shaping techniques, this allows for a great deal of information to be conveyed on a shot-by-shot basis. In the metrology sphere, the short timescales over which their intensity rapidly varies makes them suitable for probing a wide range of dynamic processes. In the classical regime, ultrashort pulses of light have become a vital tool and are commonly used for probing the internal dynamics of atomic and molecular processes [20], with applications ranging from precision metrology [21] and spectroscopy [22] to communications and control [23].

As attention on quantum optical technologies increases, the distinctive features of ultrafast pulses for use in quantum applications are increasingly being recognised. Experimental demonstrations have already taken place in many of these spheres, including quantum information processing [24, 12], quantum-enhanced sensing [25] and quantum cryptography [26].

Whilst there are advantages and disadvantages to using light from either the narrowband or broadband regimes as a platform for quantum information, ultrafast optics and quantum optics

have a broad and important interface. Amongst the most dependable processes for producing light with nonclassical properties depend on optical nonlinearities, such as spontaneous parametric down-conversion (SPDC) [5] and four-wave mixing [6]. In such processes, the efficiency scales strongly with the maximum intensity of the driving optical fields, and hence short-duration pulses with high instantaneous intensity are necessary. Often the output of these processes will be nonclassical pulses in the ultrafast regime, which will subsequently be used as a nonclassical resource.

Additionally, broadband quantum light pulses are of interest because the spectral degree of freedom is easily manipulated in a way that preserves the useful quantum properties of the pulse. Classical information can be transferred from one stage of an optical network to the next by mode-selective amplification, which amounts to detection and regeneration of the pulse, and this is the principle behind some forms of classical pulse shaper and classical repeaters. Such amplification is fundamentally not possible in a quantum optical network, where interaction with detectors/amplifiers collapses the wave function of the quantum system. Hence, unitary (phase-only) operations are of particular utility in a quantum network. In this context, broad spectral bandwidth is advantageous, since spectral phase operations are easier to execute in practice than temporal phase operations and so broadband pulses are more experimentally controllable than narrowband ones.

It goes without saying that the generation, interaction and detection of quantum light pulses in each of these uses all involve processes that depend heavily on their spectral-temporal profile. The practical development of nonclassical light sources and detectors must necessarily involve techniques to characterise the field modes with which they interact. Quantum process tomography, the full characterisation of an operation on a quantum system, will also require the complete reconstruction of the state of the returned probe, and hence full state characterisation also plays a direct role in many metrology applications.

Furthermore, in some proposed quantum networks, high coupling efficiencies at interfaces

are a crucial specification that must be met in order to perform complex quantum information processing protocols, which may involve thousands of interacting quantum systems [27]. Where light is used to convey quantum information between these separate systems, these efficiencies are maximised by mode matching between the two stages of the network. When designing such interfaces, exquisite characterisation of the optical states that couple in and out of the system is therefore indispensible. An example of this might be transferring the output of one part of a quantum logic processor to another for additional processing: full characterisation of the electromagnetic field modes with which the two processor systems interact is essential for designing a working interface.

2.3 Strategies for ultrafast quantum pulse characterisation

Nonclassical light, which is typically at the single-photon level of intensity, has very different detection criteria compared to classical light. Charge-coupled devices (CCDs), the workhorse of high-dimensional classical optical detection, and conventional photodiode-photoamplifiers typically exhibit much higher levels of background noise than are compatible with reliable single-shot single-photon detection. Consequently, myriad different types of detectors have been developed for the expressed purpose of detecting single-photon-level light, including avalanche photodiodes, nanowires and transition-edge sensors [7, 8], and homodyne detectors have been adapted for quantum measurements [28]. Single photon detectors can be compared on many different figures of merit, including temporal resolution, quantum efficiency, spectral bandwidth, dark count rate, dead time, photon number-resolving ability and cost [7]. There is an intricate series of trade-offs between each of these different parameters.

Additionally, several well-established techniques that enable measurement of the pulse-mode structure of high-intensity optical fields utilize nonlinear optical interactions in the test field. However, at the single-photon level these techniques have miniscule or zero efficiency due

to the weakness or total absence of optical nonlinear effects for such low-intensity fields. Whilst it is sometimes possible to infer the properties of quantum light pulses using an analogous classical process, such as stimulated emission characterisation of a downconversion source, this is often not feasible and quantum light pulses require either modified versions of the characterisation schemes used for classical pulses, or entirely new methods. In this section, we will introduce the methods used for classical pulse characterisation and extend this to the state of the art in the pulse characterisation of quantum pulses.

Due to the relatively weak response of most materials to magnetic fields, the electric component of the optical field is usually the part of most interest, and pulse characterisation problems are usually framed in terms of recovering the electric field $\mathbf{E}(\mathbf{r}, \mathbf{t})$. A quantity of central interest for much of this thesis will be the longitudinal or spectral-temporal mode. This will be defined rigorously in the next chapter, but here it suffices to say the mode provides a complete description of the spectral/temporal properties of the pulse. The spectral-temporal mode is most often represented either as a function of time, the temporal mode $\varepsilon(t)$ (governing the variation of the electric field in time), or frequency, the spectral mode $\tilde{\varepsilon}(\omega)$ (the relative spectral decomposition of the pulse), although an infinite number of other representations are possible. These two representations are *conjugate*, meaning they are related by the Fourier transform:

$$\tilde{\varepsilon}(\omega) = \frac{1}{\sqrt{2\pi}} \int \varepsilon(t) e^{-i\omega t} dt = \mathcal{FT}\{\varepsilon(t)\}, \tag{2.1}$$

and the inverse Fourier transform:

$$\varepsilon(t) = \frac{1}{\sqrt{2\pi}} \int \tilde{\varepsilon}(\omega) e^{i\omega t} d\omega = \mathcal{FT}^{-1}\{\tilde{\varepsilon}(\omega)\}. \tag{2.2}$$

The spectral mode and the temporal mode uniquely determine one another, which is why they are considered as two representations of the same quantity.

Both the temporal mode and the spectral mode are complex quantities, meaning that at any given time (or frequency) they have both an amplitude (the relative strength of the electric field) and a phase. This is made explicit by writing the mode functions in terms of their amplitude and phase:

$$\varepsilon(t) = |\varepsilon(t)|e^{i\phi(t)} \tag{2.3}$$

$$\tilde{\varepsilon}(\omega) = |\varepsilon(\omega)|e^{i\phi(\omega)}, \tag{2.4}$$

where $|\varepsilon(t)| \geq 0$ and $|\tilde{\varepsilon}(\omega)| \geq 0$ are the temporal and spectral amplitudes respectively, and $0 \leq \phi(t) < 2\pi$ and $0 \leq \phi(\omega) < 2\pi$ are the temporal and spectral phase, respectively. The most convenient representation depends on the characterisation scheme most appropriate for the properties of the pulse. In the case of ultrafast pulses, the total duration of the pulse is often shorter than the temporal resolution of even the fastest classical photodiodes, meaning that direct measurements of the structure of the temporal intensity is challenging. By contrast, such broadband pulses can be finely resolved by modern spectrometers. It is therefore often expedient to represent ultrafast pulses in the frequency domain by $\tilde{\varepsilon}(\omega)$. Full characterisation is then broken down into the two problems of determining the spectral intensity $|\tilde{\varepsilon}(\omega)|^2$ and spectral phase $\phi(\omega)$. Various approaches have been developed to perform these measurements. Firstly we discuss partial characterisation methods, which limit their scope to learning only some of these properties.

2.4 Partial single-mode characterisation methods

2.4.1 A note on real measurements of infinite-dimensional spaces

Before plunging into a detailed analysis of characterisation techniques, it is worth being clear what is meant when discussing real-world measurements in a continuous parameter space like

the time-frequency domain. For example, clearly the spectral intensity of a pulse $\tilde{\varepsilon}(\omega)$ is continuous and therefore spans an infinite-dimensional vector space. All real spectrometers, however, are necessarily limited by some finite resolution $\delta\omega$. Below this scale, such spectrometers are unable to distinguish spectral structure. We must therefore implement a discretisation of the frequency domain into a set of bins, where the intensity in one such bin centred at frequency ω_n is given by

$$|\tilde{\varepsilon}_n|^2 = \int_{\omega_n-\delta\omega/2}^{\omega_n+\delta\omega/2} |\tilde{\varepsilon}(\omega)|^2 d\omega \tag{2.5}$$

In reality, the property of fundamental interest when considering all-optical effects is the mode overlap, defined in the next chapter. For a finite-dimensional characterisation of this type to suffice for evaluating the mode overlap between two pulses, it is necessary to assume that there are no rapid variations of $\tilde{\varepsilon}(\omega)$ above the sampling rate provided by the resolution $\delta\omega$. We will simply bear this caveat in mind as we proceed with our analysis.

2.4.2 Spectrometry

We begin by discussing methods to determine the spectral intensity $|\tilde{\varepsilon}(\omega)|^2$ [29]. There are two broad categories of approach to gathering the spectrum of a beam of light. One approach involves scanning an optical element that maps spectral information onto the amplitude of the beam followed by direct intensity detection, and this forms the basis of spectral measurements using Fabry-Pérot etalons and Fourier-transform spectrometers. Both methods are applicable at the single-photon level. The spectra of heralded single-photon and two-photon states have been realized using scanning monochromators [30] and Michelson interferometers [31]. A significant drawback to scanning measurements is that this approach does not allow access to all spectral modes simultaneously, reducing the information content available in a single measurement outcome. This fact renders scanning measurements largely useless for real-time information processing and communications.

The alternative approach couples spectral modes with another set of modes such as transverse spatial modes. This technique underlies the standard spectrograph in which an angular dispersion element, such as a prism or grating, maps the spectral modes of an input optical beam onto a range of transverse spatial frequencies that can be transformed into localized points by a lens and monitored with an array of intensity detectors such as CCDs. In principle, mapping frequency modes of a beam onto the transverse spatial modes allows simultaneous monitoring of all spectral channels with a spatial array of detectors. However, this approach is difficult to realize with heralded single photons and two-photon states where coincidence events must be registered, owing to challenges in fabrication of large, low-noise and efficient arrays of independent single-photon-counting detectors [32].

The frequency distribution of pulsed light can be mapped onto temporal modes by a medium with high group delay dispersion (GDD) and monitored with a single intensity detector with high temporal resolution [33, 34]. This underlies the technique of fibre-assisted dispersive spectroscopy. At the single-photon level this method was first used to measure the JSI of a biphoton source at telecommunications wavelengths [35] where a 3.3 km long dispersion compensating fibre introduced the necessary GDD. Subsequent works [36] have improved the resolution by using more dispersive fibres. Within the visible spectral domain significant losses in optical fibres make this approach infeasible. A spatio-temporal arrangement, SCISSORS [37], also achieves frequency-to-time mapping mediated by spatial dispersion using a cavity-like arrangement of mirrors, which can achieve reasonable efficiency at near-infrared wavelengths. However, it lacks the all-fibre character and achieves much lower resolution over a limited spectral range.

Each approach has different advantages. For example, methods that involve scanning require only a single detector and achieve high spectral resolution. However, scanning methods suffer from the time needed to acquire full spectral information and can be limited in the overall spectral range that can be readily accessed. Concurrent monitoring of multiple spectral modes

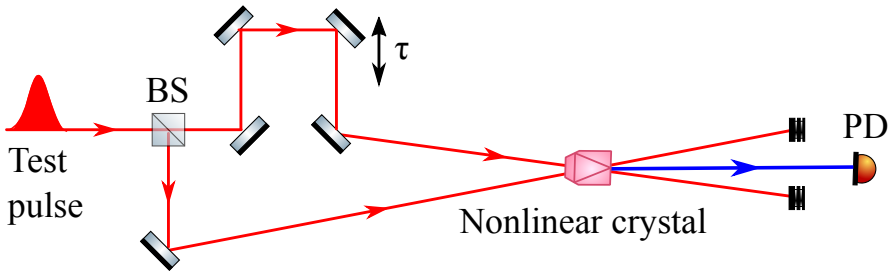


Figure 2.1: Schematic diagram of an intensity autocorrelator. The test pulse is split at a beam splitter and recombined with a variable relative time delay τ inside a nonlinear crystal. The second harmonic generated in the crystal is then routed into an intensity-detecting photodiode, where a trace of its intensity as a function of τ is generated and used to deduce the pulse duration. BS: Beam splitter

by multiplexed detection is more useful for quantum applications and possibly more efficient, but requires greater detection capacity. A resource-optimised approach to resolving this problem for ultrafast pulsed modes will constitute the subject of Chapter 4.

Recently, transition edge sensors [38] form an emerging third category of spectrally-resolved detectors that function on a principle of direct sensitivity to the energy deposited by photons. Whilst an exciting development, at present these devices suffer from low temporal resolution, high construction and operation costs (owing to the cryogenic environment required for them to function) and a long post-detection period on the order of microseconds during which the detector is less sensitive to subsequent events.

2.4.3 Temporal intensity characterisation

For most pulses, knowledge of both the spectral and temporal intensity is insufficient for a full determination of the field amplitude $\varepsilon(t)$. However, for some purposes it is sufficient, or at least instructive, to learn the temporal amplitude profile $|\varepsilon(t)|$, and several methods exist for measuring this piece of the puzzle.

Streak cameras provide a direct measurement of the temporal amplitude of ultrafast pulses, with commercially-made devices available with resolutions down to hundreds of femtoseconds.

The principle of operation of streak cameras is simply to "sweep" the pulse across a range of spatial trajectories as it passes through the device- hence, it may be thought of as the temporal analogue of a prism. There are both mechanical approaches, using a rotating mirror or electro-optic medium to deflect the pulse onto an array of photodetectors, and optoelectronic schemes in which the pulse is routed onto a photocathode, mapping its temporal profile onto a pulse of photoelectrons which are then swept by a rapidly varying electric field. This approach has been demonstrated to measure the temporal intensity of pulses down to the single-photon level across a range of wavelengths [39]. Whilst useful for many applications, others require better temporal resolution than is attainable with a streak camera, or more complete phase information.

An experimentally simple approach to measuring the duration of a bright pulse is to use an autocorrelator. This is a device that splits the pulse at a beam splitter, applies a variable relative time delay τ between the two output modes, recombines them inside a nonlinear crystal engineered for second hamonic generation, and monitors the intensity of the upconverted light as a function of the applied delay (see Fig. 2.4.3). This technique is also referred to as optical gating, since upconverted light is only generated when the intense part of the pulse passes through a gate provided by a copy of the pulse itself. Time-integrated measurement of how the second harmonic intensity $A(\tau)$, proportional to the square of the cross-product of the two fields $|\varepsilon(t)\varepsilon(t+\tau)|^2$ varies with this delay provides the temporal intensity autocorrelation:

$$A(\tau) = \int |\varepsilon(t)\varepsilon(t+\tau)|^2 dt = \int I(t)I(t-\tau)dt \tag{2.6}$$

from which it is possible to completely recover the temporal intensity $I(t)$. However, information about the temporal phase is inaccessible. Since a nonlinear (two-photon) process is fundamental to the operation of the device, there is no analogue of an intensity autocorrelator for measurements on single-photon pulses.

2.4.4 Purity measurements

In addition to characterising the mode structure of a pulse, another quantity of interest is the purity of the pulses. In classical terms, the pulse train may not always be coherent; that is, successive pulses may not always have identical spectra or spectral phase relationships. In the quantum notation, it cannot always be assumed that the density matrix of the quantum state describing the pulse is spectrally-temporally pure. In conjunction with other characterisation techniques for the mode itself, there are also several techniques for bounding the spectral-temporal purity of the density matrix.

In the case of long-duration pulses, it is usual to measure the coherence length. This is usually performed by injecting the light into a Michelson interferometer and varying the delay, generating a fringe pattern. The period over which the visibility of the fringes falls reveals the duration over which the signal is coherent. The coherence of downconverted light can also be measured using higher-order correlation measurements, which will be discussed in the next chapter.

2.5 Full single-mode characterisation methods

Whether working in the spectral or temporal representation, it is necessary to simultaneously measure both the intensity and phase domains in order to perform a complete characterisation of a pulse. Whilst spectrometers suffice to perform the spectral intensity measurement, the need to reconstruct the spectral phase demands that full characterisation schemes must make use of interferometry or otherwise involve some phase-sensitive process. Full characterisation schemes can therefore be divided into two categories: *self-referenced* and *externally-referenced*. Self-referenced schemes are those in which the only optical field in the scheme is that of the test pulse, which undergoes some phase-sensitive process to yield the final measurement. Externally referenced methods, by contrast, employ an additional well-characterised optical field

to interfere with the test pulse. Self-referencing techniques are generally considered more desirable for several reasons. Without a second optical field, which typically needs to be stable, tunable, well-characterised and appropriately mode-matched to the test pulse, they generally require simpler experimental schemes. The need for external references to have good mode overlap with the test pulse also means that *a priori* knowledge of the test pulse, such as the domain of spectral support, is often needed. By contrast, self-referencing schemes are much more flexible in this regard, and are usually limited by technical considerations such as the bandwidth of their constituent optics. Finally, externally-referencing schemes usually require repeated reconfiguration of the device, whereas some self-referencing approaches such as spectral shearing interferometry can perform complete pulse characterisation on a single-shot basis. However, the weakness of the electric field at the single-photon level limits the use of processes that are nonlinear in the test field, which excludes large classes of self-referencing methods, and until now all techniques to characterise light at the quantum level have used some sort of external optical reference field.

2.5.1 Optical gating

Whilst autocorrelators are limited in that they cannot provide temporal phase information and hence fall short of a full reconstruction of the field amplitude, a slight modification of the concept suffices to extract the extra information and provide a complete reconstruction. This is simply to replace the non-resolving detection of the upconverted light with a frequency-resolving measurement, generating a time-frequency spectrogram from which full reconstruction of the mode is algorithmically possible. This entirely self-referencing scheme is known as frequency-resolved optical gating (FROG) and, along with SPIDER (described below) it is one of the two preferred methods for full characterisation of coherent ultrafast pulses [40]. As with an autocorrelator, however, the nonlinear process needed to mediate the optical gating is prohibitively inefficient at low intensities, and so this there is no self-referencing analogue for this method at

the single-photon level.

Nonetheless, optical gating with an intense external pump is itself a useful strategy in ultrafast quantum pulse characterisation, and this is the operational principle of the so-called quantum pulse gate [41]. In this scheme, an unknown pulse undergoes a mode-selective upconversion process, gated by a strong pump field. The upconverted photon is then filtered from the transmitted signal and measured, allowing the conversion efficiency to be recorded and hence the overlap of the test pulse with the (known) accepted mode to be determined. In principle, by shaping the mode of this pump pulse, it is possible to control the accepted mode of the gate and hence construct a complete set of measurements that allows full determination of the pulse. It has also been used for partial characterisation, such as temporal intensity measurements using extremely short, intense pump pulses that create a short temporal gate [42]. Indeed, a version of this technique using an atom-mediated nonlinearity and ultrashort attosecond pulses was recently demonstrated to directly measure the electric field of an optical-frequency field, allowing direct measurement of both the temporal amplitude and phase [43].

2.5.2 Linear interferometric approaches

There are several methods to characterise quantum light using an external reference that have previously been demonstrated. Wasilewski, Kolernderski and Frankowski demonstrated a scanning method based on Hong-Ou-Mandel interference with a pair of attenuated laser pulses with tunable relative and global delay [44]. By scanning these two parameters and observing the coincidences at the output of the device it is possible to reconstruct the full spectral-temporal state of the pulse.

Additionally, there are several techniques based on homodyne detection with shaping of the local oscillator, in which the test pulse is sent into a homodyne detector where the local oscillator is earlier routed through a pulse shaper. Homodyne detection is sensitive to the photon number statistics of the test pulse in the spectral-temporal mode of the local oscillator (LO), and

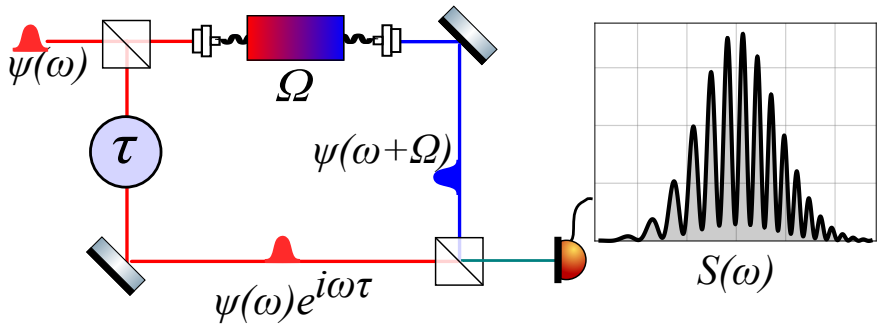


Figure 2.2: **Measurement principle.** The test pulse, in a spectral mode determined by the unknown function $\psi(\omega)$, enters a Mach-Zehnder interferometer in which one arm receives a spectral shear Ω and the other a relative time delay τ. Spectrally-resolved detection reveals an interference pattern $S^{+}_{\Omega,\tau}(\omega)$. Fourier analysis of the observed interference pattern enables extraction of $\phi(\omega+\Omega)-\phi(\omega)$ and thus determination of $\phi(\omega)$. The full amplitude and phase of the single-photon-occupied mode can be computationally reconstructed.

hence by tuning the LO mode and measuring how occupancy changes, it is possible to determine the mode of the single photon. In one scheme, the shape of the local oscillator is scanned to produce a tomographically complete set of measurements [45]. In another demonstration, the local oscillator is adaptively tuned in feedback with the photocurrent measurements until single-photon occupancy of the local oscillator mode is measured, allowing a faster convergence to the final state [46].

The above methods suffer from the disadvantage that they are limited to characterisation of single-photon pulses, since it is necessary to suppose the photon number statistics within the unknown mode of the test pulse to derive the correlation functions. Being scanning methods, where the aim is to tune the reference to achieve optimal mode-matching in response to earlier measurements, they require some measurable overlap in the initial configuration. They also require repeated reconfiguration of the set-up mid-measurement, which can prohibitively increase measurement times.

2.5.3 Spectral shearing interferometry

Besides FROG, the other self-referencing method for ultrafast pulse characterisation is spectral shearing interferometry (SSI). The principle behind SSI is to interfere different frequency modes of the same pulse such that the relative spectral phase between them imprints in the interference pattern. The protocol for obtaining the spectral phase using SSI is outlined in Fig. 2.2 [47]. This involves splitting the pulse at a $50:50$ beam splitter, applying a constant, phase-preserving spectral translation, or spectral shear, Ω, to one of the copies and a temporal delay, τ, to the other, recombining the two at a beam splitter, and measuring the resulting spectral interference pattern. For a single-photon pulse in a mode given by $\tilde{\psi}(\omega) = |\tilde{\psi}(\omega)|e^{i\phi(\omega)}$ the intensities at the outputs of the interferometer are

$$\begin{aligned} S^{\pm}_{\Omega,\tau}(\omega) =& \frac{1}{4}\{S(\omega) + S(\omega+\Omega) \\ & \pm 2\mathrm{Re}\left[\tilde{\psi}(\omega)\tilde{\psi}^{*}(\omega+\Omega)e^{i\omega\tau}\right]\}, \end{aligned} \tag{2.7}$$

where $S(\omega)$ is the spectral intensity of the original pulse. The interferogram $S^{\pm}_{\Omega,\tau}$ contains information about the spectral phase difference $\phi(\omega+\Omega) - \phi(\omega)$. If Ω and τ are known, the spectral phase can be extracted from a single interferogram using Fourier transform based algorithms [47, 48], although multiple acquisitions may be processed together to improve the reliability of the reconstruction. There are different variations of SSI, with the most important distinction being the method used to obtain the spectral shear. The most common implementation is spectral phase interferometry for direct electric field reconstruction (SPIDER), which uses sum-frequency generation, a nonlinear process. SPIDER is now a standard technique for the characterisation of bright ultrafast pulses, and like FROG the optical nonlinearity in the test field implies this is not a suitable scheme for single-photon-level light. However, there are other ways to obtain the spectral shear, and some of these have been demonstrated as alternatives to

SPIDER. One such alternative is electro-optic spectral shearing, where an electro-optic modulator is used to apply a time-varying phase across the pulse duration, creating a constant frequency translation [49]. Electro-optic spectral shearing offers several advantages that make it suitable for SSI on quantum light pulses. The spectral shear can be realized uniformly over a large wavelength range using a single device, and is largely independent of the incident pulse shape. Hence only basic knowledge about the input mode, such as wavelength compatibility with the setup, is required and the same experimental configuration can accurately characterize any of a diverse range of input pulses. Electro-optic shearing also achieves unit efficiency independently of the pulse intensity, enabling it to be used even at the single-photon level. Electro-optic shearing interferometry (EOSI) therefore ticks a great many boxes in the checklist for the perfect single-photon characterisation tool:

- It is self-referencing, simplifying the experimental scheme;
- There is no need to scan the set-up mid-measurement to build a complete reconstruction. In the classical case this implies SPIDER can characterise a pulse from a single measurement; with single photons, repeated measurements without reconfiguration suffices for full tomography. This is associated with shorter measurement times and, for adaptive schemes reduces the amount of prior knowledge of the mode needed to achieve a characterisation;
- It can be implemented without intrinsic sources of loss, so every pulse sent into the device contributes to the final characterisation;
- It does not require any prior supposition of the photon-number statistics of the pulse: it accurately characterises the spectral temporal mode regardless of whether occupied by a single photon, a coherent state or thermal state, for example;
- As discussed in Chapter 6, it can be generalised to the case where the pulse train is

only partially spectrally coherent, or exhibits quantum correlations with another photonic quantum subsystem.

For these reasons, we will return to spectral shearing interferometry in Chapter 6, where we will explain it in more detail and apply it to the problem of single-photon state characterisation.

2.6 Entangled state characterisation

So far, the emphasis of this chapter has been on characterising a single mode with few-photon occupancy. As we shall see in Chapter 3, however, it is only in certain special cases, such as a single-photon state, where quantum optical states can be fully described by a single spectral-temporal mode. This scope of this thesis extends beyond this, to the full characterisation of certain multiphoton states where this constraint does not apply. In particular, Chapter 7 will be concerned with the biphoton state- two distinguishable photons exhibiting bipartite spectral-temporal entanglement. For such systems, characterisation of the mode of each photon individually is insufficient to describe the whole state, since such an approach is intrinsically insensitive to the correlations that exist between the two subsystems. Once again, the distinction between externally and self-referenced techniques exists, indeed more severely: mode overlap is now required across a much larger parameter space, making scanning-type measurements all the less efficient. Up to now, a general approach to full characterisation of such states is yet to be published. Nevertheless, much progress has been made towards this end. Here we introduce some of the recent work that has been undertaken towards characterisation of spectrally-temporally correlated photon pairs.

2.6.1 Stimulated-emission based measurement

For some processes used to generate nonclassical light, such as SPDC or spontaneous four-wave mixing, the spontaneous process is associated with a classical stimulated process: difference

frequency generation (DFG), and (stimulated) four-wave mixing (FWM), respectively. In DFG and FWM, an intense beam known as the seed is injected into the nonlinear medium in the signal and/or idler modes in addition to the pump. The seed mode then undergoes parametric (de-)amplification in a process usually described classically, but can be related to the associated spontaneous process. This close relationship can be used to infer the properties of spontaneously generated pulses from the same source. Several experiments have been performed using this strategy, usually involving a tunable, narrowband seed field and spectrally-resolved detection of the signal using a usual grating/CCD spectrometer [29, 50]. Using phase-sensitive amplification, it is possible to conduct a reconstruction of the full joint amplitude of the down-converted photon pairs [51]

Whilst a quick and effective way to learn the joint spectral properties of parametric sources of quantum light, this technique has several drawbacks that limit its utility as a general characterisation strategy. It is specific to certain types of source, and no analogous mechanism exists for other types of single-photon source such as single emitters. It fails to account for other contributions to the spontaneous signal that do not scale in the same way in the stimulated process, such as Raman scattering noise. Finally, in common with externally-referenced techniques, it requires access to a stable and tunable seed field.

2.6.2 Joint intensity measurements

Direct, coincident measurement of the intensities of the photons in the pair are also possible. Joint spectral intensity (JSI) measurements have been performed using some of the above techniques performed in conjunction with coincident detection. Directly resolving individual photon pairs has been achieved away from telecommunications wavelengths using variants on scanning methods in which most photons are discarded [52, 30], or the spectral bins are not monitored directly [31]. Joint temporal intensity (JTI) measurements are also possible, either directly [52] or through nonlocal temporal intensity interference via. Franson interferometry

[53]. Recently, MacLean, Donohue and Resch demonstrated the ability to perform both spectral and temporal intensity measurements in coincidence on a photon pair, gathering both the JSI, JTI as well as the two joint spectral/temporal intensity functions [42]. Whilst this suffices to verify entanglement, it falls short of a full characterisation, with some phase information remaining inaccessible.

2.6.3 Photon pair self-interferometry

Narrowband photon pairs have been fully characterised using one another as a reference and using a variable delay followed by time-resolved measurement [54], although this method is restricted to spectrally narrow biphotons with good spectral and spatial overlap.

2.6.4 Two-mode homodyne tomography

As we have already noted, homodyne detection has been shown to be an effective technique for characterisation of unentangled photonic systems. Whilst homodyne detection schemes have been employed to characterise bipartite systems, the aim of this is usually limited only to entanglement verification rather than full characterisation. A complete optical homodyne tomography of an entangled two-photon system is yet to be demonstrated [55].

2.7 Chapter summary

In this chapter we have justified the technological and scientific interest in ultrafast pulse characterisation. We discussed the emerging importance of extending the large corpus of exisiting work in classical pulse characterisation to quantum applications in diverse areas such as measurement, processing and communications, and the reason for the interest in ultrafast quantum pulses in particular. We then described some of the existing methods used for ultrafast pulse characterisation at the single-photon level. This culminated in the introduction of electro-optic

spectral shearing interferometry and its suitability for quantum state reconstruction. The final part delineated the problem of characterising multi-photon systems featuring bipartite spectral temporal entanglement, and notes some of the existing methods for performing this measurement, together with their limitations.

Chapter 3

Time-frequency quantum optics

Contents

3.1 Introduction 36

3.2 Spectral-temporal modes in classical electromagnetism 37

3.2.1 Paraxial approximation 39

3.2.2 Modes and mode transformations 41

3.2.3 Temporal representation of modes 43

3.2.4 Hermite-Gauss representation of modes 45

3.2.5 Spectral representation of modes 46

3.2.6 Spectral phase and dispersion 48

3.2.7 Temporal phase operations 52

3.2.8 The chronocyclic Wigner representation 53

3.3 Quantisation of the electromagnetic field 58

3.3.1 A single mode 58

3.3.2 Approaches to quantisation 59

3.3.3 Canonical quantisation 59

3.3.4 The wave function of a single photon 64

3.3.5 Density operators 67

3.3.6 Fidelity of quantum states 69
3.3.7 Photon pairs and multimode entanglement 69
3.3.8 Gaussian states 73
3.3.9 Coherence functions 76
3.4 Chapter summary 81

3.1 Introduction

Having established a broad motivation for this thesis, we will now lay out the details required to understand its substance. In this chapter we will lay down the theoretical groundwork necessary for this task, with the chapter divided into two parts.

The first part will begin with the theory of classical electromagnetism and provide the modal solutions to Maxwell's equations, subject to two important approximations within which all the work in this thesis proceeds: the paraxial approximation and the slowly-varying envelope approximation. This naturally leads on to the formalism of the time-frequency domain of light. This leads to the introduction of the concepts of normalised temporal/spectral modes and their transformations. We introduce the Hermite-Gauss set of pulsed modes, which frequently appear in ultrafast quantum optics, and describe the properties of Gaussian pulses, which are used to exemplify the action of spectral and temporal phase operations on pulses. The first section is concluded by introducing the chronocyclic Wigner representation of pulsed modes and its properties.

We will then describe the emergence of quantum optics from classical electromagnetism, a conceptual process known fairly sensibly as *quantisation*. This section will introduce many ideas that will reappear continually throughout this thesis, including the canonical variables of the electromagnetic field, bosonic creation and annihilation operators, Hilbert spaces, Fock states and ultimately, the concept of a photon and its mathematical representation. We will

discuss what is meant by the full state of quantum light, expanding on this for the single-photon and biphoton cases, and discuss some of their properties and notion of entanglement. We introduce the idea of mixedness in a single photon state, and the general density matrix formalism used to describe it. Gaussian states are then presented in their general form, and the specific variants that appear in this thesis are introduced. Finally, we discuss the quantum coherence functions of Glauber and others, and how they are necessary to fully characterise an arbitrary multimode beam of nonclassical light.

The chapter is then concluded with a brief summary reprising these concepts.

3.2 Spectral-temporal modes in classical electromagnetism

In free space Maxwell's equations are given in their differential form by:

$$\text{Gauss' law for electricity:} \quad \nabla \cdot \mathbf{E} = 0 \tag{3.1}$$

$$\text{Gauss' law for magnetism:} \quad \nabla \cdot \mathbf{B} = 0 \tag{3.2}$$

$$\text{Faraday's law:} \quad \nabla \times \mathbf{E} = -\frac{\partial \mathbf{B}}{\partial t} \tag{3.3}$$

$$\text{Ampere-Maxwell law:} \quad \nabla \times \mathbf{B} = \mu_0 \epsilon_0 \frac{\partial \mathbf{E}}{\partial t}. \tag{3.4}$$

Here $\mathbf{E}$ and $\mathbf{B}$ are the electric and magnetic fields, respectively, and ϵ_0 and μ_0 are universal constants known respectively as the permittivity and permeability of free space. Taking the curl of both sides of Eq.3.3 and using the commutativity of linear differential operators gives

$$\nabla \times \nabla \times \mathbf{E} = -\frac{\partial}{\partial t} \nabla \times \mathbf{B}. \tag{3.5}$$

Applying Eq.3.2 to the right hand side and using the vector identity

$$\nabla \times \nabla \times \mathbf{F} = -\nabla^2 \mathbf{F} + \nabla(\nabla \cdot \mathbf{F}), \tag{3.6}$$

and remembering $\nabla \cdot \mathbf{E} = 0$, gives the wave equation

$$\boxed{\nabla^2 \mathbf{E} - \frac{1}{c^2}\frac{\partial^2 \mathbf{E}}{\partial t^2} = 0,} \tag{3.7}$$

where $1/c^2 = \epsilon_0 \mu_0$. The duality between $\mathbf{E}$ and $\mathbf{B}$ in the Maxwell equations indicates that $\mathbf{B}$ satisfies the same equation. A complete set of three-dimensional solutions to the Maxwell equations in free space are hence given by the family of plane waves of wavevector $\mathbf{k}$ and polarisation $\hat{\mathbf{e}}_{\sigma,\mathbf{k}}$, where $\hat{\mathbf{e}}_{\sigma,\mathbf{k}}$ for $\sigma = \{1, 2\}$ are orthogonal unit vectors and $\hat{\mathbf{e}}_{\sigma,\mathbf{k}} \cdot \mathbf{k} = 0$. To represent these, we introduce the complex *analytic field* $\mathbf{E}^+(\mathbf{r}, t)$, where $\mathbf{E}(\mathbf{r}, t) = \mathrm{Re}\{\mathbf{E}^+(\mathbf{r}, t)\}$ and the complex part is given by analytic continuation, which also satisfies the wave equation. A plane-wave solution to the Maxwell equations at position $\mathbf{r}$ and time t is then given by

$$\mathbf{E}^+(\mathbf{r}, t) = E_0^+ \hat{\mathbf{e}}_{\sigma,\mathbf{k}} e^{i(\mathbf{k}\cdot\mathbf{r} - \omega t)}, \tag{3.8}$$

where E_0^+ is the amplitude and $\omega = |\mathbf{k}|c$ is the frequency. Since the Maxwell equations are linear, any linear superposition of these solutions is also an allowed solution. These are given by

$$\mathbf{E}^+(\mathbf{r}, t) = \sum_\sigma \int E^+_{\mathbf{k},\sigma} \hat{\mathbf{e}}_{\sigma,\mathbf{k}} e^{i(\mathbf{k}\cdot\mathbf{r} - \omega t)} \mathrm{d}^3\mathbf{k}. \tag{3.9}$$

Since the plane wave basis consists of states that are infinite in their spatial extent, such superpositions will be needed to describe more realistic states such as those generated in the laboratory. For the time being we will assume we are working with an x-polarised beam and suppress indices of σ, noting that the general solution can always be expressed as a superposition of such linearly polarised solutions.

3.2.1 Paraxial approximation

The solutions of the Maxwell equations most commonly encountered experimentally are not those that are propagating expansively over many directions in space, but those where most of the energy is moving in one direction along a narrow path in a beam-like geometry, such as the emission of a laser. We can use this fact to simplify considerably the expression for the field by employing the *paraxial approximation*. We begin by re-writing Eq.3.9 in a way which is conducive to imposition of this approximation.

This begins by taking the beam axis to be the z-axis of our co-ordinate system and writing the x-component of the analytic field, $E_x^+(\mathbf{r},t)$, in terms of a modulation $U(\mathbf{r},t)$ of a single plane wave propagating down the z direction [56]:

$$E_x^+(\mathbf{r},t) = E_0^+ U(\mathbf{r},t) e^{i(kz-\omega t)}, \tag{3.10}$$

for some wave number $k = 2\pi/\lambda$, where λ is the wavelength.

We then proceed to substitute into the wave equation to obtain

$$\frac{\partial^2 U}{\partial x^2} + \frac{\partial^2 U}{\partial y^2} + \frac{\partial^2 U}{\partial z^2} + 2ik\frac{\partial U}{\partial z} - \left(k^2 - \frac{\omega^2}{c^2}\right) = 0. \tag{3.11}$$

The paraxial approximation consists of neglecting the second-order variation in z whilst retaining all other terms. After much manipulation, an analytic solution to the remaining equation can be ultimately be found for boundary conditions where $\mathbf{E}^+ \to 0$ for $\rho \to \infty$, where

$$\rho^2 = x^2 + y^2 \tag{3.12}$$

The solutions for the electric field, indexed by non-negative integers $\{m, n\}$, take the following

form

$$E_x^+(\mathbf{r},t) = E_0^+ \sum_{mn} \frac{c_{mn} w_0}{w(z)} H_m\left(\frac{\sqrt{2}x}{w(z)}\right) H_n\left(\frac{\sqrt{2}y}{w(z)}\right) e^{-k\rho^2/2R(z)} e^{-\rho^2/w(z)^2} e^{i(m+n+1)\phi(z)} e^{i(kz-\omega t)}, \tag{3.13}$$

where we have defined the quantities

$$\text{Width: } w^2(z) = w_0^2\left[1+\left(\frac{z}{z_R}\right)^2\right] \tag{3.14}$$

$$\text{Radius of wavefront curvature: } \frac{1}{R(z)} = \frac{z}{z^2+z_R^2} \tag{3.15}$$

$$\text{Gouy phase: } \phi(z) = \arctan\left(\frac{z}{z_R}\right) \tag{3.16}$$

$$\text{Rayleigh length: } z_R = \frac{\pi w_0^2 n}{\lambda}, \tag{3.17}$$

and where H_m are the Hermite polynomials defined by

$$H_n(t) = \sqrt{\frac{n!}{2^n\sqrt{\pi}}} \sum_{m=0}^{\lfloor \frac{n}{2} \rfloor} \frac{(-1)^m}{m!(n-2m)!} \left(\frac{2t}{\sigma_t}\right)^{n-2m}. \tag{3.18}$$

This describes a monochromatic beam with minimum radius (known as the waist) w_0 at $z = 0$. For a beam with a waist of radius $w_0 >> \lambda$, close to this waist in the z direction ($z << z_R$) this solution takes the form

$$E_x^+(\mathbf{r},t) \approx E_0^+ S(x,y) e^{i(kz-\omega t)}, \tag{3.19}$$

where

$$S(x,y) = \sum c_{mn} H_m\left(\frac{\sqrt{2}x}{w}\right) H_n\left(\frac{\sqrt{2}y}{w}\right) e^{-(x^2+y^2)/w^2} \tag{3.20}$$

is independent of z to first order and defines the *transverse spatial profile* of the beam, whilst the final part gives the time evolution. It is thus possible to partition the solution into distinct,

separable components: polarisation state, transverse spatial profile and temporal profile. We may therefore write the electric field as a superposition of these quasi-monochromatic solutions weighted by a spectral envelope $\tilde{\varepsilon}(\omega)$:

$$E_x^+(\mathbf{r},t) \approx AS(x,y)\int \sqrt{\frac{\hbar\omega}{2nc\epsilon_0 V}}\tilde{\varepsilon}(\omega)e^{i(kz-\omega t)}\mathrm{d}\omega, \tag{3.21}$$

where the system is enclosed in a volume V, A is a dimensionless number that gives the amplitude, and $\hbar$ is Planck's constant. The reason for defining $\tilde{\varepsilon}(\omega)$ with this ω-dependence and the significance of the dimensionful prefactor will later become apparent. For the remainder of this thesis, unless otherwise stated, we will assume we are working with a collimated beam operating within the paraxial regime and hence treat the electric field as separable. Since this thesis is concerned with spectral-temporal encoding of quantum information, we will largely neglect the spatial profile, whilst polarisation will play an ancilliary role in the experiments described later. Mostly, we will consider a single spatial and polarisation profile, which may then be factored out of the expression for the electric field.

3.2.2 Modes and mode transformations

Suppressing references to the spatial and polarisation modes, we write the analytic field as a linear superposition of monochromatic components:

$$E^+(\mathbf{r},t) \approx A\int \sqrt{\frac{\hbar\omega}{2nc\epsilon_0 V}}\tilde{\varepsilon}(\omega)e^{i(kz-\omega t)}\mathrm{d}\omega. \tag{3.22}$$

At this point we invoke the *slowly-varying envelope approximation*, whereby we take $\omega \approx \omega_0$ where $\tilde{\varepsilon}(\omega)$ is significant and hence Eq.3.22 can be re-written

$$E^+(\mathbf{r},t) \approx A\sqrt{\frac{\hbar\omega_0}{2nc\epsilon_0 V}}\int \tilde{\varepsilon}(\omega)e^{i(kz-\omega t)}\mathrm{d}\omega. \tag{3.23}$$

In many instances it is useful to quantify the similarity of two different modes $\varepsilon(\omega)$ and $\varepsilon'(\omega)$. This is calculated using the mode overlap, or inner product:

$$\left\langle \varepsilon \,\middle|\, \varepsilon' \right\rangle \equiv \int \tilde{\varepsilon}^*(\omega)\tilde{\varepsilon}'(\omega)\mathrm{d}\omega. \tag{3.24}$$

With the above definitions, for any pulse, one may then choose A such that $\tilde{\varepsilon}(\omega)$ satisfies

$$\langle \varepsilon \,|\, \varepsilon \rangle = \int \tilde{\varepsilon}^*(\omega)\tilde{\varepsilon}(\omega)\mathrm{d}\omega = 1. \tag{3.25}$$

Modes that satisfy this relation are said to be *normalised*. Henceforth, all modes will be assumed to be normalised. Under this definition the inner product provides a normalised metric for evaluating the similarity of the modes, irrespective of intensity. It is equal to unity when the modes are identical, and 0 when the modes are orthogonal.

A concept that will become very important in the consideration of quantum operations is that of a *unitary transformation*. A linear operation, described by an operator $L(\xi, \omega)$ is a transformation of $\varepsilon(\omega)$ to some function $\bar{\varepsilon}(\xi)$ according to

$$\bar{\varepsilon}(\xi) = \int_{-\infty}^{\infty} \tilde{\varepsilon}(\omega)L(\xi, \omega)\mathrm{d}\omega. \tag{3.26}$$

One may define the inverse of such an operation, described by the operator $L^{-1}(\omega', \xi)$:

$$\tilde{\varepsilon}(\omega') = \int \bar{\varepsilon}(\xi)L^{-1}(\omega', \xi)\mathrm{d}\xi. \tag{3.27}$$

A transformation U of the above form is called unitary if it is *self adjoint*, i.e. its inverse is equal to its own Hermitian conjugate:

$$U^{-1}(\omega, \xi) = U^*(\xi, \omega). \tag{3.28}$$

The important corollary of this property is that unitary transformations preserve the inner product between two modes:

$$\int \tilde{\varepsilon}^*(\omega)\tilde{\varepsilon}'(\omega)\mathrm{d}\omega = \int \tilde{\varepsilon}^*(\omega)\left[\int U^{-1}(\omega,\xi)\bar{\varepsilon}'(\xi)\mathrm{d}\xi\right]\mathrm{d}\omega \tag{3.29}$$

$$= \int\left[\int U^*(\xi,\omega)\tilde{\varepsilon}^*(\omega)\mathrm{d}\omega\right]\bar{\varepsilon}'(\xi)\mathrm{d}\xi$$

$$= \int \bar{\varepsilon}^*(\xi)\bar{\varepsilon}'(\xi)\mathrm{d}\xi, \tag{3.30}$$

and it follows that the the complex scalar quantity in Eq.3.24 is invariant under unitary transformation. Unitary transformations can therefore be used to generate one complete basis of modes from another: if one basis of modes $\tilde{\varepsilon}_n(\omega)$ satisfies the completeness relation

$$\sum_n \tilde{\varepsilon}_n^*(\omega)\tilde{\varepsilon}_n(\omega') = \delta(\omega-\omega'), \tag{3.31}$$

then so will the modes

$$\bar{\varepsilon}_n(\xi) = \int U(\xi,\omega)\tilde{\varepsilon}_n(\omega)\mathrm{d}\omega. \tag{3.32}$$

Since they provide a one-to-one mapping of all spectral modes which preserves the mode overlap, a unitary transformation may be interpreted as either a physical operation on the mode, or a change in the basis states used to represent the mode.

3.2.3 Temporal representation of modes

For the purposes of this work, where we will be mainly concerned with large-bandwidth pulses, it is generally more useful to represent modes in terms of their frequency components. However, there are also important time-dependent processes that will play a central role in this work, and hence it will often be necessary to cast the pulse into its temporal representation. To this end, we define the Fourier transformed frequency-space representation of the mode using the unitary

transformation $U(\omega, t) = e^{-i\omega t}/\sqrt{2\pi}$:

$$\tilde{\varepsilon}(\omega) = \frac{1}{\sqrt{2\pi}} \int \varepsilon(t) e^{i\omega t} \mathrm{d}t = \mathcal{FT}\{\varepsilon(t)\}, \tag{3.33}$$

and the inverse Fourier transform correspondingly by

$$\varepsilon(t) = \frac{1}{\sqrt{2\pi}} \int \tilde{\varepsilon}(\omega) e^{-i\omega t} \mathrm{d}\omega = \mathcal{FT}^{-1}\{\tilde{\varepsilon}(\omega)\}. \tag{3.34}$$

This defines the corresponding temporal (or longitudinal) mode $\varepsilon(t)$, defined in a frame co-moving with the light along the propagation direction. We will now go through some of the important analytical tools and associated nomenclature regarding temporal modes that will become useful later on.

In general, $\varepsilon(t)$ will be a complex quantity, and can be decomposed into its amplitude and phase components as

$$\varepsilon(t) = |\varepsilon(t)| e^{i\phi(t)}, \tag{3.35}$$

where $\phi(t)$ is the temporal phase and $|\varepsilon(t)|$ is the temporal amplitude. Often this may be written as

$$\varepsilon(t) = |\varepsilon(t)| e^{i\omega_0 t} e^{i\theta(t)}, \tag{3.36}$$

where ω_0 is referred to as the centre frequency or carrier frequency, and $\theta(t)$ is known as the time-dependent phase.

The normalised longitudinal or temporal intensity of the pulse is given by

$$I(t) = \varepsilon^*(t)\varepsilon(t) = |\varepsilon(t)|^2. \tag{3.37}$$

3.2.4 Hermite-Gauss representation of modes

One basis of spectral-temporal modes that is frequently of interest in quantum optics is the Hermite-Gauss modes. These modes are defined by $\varepsilon_{\mathrm{HG}n}(t) = H_n(t)e^{-|t|^2/2\sigma_t^2}$, where H_n is defined in Eq. 3.18. The Hermite-Gauss modes form a complete set and have the property that they are self-similar under Fourier transformation:

$$\mathcal{FT}[H_n(t)e^{-t^2/2}] = H_n(\omega\sigma_t^2)e^{-\omega^2\sigma_t^2/2}. \tag{3.38}$$

The first three of these modes are shown in Fig. 3.3. Several natural processes in quantum optics generate pulses with spectral-temporal modes of the Hermite-Gauss type. The simplest and most useful form that $\varepsilon(t)$ can take in this family is that of the Gaussian pulse, which approximates pulses produced by several real-life processes such as a mode-locked laser. The Gaussian pulse with maximum intensity at time $t = t_0$ is described by the temporal mode

$$\varepsilon_{\mathrm{HG0}}(t) = \frac{1}{\sqrt{\sqrt{\pi}\sigma_t}} \exp\left(-\frac{(t-t_0)^2}{2\sigma_t^2}\right) e^{i(\omega_0 t+\phi_{CE})}, \tag{3.39}$$

where the standard deviation σ_t determines the duration of the pulse, the quantity ω_0 is known as the centre frequency or carrier frequency, and ϕ_{CE} is known as the carrier-envelope phase. Note that this is in the form of Eq. 3.36, with $\theta(t) = \phi_{CE}$. Except for very short (close to single-cycle) pulses, ϕ_{CE} is of limited importance for physical interactions and is often neglected. Where $\theta(t)$ is constant[1], we refer to the mode as *transform-limited*.

The relative temporal intensity $I(t)$ of this pulsed mode is given by

$$I(t) = \frac{1}{\sqrt{\pi}\sigma_t} \exp\left(-\frac{(t-t_0)^2}{\sigma_t^2}\right). \tag{3.40}$$

When referring to the duration of a pulsed mode, it is common to refer to the *full width at half*

[1] Or linear in t, which amounts to redefining our co-ordinate axis for t

maximum, or FWHM, often denoted Δt. As its name implies, this is the duration over which the intensity of the pulse is at least half its maximum value. In the case of the Gaussian pulse $\varepsilon_{\text{HG0}}(t)$, it can be shown that

$$\Delta t = 2\sqrt{\ln(2)}\sigma_t \approx 1.665\sigma_t. \tag{3.41}$$

3.2.5 Spectral representation of modes

Many of the concepts applicable in the temporal representation of modes are easily extended into the spectral domain. The frequency-dependent electric field can be decomposed into its amplitude and phase:

$$\tilde{\varepsilon}(\omega) = |\tilde{\varepsilon}(\omega)|e^{i\phi(\omega)}. \tag{3.42}$$

$\phi(\omega)$ is known as the spectral phase of the mode, and is a quantity of considerable physical significance that will form a central part of much of the work in this thesis. The squared modulus of the spectral amplitude, $|\tilde{\varepsilon}(\omega)|^2$, is known as the relative spectral intensity and is denoted $\bar{I}(\omega)$. By Parseval's theorem,

$$\int \bar{I}(\omega)\mathrm{d}\omega = \int I(t)\mathrm{d}t = 1. \tag{3.43}$$

Since the Fourier transform is a unitary tranformation, the mode overlap, defined analogously to Eq.3.24, is conserved.

As previously mentioned, an important property of Gaussian pulses is that their functional form is preserved under Fourier transformation. Substituting Eq.3.39 into the Fourier transform yields:

$$\tilde{\varepsilon}_{\text{HG0}}(\omega) \equiv \mathcal{FT}\{\varepsilon_{\text{HG0}}(t)\} = \frac{1}{\sqrt{\sqrt{\pi}\sigma_\omega}} \exp\left(-\frac{(\omega-\omega_0)^2}{2\sigma_\omega^2}\right) e^{-i\omega t_0}, \tag{3.44}$$

where

$$\sigma_\omega = 1/\sigma_t. \tag{3.45}$$

This allows the definition of the FWHM spectral bandwidth, analogously to the temporal duration, as

$$\Delta\omega = 2\sqrt{\ln(2)}\sigma_\omega \approx 1.665\sigma_\omega. \tag{3.46}$$

Noting that a suitable choice of t_0 can eliminate the final linear phase term, it can be shown that the Gaussian wavepacket with no addtional spectral or temporal phase is a minimum uncertainty state, i.e. it realises the equality in

$$\text{Var}(\bar{I}(\omega))\text{Var}(I(t)) \geq \frac{1}{4}, \tag{3.47}$$

where $\text{Var}(f(x))$ is the variance defined by

$$\text{Var}(f(x)) = \int x^2 f(x)\mathrm{d}x - \left| \int x f(x)\mathrm{d}x \right|^2. \tag{3.48}$$

This inequality is known as the (Fourier) transform limit. The variance, which is real and positive by construction, is interpreted as a measure of the support of the region of the spectral or temporal domain that the pulse occupies, and the inequality may be interpreted as stipulating that pulses cannot simultaneously have arbitrarily small support in both spectral and temporal domains. For a given spectral amplitude profile, pulses with spectral phase with no dependence on terms in ω^2 or higher minimise the time duration are therefore known as transform limited. The transform-limited pulse constitutes a special case where spectral and temporal intensity measurements are together sufficient for complete pulse characterisation. In general, measurements of both spectral and temporal amplitude only are insufficient to fully characterise a pulsed mode- that is, to determine the phase.

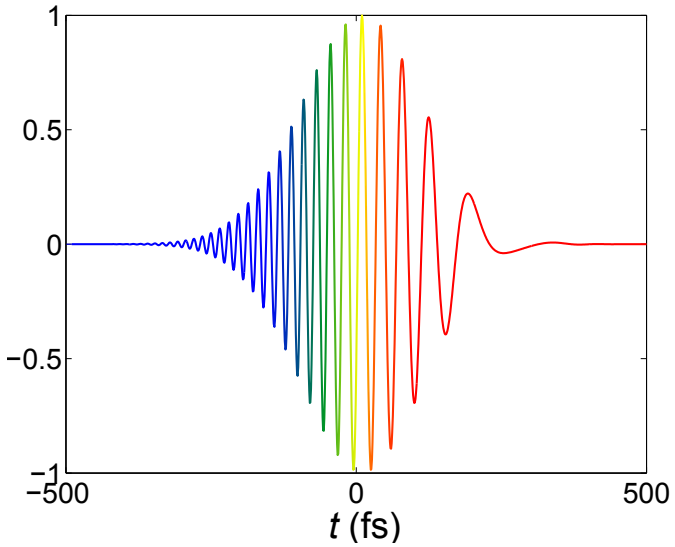


Figure 3.1: Illustration of the effect of quadratic spectral phase on an ultrafast pulse, showing increase in instantaneous frequency with time.

3.2.6 Spectral phase and dispersion

One consequence of the Fourier transform limit is that extremely short pulses must have significant spectral amplitude over a broad bandwidth. Ultrafast optics is therefore concerned with such spectrally broadband pulses, and in this regime the spectral phase $\phi(\omega)$ becomes an important parameter in the description of the pulse mode. Processes that are both passive (time-stationary) and unitary cannot vary the frequency decomposition $|\tilde{\varepsilon}(\omega)|$ of the pulse and so are described in general by the addition of spectral phase, which therefore describes the main effect of propagation through many non-absorbing optical media. Here we briefly expand on the physical effects of spectral phase on a pulse, and lay down the associated nomenclature.

We can define the instantaneous angular frequency $\hat{\omega}$ of a pulse at a given time by

$$\hat{\omega} = \frac{\partial}{\partial t}\text{Arg}\{\varepsilon(t)\}. \tag{3.49}$$

For the transform-limited Gaussian pulse $\varepsilon_{\text{HG0}}(t)$ given in Eq.3.39, the instantaneous frequency

is ω_0 at all times. If we consider what happens after the pulse has propagated through a medium where quadratic spectral phase ϕ_2 is applied, i.e.

$$\tilde{\varepsilon}_{\mathrm{HG0}}(\omega) \rightarrow \tilde{\varepsilon}_{\mathrm{HG0}}(\omega)e^{i\phi_2\omega^2} \equiv \tilde{\varepsilon}'_{\mathrm{HG0}}(\omega), \tag{3.50}$$

then we can apply the inverse Fourier transform to see the effect on the temporal profile:

$$\varepsilon'_{\mathrm{HG0}}(t) \equiv \mathcal{FT}^{-1}\{\tilde{\varepsilon}_{\mathrm{HG0}}(\omega)e^{i\phi_2\omega^2}\} = \frac{1}{\sqrt{\sqrt{\pi(\sigma_t^2 + 2i\phi_2)}}} \exp\left\{\frac{(t - t_0 + i\omega_0\sigma_t^2)^2}{2(\sigma_t^2 + 2i\phi_2)}\right\}. \tag{3.51}$$

The instantaneous frequency, the time-derivative of the argument of the right hand side of Eq.3.51, is then

$$\hat{\omega} = \frac{2t\phi_2 + \omega_0\sigma_t^4}{\sigma_t^4 + 4\phi_2^2}. \tag{3.52}$$

For positive spectral phase, the instantaneous frequency thus increases linearly with time. Due to the acoustic analogue being a sound of linearly increasing pitch, this phenomenon is known as "chirp". This effect is illustrated in Fig. 3.1. Chirp is often interpreted as a frequency-dependent delay. Writing down the expression for the pulsed mode in the spectral domain,

$$\begin{aligned}\tilde{\varepsilon}_{\mathrm{HG0}}(\omega)e^{i\phi_2\omega^2} &= \frac{1}{\sqrt{\sqrt{\pi}\sigma_\omega}} \exp\left(-\frac{(\omega - \omega_0)^2}{2\sigma_\omega^2}\right) e^{i(-\omega t_0 + \phi_2\omega^2)} \\ &= \frac{1}{\sqrt{\sqrt{\pi}\sigma_\omega}} \exp\left(-\frac{(\omega - \omega_0)^2}{2\sigma_\omega^2}\right) e^{i\omega(-t_0 + \phi_2\omega)},\end{aligned} \tag{3.53}$$

The frequency-dependent delay $t_0 \rightarrow t_0 - \phi_2\omega$ of the various chromatic components of the pulse, and the resultant separation of frequencies in time, is why the effect of higher-order spectral phase is formally known as *dispersion*. At optical frequencies, most materials exhibit positive quadratic spectral phase, which is thus referred to as *normal* dispersion. By contrast, negative spectral phase is known as *anomalous* dispersion.

Taking the modulus square of Eq.3.51 also allows the energy envelope of the pulse to be

evaluated. It can be shown that the relative intensity varies with t as

$$|\varepsilon'_{\mathrm{HG0}}(t)|^2 \propto \exp\left(\frac{-\sigma_t^2(t+2\omega_0\phi_2)^2}{2(\sigma_t^4+4\phi_2^2)}\right). \tag{3.54}$$

We can therefore see that the pulse is lengthened in time to beyond its transform limit, and also that the envelope is delayed by an amount $2\omega_0\phi_2$. Note that at $t=-2\omega_0\phi_2$, the instantaneous frequency according to Eq.3.52 is equal to ω_0: frequencies lower than the carrier are advanced ahead of the intensity maximum, whereas those of higher frequency are delayed.

It is convenient to expand the spectral phase as a power series in ω about some frequency (usually the centre frequency ω_0):

$$\phi(\omega) = \phi_0 + \phi_1(\omega-\omega_0) + \phi_2(\omega-\omega_0)^2 + \phi_3(\omega-\omega_0)^3 + ... \tag{3.55}$$

- $\phi_0 = \phi(\omega_0)$ is the so-called global phase and is related to the carrier-envelope phase ϕ_{CE}. It is of limited physical significance for many-cycle pulses and is often neglected.

- $\phi_1 = \frac{\partial\phi}{\partial\omega}|_{\omega_0}$ is the linear spectral phase and is known as the group delay. A pulse acquires group delay from propagation, and so the group delay is the parameter of interest in time-of-flight measurements. As the name suggests, a group delay leads to a global translation of the pulse envelope in time:

$$\begin{aligned}\varepsilon(t)_{\phi_1} &= \frac{1}{\sqrt{2\pi}}\int \tilde{\varepsilon}(\omega)e^{-i\phi_1\omega}e^{i\omega t}\mathrm{d}\omega \\ &= \frac{1}{\sqrt{2\pi}}\int \tilde{\varepsilon}(\omega)e^{i\omega(t-\phi_1)}\mathrm{d}\omega \\ &= \varepsilon(t-\phi_1)\end{aligned} \tag{3.56}$$

- $\phi_2 = \frac{1}{2}\frac{\partial^2\phi}{\partial\omega^2}|_{\omega_0}$ is the quadratic spectral phase. For most transparent, dispersive materials, it typically dominates over the higher-order spectral phase terms. As shown above, the

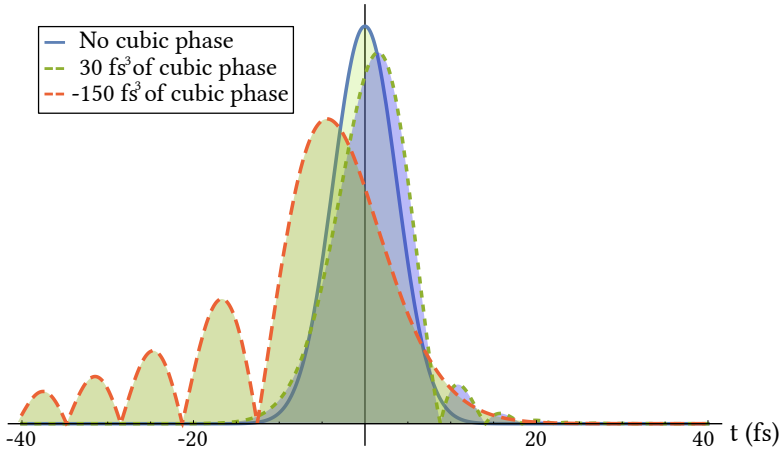


Figure 3.2: Envelope of a 6 fs pulse with Gaussian spectrum with varying levels of applied cubic phase.

effect of ϕ_2 on Gaussian pulses is to preserve their Gaussian functional form, but to stretch them in the time domain. This is illustrated in Fig. 3.1.

- $\phi_3 = \frac{1}{6}\frac{\partial^3\phi}{\partial\omega^3}|_{\omega_0}$ is the cubic spectral phase. It is the lowest-order spectral phase that varies the functional form of a Gaussian pulse in the time domain. Cubic and higher-order phase terms have more varied effects on the envelop, such as creating replicas of the pulse at later times (Fig. 3.2).

There are also a few related concepts that will come in useful:

- The group delay dispersion (GDD), defined as $D \equiv \frac{\partial^2\phi}{\partial\omega^2}|_{\omega_0} = 2\phi_2$, is the constant of proportionality that gives the variation of instantaneous frequency in time. It is the most useful and often-quoted measure of chromatic dispersion. The dimensions of D are [time]^2 and so at optical frequencies it is sometimes given in units of fs^2. Often, however, it is given in terms of delay per unit wavelength at some central wavelength λ_0. This quantity usually has units of ps/nm, and is related to D by

$$[\text{GDD}] = \frac{\lambda^2 D}{2\pi c} \tag{3.57}$$

- The group velocity dispersion, which is simply the GDD per unit length of a material. Typical values for glass at visible wavelengths are on the order of 100 fs^2/mm. It is also often quoted in units of ps/nm·km for pulses with specific central wavelengths.

3.2.7 Temporal phase operations

Temporal phase operations are typically given less precedence in optics, because they require the optical properties of the system to change on a timescale comparable to the optical frequency, typically in the petahertz. Nonetheless, the development of electro-optic techniques and nonlinear optics means it is now possible to modulate optical media on these timescales. The effect of temporal phase operations on optical pulses can be compared directly to that of spectral phases by analogy. Similar to the case with spectral phase, it is instructive to perform a polynomial expansion of the temporal phase around the first moment of the pulse t_0:

$$\phi(t) = \phi_{CE} + \bar{\phi}_1(t - t_0) + \bar{\phi}_2(t - t_0)^2 + \bar{\phi}_3(t - t_0)^3 + ... \tag{3.58}$$

The first term in this expansion is the familiar carrier-envelope phase. The linear phase term tells us how fast the electric field is winding round as a linear function of time: $\bar{\phi}_1$ is clearly equal to the instantaneous frequency at the time t_0, as defined by Eq.3.52. The duality of the Fourier transform in frequency and time implies an analogue process to Eq.3.56, where a linear spectral phase gives rise to a time delay, an applied linear temporal phase creates a spectral shift:

$$\begin{aligned}\tilde{\varepsilon}(\omega)_{\bar{\phi}_1} &= \frac{1}{\sqrt{2\pi}} \int \varepsilon(t) e^{i\bar{\phi}_1 t} e^{-i\omega t} \mathrm{d}t \\ &= \frac{1}{\sqrt{2\pi}} \int \varepsilon(t) e^{-it(\omega - \bar{\phi}_1)} \mathrm{d}t \\ &= \tilde{\varepsilon}(\omega - \bar{\phi}_1)\end{aligned} \tag{3.59}$$

By direct analogy with the spectral phase, the quadratic temporal phase term stretches pulses in the spectral direction, and for Gaussian pulses it does not affect the Gaussian functional form. These operations are therefore useful for bandwidth manipulation of quantum pulses. Together with quadratic spectral phase operations and linear spectral and temporal phase operations, quadratic temporal phase operations on Gaussian pulses constitute a symplectic group [57]. Loosely speaking, this implies that any combination of these operations can be represented by a small number of these transformations applied sequentially. Quadratic spectral and temporal phase manipulations are therefore of considerable interest for the general transformation of Gaussian-envelope pulses.

3.2.8 The chronocyclic Wigner representation

As well as their representation in either the spectral or temporal basis, there are some alternative representations that are often useful in describing optical pulses. One of the most useful of these is the *chronocyclic Wigner function* $W(\omega, t)$, which specifies the pulse mode in terms of a real function of the time-frequency phase space [58]. The Wigner function has some useful properties, not least because it treats time and frequency on an equal footing, which allows unitary transformations to be represented in an intuitive manner.

The chronocyclic Wigner function is obtained by first considering the mutual temporal intensity $I_m(t, t')$, or two-time correlation function, defined by

$$I_m(t, t') = \langle \varepsilon(t + \frac{t'}{2}) \varepsilon^*(t - \frac{t'}{2}) \rangle, \tag{3.60}$$

where the angle brackets indicate an ensemble average. The mutual temporal intensity satisfies $I_m(t, t') = I_m^*(t, -t')$ by construction and so its Fourier transform with respect to t' is real, but

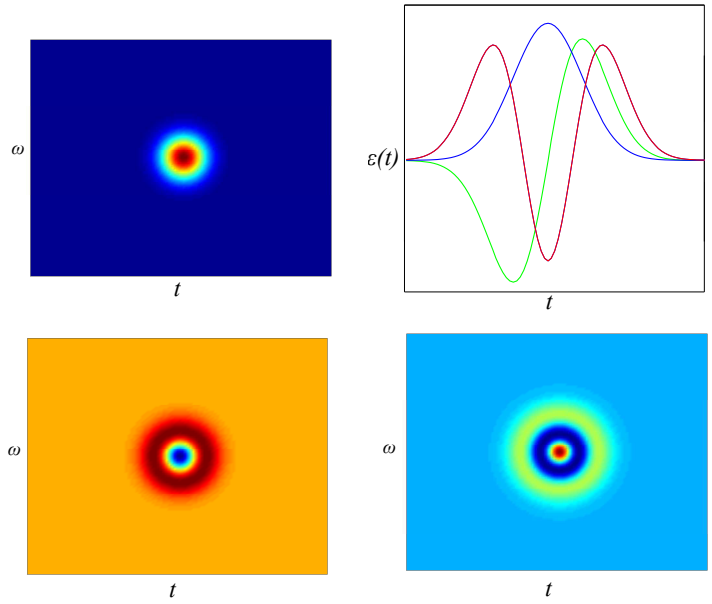


Figure 3.3: Depiction of the first three Hermite-Gauss modes in their temporal representation (top right). HG0-blue; HG1-green; HG2-red. Chronocyclic Wigner functions also shown- HG0- top left; HG1, bottom left; HG2-bottom right. Axes are set such that $\sigma_\omega = \sigma_t$. Note the self-similarity of the Hermite-Gauss modes in the spectral and temporal domains.

not always positive:

$$W(\omega,t) \equiv \mathcal{FT}\{I_m(t,t')\} = \frac{1}{\sqrt{2\pi}}\int \langle \varepsilon(t+\frac{t'}{2})\varepsilon^*(t-\frac{t'}{2})e^{i\omega t'}\rangle \mathrm{d}t', \tag{3.61}$$

and this defines $W(\omega,t)$. Under this definition of $W(\omega,t)$, its form is preserved by Fourier transformation of the mode:

$$W(\omega,t) \equiv \frac{1}{\sqrt{2\pi}}\int \langle \tilde{\varepsilon}(\omega+\frac{\omega'}{2})\tilde{\varepsilon}^*(\omega-\frac{\omega'}{2})e^{i\omega' t}\rangle \mathrm{d}\omega', \tag{3.62}$$

The Wigner functions for the first 3 Hermite-Gauss mode is shown in Fig. 3.3. The Wigner function has the following useful properties:

- Its integral over all phase space is constant:

$$\int W(\omega,t)\mathrm{d}\omega\mathrm{d}t = 2\pi. \tag{3.63}$$

- Whilst its negative values preclude it from being interpreted as a true intensity distribution, its marginal values (i.e. its integral with respect to a single variable) recovers the intensity:

$$\int W(\omega,t)\mathrm{d}\omega = I(t) \qquad \int W(\omega,t)\mathrm{d}t = \bar{I}(\omega). \tag{3.64}$$

- The frequency-time uncertainty relation places a lower limit to the "footprint" of the Wigner function in phase space subject to the peak-value condition:

$$|W(\omega,t)| \leq 2 \tag{3.65}$$

  which constrains the area of phase space occupied by the Wigner function to be greater than π.

Consider the action of a quadratic temporal phase operation on the mutual temporal intensity:

$$I_m(t,t') = \langle \varepsilon(t+\frac{t'}{2})\varepsilon^*(t-\frac{t'}{2})e^{i(\bar{\phi}(t+t'/2)-\bar{\phi}(t-t'/2))}\rangle \tag{3.66}$$

The added phase may be expanded about t:

$$\begin{aligned}\bar{\phi}(t+\frac{t'}{2}) - \bar{\phi}(t-\frac{t'}{2}) &= \bar{\phi}(t) + \frac{\partial\bar{\phi}}{\partial t}\frac{t'}{2} + \frac{1}{2}\frac{\partial^2\bar{\phi}}{\partial t^2}\left(\frac{t'}{2}\right)^2 - \bar{\phi}(t) + \frac{\partial\bar{\phi}}{\partial t}\frac{t'}{2} - \frac{1}{2}\frac{\partial^2\bar{\phi}}{\partial t^2}\left(\frac{t'}{2}\right)^2 \\ &= \frac{\partial\bar{\phi}}{\partial t}t' = \bar{\phi}_1 + 2\bar{\phi}_2 t\end{aligned} \tag{3.67}$$

where $\bar{\phi}_1$ and $\bar{\phi}_2$ are defined according to Eq.3.58. Substituting this into the Wigner function

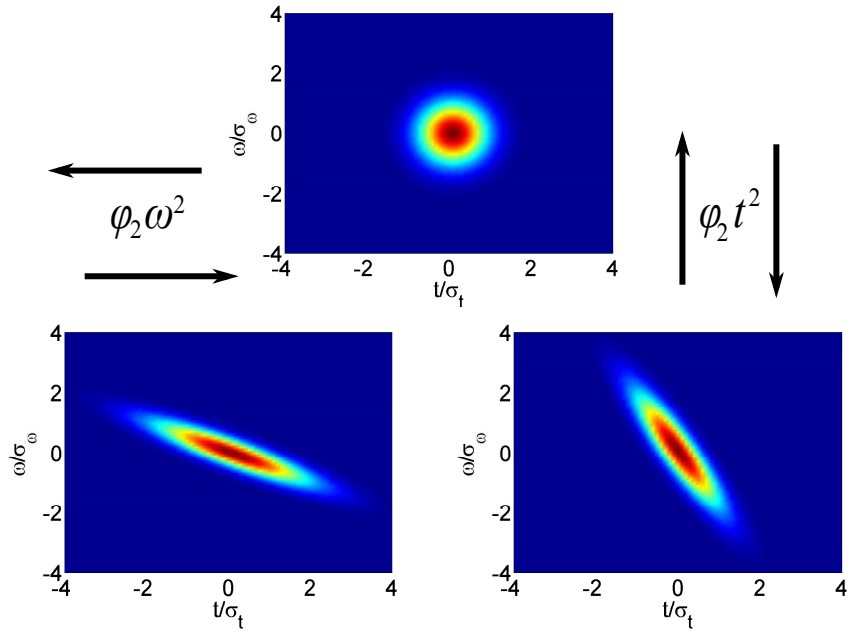


Figure 3.4: Chronocyclic Wigner functions of a transform-limited pulse (top), and the same pulse with quadratic spectral phase (bottom left) or quadratic temporal phase (bottom right). This illustrates the geometric effect of quadratic phase operations on the Wigner function as a linear shear.

defintion, Eq.3.61, gives

$$W(\omega, t) \to W(\omega + \bar{\phi}_1 + 2\bar{\phi}_2 t, t) \tag{3.68}$$

Hence, linear phase operations give rise to translations in the Wigner function and quadratic phase operations give rise to linear shears. This is depicted in Fig. 3.4. Since time and frequency are on an equal footing, the same argument may be applied for spectral phases. We therefore obtain an intutitive geometrical understanding of why these transformations form a group.

One might wonder why a real-valued function of two variables is necessary to describe the state when a complex function of a single variable is already known to be sufficient to describe a single mode. The reason is that unlike the mode formalism, the Wigner function is also able to accommodate a full description of incoherent optical systems. We will describe how Wigner

functions extend to this formalism later in the chapter.

It is convenient that we end the section on classical modes with the chronocyclic Wigner function. The history of quantum mechanics was generally one where concepts initially developed for analysing classical systems were generalised and extended to describe the newly-discovered quantum phenomena. As a peculiarity of history, the Wigner function travelled in the opposite direction: it was originally devised as a tool for quantum calculations, before its usefulness in the analysis of classical modes was realised. It therefore serves to illustrate quite neatly the relationship between the wave theory of classical modes, and the quantum theory of light.

The corpuscular theory of light endured for so long because, on distance scales much greater than the wavelength, it was difficult to directly observe many of the consequences of the wave nature of light. A geometric or ray-like vision of light, comprising of a stream of particles with definite position, momentum, and colour was satisfactory to the likes of Newton. Only with more precise measurements did the wave nature of light become apparent. Now that we see that the spectral-temporal properties, which were previously believed to be described by a single point in phase space, can only be described by a diffuse dsitribution like the Wigner function, we might wonder what other properties, which we thought had definite values, might also be described instead by a distribution.

For a single mode, it turns out that the components of the electric and magnetic fields are themselves not described by scalar quantities, but by a distribution across phase space, and it was to describe the quasi-probability distribution in this space that the Wigner function was originally invented. It is when we consider the implications of this uncertainty relation that we cross the threshold of quantum mechanics.

3.3 Quantisation of the electromagnetic field

3.3.1 A single mode

The usual approach to introducing quantum optics is first to describe a single mode in the existing classical theory of electromagnetism, given by a solution to Maxwell's equations, and then apply quantisation of the field. To obtain a single field mode for our consideration, we can impose cavity boundary conditions constraining $\mathbf{E} = 0$ along two infinite planes at position $z = 0$ and $z = L$, as would be the case with a cavity of length L bounded by perfectly conducting and hence reflecting surfaces that are infinite in their transverse extent. A solution to Maxwell's equations corresponding to an x-polarised excitation is then given by [59]

$$E_x(z,t) = \left(\frac{2\omega^2}{V\epsilon_0}\right)^{1/2} q_\omega(t)\sin(n\omega z/c) \tag{3.69}$$

$$B_y(z,t) = \left(\frac{2}{V\mu_0}\right)^{1/2} p_\omega(t)\cos(n\omega z/c), \tag{3.70}$$

where V is the volume of the cavity, c is the speed of light, $q_\omega(t)$ is a time-dependent quantity with dimensions of position, $p_\omega(t) = \partial q_\omega/\partial t$ and $\omega = 2n\pi c/L$ is the frequency. Each possible value of $n \in \mathbb{N}$ defines a longitudinal solution to the Maxwell equations in the cavity. We can interpret this as a standing wave of light supported by reflections off the internal walls of the cavity, with nodes (points of maximum amplitude) found at certain postions along the z axis. There is a direct analogy to be drawn between this situation and a plucked guitar string. The quantity $q_\omega(t)$ may be envisioned as the displacement of the nodes of the guitar string off the z axis at any given time, whilst $p_\omega(t)$ measures their speed. We see from the above equations that $q_\omega(t)$, known as the *canonical position*, is a rescaled proxy for the electric field, and $p_\omega(t)$ (the *canonical momentum*) is similarly associated with the magnetic field.

It can be shown from standard results of classical field theory that the classical energy of

this system, or Hamiltonian H, is given by

$$H = \frac{1}{2}(p_\omega^2 + \omega^2 q_\omega^2). \tag{3.71}$$

This quantity will prove important in the quantisation of the field.

3.3.2 Approaches to quantisation

Traditionally, there are two major approaches to recovering theories of quantum fields, such as that of light, from the pre-existing classical theory. These are known as *canonical quantisation*, instigated by Dirac in the 1920s, and the *path integral* formalism, discovered later and most commonly associated with Feynman. It is relatively straightforward, though not trivial, to demonstrate the mathematical equivalence of the two approaches, but the conceptual interpretations are quite different. The path integral formulation provides an elegant route to understanding how classical physics and quantum mechanics transition into one another. Canonical quantisation is more conceptually straightforward and is almost invariably the approach taken to teaching quantum field theories in the first instance. A brief introduction to the path integral formulation is included in the Appendices. For the main text of this thesis, however, we proceed with canonical quantisation.

Before proceeding, we make a brief note on Dirac notation. In this formalism, a vector is represented completely as $|\psi\rangle$. The inner product of two vectors $|\phi\rangle$ and $|\psi\rangle$ is denoted $\langle\phi \,|\, \psi\rangle$, whilst the outer product is written $|\phi\rangle \langle\psi|$.

3.3.3 Canonical quantisation

For a classical system, q_ω and p_ω can be interpreted as phase-space co-ordinates for the system at a given time. We assert that all the information about the system is contained within some vector $|\psi_\omega\rangle$, and we associate with the co-ordinates q_ω and p_ω some linear operators $\hat{q}_\omega$ and $\hat{p}_\omega$,

with the property that

$$\hat{q}_\omega \left|\psi_\omega\right\rangle = q_\omega \left|\psi_\omega\right\rangle \tag{3.72}$$

$$\hat{p}_\omega \left|\psi_\omega\right\rangle = p_\omega \left|\psi_\omega\right\rangle . \tag{3.73}$$

Canonical quantisation begins by making the assertion that instead, these operators satisfy the canonical commutation relation

$$[\hat{q_\omega}, \hat{p_\omega}] \equiv \hat{q_\omega}\hat{p_\omega} - \hat{p_\omega}\hat{q_\omega} = i\hbar\hat{\mathbb{1}}, \tag{3.74}$$

where $\hat{\mathbb{1}}$ is the identity operator. These objects are understood to be infinite-dimensional linear operators acting on a vector space, or Hilbert space, and may be represented by matrices. The physical state of the system itself is represented as a vector on this space, written in Dirac notation as $|\psi_\omega\rangle$, known as the state vector or wave function. Since these linear operators do not commute, they cannot have the same set of eigenvectors and hence there is no state vector $|\psi_\omega\rangle$ that satisfies both Eq.3.72 and Eq.3.73. With no meaningful way of attributing co-ordinates $\hat{q}_\omega$ and $\hat{p}_\omega$ to the system, we must assume that the fundamental description of the system is given by the state $|\psi_\omega\rangle$, which therefore describes a distribution over the $\{q, p\}$ phase space. We will refer to this as the excitation state of the mode ω.

According to the postulates of quantum mechanics, Hermitian operators correspond to observable (physically measurable) quantities. The outcomes of measurements of these quantities are probabilistic, and the probability P_X of some outcome X, where X is an eigenvalue of the operator $\hat{x}$ with eigenstate $|X\rangle$, is given by

$$P_X = |\left\langle X \,|\, \psi \right\rangle|^2 = \left\langle \psi \,|\, X \right\rangle \left\langle X \,|\, \psi \right\rangle . \tag{3.75}$$

This relation is known as the *Born rule*. Hence, the expectation value of the measurement is

given by

$$\begin{aligned}\sum_X P_X X &= \sum_X X \langle\psi \,|\, X\rangle \langle X \,|\, \psi\rangle \\ &= \langle\psi| \sum_X X \,|X\rangle \langle X \,|\, \psi\rangle \\ &= \left\langle \psi \,\middle|\, \hat{X} \,\middle|\, \psi \right\rangle .\end{aligned} \tag{3.76}$$

The operators $\hat{p}_\omega$ and $\hat{q}_\omega$ are Hermitian and hence correspond to observables. The quantum mechanical Hamiltonian operator, also an observable, is given by

$$\hat{H}_\omega = \frac{1}{2}(\hat{p}_\omega^2 + \omega^2 \hat{q}_\omega^2). \tag{3.77}$$

It will become convenient to recast the Hamiltonian in terms of a single (dimensionless and non-Hermitian) operator and its Hermitian conjugate:

$$\begin{aligned}\hat{H}_\omega =& \hbar\omega \left(\hat{a}^\dagger(\omega)\hat{a}(\omega) + \frac{1}{2} \right) \\ \hat{a}(\omega) \equiv \frac{1}{\sqrt{2\hbar\omega}}(\omega\hat{q}_\omega + i\hat{p}_\omega), &\qquad \hat{a}^\dagger(\omega) \equiv \frac{1}{\sqrt{2\hbar\omega}}(\omega\hat{q}_\omega - i\hat{p}_\omega),\end{aligned} \tag{3.78}$$

Henceforth we will write these as a and $a^\dagger$, remembering they represent operators on a Hilbert space associated with a particular spectral mode ω. It is possible to derive from Eq.3.74 the commutation relation obeyed by these operators:

$$[a, a^\dagger] = 1. \tag{3.79}$$

If we allow some state $|n\rangle$ to be an eigenstate of the Hamiltonian such that $H\,|n\rangle = E_n\,|n\rangle$, we

can therefore see that

$$\hat{H}a\left|n\right\rangle = (E_n - \hbar\omega)a\left|n\right\rangle, \qquad \hat{H}a^\dagger\left|n\right\rangle = (E_n + \hbar\omega)a^\dagger\left|n\right\rangle. \tag{3.80}$$

The states $a\left|n\right\rangle$ and $a^\dagger\left|n\right\rangle$ are clearly eigenstates of the Hamiltonian themselves. They are, however, unnormalised, so we need to deal with this first. Taking $\left|n\right\rangle$ to be normalised, we see that

$$\begin{aligned}\left\langle n\right| aa^\dagger\left|n\right\rangle &= \left\langle n\right|\left(a^\dagger a + [a, a^\dagger]\right)\left|n\right\rangle \\ &= (n+1)\left\langle n\,\middle|\, n\right\rangle \\ &= n+1.\end{aligned} \tag{3.81}$$

Hence we see that $a^\dagger\left|n\right\rangle = \sqrt{n+1}\left|n+1\right\rangle$, and by a similar argument that $a\left|n\right\rangle = \sqrt{n}\left|n-1\right\rangle$.

The physical significance of the operator $a(a^\dagger)$ then becomes clear: it lowers (raises) the energy of the system by one allowed graduation to the next energy eigenstate. This ability to remove (add) exactly one field excitation explains their most common name: the *annihilation (creation)* operators.

We are now in a position to apply a or $a^\dagger$ repeatedly to construct the entire series of normalised eigenstates of the Hamiltonian. Since the energy must always be positive, we can define the lowest-energy eigenstate $\left|0\right\rangle$ (known as the ground state, or vacuum state). We can go on to construct a lowest occupied state $a^\dagger\left|0\right\rangle \equiv \left|1\right\rangle$, a doubly excited state $(a^\dagger)/\sqrt{2}\left|1\right\rangle \equiv \left|2\right\rangle$, etc., to create the basis of energy eigenstates $\left|n\right\rangle$,

$$\left|n\right\rangle = \frac{a^{\dagger n}}{\sqrt{n!}}\left|0\right\rangle, \tag{3.82}$$

known as the *Fock states*. The form of these states and their energy levels are depicted in Fig.

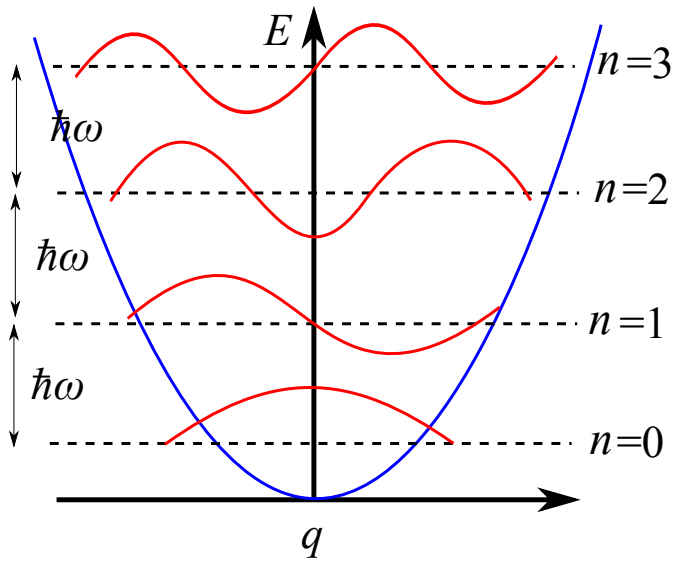


Figure 3.5: Quantised energy levels of the simple harmonic oscillator potential (blue), also showing the n={0,1,2,3} Fock state distributions (red) as a function of the field quadrature.

3.5. It is straightforward to show that the Fock states satisfy the completeness relation,

$$\sum_{n=0}^{\infty} |n\rangle \langle n| = \hat{\mathbb{1}}, \tag{3.83}$$

and that they are orthonormal.

$$\langle n \,|\, m\rangle = \delta_{nm}. \tag{3.84}$$

The Fock states therefore constitute a complete, orthonormal and non-degenerate (in energy) basis over the space of the field quadratures q_ω and p_ω, and this precludes the existence of other eigenstates of the Hamiltonian. One result of quantisation, therefore, is that any interaction with this spectral mode, including with detectors, can be completely understood in terms of the exchange of energy in discrete values of $\hbar\omega$, or one excitation. Each excitation therefore seems to have the particle-like quality of indivisibility, and have therefore become attached to the name "photon". Whilst the photon is a notoriously difficult concept to concisely define, it is

nonetheless an extremely useful one. We will proceed for now with the notion that a monochromatic photon is a single excitation of a particular electromagnetic field mode, resulting from the normalised action of the operator $a^\dagger_\omega$.

3.3.4 The wave function of a single photon

In contrast to the first half of this chapter, which considered the many different spectral-temporal modes of the field and their representations and transformations, this second half has so far considered only the different states of excitation of a single monochromatic mode. We will now generalise this to discuss the quantum treatment of spectrally broadband systems.

The first point to note is that the excitation states of separate modes are entirely independent. The excitation state of the field is a separate part of the Hilbert space to the spectral-temporal mode, the spatial mode, and the polarisation. Factoring out the latter two, we can write the global Hilbert space $\mathcal{H}_\Psi$ as a product of the field quadrature and spectral-temporal subspaces $\mathcal{H}_{q,p}$ and $\mathcal{H}_{t,\omega}$, respectively:

$$\mathcal{H}_\Psi = \mathcal{H}_{q,p} \otimes \mathcal{H}_{t,\omega}, \tag{3.85}$$

where $\otimes$ indicates a tensor product. A vector on this space $|\Psi\rangle$, describing the state of the system, must therefore include a specification of the spectral-temporal mode and the excitation state of that mode in the Fock basis $\sum c_{ij} |i\rangle$. Working in a particular basis, say the monochromatic basis $|\varepsilon_{t,\omega}\rangle = |\omega\rangle$, we can index the excitation state by the mode it occupies to express the full excitation state of a single mode $|\omega\rangle$:

$$\sum_n c_n(\omega) \, |n\rangle_\omega \, , \tag{3.86}$$

such that $|n\rangle_\omega$ is the n-photon state of the mode ω. Including all the other modes, a general

state that spans the full spectral degree of freedom is

$$|\Psi_S\rangle = \otimes_{\omega=0}^{\infty} \left[\sum_n c_n(\omega) \, |n\rangle_\omega \right]. \tag{3.87}$$

We may have linear superpositions of multiple such components, weighted by coefficients λ_i, so we arrive at the general form for a pure quantum optical state in a single spatial and polarisation mode:

$$|\Psi\rangle = \sum_i \lambda_i \left(\otimes_{\omega=0}^{\infty} \left[\sum_n c_{in}(\omega) \, |n\rangle_\omega \right] \right). \tag{3.88}$$

When acting on the state $|\Psi\rangle$ with the operators a and $a^\dagger$, it is necessary to specify the spectral-temporal mode being addressed, and so we must index these operators by that mode. We therefore invoke the monochromatic operators $a(\omega),\ a^\dagger(\omega)$, which we interpret as annihilating or creating a single photon in the monochromatic spectral mode defined by the frequency ω.

An operator on such states with an interesting interpretation is the total photon number operator $\hat{N}$ [2]:

$$\hat{N} = \int \sum_n n \, |n\rangle \, \langle n|_\omega \, \mathrm{d}\omega = \int a^\dagger(\omega) a(\omega) \mathrm{d}\omega. \tag{3.89}$$

The number operator $\hat{N}$ is Hermitian and hence corresponds to a physical observable. The eigenstates of this operator with eigenvalue one are interpreted as all the states where there exists a single photon in one and only one mode. This occurs when $c_{in}(\omega) = \delta_{1n}\delta(\omega - \omega_i);\ \ \lambda_i = \psi(\omega_i)$, i.e. the state is a superposition of states with exactly one photon at one frequency mode and exactly none at all others. The general form for such a state reduces to

$$\boxed{|1\rangle_\psi = \int \mathrm{d}\omega \ \psi(\omega) a^\dagger(\omega) \, |\mathrm{vac}\rangle \,,} \tag{3.90}$$

[2] It is interesting to compare the total number operator to the Hamiltonian. They are not the same- besides the vacuum energy, the photon-number terms in the Hamiltonian are weighted by a factor $\hbar\omega$. This means that eigenstates of $\hat{N}$ are not necessarily eigenstates of the Hamiltonian if they contain occupied modes at different frequencies. This is just as well for the sake of this thesis, or else single-photon states in pulsed modes would not propagate in time and so would not be of much interest to anybody!

where $\psi(\omega)$ is a complex quantity and $|\text{vac}\rangle$ is the global vacuum state, i.e.

$$|\text{vac}\rangle = \otimes_{\omega=0}^{\infty} |0\rangle_{\omega} \,. \tag{3.91}$$

Mandel defined a single photon as any eigenstate of the total number operator $\hat{N}$ with eigenvalue one, i.e. a state of this form [60]. For the remainder of this thesis we will use the term 'single photon' in this sense. If we imagine the single photon in the spirit of its name- as a single particle- we can attribute a wave function to it, in precisely the same way we consider the wavefunction of an electron or an atom. The function $\psi(\omega)$, which fully describes the spectral-temporal state of the photon, also defines a mode. We can therefore define an inner product in the same way as with the classical mode, and apply unitary transformation, such as the Fourier transform:

$$\int \mathrm{d}\omega \; \psi(\omega) a^{\dagger}(\omega) \, |\text{vac}\rangle = |1\rangle_{\psi} = \int \mathrm{d}t \; \tilde{\psi}(t) a^{\dagger}(t) \, |\text{vac}\rangle \,, \tag{3.92}$$

where

$$\tilde{\psi}(t) \equiv \frac{1}{\sqrt{2\pi}} \int \psi(\omega) e^{-i\omega t} \mathrm{d}\omega \qquad \text{and} \qquad a^{\dagger}(t) \equiv \frac{1}{\sqrt{2\pi}} \int a^{\dagger}(\omega) e^{-i\omega t} \mathrm{d}\omega. \tag{3.93}$$

It is straightforward to show the new field operators defined in this manner satisfy the canonical communtation relation of Eq.3.74. As in the above case, unitary transformation of the mode can also be used to define new creation and annihilation operators for photons in the mode defined by $\psi(\omega)$:

$$\boxed{a_{\psi}^{\dagger} \equiv \int \psi(\omega) a^{\dagger}(\omega) \mathrm{d}\omega.} \tag{3.94}$$

The probability of the photon being measured in some state $|\xi\rangle$ is exactly the relative intensity $|\psi(\xi)|^2 = |\, \langle \xi \,|\, \psi \rangle \,|^2$ of the mode in that state. Whilst the situation becomes somewhat more complicated for multi-photon systems, in the case of single photons, we can simply consider

the mode function $\psi(\omega)$ to fully describe the spectral-temporal wave function.

3.3.5 Density operators

Whilst state vectors such as Eq.3.88 are the most general way of writing fully coherent quantum optical states, in many circumstances experimentalists are faced with what is known as an incoherent mixture. This is an ensemble of quantum systems where the phase relationships between different modes is not precisely defined. A general way of expressing such an ensemble in terms of some orthonormal basis of states $\{|\psi_i\rangle\}$ is with a density operator $\hat{\rho}$ on the outer product space of the system,

$$\hat{\rho} = \sum_{ij} \rho_{ij} |\psi_i\rangle \langle\psi_j| . \tag{3.95}$$

The density operator has the following properties:

- The density matrix is Hermitian by construction and so corresponds to an observable. The eigenvectors are an orthonormal series of pure states $|\phi_k\rangle$ that exist in perfectly incoherent mixture with one another, and the eigenvalues are simply the probabilities P_k of their appearance. The density matrix may therefore be written

$$\rho = \sum_{k} P_k |\phi_k\rangle \langle\phi_k| . \tag{3.96}$$

- Operator expectation values are given by the trace of the operator times the density ma-

trix:

$$\begin{aligned} \mathrm{Tr}[\hat{X}\rho] &= \sum_k P_k \sum_i \left\langle \phi_i \right| \hat{X} \left| \phi_k \right\rangle \langle \phi_k \,|\, \phi_i \rangle \\ &= \sum_k P_k \langle \phi_k | \left(\sum_i |\phi_i\rangle \langle \phi_i| \right) \hat{X} |\phi_k\rangle \\ &= \sum_k P_k \langle \phi_k \,|\, X \,|\, \phi_k \rangle = \langle X \rangle \,. \end{aligned} \tag{3.97}$$

- Consequently, its own trace must be unity:
  $\mathrm{Tr}[\rho] = \sum_i \langle \psi_i | \, \rho \, | \psi_i \rangle = \sum_k P_k = 1$.

- States with a single nonzero $P_k = 1$ are called *pure states*; all others are called *mixed states*.

- The square trace of the density operator, $\mathrm{Tr}[\rho^2]$, is equal to one if and only if the state is pure. This can be seen easily by computing the trace in the eigenbasis $\{|\phi_k\rangle\}$. Hence, $\mathrm{Tr}[\rho^2]$ is often known as the *purity* of the state represented by ρ.

- Off-diagonal entries of the corresponding density matrix (the elements $\rho_{ij} \equiv \langle \psi_i \,|\, \rho \,|\, \psi_j \rangle$, where $\langle \psi_i \,|\, \psi_j \rangle = 0$) are known as *coherences*. They are associated with what is known about the phase relationships between the occupation of the states $|\psi_i\rangle$ and $|\psi_j\rangle$.

  As alluded to in the previous section, the chronocylic Wigner function may be used to uniquely represent incoherent mixtures in the spectral-temporal basis. It is simply the sum of the Wigner functions W_k of the eigenstates $|\phi_k\rangle$ of ρ weighted by their probabilities:

$$W(\omega, t) = \sum_k P_k W_k(\omega, t). \tag{3.98}$$

3.3.6 Fidelity of quantum states

Finally, we generalise the concept of the inner product to the realm of mixed states. The *fidelity* F of two quantum states ρ_1, ρ_2 is defined to be

$$F \equiv \left(\mathrm{Tr} \left[\sqrt{\sqrt{\rho_1}\rho_2\sqrt{\rho_1}} \right] \right)^2 . \tag{3.99}$$

In spite of the slightly obfuscated definition, the fidelity has some useful properties:

- For pure states $|\psi_1\rangle$,$\langle\psi_2|$, it reduces to the familiar square inner product $F = |\langle\psi_1|\psi_2\rangle|^2$.
- It is equal to the overlap of the Wigner functions:

$$F = \int \mathrm{d}\omega \, \mathrm{d}t \, W_{\rho_1}(\omega, t) W_{\rho_2}(\omega, t). \tag{3.100}$$

3.3.7 Photon pairs and multimode entanglement

"I would not call that one but rather the *characteristic trait of quantum mechanics, the one that enforces its entire departure from classical lines of thought."*

-Erwin Schroedinger, 1935

With a clear view of what is meant by the state of a single photon, we can now proceed to discuss more complex quantum states. The straighforward representation of the state in the case of a single photon as simply the field mode occupied by the photon does not extend to more general states. We will now consider a class of states that contain two excitations in different modes: the biphoton states. The general form for a pure biphoton state is given by

$$\boxed{|\Psi\rangle = \int f(\omega_1, \omega_2) a^\dagger(\omega_1) b^\dagger(\omega_2) \mathrm{d}\omega_1 \mathrm{d}\omega_2 \, |\mathrm{vac}\rangle \, .} \tag{3.101}$$

Here we have allowed the two photons to be distinguishable: they are created in separate modes $a^\dagger$ and $b^\dagger$ which are differentiated by one of the other degrees of freedom (such as polarisation or spatial path)[3].

The biphoton allows for a much richer structure than the single-photon wavefunction. The attribution of a single classical mode to each photon independently is no longer applicable in the general case: the state is now described by the higher-dimensional complex joint amplitude $f(\omega_1, \omega_2)$, which depends on both frequencies and which we can treat as the two-particle wave function. Much insight can be gained from the representation of $f(\omega_1, \omega_2)$ in terms of products of functions of each photon individually. $f(\omega_1, \omega_2)$ may be expressed as a sum of the form

$$f(\omega_1, \omega_2) = \sum_i \lambda_i \psi_i(\omega_1) \chi_i(\omega_2). \tag{3.102}$$

Such a decomposition is always possible. Moreover, if one chooses the functions $\psi_i(\omega_1)$ and $\chi_i(\omega_2)$ to be orthonormal, there is always one such decomposition, known as the singular value decomposition (SVD), that is unique up to the phase of the coefficients λ_i and the global phases of the states. The coefficients λ_i are known as the singular values. In the context of bipartite quantum entanglement in a continuous variable, this is also known as a Schmidt decomposition [61]. This results from the fact that it is always possible to decompose a matrix $\mathbf{F}$ into a product $\mathbf{U}^\dagger \mathbf{\Lambda} \mathbf{V}$ such that $\mathbf{U}$ and $\mathbf{V}$ are unitary and $\mathbf{\Lambda}$ diagonal. Taking row coordinates to be the position in ω_1 and column coordinates to be ω_2, the form in Eq.3.102 follows, with $\psi_i(\omega_1)$ the rows of $\mathbf{U}$, $\chi_i(\omega_2)$ the columns of $\mathbf{V}$, and the coefficients λ_i, henceforth chosen to be real, the eigenvalues (diagonal entries) of $\mathbf{\Lambda}$. If $f(\omega_1, \omega_2)$ is to satisfy

$$\int |f(\omega_1, \omega_2)|^2 \mathrm{d}\omega_1 \mathrm{d}\omega_2 = 1, \tag{3.103}$$

[3] Note that it is therefore *not* a state of the form of Eq.3.88, which is only for a specific spatial and polarisation mode and hence does not allow spectrally identical photons to be distinguishable.

then the coefficients must satisfy $\sum_i \lambda_i^2 = 1$.

The quantum properties of the state depend crucially on the distribution of singular values λ_i. In the case where there is a single nonzero $\lambda_i = 1$ then $f(\omega_1, \omega_2)$ has a unique representation as a product of single-photon states. In this case, the biphoton state is said to be *separable*. In all other cases, the state is said to be *entangled*.

As will soon become clear, entanglement is one of the most important properties, perhaps the defining property, of quantum theory. In the remainder of this section, we will discuss an approach to quantify entanglement, and the effects of local measurements on entangled systems.

We use as our measure of entanglement the effective Schmidt rank K, defined as

$$K = \frac{[\sum_i \lambda_i^2]^2}{\sum_i \lambda_i^4} = \frac{1}{\sum_i \lambda_i^4}. \tag{3.104}$$

K takes values in the range $1 < K < d$, where d is the dimensionality of each system. $K > 1$ implies entanglement. If there are X nonzero terms in the Schmidt decomposition, each with equal values of λ_i, then $K = X$. The effective Schmidt rank therefore has the property that it coincides with the number of modes of entanglement for finite-dimensional systems and may be interpreted as a generalisation of this to continuous-variable quantum systems such as time-frequency encoded states.

When one of the photons is measured in some state $|\phi\rangle = \sum_i c_i |\psi_i\rangle$, the other photon is projected into a coherent superposition $|\Psi_f\rangle$ of its Schmidt modes:

$$|\Psi_f\rangle = \langle\phi| \sum_i \lambda_i |\psi_i\rangle \otimes |\chi_i\rangle \tag{3.105}$$

$$= \sum_{ij} c_j^* \lambda_i \langle\psi_j \,|\, \psi_i\rangle |\chi_i\rangle \tag{3.106}$$

$$= \sum_{ij} c_j^* \lambda_i \delta_{ij} |\chi_i\rangle = \sum_i c_i^* \lambda_i |\chi_i\rangle . \tag{3.107}$$

In the event that $f(\omega_1, \omega_2)$ is separable, the two photons are wholly independent of one another, and local measurements on one or the other are not correlated: the resultant states $|\Psi_f\rangle$ are all the same regardless of the outcome of the projective measurement on the first. However, if $K > 1$, then such measurements are correlated. In the event that the information on the state of the first photon is lost, the final state ρ_{2f} of the second photon is a density matrix formed from an incoherent mixture of the states it would be projected into by measurement of the first photon. Mathematically this is expressed with the partial trace over the states $|\psi_i\rangle$:

$$\begin{aligned}
\rho_{2f} &= \mathrm{Tr}_1[|1,1\rangle\langle 1,1|] \\
&= \sum_{ijk} \lambda_j \lambda_k \langle\psi_i \,|\, \psi_j\rangle |\chi_j\rangle \langle\chi_k| \langle\psi_k \,|\, \psi_i\rangle \\
&= \sum_{ijk} \lambda_j \lambda_k \delta_{ij} |\chi_j\rangle \langle\chi_k| \delta_{ik} \\
&= \sum_i \lambda_i^2 |\chi_i\rangle \langle\chi_i| .
\end{aligned} \tag{3.108}$$

The purity of ρ_{2f}, or the trace of ρ_{2f}^2, is precisely the inverse of the Schmidt number K: the more entangled $f(\omega_1, \omega_2)$, the more mixed one photon is if information is lost on the other.

Maximally entangled states

If we consider two arbitrary d-dimensional quantum systems, spanned by orthonormal basis states $|\phi_i\rangle$ and $|\chi_i\rangle$, then it is possible to construct a basis of states that span the full d^2 joint Hilbert space each with the property that their Schmidt number $K = d$. One such basis of so-called maximally entangled states is given by

$$|k, m\rangle = \frac{1}{\sqrt{d}} \sum_{j=1}^{d} e^{2i\pi jk/d} |\phi_j\rangle |\chi_{j+m}\rangle , \tag{3.109}$$

such that $1 \leq k \leq d, 1 \leq m \leq d$ and where labelling of the states $\{|\phi_i\rangle\}$ and $\{|\chi_i\rangle\}$ is understood to be cyclic with period d.

The states $|k, m\rangle$ form an orthogonal basis:

$$\begin{aligned}
\langle k', m' \,|\, k, m \rangle &= \frac{1}{d} \sum_{j=1,j'=1}^{d} e^{2i\pi(jk - j'k')/d} \langle \phi_{j'} \,|\, \phi_j \rangle \langle \chi_{j'+m'} \,|\, \chi_{j+m} \rangle \\
&= \frac{1}{d} \sum_{j=1,j'=1}^{d} e^{2i\pi(jk - j'k')/d} \delta_{jj'} \delta_{mm'} \\
&= \frac{1}{d} \delta_{mm'} \sum_{j=1}^{d} e^{2i\pi j(k-k')/d} \\
&= \delta_{kk'} \delta_{mm'}.
\end{aligned}$$

3.3.8 Gaussian states

The last class of pure states we will consider in this chapter are the so-called Gaussian states. A Gaussian transformation is one which can be expressed as a Gaussian function of the field operators $\hat{p}$ and $\hat{q}$ (and hence a and $a^\dagger$), and a Gaussian state is a state created by the action of such a transformation on the vacuum. The vacuum state is Gaussian, as are the most common transformations (where the Hamiltonian is linear or quadratic in the field operators), and hence they are amongst the most easy to produce in practice and form the most common class of resource states in quantum optics. As will be shown below, multimode Gaussian transformations can be deconstructed entirely into sequential Gaussian processes on one or two modes at most, and so can be described entirely by covariance matrices expressing the field correlations between these pairs of modes. Gaussian states are also of interest in metrology as they form the general class of minimum uncertainty states in the phase-amplitude basis. In this thesis, we will be mostly concerned with Gaussian states as a resource from which to produce single-photon and biphoton states.

The general form for a pure Gaussian state is

$$|\Psi\rangle = \exp\left(\sum_{i,j} \lambda_{ij} a_i^\dagger a_j^\dagger - \lambda_{ij}^* a_i a_j\right) |\text{vac}\rangle\,, \tag{3.110}$$

where $a_0 = I$ and a_i for $i \neq 0$ is an annihilation operator for a photon in some mode i. From this general form, we can deduce the following special cases:

- $\lambda_{ij} = \delta_{0i}\delta_{0j}$. In this case $|\Psi\rangle$ is simply the vacuum state.

- $\lambda_{ij} = \alpha_i \delta_{j0}$. The state then reduces to

$$|\Psi\rangle = \exp\left(\sum_i \alpha_i a_i^\dagger - \alpha_i^* a_i\right) |\text{vac}\rangle \tag{3.111}$$

$$\equiv \prod_i D_i(\alpha) |\text{vac}\rangle\,, \tag{3.112}$$

The operators $D_i(\alpha) \equiv \exp\left(\sum_i \alpha_i a_i^\dagger - \alpha_i^* a_i\right)$ are known as displacement operators, and the states resulting from their action on the vacuum are known as the coherent states. They are one of the most common and useful classes of states in quantum optics, with many important properties. For example, by invoking the Baker-Campbell-Hausdorff identity one can show that

$$D(\alpha) |\text{vac}\rangle = e^{\frac{-|\alpha|^2}{2}} \exp(\alpha a^\dagger) |\text{vac}\rangle \tag{3.113}$$

$$= e^{\frac{-|\alpha|^2}{2}} \sum_{n=0} \frac{\alpha^n}{\sqrt{n!}} |n\rangle\,, \tag{3.114}$$

and hence

$$\begin{aligned} aD(\alpha)\left|\text{vac}\right\rangle &= e^{\frac{-|\alpha|^2}{2}} \sum_{n=0} \frac{\alpha^n}{\sqrt{n!}} a\left|n\right\rangle \\ &= e^{\frac{-|\alpha|^2}{2}} \sum_{n=1} \frac{\alpha \cdot \alpha^{n-1}}{\sqrt{(n-1)!}} \left|n-1\right\rangle \\ &= \alpha D(\alpha)\left|\text{vac}\right\rangle . \end{aligned} \tag{3.115}$$

Coherent states are therefore eigenstates of the annihilation operator and hence are preserved (to first order in the reflectivity r) by beamsplitter transformations. Since the generator of the displacement operator is simply a Hamiltonian that is first-order in the field, they are amongst the most easily-generated pure quantum states and describe the output of stable laser sources.

- $\lambda_{ij} = 0$ for $i = 0$ or $j = 0$. In this case, we can perform a Schmidt decomposition on $\lambda_{ij} = U^{\dagger}_{im}\Lambda_{mn}V_{nj}$, with $\mathbf{U}, \mathbf{V}$ unitary and $\mathbf{\Lambda}$ diagonal as before. Defining $A_i = U_{ij}a_j$, $B_i = V^{\dagger}_{ij}b_j$, and $\xi_i \equiv \Lambda_{ii}$ we then obtain

$$\begin{aligned} \left|\Psi\right\rangle &= \exp\left(\sum_i \xi_i A_i^{\dagger} B_i^{\dagger} - \xi_i^* A_i B_i\right)\left|\text{vac}\right\rangle \\ &= \prod_i \exp\left(\xi_i A_i^{\dagger} B_i^{\dagger} - \xi_i^* A_i B_i\right)\left|\text{vac}\right\rangle . \end{aligned} \tag{3.116}$$

  with the second equality following from the fact that operators in separate modes commute. The operator $S_i(\xi_i) \equiv \exp\left(\xi_i A_i^{\dagger} B_i^{\dagger} - \xi_i^* A_i B_i\right)$ is known as the two-mode squeezing operator, the state $\left|\xi\right\rangle = S(\xi)\left|\text{vac}\right\rangle$ is known as a two-mode squeezed vacuum state, and ξ is known as the squeezing parameter. It is possible to show that this state can be represented in terms of the two-mode photon-number states as

$$\left|\xi\right\rangle = \frac{1}{\cosh r} \sum_n^{\infty} (-1)^n e^{in\theta} (\tanh r)^n \left|n, n\right\rangle , \tag{3.117}$$

where $r = |\xi|$ and $\theta = \arg(\xi)$. The two-mode squeezed vacuum state exhibits strong photon-number correlations, with photons always appearing in pairs. Expanding the full multimode state $|\Psi\rangle$ in powers of $A^\dagger B^\dagger$, the lowest-order non-vacuum term is given by

$$\left|\Psi_{(1,1)}\right\rangle \sim \sum_i \xi_i A_i^\dagger B_i^\dagger \left|\text{vac}\right\rangle . \tag{3.118}$$

Note that this leading order term from a two-mode squeezed vacuum state is precisely the biphoton state described in Eq.3.101, represented in the Schmidt basis. A dim source of two-mode squeezed light is therefore often approximated as a non-deterministic source of photon pairs. Spontaneous parametric down conversion sources are a class of nonclassical light source that produces such a state, and extensive use will be made of them in this thesis. In the event that the source is engineered such that there is only one nonzero Schmidt coefficient ξ_0, (which can be achieved either through filtering the state or, as is the case with the source used in this work, source engineering) the mere detection of one photon in the B path mode suffices to project the state of the other mode into a spectro-temporally pure single photon state, $A_i^\dagger \left|\text{vac}\right\rangle$. This detection event is said to "herald" the single photon in the A-mode, and is one of the most effective ways to generate a pure single-photon state.

3.3.9 Coherence functions

"...each photon then interferes only with itself. Interference between different photons never occurs."

-Paul Dirac, referring specifically to first-order coherence.

We now have a picture emerging of the most general structure of quantum optical states as consisting of a multiple modes populated by varying and possibly correlated numbers of photons. This final section explores the methods to characterise the quantum properties of a

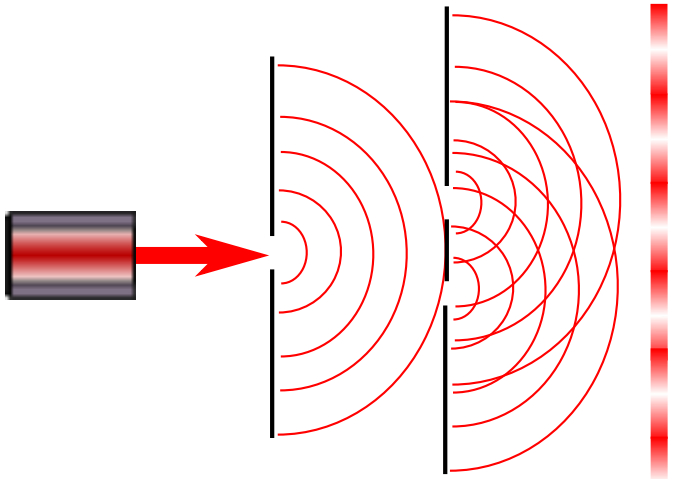


Figure 3.6: Young's double slits, a first order correlation function measurement. An optical field passing through two spatially separated slits interfere. Field correlations are measured through the interference pattern on a screen.

field through the quantum theory of coherence. The basic principle behind quantum coherence theory is to characterise an optical field in terms of the results of interferometric measurements.

In Young's double slit experiment, illustrated in Fig. 3.6, the field of the interference at some point $\mathbf{r}$ and time t is given by the superposition of the field at the two slits:

$$\varepsilon(\mathbf{r},t) = K_1\varepsilon(\mathbf{r}_1,t_1) + K_2\varepsilon(\mathbf{r}_2,t_2), \tag{3.119}$$

where K_1 and K_2 are geometric factors governed by the distances to the points in the slits $\mathbf{r}_1$ and $\mathbf{r}_2$ and $t_1 = t - |\mathbf{r}-\mathbf{r}_1|/c$, and $t_2 = t - |\mathbf{r}-\mathbf{r}_2|/c$ are the retarded time parameters describing when the lines of constant phase from each slit passed through each slit.

The interference pattern at the screen is then given by the intensity

$$\begin{aligned} I(\mathbf{r},t) &= \langle K_1\varepsilon(\mathbf{r}_1,t_1) + K_2\varepsilon(\mathbf{r}_2,t_2)\rangle^2 \qquad (3.120)\\ &= |K_1|^2 G^{(1)}(\mathbf{r}_1,t_1;\mathbf{r}_1,t_1) + |K_2|^2 G^{(1)}(\mathbf{r}_2,t_2;\mathbf{r}_2,t_2) + 2\mathrm{Re}\{K_1^* K_2 G^{(1)}(\mathbf{r}_1,t_1;\mathbf{r}_2,t_2)\}, \end{aligned}$$

where we have defined the first-order correlation function

$$G^{(1)}(\mathbf{r}_1, t_1; \mathbf{r}_2, t_2) = \langle \varepsilon^*(\mathbf{r}_1, t_1)\varepsilon(\mathbf{r}_2, t_2)\rangle. \tag{3.121}$$

We may then define the normalised first-order coherence function

$$g^{(1)}(\mathbf{r}_1, t_1; \mathbf{r}_2, t_2) = \frac{G^{(1)}(\mathbf{r}_1, t_1; \mathbf{r}_2, t_2)}{\sqrt{G^{(1)}(\mathbf{r}_1, t_1; \mathbf{r}_1, t_1)G^{(1)}(\mathbf{r}_2, t_2; \mathbf{r}_2, t_2)}}, \tag{3.122}$$

which satisfies

$$0 \leq g^{(1)}(\mathbf{r}_1, t_1; \mathbf{r}_2, t_2) \leq 1. \tag{3.123}$$

Where $|g^{(1)}(\mathbf{r}_1, t_1; \mathbf{r}_2, t_2)| = 1$ we say that the field is coherent at these two events; where $|g^{(1)}(\mathbf{r}_1, t_1; \mathbf{r}_2, t_2)| = 0$ the field is said to be completely incoherent. Coherence can be determined by observing the visibility of interference fringes when extra phase is added to one field contribution, such as by a variable phase plate over one of the slits. Such measurements are extremely useful for classical mode characterisation. Indeed, for a single-mode field, it is possible to completely reconstruct the mode merely through first-order coherence measurements. However, such measurements are intrinsically insensitive to the higher moments of the field and hence the photon number statistics. Each photon in the input pulse makes an independent contribution to the measured intensity, which add linearly. Only the intrinsic intensity depends on the total photon number, and first-order coherence can be reached with single-mode beams with arbitrary Fock state decomposition. For this reason it is necessary to further extend the concept of coherence functions.

In the 1950s, Hanbury-Brown and Twiss developed an interferometric scheme that does indeed yield different results depending on the photon number statistics of the test beam. The difference between this scheme and the Young's slit experiment, which measures field correlations, is that the Hanbury-Brown-Twiss interferometer instead measures intensity correlations.

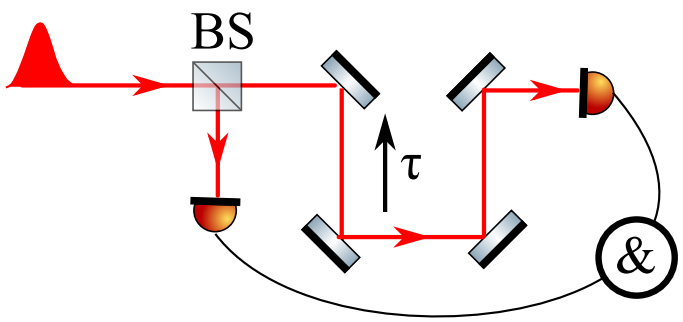


Figure 3.7: Schematic of a Hanbury-Brown-Twiss interferometer for measurement of the second-order quantum coherence function $g^{(2)}$. The test pulse is dispatched into a beam splitter, both outputs of which are monitored by integrating photodiodes. The signal in one mode is delayed, and the results compared in coincidence.

The scheme is illustrated in fig.3.7, and measures coincidence counts between two outputs of a beamsplitter, with a variable relative delay τ. The intensity correlations are given by the second order correlation function

$$G^{(2)}(t, t+\tau) = \langle I(t) I(t+\tau) \rangle. \tag{3.124}$$

By analogy with the first-order correlation function, we can now define a normalised second-order coherence function between the field at two points in time and the same point in space (the beam splitter):

$$g^{(2)}(t, t+\tau) = \frac{\langle \varepsilon^*(t)\varepsilon(t+\tau)\varepsilon(t)\varepsilon^*(t+\tau)\rangle}{\langle \varepsilon(t)\varepsilon^*(t)\rangle\langle \varepsilon(t+\tau)\varepsilon^*(t+\tau)\rangle}. \tag{3.125}$$

For a single-mode field a, this may be represented as

$$g^{(2)}(t, t+\tau) = \frac{\langle a^\dagger a^\dagger a a\rangle}{\langle a^\dagger a\rangle\langle a^\dagger a\rangle}. \tag{3.126}$$

It is straightforward to see that this measurement is sensitive to the photon number statistics of the mode. For a coherent state, $g^{(2)} = 1$. For a Fock state with $n \geq 1$, however, $g^{(2)} = 1 - \frac{1}{n}$. In the case of a single photon, where $g^{(2)} = 0$, the interpretation of this is quite intuitive: it

is not possible for both detectors to register a single-photon coincidence if there was only ever one photon sent into the interferometer! Hence, $g^{(2)}$ is used as an important indicator of the single-photon occupancy of a pulse of light.

One can continue to define higher-order correlation functions, and it can be seen that together these suffice to completely reconstruct an arbitrary quantum state [62]. In this thesis, we will use first-order coherence measurements in conjunction with second-order coherence measurements to characterise both the mode and photon number statsistics of nonclassical beams of light.

In the case of downconverted light, correlation measurements are the most common way to measure the purity. This is accomplished by sending the pulse into a Hanbury-Brown-Twiss interferometer and measuring the correlations between detection events at the two output modes. The $g^{(2)}$ may be written as [29]

$$g^{(2)} = \frac{\left\langle \left(\sum_{i=1} \hat{N}_i\right)^2 \right\rangle}{\langle \sum_{i=1} \hat{N}_i \rangle^2} \tag{3.127}$$

where the sum is over the various incoherent modes in the pulse (the eigenstates of the density matrix). For a pulse in a single, coherent mode, there is only a single term in the sum, and we expect the $g^{(2)}$ characteristic for the occupation for that field. For example, if we are measuring one output mode of a two-mode squeezer, then marginally we would expect thermal statistics, giving a $g^{(2)}$ of 2. However, if the pulse contains a spectrally-temporally incoherent mixture of K modes, each individually in a thermal state and with equal occupation, then we find that detection events in the two arms become more weakly correlated with increasing K:

$$g^{(2)} = 1 + \frac{1}{K} \tag{3.128}$$

One may also calculate $g^{(2)}$ for a subset of measurements, such as those conditioned on the

detection of a heralding photon. Conditional $g^{(2)}$ measurements such as this are important in experiments that make use of probabilistic sources of nonclassical light, such as those used throughout this thesis.

3.4 Chapter summary

In this chapter we have described the spectral-temporal modes of the electromagnetic field and their properties. Starting from Maxwell's equations, the plane-wave solutions to the wave equation were derived. We then applied the paraxial approximation to reduce our scope to the spectral-temporal modes of Gaussian beams. We introduced the inner product to calculate mode overlap and showed it is preserved by unitary mode transformations. We introduced Hermite-Gaussian pulses and showed their form is invariant under Fourier tranformation. We introduced the spectral and temporal representations and presented the transform limit constraint on their form. The effects of spectral and temporal phase were explored and their effect on Gaussian pulses derived. The chronocyclic Wigner function was derived as a representation of spectral-temporal modes.

The second part of the chapter laid out the theory describing the quantum state of pulsed modes, and introduced the wave functions of single-photon and biphoton states. The concepts of mixedness, higher-order coherence functions and entanglement were introduced to describe these states, which will be used in the experimental work presented in upcoming chapters.

Chapter 4

Single-photon spectrometry with dispersive optics

Contents

4.1 Introduction **84**

4.2 Single-photon sources **85**

4.3 Time-resolved single-photon spectrometry **88**

4.4 Building the spectrometers **89**

4.4.1 Device construction 89

4.4.2 Device characteristics 92

4.4.3 Device calibration 93

4.5 Results **95**

4.5.1 Spectrum of heralded single photons 95

4.5.2 Joint spectral intensity of a photon pair 97

4.6 Improvements **98**

4.7 Chapter summary **99**

4.1 Introduction

In Chapter 2, we motivated the interest in the spectral-temporal domain of ultrafast light as a platform in which to encode quantum information and laid out the various approaches to their characterisation in terms of amplitude and phase measurements. In Chapter 3 we formalised the concept of a spectral-temporal mode, described the effect of spectral and temporal phase operations on them, and showed how such modes completely encapsulate the spectral-temporal state of a single photon. This chapter introduces how we can perform such measurements in practice, beginning with a measurement of the spectral intensity of a single photon. As described in Chapter 2, high-dimensional measurements on single photons using large arrays of detectors, the usual scheme for classical spectrometry, are difficult at the single-photon level due to the size and cost of single-photon detectors.

In this chapter, we combine a spectral phase operation on a single photon with fast time-resolving detection to perform a partial characterisation of the pulse, by direct measurement of the relative spectral intensity $\bar{I}(\omega) = |\tilde{\varepsilon}(\omega)|^2$ [63]. This experiment uses a chirped fibre Bragg grating (CFBG), a device designed to apply very large amounts of group-delay dispersion (GDD), or quadratic spectral phase ϕ_2, to an optical pulse across a broad spectral range. In conjunction with time-resolved measurement, such a device utilises the dispersive Fourier transform concept [33, 64, 34], illustrated in Fig.4.1, to map the frequency of a temporally-short optical pulse onto the temporal envelope of the output pulse. Through time-resolved measurement of this temporal envelope, the spectrum of the original pulse can be inferred.

This chapter introduces some common features of the experimental set-up used in this thesis, before describing the construction, calibration and testing of these time-resolved single photon spectrometers (TRSPSs). In contrast with scanning spectral measurements, where only a single spectral mode can be sampled in a given experimental configuration, this method allows the simultaneous monitoring of hundreds of spectral modes, enabling multiple bits of

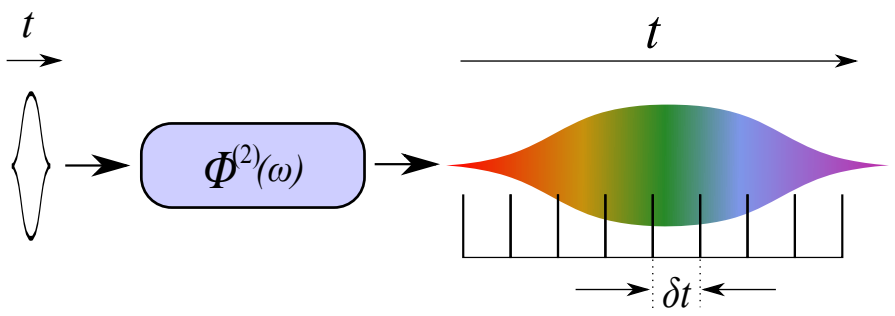


Figure 4.1: Principle of dispersive spectrometry. A short, broadband pulse receives a large, known quadratic spectral phase, or GDD, from a dispersive element. This maps its spectral components into known time bins of width δt, which can be resolved by a fast time-resolved single photon detector.

information to be encoded in a single photon. This device, the first spectrometer to use a CFBG in conjunction with fast single-photon level detection and coincidence measurement, is capable of spectrally-resolved single-photon detection with resolution unprecedented away from telecommunications wavelengths and comparable with that achieved at telecommunications wavelengths using fibre-assisted single-photon spectrometry [36].

4.2 Single-photon sources

To preface the experimental part of this thesis, we first describe the optical source used in the calibration and testing of the spectrometers, as well as in subsequent work in this thesis.

The laser source used throughout this work is a commercial Ti:Sapph femtosecond oscillator (Spectra-Physics Tsunami). This source delivers pulses with a bandwidth-limited duration of 100 fs FWHM at 12.5 ns intervals, corresponding to a spectrum centered at 830 nm and a bandwidth of 8 nm FWHM with a comb structure with a spacing of 80 MHz. An illustration of the spectral and temporal structure of this pulse train is shown in Fig. 4.2. Some of the light at the output of the laser is deflected by a beam pick-off to a fast photodiode, which generate an electronic time-reference signal or 'clock' that is used throughout the experiment.

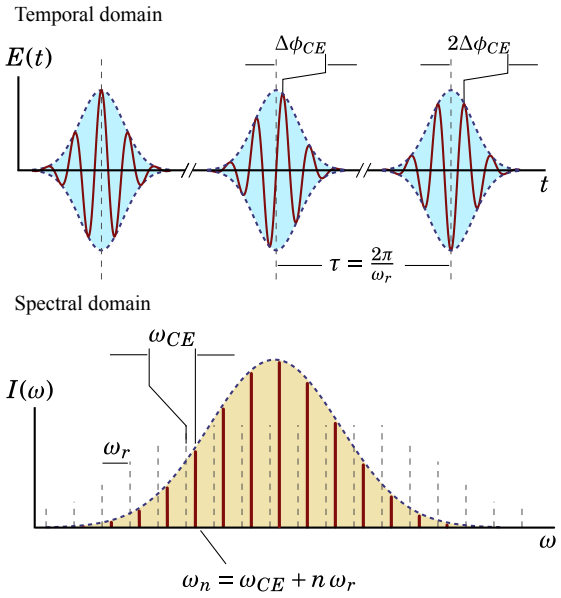


Figure 4.2: Structure of the laser pulse train in time (top) and frequency (bottom). Here $\omega_r = 2\pi \cdot 80$ MHz is the repetition frequency of the laser and $\omega_{CE} = \omega_r \Delta\phi_{CE}/2\pi$ is the carrier-envelope offset frequency.

The workhorse of nonclassical state generation in this work is frequency-degenerate spontaneous parametric down conversion (SPDC), which generates a weak two-mode squeezed vacuum state of the form described in Sec. 3.3.8 from a pump operating at double the frequency of the downconverted light. It is often expedient to work in a set-up where light from the laser has similar spectral properties to the nonclassical states we will be using, such that single photon and the laser output can be manipulated by the same (wavelength-sensitive) optics and to allow for the possibility of interfering the two signals. Hence, the SPDC source must be driven by a pump operating at double the frequency of the laser output. To provide such a pump, we use second harmonic generation, a classical nonlinear optical process which frequency-doubles the output of the laser.

Second harmonic generation is achieved in a 700 μm-long bismuth borate (BBO) crystal, generating a 3 nm FWHM spectrum at 415 nm. Heralded single photons are generated by

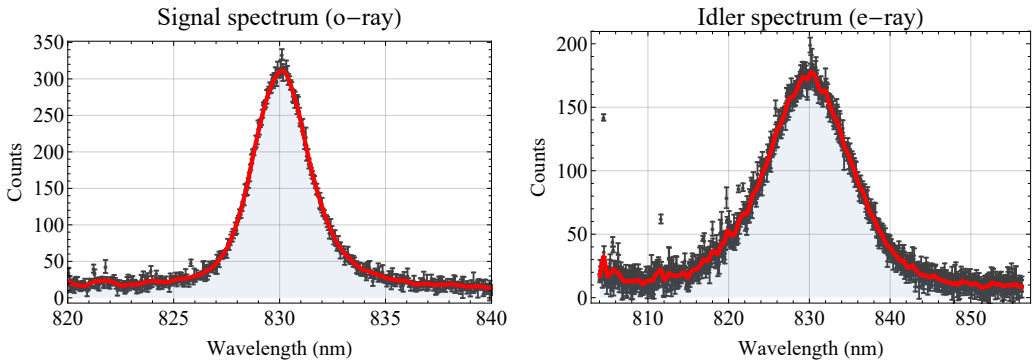


Figure 4.3: Marginal spectra of the two output modes of the KDP downconversion source.

collinear, type-II SPDC in an 8 mm-long potassium dihydrogen phosphate (KDP) crystal [52]. The orthogonally-polarised signal and idler fields have, respectively, 12 nm and 3 nm bandwidths (due to the asymmetric phase matching conditions) and degenerate 830 nm centre wavelengths. The two beams are separated at a polarising beam splitter (PBS), with a photodetection event in the idler mode heralding the creation of a photon in the signal mode. The marginal (unheralded) spectra of these downconverted modes are shown in Fig. 4.3. The phase matching of the source is chosen such that the complex joint amplitude of the two-photon state produced by the source is separable, so that detection of a heralding photon in the idler arm projects the signal into a spectrally pure single-photon state [65][1]. The downconverted photon pairs therefore do not exhibit any of the usual spectral correlations from a parametric down conversion source, and spectrally pure single photons are produced without the need to filter the herald. Multiple-photon-pair events are shown to be negligible compared to single-photon events by measurement of the conditional degree of second-order coherence, $g^{(2)}(0) = 0.06 \pm 0.04$. This also indicates the non-classical nature of the state [66, 67] and is measured using a Hanbury-Brown-Twiss-type measurement, with each detector gated by herald photon detection events. In terms of the conditioning (heralding) count rate R_H, the conditional count rates in each arm

[1]The joint spectral intensityof this source is shown in Fig.4.8 b).

of the Hanbury-Brown-Twiss interferometer R_{H1} and R_{H2} and the rate of triple coincidences R_{H12}, the conditional second-order coherence function is given by

$$g^{(2)}(0) = \frac{R_H R_{H12}}{R_{H1} R_{H2}} \tag{4.1}$$

4.3 Time-resolved single-photon spectrometry

In principle, mapping frequency modes of a beam onto the transverse spatial modes allows simultaneous monitoring of all spectral channels with a spatial array of detectors [30]. However, this approach is difficult to realise with heralded single photons and two-photon states where coincidence events must be registered, owing to challenges in fabrication of large, low-noise, balanced and efficient arrays of independent single-photon-counting detectors [32]. The frequency distribution of pulsed light can be mapped onto temporal modes by a medium with high group delay dispersion (GDD) and monitored with a single intensity detector with high temporal resolution [33, 34]. At the single-photon level this method was first used to measure the JSI of a biphoton source at telecommunications wavelengths [35] where a 3.3 km long dispersion compensating fibre introduced appropriate GDD to achieve spectral resolution of 0.72 nm at 1550 nm centre wavelength. Subsequent works [36] have improved the resolution by using more dispersive fibres and improved temporal resolution. Within the visible spectral domain significant propagation losses in optical fibres, typically 1-10 dB/km, make this approach infeasible. This challenge can be overcome for classical light by using low-loss chirped fibre Bragg gratings (CFBGs) as the dispersive medium [68, 63, 69].

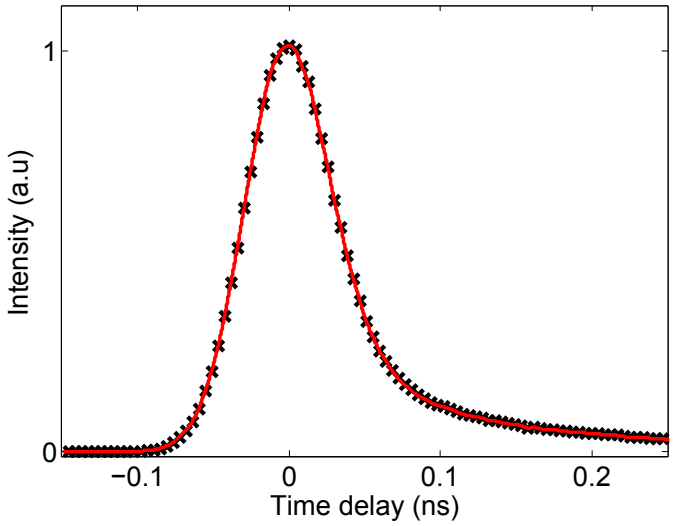


Figure 4.4: Detector response to a single fast pulse, bypassing the CFBG. The markers indicate the number of events attributed to a particular time bin by the time-to-digital converter and the red line is a cubic spline interpolation between them. The detector response function is much broader than the original duration of the pulse, and hence the spectrometer operates far from the Fourier transform limit on its resolution.

4.4 Building the spectrometers

4.4.1 Device construction

The TRSPS is constructed from a fibre-coupled optical circulator (FCIR-2285-14B181, Haphit) with specified insertion loss of 1.7 dB spliced to a CFBG (TeraXion) operating in reflection, with the circulator output is directed to a fast single-photon counting module (SPCM) as depicted in Fig. 4.5 (inset). The CFBG reflectivity $R \approx 0.5 \pm 0.05$ is nearly constant across a wavelength range of $825 - 835$ nm. The pulse to be characterised is launched into port 1 of the circulator and directed to port 2, where it is reflected by the CFBG, which provides nearly constant GDD. The reflected pulse emerges from port 3 of the circulator and is detected by a fast SPCM (PDM, Micro Photon Devices) with approximately $\delta t = 50$ ps at FWHM timing jitter and specified detection efficiency at 830 nm of approximately 10%. The SPCM signal is monitored by a time-to-digital converter (TDC, PicoQuant, HydraHarp 400) triggered by a

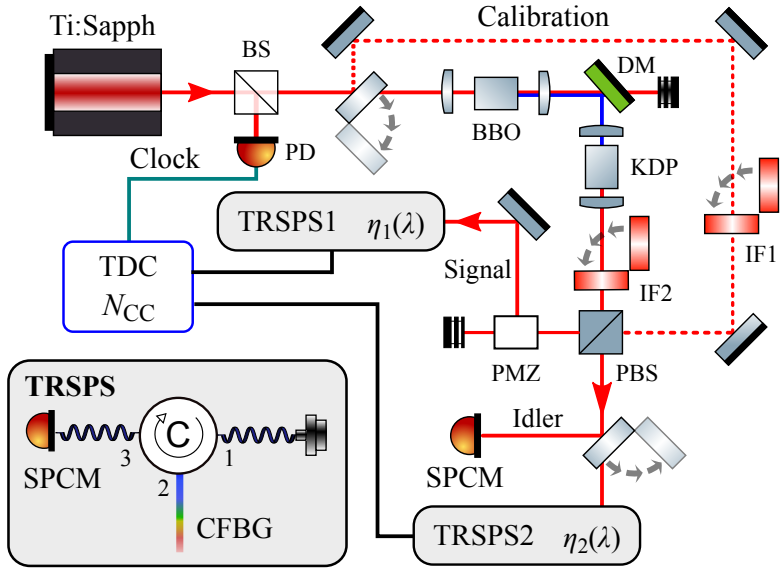


Figure 4.5: Experimental setup. Ti:Sapph, Ti:sapphire femtosecond oscillator; BBO, beta barium borate crystal;KDP, potassium dihydrogen phosphate crystal; (P)BS, (polarizing) beam splitter; PD, fast photodiode; TDC, time-to-digital converter; DM, dichroic mirror; IF, bandpass filters; PMZ, polarisation Mach-Zehnder interferometer; TRSPS, time-resolved single photon spectrograph; SPCM, single photon counting module. For calibration the TRSPSs were fitted with silicon photodiodes.

fast photodiode signal that samples the laser pulse train acting as the experiment clock. The TDC has a root-mean-square (RMS) timing resolution of < 12 ps, below the SPCM timing resolution. The trigger photodiode (Alphalas, UPD-15-IR2-FC) has approximately 15 ps rise time and timing resolution less than 1 ps. The response of the trigger-SPCM-TDC set-up to a temporally short test pulse, the temporal point-spread function, determines the resolution of the device as illustrated in Fig.4.4. The TDC records a list of times between trigger events and SPCM signals, $\{\tau_j\}$, which are then converted into a histogram of coincidence counts as a function of time delay, $N_{\mathrm{CC}}(\tau)$. The histogram time bin size of 32 ps is chosen to be smaller than the SPCM timing jitter.

The GDD and wavelength range of CFBGs are mutually constrained by the maximum optical delay introduced between the two extremes of the CFBG reflection window (determined by

its length and refractive index). For a given length of grating, a greater GDD (and hence greater spectral resolution) results in a narrower reflection bandwidth. This trade-off can be eased by using longer CFBGs or by splicing together multiple CFBGs with adjacent reflection windows in succession. For all time-of-flight spectrometry schemes, extending the maximum optical delay of the dispersive element in this manner is ultimately limited by the repetition rate of the experiment, since one must be able to discern from the time of arrival exactly which cycle of the experiment clock the pulse originated. Hence, we see that when the detector timing resolution limits the resolution of the device, spectrometers of this architecture face the trade-off relation

$$[\text{GDD}] \cdot \Delta\omega \cdot R = \frac{\delta t \cdot \Delta\omega \cdot R}{\delta\omega} \leq 1, \tag{4.2}$$

where $\Delta\omega$ is the CFBG refelectivity bandwidth, R is the repetition rate of the pulse train, δt is the timing resolution of the detector and $\delta\omega$ is the achievable spectral resolution. In our case, $[\text{GDD}] \cdot \Delta\omega \approx 9.5$ ns whereas $1/R = 12.5$ ns, and hence these spectrometers achieve upwards of 75% of the achievable resolution given the speed of the detectors. There is nonetheless a fundamental limit on the spectral resolution achievable using this method, which comes from the finite duration of the unchirped pulses entering the device, and is analogous to the diffraction limit in spatial imaging. In particular, for a Gaussian pulse with FWHM bandwidth equal to the acceptance window $\Delta\omega$, the time-bandwidth limit on the FWHM duration of the pulse δt is given by $\delta t \approx 0.44/\Delta\omega$ and hence from Eq.4.2 the ultimate resolution of time-of-flight spectrometers is given by

$$\frac{0.44R}{\delta\omega} \leq 1. \tag{4.3}$$

Time-of-flight spectrometers are fundamentally limited in spectral resolution by the repetition rate and hence the spacing of the frequency comb.

We assume that the original temporal duration of the pulse is considerably less than the SPCM timing jitter of 52 ps such that the pulse undergoes perfect frequency-to-time mapping

on the timescale of the detector resolution. Since the transform-limited duration of our pulses is less than 1 ps this is a valid approximation in our demonstration, which is thus limited by the timing jitter of our single-photon detectors.

The wavelength-dependent time of arrival relative to a pulse centred on the central wavelength of the CFBG ($\lambda_0 = 830$ nm) is $t = D(\lambda - \lambda_0)$, where D is the GDD of the CFBG defined in Sec.3.2.6. Thus the normalised spectral intensity distribution of heralded single photons, $S(\lambda)$, from this histogram will be

$$S(\lambda) = N_{\mathrm{CC}}(D[\lambda - \lambda_0] - \delta\tau)/\eta(\lambda), \tag{4.4}$$

where $\eta(\lambda)$ is the wavelength-dependent efficiency of the TRSPS, including contributions from both the circulator-CFBG setup and the quantum efficiency of the SPCM. The time offset $\delta\tau$ depends upon optical and electronic delays in the experiment and sets the central wavelength of the device response. Thus, to determine the spectrum of pulsed single photons, the time $\delta\tau$, GDD D, and efficiency $\eta(\lambda)$ must be ascertained.

4.4.2 Device characteristics

The temporal point-spread function of the detector-TDC setup has FWHM width $\delta t = 52$ ps, which is determined by sending single photons directly into the setup, bypassing the CFBG, and measuring the resulting temporal distribution. The CFBG introduces approximately $950\ \mathrm{ps/nm}$ of GDD to the optical pulse train centred about 830 nm wavelength, resulting in a frequency-dependent group delay that allows direct measurement of the pulse spectrum with time-resolved detection. The spectral resolution is set by the ratio of detector timing resolution and GDD, $\Delta\lambda = \Delta t/D = 0.055$ nm FWHM.

The total optical transmission through the device was measured by launching broadband classical pulses into the spliced circulator-CFBG combination and monitoring the input and

output spectral intensity with a standard grating spectrometer (Andor Shamrock 303i) with 0.054 nm resolution. The total loss is approximately 10 dB across the $825-835$ nm wavelength range, comprising 3.4 dB from the two passes through the circulator, 3 dB from the CFBG and the remainder from coupling and mode-mismatching losses in the fibre splices. These losses are technical in nature and could be readily reduced with further development. By comparison, if single-mode fibre is used instead of a CFBG as the dispersive element, for a scheme achieving comparable resolution one would expect the losses from attenuation alone to be approximately 30-35 dB, using typical values of the loss and GDD of single-mode fibre at 830 nm (3.5 dB/km and 0.1 ps/(nm·m) respectively). If direct filtering were used to sample the spectrum, as in a standard scanning monochromator, one would have to scan up to 200 spectral bins to achieve comparable resolution across the whole $825-835$ nm range. Assuming this could be done without loss and using an SPCM of the same detection efficiency, this would increase single-photon spectrum measurement times by up to a factor of 20[2]. Such an approach would also not allow the concurrent monitoring of multiple spectral modes and hence is of greatly reduced use for numerous applications, such as communications.

4.4.3 Device calibration

To determine D, laser pulses with narrow spectral bandwidth derived from the spectrally filtered Ti:Sapphire oscillator were routed into the device. The pulse train was passed through a 1 -nm-bandwidth interference filter (Andover Corp., USA; IF2 in Fig. 4.5), which was tilted such that the narrowband transmitted light could be tuned across the range $825-835$ nm. The spectrum of light emerging from the filter was measured with the grating spectrometer. The output of the circulator was coupled into a fast photodiode (DET10C, Thorlabs) and the delay of the signal relative to the experiment clock was measured on an oscilloscope (Tektronix MSO 5104).

[2]We note that without the need for precise timing resolution, more efficient SPCMs could be used to improve this.

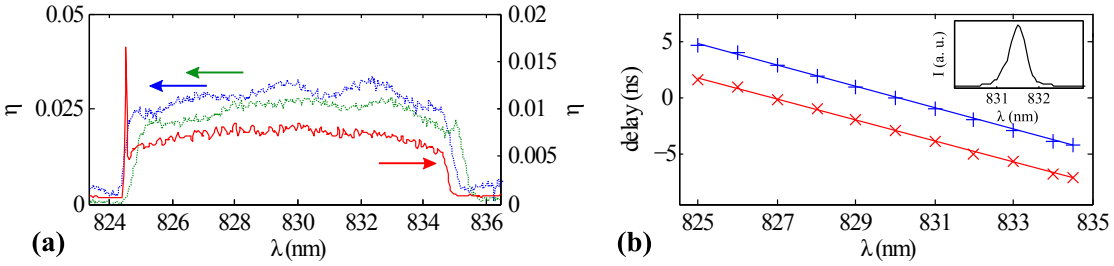


Figure 4.6: (a) Spectral response functions of the three TRSPS setups. Response is close to zero outside of the $825 - 835$ nm reflection window of the CFBGs. CFBG1 (dotted, blue) and CFBG2 (dotted, green) with PerkinElmer (slow) SPCMs. CFBG1 with MPD (fast, less efficient) SPCM (solid red, right scale). The peak at 824.6 nm is caused by back-reflection from a fibre splice. This feature is present in the dotted blue dataset as well but is not resolved by the slower SPCM. (b) Wavelength-dependent delays introduced by the CFBGs, obtained using bright laser pulses for TRSPS1 (blue, $+$) and 2 (red, $\times$) with linear fits (solid lines). INSET: Example of narrowband filtered spectrum used for calibration.

The measured delay as a function of wavelength is presented in Fig. 4.6(b) for two different circulator-CFBG setups. A polynomial fit applied to the data yields a GDD of 938 ps/nm and 958 ps/nm in TRSPS 1 and 2 respectively. Higher-order wavelength dependence of the time delay was negligible and is henceforth disregarded. The value of $\delta\tau$ depends on electronic and optical delays and needs to be determined independently for each experimental configuration. For the calibration setup, shown by the dotted line in Fig. 4.5, the spectrally filtered bright pulses were set to 830 nm central wavelength and the CFBG-circulator setup attached to a fast SPCM and TDC to complete the TRSPS. The peak in the temporal histogram can then be associated with the central wavelength of the calibration pulse, and with D known, all the single-photon time tags τ_i can be attributed to specific wavelength values. In the subsequent demonstrations involving single photons, where the beam follows a different path (the downconversion path shown by the solid line in Fig. 4.5), the timing offset $\delta\tau$ is recovered in the same fashion by using narrowband filtration of the single-photon light source itself with filter IF2 and comparing with the spectrum transmitted by the filter, obtained with a long integration time measurement on the standard spectrometer.

To determine the efficiency $\eta(\lambda)$, the same beam path – the dotted line in Fig. 4.5 – is used without the filter IF1. Removing this filter subtracts only 6 ps of delay, less than the temporal resolution of the SPCM, and therefore to within the resolution of the device the same value for $\delta\tau$ is retained. The spectrum, $I_{\text{in}}(\lambda)$, of an attenuated classical pulse is measured with the grating spectrometer. This pulse is then directed through the TRSPS setup and the total count rate at the output as a function of wavelength, $N_S(\lambda)$, is calculated from the resulting temporal histogram. This enables characterisation of the wavelength-dependent response $\eta(\lambda) = N_S(\lambda)/AI_{\text{in}}(\lambda)$, where A is a normalisation chosen such that $\int \eta(\lambda)d\lambda = H$, where H is the total heralding efficiency of the set-up. Therefore $\eta(\lambda)$ is normalised such that it corresponds to the probability density of detecting a photon at λ, conditioned on a heralding event. The resulting response function $\eta(\lambda)$ for the three TRSPS devices used is shown in Fig. 4.6(a).

4.5 Results

4.5.1 Spectrum of heralded single photons

The ability of the spectrometer to resolve fine structures in the spectrum of a single photon was tested by preparing the single photon in a double pulse, which displays interference fringes in the frequency domain. To produce a single photon in a double pulse, the heralded photon is sent through an unbalanced polarisation Mach-Zehnder (PMZ) interferometer. This is a collinear configuration in which the two arms of the interferometer are realised in polarisation rather than spatial path. It consists of a half-wave plate (HWP) which rotates the (initially horizontal) polarisation to $45°$, followed by a pair of birefringent (calcite) wedges mounted so as to produce a birefringent block of variable thickness in the beam, known as a Babinet-Soleil compensator (BSC), that introduces a controllable group delay, T, between horizontal (H) and vertical (V) polarisation modes. The PMZ is then closed with a PBS and one of the outputs monitored by the TRSPS (see fig.4.7).

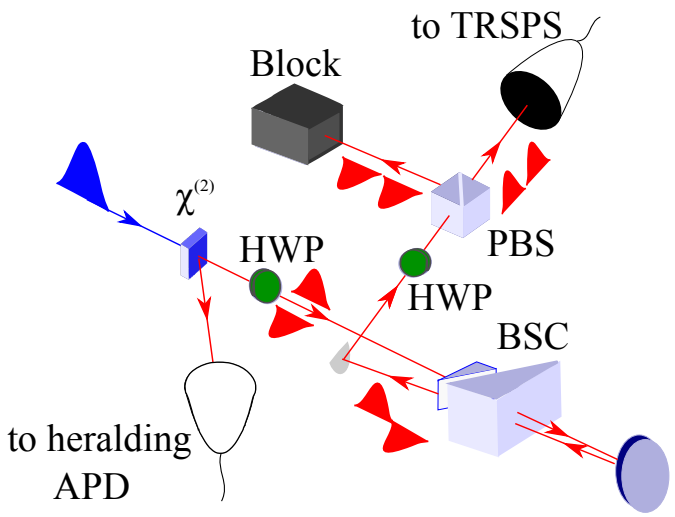


Figure 4.7: Polarisation Mach-Zehnder interferometer (PMZ). A heralded single photon produced at an SPDC source ($\chi^{(2)}$ is routed into $45°$ polarisation relative to the optical axes of a Babinet-Soleil compensator (BSC) by a half-wave plate (HWP). The resulting double pulse is then rotated such that each lobe is at $45°$ polarisation to the axes of a polarising beam splitter (PBS), which closes the PMZ. One output is then coupled into the spectrometer, whilst the other is sent towards a beam dump.

The delay T was determined from the fringe spacing in the spectral interference pattern of classical light. An additional HWP rotates the H (V) polarisation to (anti-)diagonal and a polariser selects H-polarised components of the field to be transmitted, probabilistically yielding a single-photon double pulse. The double pulse train output was sent to the TRSPS to analyse the spectrum, which was obtained by using the heralding detection event to prime the TDC to log the detection time of the signal photon. The resulting spectral interference pattern, shown in Fig. 4.8(a), displays an oscillation period of 0.2 nm, matching the time delay $T = 11$ ps introduced by the SBC. This spectrum, acquired over 300 s, contains $3\,000$ heralded single-photon detection events. The red curve shows the expected spectrum given the underlying single-photon spectrum and the time delay, with visibility and phase chosen freely in order to give the best fit. To obtain this curve, a Gaussian fit to the underlying spectrum was obtained from a separate measurement of the photon spectrum, and was modulated by a sinusoidal signal

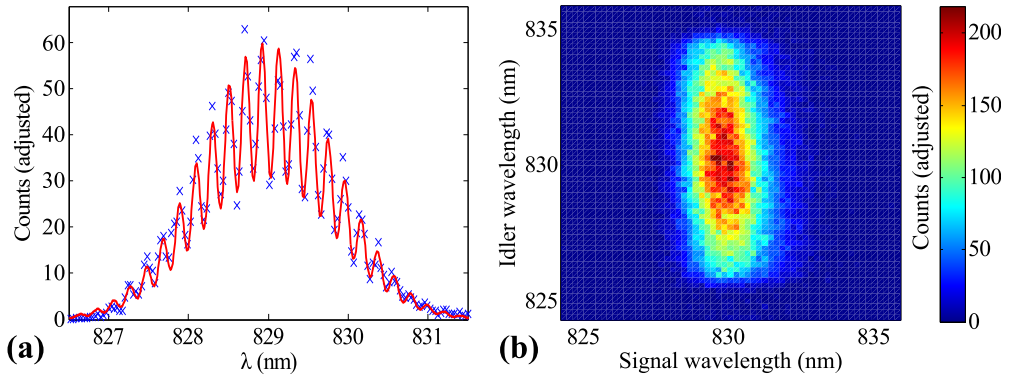


Figure 4.8: (a) Experimental heralded single-photon spectrum in a double-pulse mode. The number of counts is adjusted to account for nonuniform efficiency of the TRSPS whilst conserving the total number of counts. Solid line indicates best fit to a general Gaussian envelope with sinusoidal modulation. (b) Measured JSI of SPDC photon pair source. Coincidence counts per bin, adjusted to account for the spectral variation of TRSPS efficiency whilst conserving total count number.

with known period given by the time delay. The visibility of 24% is primarily reduced by the point-spread function of the TRSPS, although phase instability in the interferometer over the 300 s acquisition time also plays a singificant role.

4.5.2 Joint spectral intensity of a photon pair

The two TRSPSs were then used in coincidence to measure the JSI of the SPDC source. This was achieved by directing the idler photon to a second TRSPS and observing coincidence events between the signal and idler detection events at the output of both TRSPSs. This spectrum, acquired over 600 s, contains approximately 28 000 spectrally-resolved coincidence detection events.

The joint spectral measurement employed more efficient SPCMs (PerkinElmer SPCM-AQ4C) to enable sufficient coincidence count rates. These detectors have quantum efficiency of approximately 0.4 at 830 nm central wavelength, which comes at the cost of reduced timing resolution, $\Delta t = 200$ ps, and thus lower spectral resolution $\Delta\lambda = 0.2$ nm. The coincidence

timing was implemented using a lower-timing-resolution TDC (quTAU, quTOOLS; 81 ps timing resolution), capable of a higher number of input channels than the fast TDC, which allowed us to monitor two TRSPS triggered by the clock signal. To extract the JSI for the SPDC source each TRSPS was calibrated in the same manner as for the heralded single-photon interferogram experiment, and then time stamps at each SPCM were used to determine the corresponding wavelengths. The normalised JSI is shown in Fig. 4.8(b). Note that full spectral range of the idler photon is not accessible because the reflectivity of the CFBG is limited to a 10 nm range about 830 nm. This could be improved by exchanging the CFBGs by those with broader spectral range.

4.6 Improvements

Having demonstrated single-photon-level spectrometry using the dispersive Fourier transform principle, a number of major improvements were made to the experimental set-up to facilitate more sophisticated experiments utilising these devices. The BBO SHG crystal was replaced with a more efficient Type-II phase-matched bismuth borate (BiBO) crystal 400μm in length and tighter focussing into the crystal was employed. Additionally, the filter used to remove any residual infra-red light from the 415 nm pump beam, which had become damaged through moisture absorption, was replaced. Together, this increased the second-harmonic pump power after filtering from 320 mW to 550 mW. The silver mirrors used to direct the photon pairs into fibre were removed and replaced with a smaller number of dielectric mirrors (Layertec) with a much higher individual reflection efficiency of 99.98%, compared to 95% previously. To improve heralding efficiency[3], the pump beam was also passed through a spatial mode filter consisting of a circular pinhole of diameter 25μm situated between two lenses of 75 mm focal length in the focal plane. This ensured that only spatially mono-mode pumping of the downconversion

[3]Heralding efficiency is taken to be the ratio of coincidence rate to the rate of heralding photon detection events

source took place, hence reducing the number of false heralding events. All of these changes contributed to a considerable increase in the brightness and efficiency of the photon pair source, from 60 kHz of coincidences and 18% heralding efficiency to 250 kHz of coincidences and 28% heralding efficiency.

4.7 Chapter summary

In this chapter it was shown how a partial characterisation of a single photon and biphoton could be performed using frequency-to-time mapping using dispersive Fourier transform spectrometry. CFBG-based dispersive spectrometers provide simultaneous high-resolution monitoring of the spectrum of pulsed modes at the few-photon level in an all fibre set-up outside the telecommunication wavelength range. The method is limited in practice by the timing resolution of the detectors, and fundamentally by the spacing of the frequency comb. The calibration of the device can be achieved using a narrowband classical light source and conventional spectrometer. This approach enables conditional high-resolution spectral measurement of light allowing acquisition rates that are orders of magnitude faster than previously achieved. The main limitation of this approach is that it only works for a pulse train with a stable and well-characterised clock signal, and it is most effective when the input pulses are short relative to the repetition time of the pulse train. Spectrally-resolved measurements also play an important role in strategies for full mode characterisation. In the next chapter, we see how coincident spectrally-resolved measurements enable an externally-referenced strategy for full single-photon state characterisation.

Chapter 5

Spectrally-resolved Hong-Ou-Mandel interference

Contents

5.1 Introduction 101
5.2 Spectrally-resolved HOMI for partially distinguishable modes 103
5.3 Pulse shaping 108
5.4 Attenuated coherent state reference 111
5.5 Twin photon reference 112
5.6 Results 116
5.7 Chapter summary 119

5.1 Introduction

For pure-state single photons, measurement of the spectrum is insufficient to fully describe the single-photon spectral-temporal wave function $\psi(\omega)$, since such measurements are insen-

sitive to the spectral phase. We now consider how the relatively efficient[1] spectrally-resolved detection enabled by the TRSPSs described in Chapter 4 allows a phase-sensitive, externally-referenced characterisation of the full complex spectral amplitude $\tilde{\varepsilon}(\omega)$ of a heralded single photon. When combining the photon at a beam splitter with a second photon, the two photons exhibit a nonclassical effect known as Hong-Ou-Mandel interference [70], where the paths taken by each photon after the beam splitter become correlated in a manner that depends on their mode overlap. A Hong-Ou-Mandel interferometer is shown in Fig. 5.1. By spectrally resolving the output of this interferometer with a pair of TRSPSs, it becomes possible to fully reconstruct the state. The theory underlying this is described before presenting experimental results and explaining the drawbacks and benefits of this method of photon characterisation.

Hong-Ou-Mandel interference (HOMI) is a nonclassical interference effect exhibited by bosons, including photons, as a consequence of their indistinguishability. It manifests in the form of so-called photon bunching, where identical photons meeting at a beam splitter exhibit correlations in their output path that would not be expected from distinguishable noninteracting particles. In the case of two input modes a and b that are ideally coupled by a $50:50$ beam splitter, HOMI is seen by considering the action of the beam splitter, $a \to (c+d)/\sqrt{2}$, $b \to (c-d)/\sqrt{2}$, on an input state of the form $a^\dagger b^\dagger \left|\text{vac}\right\rangle$:

$$a^\dagger b^\dagger \left|\text{vac}\right\rangle = \frac{1}{2}(c^\dagger + d^\dagger)(c^\dagger - d^\dagger)\left|\text{vac}\right\rangle \tag{5.1}$$

$$= \frac{1}{2}(c^\dagger c^\dagger - c^\dagger d^\dagger + d^\dagger c^\dagger - d^\dagger d^\dagger)\left|\text{vac}\right\rangle \tag{5.2}$$

$$= \frac{1}{2}(c^\dagger c^\dagger - d^\dagger d^\dagger)\left|\text{vac}\right\rangle, \tag{5.3}$$

where the last step can be made because the creation operators in the output modes, $c^\dagger$ and $d^\dagger$, commute. The interpretation of this result is that amplitudes where each photon exits the interferometer at a different output port interfere destructively. Where the photons in the two

[1] Compared to scanning monochrometers.

input modes are otherwise indistinguishable, no coincidences can be observed.

Since HOMI is intimately related to the distinguishability of the photon pair, which depends on the pulse mode, it can be used to characterise an unknown single photon by interference with a known reference photon. One such scheme was demonstrated by Wasilewski et al. [44], where single photons were interfered with a well-characterised weak coherent state reference derived from a highly attenuated laser, and the outputs of the interferometer monitored in coincidence as the reference is scanned across a variety of pulse shapes. Since the detectors used in that demonstration were insensitive to the mode, a full mode reconstruction required continuous variation of the spectral-temporal properties of the reference signal, which was achieved by preparing the reference in a double-pulse mode with both variable separation and mean delay relative to the test pulse. As well as complicating the experimental scheme, the need to scan these two parameters leads to a significant increase in the number of measurements necessary to accomplish a full reconstruction.

Building on this concept, in this chapter we show that a train of single-photon reference pulses in a single mode with nonzero spectral amplitude over at least the same region as the test pulse, combined with spectrally-resolved coincident detection using the previously described TRSPSs, is sufficient for a full characterisation of a pure test photon. Furthermore, if the assumption of purity is not made this approach suffices to perform a full characterisation of the spectral density matrix $\rho(\omega_1, \omega_2) \equiv \langle \omega_1 \,|\, \hat{\rho} \,|\, \omega_2 \rangle$. We then describe the experimental work undertaken towards this end, culminating in the results illustrating full characterisation of a pure single photon pulse by spectrally-resolved HOMI.

5.2 Spectrally-resolved HOMI for partially distinguishable modes

We now consider the case where the two photons incident on the beam splitter are further distinguished by their spectral-temporal mode. We will denote the input state on the path mode

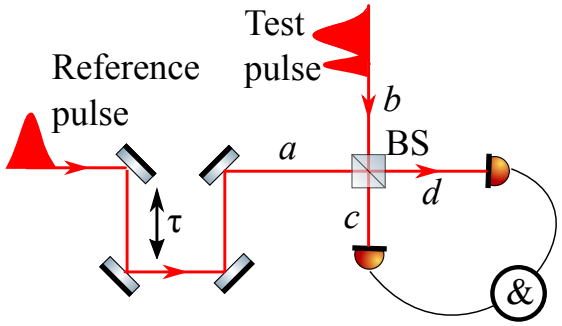


Figure 5.1: A simple Hong-Ou-Mandel interferometer. Two single-photon pulses interfere at a 50:50 beam splitter (BS), with a controllable relative delay. The output modes are then monitored in coincidence by single-photon detectors.

a, a single photon in pulse mode $\psi(\omega)$, as $a^\dagger_\psi |\text{vac}\rangle$, where $a^\dagger_\psi$ is defined in Eq.3.94, and similarly the other photon in input path mode b with temporal mode $\chi(\omega)$ as $b^\dagger_\chi |\text{vac}\rangle$. Note that $\psi(\omega)$ and $\chi(\omega)$ may or may not be identical. Then:

$$\begin{aligned} a^\dagger_\psi b^\dagger_\chi |\text{vac}\rangle =& \frac{1}{2}(c^\dagger_\psi + d^\dagger_\psi)(c^\dagger_\chi - d^\dagger_\chi) |\text{vac}\rangle \\ =& \frac{1}{2}(c^\dagger_\psi c^\dagger_\chi - c^\dagger_\psi d^\dagger_\chi + d^\dagger_\psi c^\dagger_\chi - d^\dagger_\psi d^\dagger_\chi) |\text{vac}\rangle \end{aligned} \tag{5.4}$$

Considering only the coincidence terms, with one photon in both the c and d path modes, we see that the amplitude contributing to coincidence events is

$$\begin{aligned} |c.c.\rangle =& -\frac{1}{2}(c^\dagger_\psi d^\dagger_\chi - d^\dagger_\psi c^\dagger_\chi) |\text{vac}\rangle \\ =& -\frac{1}{2}\int \psi(\omega_1)\chi(\omega_2)[c^\dagger(\omega_1)d^\dagger(\omega_2) - d^\dagger(\omega_1)c^\dagger(\omega_2)]\text{d}\omega_1\text{d}\omega_2 |\text{vac}\rangle \\ =& -\frac{1}{2}\int [\psi(\omega_1)\chi(\omega_2) - \chi(\omega_1)\psi(\omega_2)]c^\dagger(\omega_1)d^\dagger(\omega_2)\text{d}\omega_1\text{d}\omega_2 |\text{vac}\rangle . \end{aligned} \tag{5.5}$$

When spectrally resolving the outputs of the beam splitter, the probability of a coincidence event with the c-photon in frequency mode ω_c and the d-photon in frequency mode ω_d is given

by

$$P(\omega_c, \omega_d) = |\langle \omega_c, \omega_d \,|\, c.c. \rangle|^2, \tag{5.6}$$

where $|\omega_c, \omega_d\rangle = c^\dagger(\omega_c) d^\dagger(\omega_d) |\text{vac}\rangle$. Evaluating the inner product, we see

$$\begin{aligned}
\langle \omega_c, \omega_d \,|\, c.c. \rangle &= -\frac{1}{2} \langle \text{vac}| \int [\psi(\omega_1)\chi(\omega_2) - \chi(\omega_1)\psi(\omega_2)] c(\omega_c) c^\dagger(\omega_1) d(\omega_d) d^\dagger(\omega_2) \mathrm{d}^4\omega \, |\text{vac}\rangle \\
&= -\frac{1}{2} \langle \text{vac}| \int [\psi(\omega_1)\chi(\omega_2) - \chi(\omega_1)\psi(\omega_2)] ... \\
&\quad ... \Big([c(\omega_c), c^\dagger(\omega_1)] + c^\dagger(\omega_1) c(\omega_c) \Big) \Big([d(\omega_d), d^\dagger(\omega_2)] + d^\dagger(\omega_2) d(\omega_d) \Big) \mathrm{d}^4\omega \, |\text{vac}\rangle \\
&= -\frac{1}{2} \langle \text{vac}| \int [\psi(\omega_1)\chi(\omega_2) - \chi(\omega_1)\psi(\omega_2)] \delta(\omega_c, \omega_1) \delta(\omega_d, \omega_2) \mathrm{d}^4\omega \, |\text{vac}\rangle \\
&= -\frac{1}{2} [\psi(\omega_c)\chi(\omega_d) - \chi(\omega_c)\psi(\omega_d)],
\end{aligned} \tag{5.7}$$

where $\mathrm{d}^4\omega = \mathrm{d}\omega_1 \mathrm{d}\omega_2 \mathrm{d}\omega_c \mathrm{d}\omega_d$, and hence

$$P(\omega_c, \omega_d) = \frac{1}{4} |\psi(\omega_c)\chi(\omega_d) - \chi(\omega_c)\psi(\omega_d)|^2. \tag{5.8}$$

This expression provides us with the joint spectral count distribution $S(\omega_c, \omega_d)$ after repeated measurements:

$$S(\omega_c, \omega_d) \sim |\psi(\omega_c)\chi(\omega_d) - \chi(\omega_c)\psi(\omega_d)|^2. \tag{5.9}$$

Note that coincident measurements of HOM interference therefore projects onto the anti-symmetric component of the state. In this implementation, we will assume that the reference photon is in the well-characterised mode $\chi(\omega)$, and the test photon is in the unknown mode $\psi(\omega)$.

Some algorithmic manipulation is necessary to extract the amplitude and phase of $\psi(\omega)$ from Eq. 5.9. We will see that some prudent assumptions, combined with Fourier techniques used extensively in classical spectral interferometry, suffice to perform reconstruction of the

amplitude and phase of the density matrix $\rho(\omega_1, \omega_2)$.

We will first make the assumption that the temporal duration of each pulse is much less than some time τ, and hence the spectral intensity of neither pulse contains rapid changes in spectral amplitude. In particular, it allows us to apply delay τ in the reference pulse relative to the signal, such that $\chi(\omega) \rightarrow \chi(\omega)e^{i\omega\tau}$, and be confident that the pulses do not overlap in time when passing through the beam splitter. This proves to be a vital step in the mode reconstruction algorithm, since it allows us to distinguish the terms in the expansion of Eq. 5.9:

$$\begin{aligned} S(\omega_c, \omega_d) \sim & |\psi(\omega_c)\chi(\omega_d)e^{i\omega_d\tau} - \chi(\omega_c)\psi(\omega_d)e^{i\omega_c\tau}|^2 \\ = & |\psi(\omega_c)|^2|\chi(\omega_d)|^2 + |\chi(\omega_c)|^2|\psi(\omega_d)|^2 \\ & + \psi(\omega_c)\psi^*(\omega_d)\chi(\omega_d)\chi^*(\omega_c)e^{i(\omega_d-\omega_c)\tau} + \psi^*(\omega_c)\psi(\omega_d)\chi^*(\omega_d)\chi(\omega_c)e^{i(\omega_c-\omega_d)\tau}. \end{aligned} \tag{5.10}$$

Performing a 2D Fourier transform on the recovered interference pattern yields the pseudo-temporal intensity distribution $\bar{S}(T_c, T_d)$, which features three non-overlapping peaks separated by the delay τ (see Fig.5.2). The central peak corresponds to the first two terms, whilst the displaced peaks each correspond to one of the phase-sensitive terms. Since the peaks do not overlap in the pseudo-temporal domain, it is possible to multiply by some filter $f(T_c, T_d)$[2] to obtain the part of the distribution that is attributable only to one of the interference terms, $\bar{S}_f(T_c, T_d)$. This filtering operation is depicted in Fig. 5.2, in which the contours correspond to the boundaries of the filters.

$$\begin{aligned} \bar{S}_f(T_c, T_d) = & f(T_c, T_d)S(T_c, T_d) \\ = & \mathcal{F}\{\psi(\omega_c)\psi^*(\omega_d)\chi(\omega_d)\chi^*(\omega_c)e^{i(\omega_d-\omega_c)\tau}\}. \end{aligned} \tag{5.11}$$

From this point, it remains only to inverse-Fourier transform and divide by the known quantity

[2]Typically one would choose $F(T_c, T_d)$ to have a value close to unity in the region of pseudo-temporal space where one expects to find the interference term, and zero elsewhere.

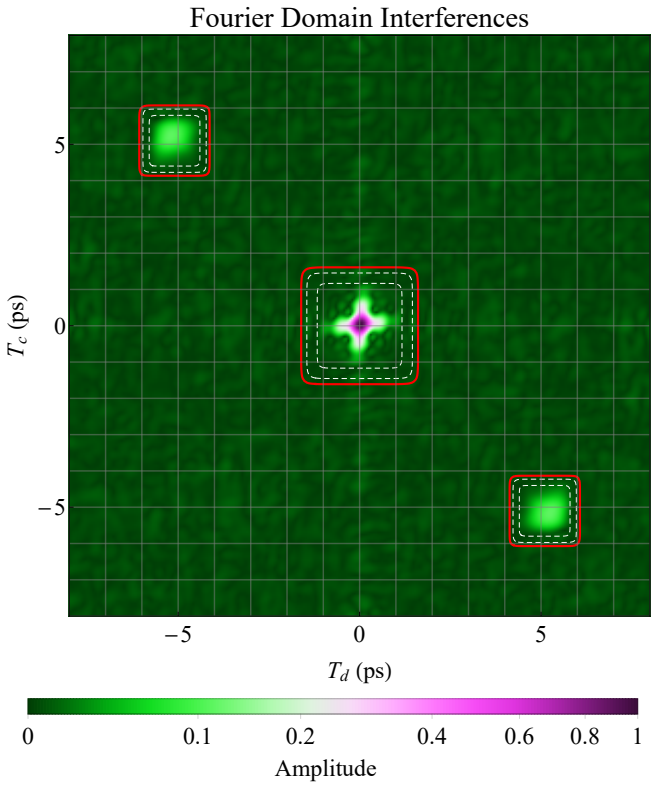


Figure 5.2: Example 2-dimensional Fourier transform of two-photon spectral interferogram $S(\omega_c, \omega_d)$, giving the pseudo-temporal distribution $\bar{S}(T_c, T_d)$ in which the three peaks corresponding to the one unmodulated and two oscillatory terms are evident.

$\chi(\omega_d)\chi^*(\omega_c)e^{i(\omega_d-\omega_c)\tau}$, after which the full complex quantity $\psi(\omega)$ can be easily extracted, for example by matrix diagonalisation.

Where it cannot be assumed that the test pulse is in a pure state, this method generalises straightforwardly to the mixed-state formalism. The state of the single photon is then represented by a density matrix:

$$\rho(\omega_1, \omega_2) = \sum_i P_i \psi_i(\omega_1)\psi_i^*(\omega_2), \tag{5.12}$$

where the states $\psi_i(\omega)$ are the eigenstates of the density operator and P_i are their respective

probabilities. In this case, the filtered oscillatory term is simply the weighted sum of its pure-state contributions:

$$\bar{S}_f(T_c, T_d) = \sum_i P_i(\mathcal{FT}\{\psi_i(\omega_c)\psi_i^*(\omega_d)\chi(\omega_d)\chi^*(\omega_c)e^{i(\omega_d-\omega_c)\tau}\}). \tag{5.13}$$

Through the linearity of the Fourier transform we thus obtain

$$\begin{aligned}\mathcal{FT}^{-1}\{\bar{S}_f(T_c, T_d)\} =& \left[\sum_i P_i\psi_i(\omega_c)\psi_i^*(\omega_d)\right]\chi(\omega_d)\chi^*(\omega_c)e^{i(\omega_d-\omega_c)\tau} \\ =&\rho(\omega_c, \omega_d)\chi(\omega_d)\chi^*(\omega_c)e^{i(\omega_d-\omega_c)\tau},\end{aligned} \tag{5.14}$$

and hence we directly sample the elements of the spectral density matrix.

Since the final stage of the extraction is division by the spectral amplitude of the reference, it is necessary that the reference pulse completely covers the spectral support of the test signal. Spectral gaps in the reference photon will lead to the inability to characterise the phase of the signal at those frequencies.

5.3 Pulse shaping

To be able to claim that a characterisation scheme can perform arbitrary mode reconstruction, it is necessary to be able to prepare test pulses in a wide range of modes. To that end, pulse shaping is an important part of the experiments in this thesis that aim to show full phase-sensitive reconstruction. In this experiment, the signal photon is directed to a fibre-coupled pulse shaper capable of performing arbitrary spectral phase operations, as well as spectral amplitude carving [20]. The shaper consists of a standard 4-f line built with a 2000 lines/mm diffraction grating (Spectrogon) and 200 mm focal length cylindrical lens (Thorlabs) with a 2D phase mask (Hamamatsu SLM, 1272×1024 pixel mask) and is capable of achieving arbitrary spectral

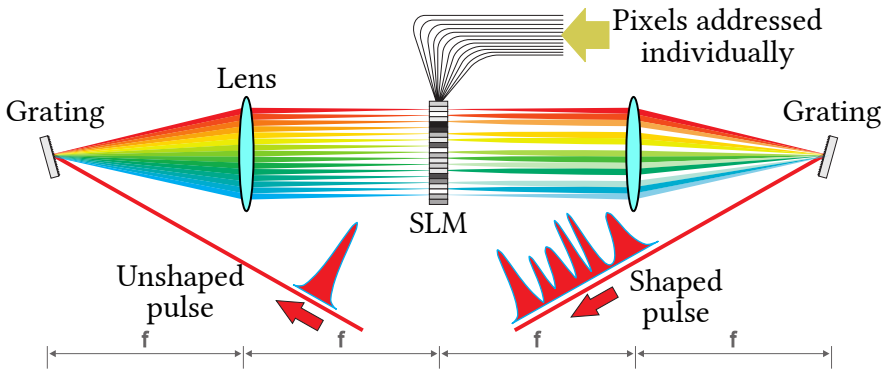


Figure 5.3: Schematic diagram of a pulse shaper appying arbitrary spectral phase. Note that in our implementation, the SLM operates in reflection rather than transmission, with the returned beam separated by a cut mirror.

phase shaping with a resolution of 0.015 nm/pixel and near-uniform spectral intensity transmission of $\approx 60\%$. A schematic is presented in Fig. 5.3. Losses are equally distributed between the diffraction grating efficiency and the insertion losses in fibre coupling at the output of the device.

The shaper is calibrated by leaving the phase profile of the SLM uniform except for a single pixel with a π phase shift scanned across the mask. This creates a spatial discontinuity in the phase over an aperture comparable in size to the wavelength, which causes diffraction at the wavelength corresponding to the pixel position. The pixel position of the SLM can therefore be mapped to the wavelength by sending in bright classical pulses through the SLM and then into a conventional spectrometer (Shamrock 303i monochromator, 1200 mm^{-1} grating, Andor) and then monitoring the position of the dip in the spectral intensity caused by diffraction around the phase-shifted aperture.

Since the shaper itself introduces spectral phase, it needed to be calibrated. The exact phase introduced by the shaper in its unmodulated state was determined by spectral interferometry[71]. This consisted of building second, free-space beam path around the pulse shaper to form a Mach-Zehnder interferometer with the shaper in one arm, into which bright classical pulses

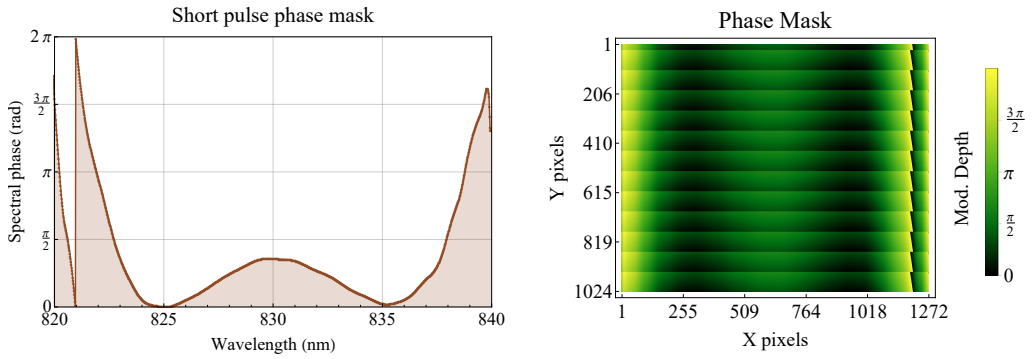


Figure 5.4: Left: Default phase mask for the SLM, designed to cancel spectral phase introduced by the pulse shaper itelf. Right: 2D phase mask, showing the grating-like features used to control spectral amplitude.

were sent. The relative spectral phase in the two arms introduced by the pulse shaper was then extracted using Fourier-space algorithms[3] [23]. This was eventually used to create a default mask for the SLM, designed to compensate for the nonuniform spectral phase introduced by the device itself and to therefore allow complete control and manipulation of the spectral phase. This is shown in Fig. 5.4.

The SLM writes different amounts of spectral phase onto the two polarisation states, so it is important that only light linearly polarised in the correct orientation (the vertical direction along the phase mask) is sent into the pulse shaper. However, due to slight misalignment and imperfection in the grating, a small amount of the other polarisation appears in the line. A PBS was added after the output to remove the unwanted polarisation, which would add noise to the final mesaurement and hence interfere with the reconstruction.

The amplitude shaping of the device is achieved by writing a saw-tooth diffraction grating on the SLM mask across the vertical dimension. This creates an additional beam at the output of the device, separated by a few micrometers from the zero-th order. Only the diffracted (first-order) term couples into fibre, so by controlling the splitting ratio with the depth of the

[3] A similar phase extraction algorithm, but with spectral shear, is described in Chapter 4.

grating feature, it is possible to implement spectrally-selective loss and hence spectral amplitude carving.

5.4 Attenuated coherent state reference

To reconstruct the state of an ensemble of single photons we consider two different reference sources: an attenuated coherent state, as was used in the demonstration reported in [44], or the paired photon from a downconversion source.

We first consider the case with attenuated coherent light from the laser beam to provide the reference signal. This approach has the advantage that having derived from an attenuated classical source, the reference could be easily characterised by existing, nonlinear-based techniques such as SPIDER or FROG prior to attenuation. Hence, no prior knowledge of the output of the downconversion source (besides its spectral support) was necessary to perform a mode characterisation on one of the daughter photons.

The test pulses are heralded single photons generated by the KDP parametric downconversion source described in the previous chapter. The reference pulse was provided by a weak pick-off derived from the laser itself, heavily attenuated to bring the intensity down to the single-photon level. This creates a weak coherent state with Poissonian photon number probability distribution

$$p_n = \frac{\mu^n}{n!} e^{-\mu}, \tag{5.15}$$

where p_n is the probability of a photon occupation number n and $\mu = |\alpha|^2$ is the average number of photons per pulse 3.3.8. On the one hand, it is desirable to choose μ in order to increase the number of single-photon events in the reference beam, since this increases the probability of a coincidence with the test photons. However, on the other hand, the term where the reference pulse mode has two-photon occupation can give rise to a background coincidence, even in the absence of a single photon in the test pulse. Since there is no way to distinguish

such events from the coincidences corresponding to one photon in each input, they need to be supressed or they will create an excessively noisy background that precludes phase extraction. The photon number statistics of the coherent state thus create a dilemma: μ must be chosen high enough to ensure some desired (reference-signal) coincidences, but not too high to drown them in undesirable (reference-reference) coincidences. Hence we require $p_1 >> p_2$, or $\mu << 1$.

This proved to be a severe constraint on data acquisition rates. The comparatively high losses of the TRSPS and fast detector lead to a low heralding efficiency $h \sim \mathcal{O}(10^{-3})$ for heralded signal photons by the detection stage. This creates much opportunity for accidentally-heralded coincident events deriving from the two-photon term in the coherent state. The ratio r of desired to unwanted coincidences is then given by

$$r = \frac{hp_1}{p_2} = \frac{2h}{\mu}. \tag{5.16}$$

To achieve a value of $r > 1$, it was necessary to attenuate the laser so severely that heralded coincidences were detected at a rate of only several hundred mHz. Since the full joint interferogram requires on the order of 10^4 coincidences for phase reconstruction, this would require on the order of a full day of accumulation. Thus, without improvements in our spectral measurement efficiency, which is encapsulated in the heralding efficiency at the detection stage, h, the use of coherrent states as a reference is infeasible, and hence we consider the alternative source of reference photons.

5.5 Twin photon reference

To suppress accidental background coincidence counts, one needs a reference pulse with low populations in photon number states greater than one. Here, we take advantage of the spectrally uncorrelated nature of the KDP SPDC source, together with the strong correlations in

photon number between its two output modes, to provide a reference that greatly reduces the background coincidence term.

We use as a reference the broadband photon produced by the KDP downconversion source, known as the idler photon. Due to the strong correlations in photon number between the signal and idler arms, this approach greatly increases the probability of desired coincidences relative to the background two-photon events. However, this solution has the drawback of requiring the independent characterisation of the idler photon. In the next chapter, we will demonstrate a means of performing such a characterisation directly, without the need for an external reference. For the purposes of this demonstration, the spectrum of the idler was well-known from the TRSPS measurements described in the previous section, and the assumption was made that the spectral phase was constant (i.e. that the pulse was transform limited). Alternatively, if full characterisation of the reference photon is not possible, the scope of the measurement can be reduced to a relative phase measurement, which is still of considerable interest for mode-matching applications.

The experimental set-up is illustrated in fig. 5.5. The broadband (idler) photon with bandwidth 12 nm is taken to be the reference whilst the narrowband (signal) photon with bandwidth 3 nm is treated as the test pulse. After the two photons are separated by a PBS, they are routed into separate optical paths. The path of the signal mode passes through the pulse shaper, which also served to fine-tune the relative delay τ between the two arms by writing linear spectral phase onto the signal photon.

The first experimental requirement is to ensure that the photons are indistinguishable in both the spatial and polarisation domains. The former was accomplished by implementing the interferometer in polarisation-maintaining single-mode fibre, including an evanescently coupled fibre beam splitter. This ensured any photon events registering at the outputs correspond only to photons propagating in the fundamental spatial mode of the fibre. Polarisation matching was achieved by constructing a polariser consisting of an auxiliary free-space path, coupled at

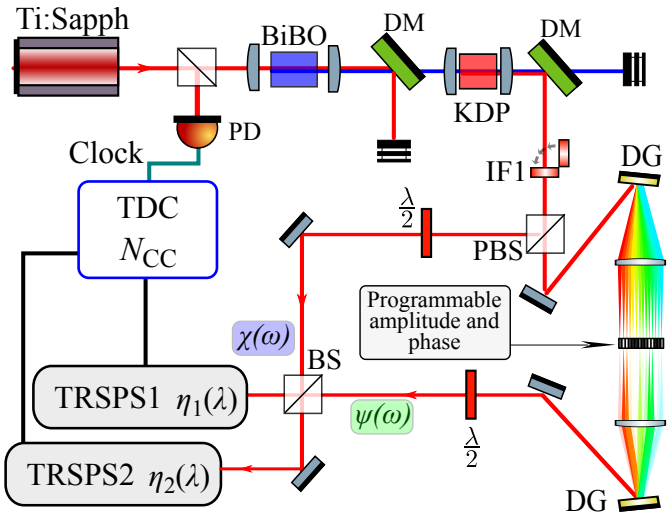


Figure 5.5: Experimental scheme for pulse characterisation by spectrally-resolved Hong-Ou-Mandel interference using the idler photon as a reference. Note that the final beam splitter and the spectrometers are fibre-coupled. PD: photodiode. DM: dichroic mirror. DG: diffraction grating. BS: Beam splitter. PBS: Polarising beam splitter

both ends by polarisation-maintaining fibres, into which a PBS was inserted, such that only light in the transmission polarisation of the beam splitter would be detected at the output. One end of this path was directly coupled to the high-efficiency single-photon detector. Half-wave plates were then inserted into both the signal and idler arms after downconversion prior to fibre coupling[4]. The two downconverted modes were sequentially coupled into the input polariser apparatus and the half-wave plates in each configured to maximise transmission at the output, thus verifiying that the two photons were in the same polarisation mode.

Another crucial step in the experimental preparation is to precisely set an appropriate value of τ, which must be large enough for the terms in Eq.5.10 to be distinguishable in the pseudo-temporal domain, but small enough that the spectral fringes are slow enough to be resolvable by the TRSPSs. A value in the range of several picoseconds was determined to be optimal, allowing the interference fringes to be clearly distinguished without loss of contrast from the

[4]Since the signal and idler photons are separated at a PBS, linear polarisation can be assumed.

spectral point-spread function of the TRSPSs.

Since it is known that the photons are generated in the downconversion crystal at the same time, direct time-of-flight measurements of the single photons sufficed to measure the delay in arrival time at the beam splitter between the signal and idler arms to within tens of picoseconds. One output of the beam splitter was coupled directly into a fast single photon detector and each of the two photon paths were alternately blocked, providing a direct comparative measurement of the difference in path length to within the timing resolution of the APDs. This allowed the two arms of the HOM interferometer to be constructed to within a few millimeters of their desired length.

Determining the precise value of τ down to the femtosecond range could not be accomplished by direct time-of-flight measurements, due to timing jitter in the detectors and monitoring electronics, and hence needed to be done optically. This was achieved with a Hong-Ou-Mandel measurement without spectrally-resolved detection. Once the highest precision had been accomplished with the time-of-flight measurements, a 3 nm bandpass filter centred at 830 nm (IF1 in Fig. 5.5) was placed in the section of common path between the KDP crystal and PBS in order to improve mode overlap and photon pairs were sent into the interferometer. The pulse shaper was used to scan the relative delay across a range of ± 15 ps, with the outputs monitored in coincidence. The delay that minimised the distinguishability of the two photons, and hence the number of coincidences, was taken to correspond to the point where $\tau = 0$. The delay line was then moved to the setting where $\tau = 5.5$ ps, the interference filter was removed, and the outputs of the interferometer routed into the two TRSPSs, using the faster MPD single-photon detectors.

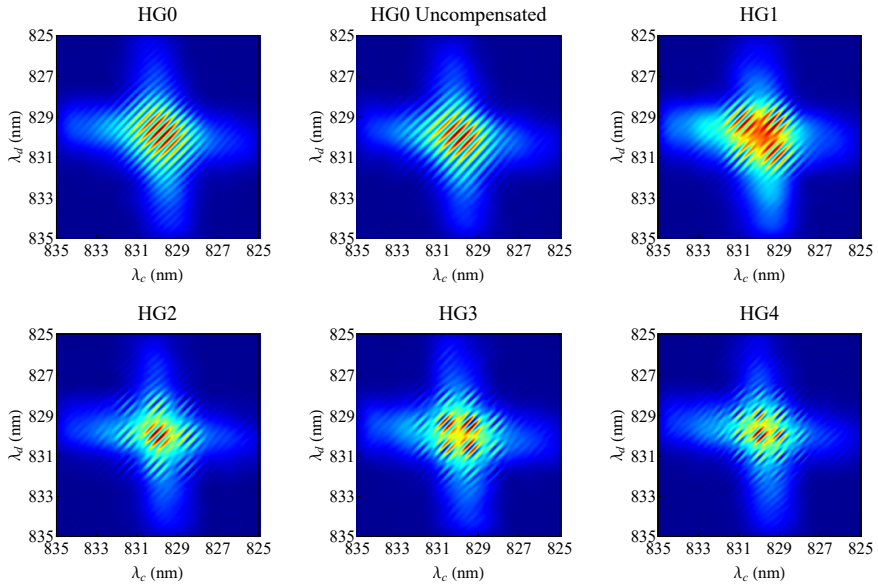


Figure 5.6: Interferograms showing the spectrally-resolved HOMI patterns for the first 5 psuedo-Hermite-Gauss (HG) modes as a function of wavelength in the two detection modes. The interferograms have been processed such that only the terms within the boxes of Fig. 5.2 are shown.

5.6 Results

To test the reconstruction method, the signal photon was prepared in a variety of different modes by the pulse shaper. Since the spectrum at the output of the SPDC source was already known and the spectral phase could be reasonably assumed to be close to constant, it was possible to prepare the single-photon pulses in a series of modes approximating the first five Hermite-Gauss modes, defined in Sec. 3.2.4, by applying a π-phase shift across the points in the spectrum corresponding to the nodes of those states (Fig. 5.7). This allowed a nontrivial and near-orthogonal basis of pseudo-Hermite-Gaussian modes to be prepared without the need for spectral amplitude carving, which introduces losses. Through propagation, the signal photon acquires a quadratic component of the spectral phase in propagation through 2 m of coupling fibre (approximately 90,000 fs^2). In the case of the zero-order mode HG0, this extra contribution was measured by

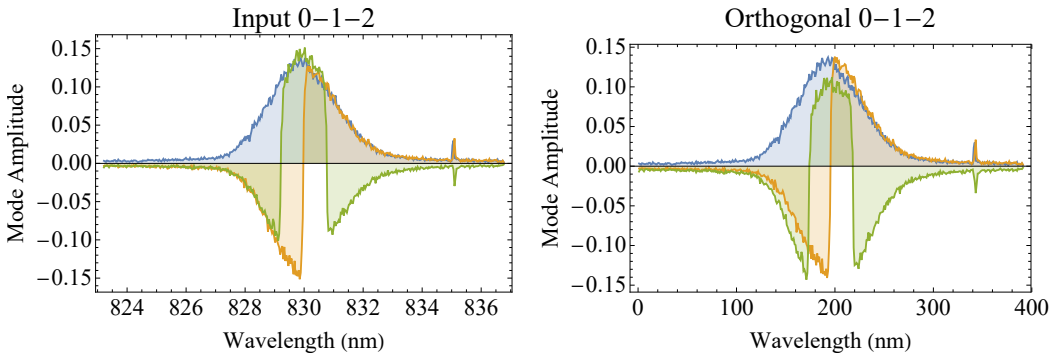


Figure 5.7: Left: The first three pseudo-Hermite-Gauss modes, HG0 (blue), HG1 (orange) and HG2 (green). Right: Eigenstates of the density operator for the mixed-state photon.

the experiment. The pulse shaper then applied an additional component to the spectral phase to compensate for this, yielding a resultant flat spectral phase. This is shown in Fig. 5.8. In the subsequent cases, the measurement was taken with this quadratic spectral phase component compensated for.

The interferograms[5] $S(\omega_c, \omega_d)$ are shown in fig. 5.6. From this, the density matrices were extracted using the procedure described in Sec. 5.2. The modulus of these, $|\rho(\omega_1, \omega_2)|$ are presented in fig.5.8 and the phase $\phi(\omega_1, \omega_2) = \text{Arg}\{\rho(\omega_1, \omega_2)\}$ in fig.5.9.

The boundaries of the regions of alternating phase are consistent with their predicted positions, indicating good agreement between the TRSPSs and the pulse-shaper calibration. In addition, a phase difference of approximately π was measured between these regions, demonstrating the capability of this technique to characterise spectral phase.

Lastly, a mixed state was simulated by flickering the pulse shaper alternately between the HG0, HG1 and HG2 modes for approximately equal periods of time. This has the effect of simulating a mixed state described by a density operator with those three states as its eigenvalues.

The interferogram for this state is shown in fig. 5.10a), in which overlayed interference patterns from the different contributions are visible. The modulus of the density matrix is shown

[5]High-frequency noise, including most shot noise, has been removed by Fourier filtration.

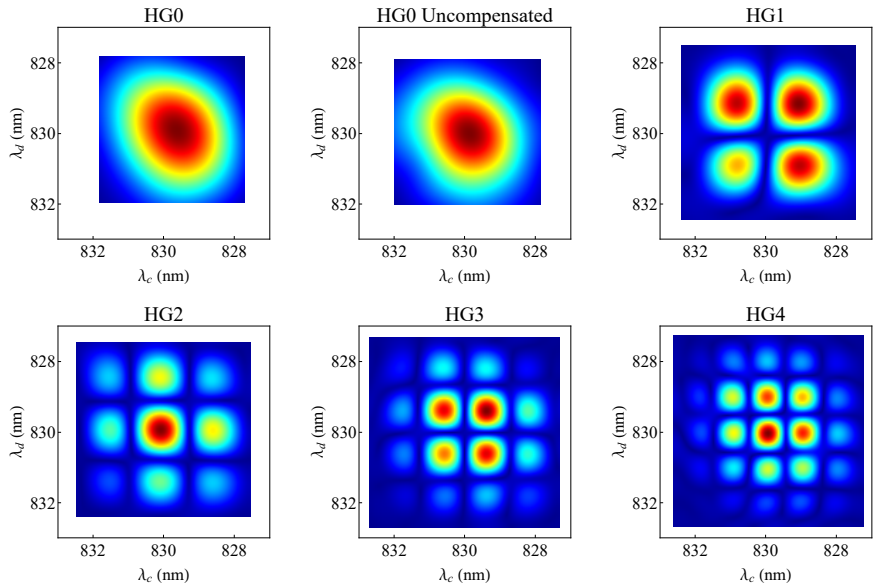


Figure 5.8: Reconstructed density matrix modulus $|\rho(\lambda, \lambda')|$ for first five pseudo-Hermite-Gaussian (HG) modes plus uncompensated HG0 mode as a function of wavelength in the two detection modes.

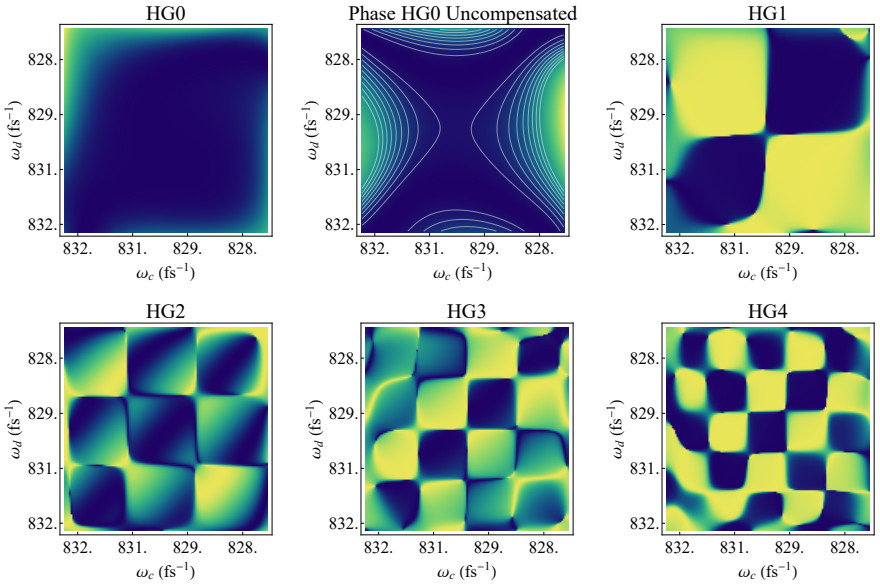


Figure 5.9: Cosine of reconstructed density matrix phase $\phi(\omega_1, \omega_2) = \text{Arg}\{\rho(\omega_1, \omega_2)\}$ for first five pseudo-Hermite-Gaussian (HG) modes plus uncompensated HG0 mode as a function of frequency in the two detection modes.

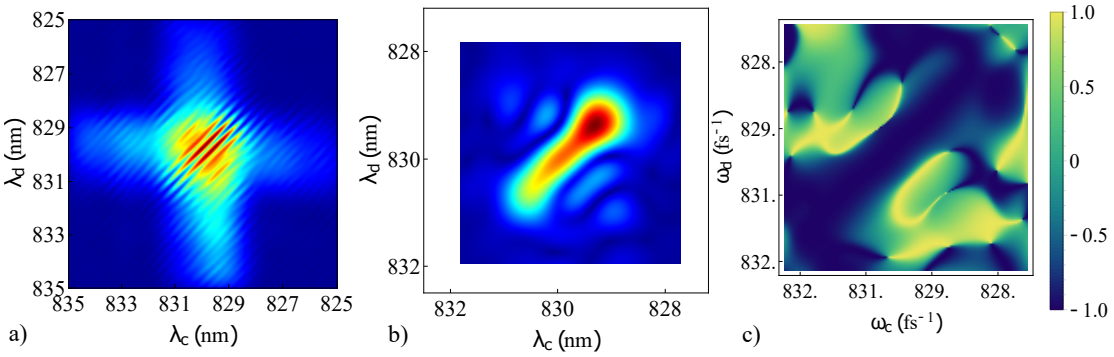


Figure 5.10: a) Fourier-filtered interference pattern from spectrally-resolved HOMI with a test pulse prepared in an equal mixture of the first three spectral pseudo-Hermite-Gauss modes. b) Modulus of the reconstructed spectral density matrix. c) Phase of the reconstructed density matrix.

in Fig.5.10b). The suppression of the off-diagonal elements of the density matrix is clear, as the state begins to approximate a spectrally incoherent mixture. Lastly, the phase of the density matrix, which is approximately constant over the region of support, is shown in Fig.5.10c).

5.7 Chapter summary

In this chapter, we proposed and demonstrated an externally-referenced technique to reconstruct the full spectral density matrix of an unknown single photon. The method has the advantages that it uses resolved measurements and hence does not require repeated reconfiguration in order to perform a reconstruction. Furthermore, there is no need to make the assumption of state purity- the full spectral density matrix of the photon is directly extracted from the interference pattern. This approach may be of particular use when one photon from a well-characterised photon pair source is used to probe some unknown process and the other retained, in which case tomography on the state of the probe using this method can provide useful information about its evolution under the unknown process. In Chapter 8 we will return to considering this experimental configuration, in the case where the two photons exhibit spectral-temporal

entanglement.

Nonetheless, this technique suffers from the caveat that a well-characterised single photon source needs to be on hand to act as the reference; that this source must have a small, precisely-known and stable relative delay with respect to the test pulse; and that it must have at least the same spectral support in order to perform a complete characterisation. Furthermore, the reconstruction requires coincident spectrally-resolved measurement of both outputs of the interferometer. In the case where spectrally-resolved detection introduces serious losses, this can substantially increase measurement times. Finally, this method measures intensity correlations and so is a second-order coherence function measurement. Such measurements are sensitive to photon number statistics, and so it is necessary to assume that the occupation of the test pulse is at most one photon. In the case where the unknown mode is also populated with unknown photon number statistics, this approach breaks down.

Future work on this technique may revisit the strategy of using a reference other than the twin photon from the same downconversion source. This strategy becomes practical when the spectrally-resolved detection efficiency is sufficiently high, and hence with advances in detector technology may become a feasible measurement. Alternatively, a reference with sub-Poissian photon number statistics could be used to suppress the two-photon term. Ideally, the reference would be another single photon, with $g^{(2)} = 0$. In the next chapter we will explore a complimentary approach for full state reconstruction that circumvents many of these disadvantages by using the single photon as its own reference and performing a first-order spectral coherence measurement at the output.

Chapter 6

Single photon characterisation by electro-optic spectral shearing interferometry

Contents

6.1 Introduction 122

6.2 Measurement principle 123

6.2.1 Background 123

6.2.2 Phase reconstruction 126

6.3 Experiment 130

6.3.1 Obtaining spectral shear 130

6.3.2 Experimental set-up 135

6.4 Calibrating the interferometer 136

6.5 Results 140

6.5.1 Data acquisition 140

6.5.2 Reconstruction of phase that is polynomial in frequency 141

6.5.3 Arbitrary phase reconstruction 146
6.5.4 Time-frequency distributions 148
6.6 Discussion 149
6.6.1 Characterisation of single-mode fields 149
6.6.2 Mixed state reconstruction 153
6.6.3 Heralding 155
6.6.4 Practical considerations 157
6.7 Chapter summary 159

6.1 Introduction

In the previous chapter a novel method to characterise the full spectral-temporal state of an ensemble of single photons based on spectrally resolved Hong-Ou-Mandel interference was introduced. Although able to recontruct spectrally mixed states, this approach suffered from the suite of preconditions associated with using an external reference, including mode-matching in the transverse-spatial and polarisation as well as spectral-temporal domains, faithful reference characterisation, and *a priori* knowledge of the pulse in the form of its spectral support. This chapter seeks instead to demonstrate a "black box" quantum pulse characterisation device, into which one can send successive copies of an unknown pulse mode with single-photon level occupancy and achieve full phase-sensitive mode reconstruction with as few constraints as possible. The operating principle of this device is electro-optic spectral shearing interferometry (EOSI), introduced in Section 2.5.3, the feasibility of which has previously been demonstrated with classical light [49]. EOSI is a form of spectral-shearing interferometry (SSI) in which the spectral shear is provided by linear temporal phase modulation [49]. This device directly measures the first-order coherence function of the pulse in the spectral domain. As such it is entirely self-contained and self-referenced, and for pure states performs a full reconstruction without any feedback or reconfiguration mid-measurement. Without relying on intensity correlations, it

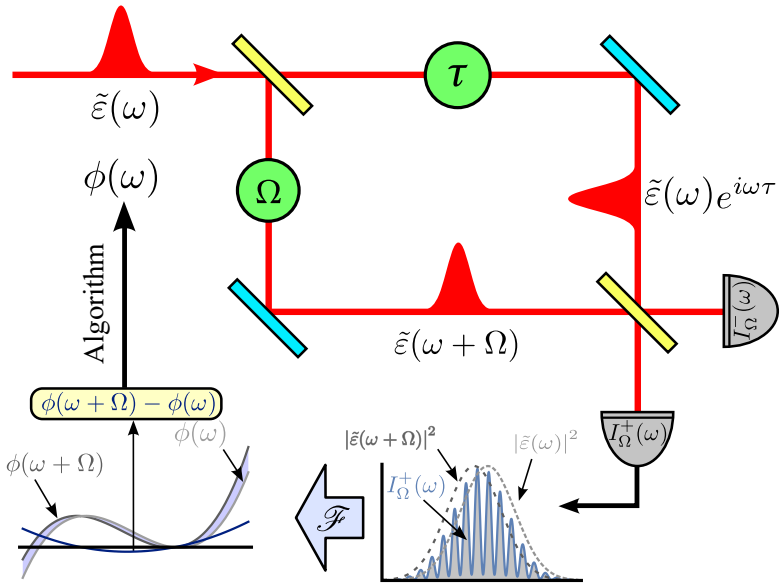


Figure 6.1: A pulse is sent into a Mach-Zehnder interferometer which imparts a frequency shear and relative temporal delay to the two arms. Spectrally-resolved detection at the output reveals a interference pattern $S(\omega)$, from which it is possible to recover the spectral amplitude and phase of the test pulse.

is robust to the photon number statistics of the mode and so suffices to characterise single-mode pulses with unknown photon occupancy. The wavelength range of pulses which the device can characterise is wide, limited not by the strict need for mode overlap with an optical reference but rather by technical considerations such as the admittance window of the spectrometers.

6.2 Measurement principle

6.2.1 Background

We begin by illustrating how the SSI protocol extracts the spectral phase of an electromagnetic field mode, and hence the field mode of a single photon [72, 73, 48, 47]. We will begin with the representation of the spectral mode function in terms of the spectral amplitude and spectral phase, $\tilde{\psi}(\omega) = |\tilde{\psi}(\omega)|e^{i\phi(\omega)}$.

The spectral mode function $\tilde{\psi}(\omega)$ can be fully reconstructed from measurements of the spectral intensity $S(\omega) = |\tilde{\psi}(\omega)|^2$ and the spectral phase $\phi(\omega)$. At the single-photon level, measurement of $S(\omega)$ can be obtained using the TRSPS described in Chapter 4. However the spectral phase is more difficult to obtain and measurements must be made indirectly.

The EOSI protocol for obtaining the spectral phase works by splitting the pulse with a $50:50$ beam splitter, applying a spectral shift Ω to one of the copies and a temporal shift τ to the other, recombining the two at a second beam splitter, and analyzing the spectral interference pattern (see Fig. 6.1). The intensity of the spectral interference pattern from the two outputs $S^{+}_{\Omega,\tau}(\omega)$ and $S^{-}_{\Omega,\tau}(\omega)$ is

$$\begin{aligned} S^{\pm}_{\Omega,\tau}(\omega) &= \frac{1}{4}|\tilde{\psi}(\omega)e^{i\omega\tau} \pm \tilde{\psi}(\omega+\Omega)|^2 \\ &= \frac{1}{4}(S(\omega)+S(\omega+\Omega)) \\ &\quad \pm\frac{1}{2}\mathrm{Re}\{\tilde{\psi}(\omega)\tilde{\psi}^*(\omega+\Omega)e^{i\omega\tau}\}. \end{aligned} \tag{6.1}$$

This can also be expressed in terms of the first-order spectral correlation function of the field, $G^{(1)}(\omega,\omega') = \tilde{\psi}^*(\omega)\tilde{\psi}(\omega')$, as

$$\begin{aligned} S^{\pm}_{\Omega,\tau}(\omega) &= \frac{1}{4}\left(G^{(1)}(\omega,\omega)+G^{(1)}(\omega+\Omega,\omega+\Omega)\right) \\ &\quad \pm\frac{1}{2}\mathrm{Re}\left\{G^{(1)}(\omega+\Omega,\omega)e^{i\omega\tau}\right\}. \end{aligned} \tag{6.2}$$

The Fourier transform of this spectral interference pattern with respect to ω results in three

terms

$$\begin{aligned} & \overline{S}^{\pm}_{\Omega,\tau}(T) \equiv \mathcal{FT}\{S^{\pm}_{\Omega,\tau}(\omega)\} \\ = \; & \frac{1}{2}\overline{S}(T)(1+e^{iT\Omega}) \\ \pm \; & \mathcal{FT}\{|\tilde{\psi}(\omega)\tilde{\psi}^{*}(\omega+\Omega)|\exp[i\Delta\phi(\omega,\Omega)]\} \circledast \delta(T-\tau) \\ \pm \; & \mathcal{FT}\{|\tilde{\psi}^{*}(\omega)\tilde{\psi}(\omega+\Omega)|\exp[-i\Delta\phi(\omega,\Omega)]\} \circledast \delta(T+\tau), \end{aligned} \tag{6.3}$$

where $\circledast$ indicates a convolution, $\Delta\phi(\omega,\Omega) = \phi(\omega) - \phi(\omega+\Omega)$ and $\overline{S}(T) \equiv \mathcal{FT}\{S(\omega)\}$, which has a width determined by the transform-limited duration of pulses with the spectrum $S(\omega)$.

If τ is chosen to greatly exceed the pulse duration, then the three terms of the above expression can be resolved from one another, and it is possible to computationally filter one of the two side bands centered about $\pm\tau$ in the Fourier domain, e.g.

$$G^{(1)}(\omega+\Omega,\omega)e^{i\omega\tau} = |\tilde{\psi}(\omega)\tilde{\psi}^{*}(\omega+\Omega)|\exp\{i[\omega\tau+\Delta\phi(\omega,\Omega)]\}, \tag{6.4}$$

where the equality holds for spectrally pure, single-pulse mode states. Taking the argument of this yields

$$\mathrm{Arg}[G^{(1)}(\omega+\Omega,\omega)e^{i\omega\tau}] = \theta(\omega,\Omega,\tau) \equiv \omega\tau + \Delta\phi(\omega,\Omega), \tag{6.5}$$

from which the spectral phase, $\phi(\omega)$, can be faithfully reconstructed if τ is well calibrated, as described below. Up to an irrelevant constant phase, Eq. (6.5) can be rewritten as

$$\theta(\omega,\Omega,\tau) = (\omega-\omega_0)\tau + \phi(\omega) - \phi(\omega+\Omega) \tag{6.6}$$

where ω_0 is the centre frequency of the interference term. We call $\theta(\omega,\Omega,\tau)$ the phase gradient, since to first order in Ω it increases linearly with the first derivative of the spectral phase.

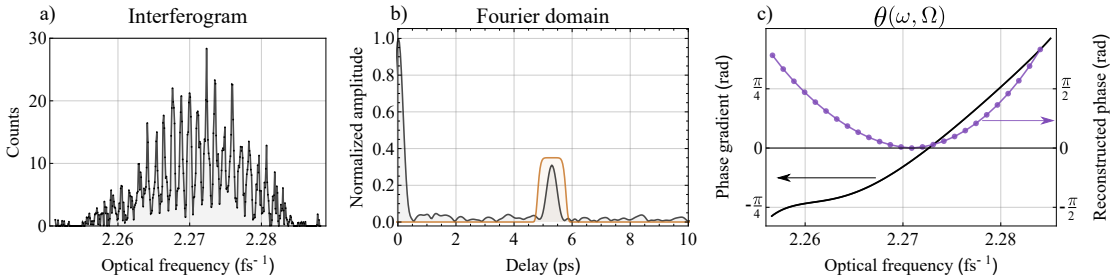


Figure 6.2: Phase extraction process for unshaped heralded single photons. a) output of the interferometer, showing a 20 seconds acquisition. b) Fourier transform of the interferogram, showing a peak centered around the delay τ of 5 ps. Overlay: filter used to isolate the sideband. c) argument of the inverse Fourier transform of the filtered sideband (black) and reconstructed phase (purple). The delay τ has been removed, showing a linear slope due to the quadratic phase accumulated through fibre propagation.

The Fourier analysis method used to extract the envelope and the phase from the interference pattern is similar to that previously described in Section 5.2. It is achieved by digitally filtering one sideband in the pseudo-temporal domain and taking either the modulus or the argument of the inverse Fourier transform. This procedure is depicted using experimental data in Fig. 6.2. Knowledge of Ω and τ is therefore sufficient to reconstruct the spectral phase up to a constant offset (ϕ_0).

6.2.2 Phase reconstruction

There are several mathematical approaches to extracting the spectral phase $\phi(\omega)$ from the measured phase gradient $\theta(\omega, \Omega, \tau)$. Although in principle any of these algorithms suffices to reconstruct any spectral phase, a different reconstruction method might be appropriate depending on what the expected spectral phase profile behavior. For many applications, only the low-order terms in ω of the spectral phase $\phi(\omega)$ are of interest and so it is most appropriate to proceed by finding a polynomial expansion of $\phi(\omega)$. It is helpful to reformulate Eq. (6.5) using a Taylor

series expansion of $\phi(\omega+\Omega)$ in Ω about ω,

$$\begin{aligned}\theta(\omega,\Omega,\tau) =&(\omega-\omega_0)\tau-\Omega\frac{d\phi(\omega+\Omega)}{d\Omega}\bigg|_{\Omega=0}-\frac{\Omega^2}{2}\frac{d^2\phi(\omega+\Omega)}{d\Omega^2}\bigg|_{\Omega=0}-\cdots\\ =&(\omega-\omega_0)\tau-\Omega\frac{d\phi(\omega)}{d\omega}-\frac{\Omega^2}{2}\frac{d^2\phi(\omega)}{d\omega^2}-\cdots.\end{aligned} \tag{6.7}$$

We express $\phi(\omega)$ as a power series about ω_0 and defining $\delta\omega \equiv (\omega-\omega_0)$,

$$\phi(\omega_0+\delta\omega)=\phi_0+\phi_1\delta\omega+\phi_2\delta\omega^2+\phi_3\delta\omega^3\cdots \tag{6.8}$$

Substituting into Eq. 6.7 we obtain

$$\begin{aligned}\theta(\delta\omega,\Omega,\tau)=\delta\omega\,\tau \quad &- \quad \Omega(\phi_1+2\delta\omega\phi_2+3\delta\omega^2\phi_3\cdots)\\ &- \quad \Omega^2(\phi_2+3\phi_3\delta\omega+\cdots)\\ &- \quad \Omega^3(\phi_3+\cdots\end{aligned} \tag{6.9}$$

At this point we remark that if Ω is small compared to the bandwidth of the pulse, then for most of the frequency range where $\theta(\delta\omega,\Omega,\tau)$ is large compared to its error (i.e., the spectral overlap region of the pulses) Eq. (6.7) reduces to

$$\theta(\delta\omega,\Omega,\tau)=\tau\delta\omega-\Omega\frac{d\phi}{d\omega}, \tag{6.10}$$

and hence $\phi(\delta\omega)$ can be directly extracted as

$$\phi(\delta\omega)=\frac{1}{\Omega}\int[\tau\delta\omega-\theta(\delta\omega,\Omega,\tau)]d\omega, \tag{6.11}$$

with the integration performed over the region where $\theta(\delta\omega,\Omega,\tau)$ can be reliably measured, set by the spectral range over which there is sufficient amplitude to measure spectral interference.

Note that in this limit Eq. (6.9) shows

$$\theta(\delta\omega, \Omega, \tau) = -\Omega\phi_1 + \delta\omega(\tau - 2\Omega\phi_2) - 6\Omega\delta\omega^2\phi_3 + \cdots \tag{6.12}$$

and hence any error in the calibration of τ manifests after the integration over ω as an error in the extracted value of ϕ_2, the second-order spectral phase or "chirp", introduced in Section 3.2.6. It is therefore vital that τ is accurately characterised, with error much less than $2\Omega\phi_2$. We will return to this in section 6.4. Within the regime of the shear Ω being much less than the bandwidth of the pulse, the errors in the phase reconstruction will be smaller with increasing shear. If the shear were comparable to the pulse bandwidth, the visibility of interference fringes will be lost due to the reduced overlap of the sheared and unsheared pulses, which would negatively affect phase reconstruction. The spectral shear applied by our experimental set-up can be tuned up to a maximum of approximately 0.6 nm, for a pulse bandwidth of several nanometers, and so the interferometer operates comfortably within the regime where the overlap of sheared and unsheared pulses is close to unity. However the shear is large enough relative to the bandwidth that the successive terms in Eq. (6.9) contribute significantly across much of the range of the integral in Eq. (6.11) and may not be ignored. Therefore, to extract the phase terms, we note that Eq. (6.9) is linear in the spectral phase terms ϕ_i and hence may be expressed as

$$\delta\omega\ \tau - \theta(\delta\omega, \Omega) = A\vec{\phi}, \tag{6.13}$$

where $\vec{\phi}$ is the vector $(\phi_1, \phi_2, \phi_3 \cdots)^T$ and A is a matrix defined with its columns as

$$A \equiv (\Omega, (\delta\omega + \Omega)^2 - \delta\omega^2, (\delta\omega + \Omega)^3 - \delta\omega^3, \cdots). \tag{6.14}$$

In this analysis, we choose A to include terms up to $(\Omega/\delta\omega)^4 \approx 10^{-4}$ to keep calculation errors small. Eq. (6.13) can be efficiently and accurately solved numerically using a matrix division

routine to obtain the spectral phase.

For arbitrary spectral phase, provided the pulse's temporal support is limited to the region $[-\pi/\Omega,\ \pi/\Omega]$, the phase can also be recovered through a concatenation approach [48]. This method is more suitable for spectral phase profiles that are non-analytic in ω about the center frequency ω_0 or contain high-order polynomial contributions in ω that would not be reconstructed by the above approach. This approach begins by setting the spectral phase at some value $\phi(\omega_0)$ to be some constant arbitrary value, typically zero, and then iteratively reconstructing the phase at every point $\omega + n\Omega$ for integer n, such that

$$\begin{aligned} \phi(\omega_0 + (n+1)\Omega) &= \phi(\omega_0 + n\Omega) \\ &\quad +\theta(\omega_0 + n\Omega, \Omega, \tau) - \Omega\tau \end{aligned} \tag{6.15}$$

According to the Shannon theorem [47], this concatenation approach suffices to completely characterise the pulse if it has no temporal support outside the range $[-\pi/\Omega, \pi/\Omega]$.

When processing the EOSI interferogram, care must be taken since most spectrometers will sample the intensity profile in wavelength, rather than frequency. For narrowband pulses it is acceptable to assume that the bandwidth of the pulse is sufficiently small compared to the central wavelength that a linear relationship is sufficient to translate the spectrum from the wavelength domain to the frequency domains. However this approximation is not valid in our demonstration and thoroughly corrupts the extracted spectral phase if implemented [74]. In our implementation we corrected for the problem by using Fourier transform interpolation, which functions well even up to fringe spacing at the Nyquist limit.

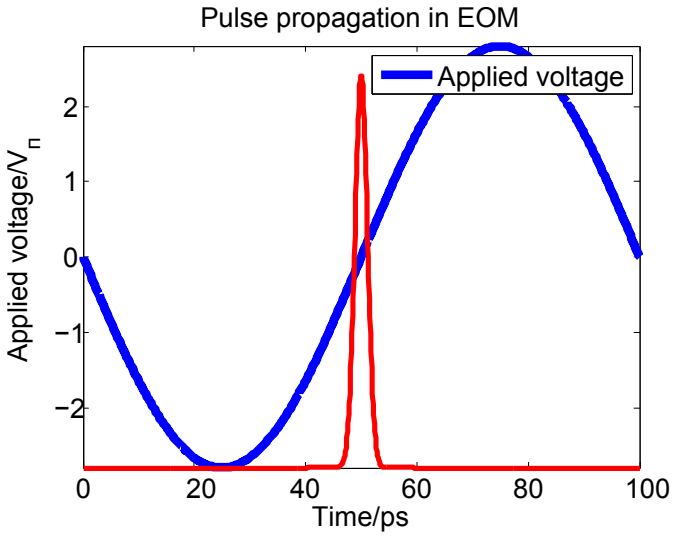


Figure 6.3: Electro-optic phase modulation. An optical pulse (red) co-propagates through an electro-optic medium in step with an applied voltage wave (blue), which varies the refractive index of the medium, inducing a time-dependent phase in the pulse.

6.3 Experiment

6.3.1 Obtaining spectral shear

Spectral shear is obtained through electro-optic temporal phase modulation. This involves passing the light through an electro-optically responsive material in which the refractive index is simultaneously varied such that a temporally varying phase is applied to the pulse. The effect of linear temporal phase modulation is the desired uniform frequency shift. This method has the advantage that it is deterministic and largely independent of the incident pulse shape or amplitude, and is thus applicable at the single-photon level. Recently, the feasibility of this method of applying a spectral translation has been shown at the single-photon level [75]. This experiment used an EOSpace $LiNbO_3$-waveguide electro-optic modulator (EOM). The principle of using an EOM to achieve constant frequency shift is illustrated in Fig. 6.3. The modulator is driven by a 10 GHz sinusoidal voltage emitted by a parametric dielectric resonant oscillator (PDRO) and amplifier (Aspen Electronics). The PDRO upconverts by a factor of 125 the 80

MHz signal derived from the laser cavity photodiode, ensuring that the 10 GHz output signal is phase-locked to the optical pulse train. The modulator is designed such that an applied radio-frequency (RF) signal propagates through the device with phase velocity equal to the group velocity of an optical pulse centered at 830 nm wavelength. A pulse traveling through the device therefore acquires a time-dependent phase $\phi(t)$, depending on the temporally locked RF field amplitude with which it co-propagates. This results in a temporal variation in the refractive index of the waveguide viewed from the reference frame of the optical pulse. The voltage difference necessary to achieve a relative phase shift of π between orthogonal polarisation propagating through the EOM is referred to as the half-wave voltage V_π and depends on the length of the modulator and the electro-optic coupling at a given RF frequency.

The time-varying refractive index of the waveguide can then be used for deterministic manipulation of the frequency spectrum of the pulse, such as spectral shear [75] and bandwidth manipulation [76]. If the centre of the pulse co-propagates with the steepest part of the sinusoidal RF waveform, then the optical field at the output of the modulator when the input state $\psi_{\text{in}}(t)$ is launched may be written

$$\psi_{\text{out}}(t) = \psi_{\text{in}}(t)\text{exp}\left(-i\pi\frac{V\text{max}}{V_\pi}\sin(2\pi f t)\right), \tag{6.16}$$

where $V\text{max}$ is the maximum voltage of the applied RF field, f is the frequency of the RF signal and $\psi_{\text{in}}(t) = |\psi_{\text{in}}(t)|e^{i\omega_0 t}$ is the temporal profile of the incident pulse. If the pulse is temporally short compared to the period of the modulation (in our case, 100 ps), then we can neglect higher-order terms in the expanded temporal phase, resulting in

$$\psi_{\text{out}}(t) = |\psi_{\text{in}}(t)|\text{exp}\left(i\left(\omega_0 - \frac{2\pi^2 f V\text{max}}{V_\pi}\right)t\right). \tag{6.17}$$

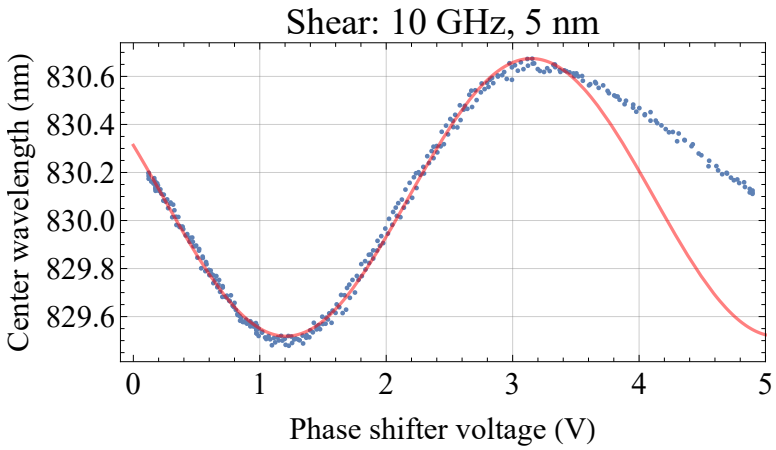


Figure 6.4: Measured centre frequency of a bright, spectrally narrow pulse after propagation through the EOM, plotted against the control voltage of the RF phase shifter. Red curve- sinusoidal fit to the region $V < 3$.

The result is therefore a frequency shift of $\Omega = 2\pi^2 f V_{\max}/V_\pi$. The maximum value of the attainable shift Ω was determined experimentally by tuning the control voltage of the phase shifter across its whole range- see fig.6.4. This measurement also allowed us to calibrate the control of the phase shifter and hence tune with which section of the RF waveform the pulse train co-propagates. Since the temporal support of the pulse must be within the region where the RF signal is linear, there is a limit on the maximum temporal duration of pulses to which a uniform shift can be applied without distorting the shape of the spectral envelope. This temporal aperture is taken to be approximately 25 ps, or one-quarter RF waveform with sinusoidal driving signal of frequency 10 GHz.

In practice, the phase-lock between the RF signal and the optical pulse train will have some noise, resulting in each pulse experiencing timing jitter with respect to the RF signal. However, provided this does not cause the pulse to fall outside the temporal aperture, this amounts only to a fluctuation of the carrier-envelope phase ϕ_{CE}. The effect of this is simply to reduce the visibility of the fringes in the interferogram, and does not systematically affect the calculated spectral phase [77].

The electro-optic response of the medium is much greater in the crystal axis aligned with the applied electric field. For light polarised along the extraordinary axis of the crystal, the coefficient of the electro-optic tensor has a magnitude of 33 pm/V. Light propagating in the orthogonal polarisation is less affected since the electro-optic response in this direction to the applied RF field is much less. By propagating the unshifted pulse through the modulator in an orthogonal polarisation, it is possible to achieve a common spatial path for the two pulses [74]. This common path approach has the advantage of making the set-up more resistant to vibrational and thermal fluctuations in path length and so improving interference visibility, as well as minimizing the relative spectral phase between the two arms of the interferometer. Overall in our set-up we were able to achieve a relative spectral shear between the two arms of the interferometer of approximately 0.58 nm at 830 nm central wavelength.

Generally, when the RF source is turned on, it will lock to an arbitrary phase of the pulse train, meaning the pulse co-propagates at a random point of the RF waveform. Furthermore, when the EOM is being driven, the phase lock is dependent on thermal fluctuations that can result in a slow drift of the RF waveform relative to the optical pulse. It is therefore necessary to stabilise the temperature environment of the EOM, which was achieved by fastening it to a metallic heat sink and applying thermally conductive paste to the interface. The amplitude and phase of the RF signal wave can be adjusted in real time through a variable time delay and attenuator [75]. For bright classical light, it suffices to send the beam (of the modulated polarisation) into the EOM and spectrally resolve the output, and then select the setting of the RF phase control such that the center wavelength of the pulse is extremised. However, the single-photon signal produces far fewer counts, making reliable alignment to the RF in real time vastly more challenging. To make the process easier, a bright coherent beam line is coupled into the same beam path as the downconverted light during the phase-locking of the photon source to the RF. This bright classical beam line was constructed such that the delay in the pulse train relative to the single-photon pulses was an exact integer multiple of the RF waveform period

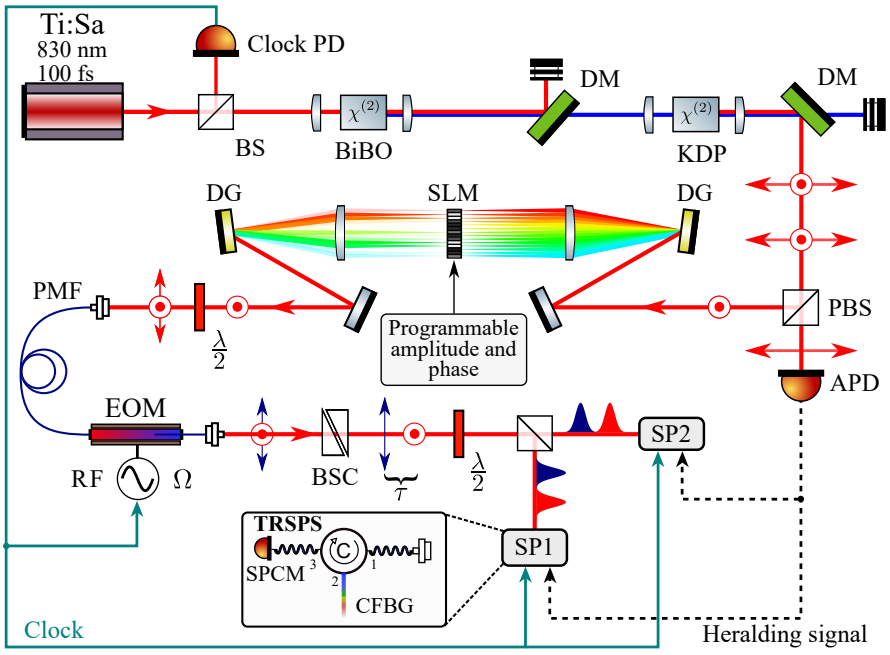


Figure 6.5: Experimental setup for single-photon generation, shaping and EOSI detection (see text for detailed description). Ti:Sa: Titanium-Sapphire femtosecond oscillator; BS: beam-splitter; PD: photodiode; DM: dichroic mirror; PBS: polarizing beam-splitter; APD: single-mode-fibre-pigtailed avalanche photodiode; DG: diffraction grating; SLM: spatial light modulator; PMF: polarisation-maintaining fibre; EOM: electro-optic phase modulator; RF: radio-frequency signal; BSC: Babinet-Soleil compensator; $\lambda/2$: half-waveplate; SP: spectrometer; CFBG: chirped fibre Bragg grating; SPCM: single photon counting module; TRSPS: time-resolved single-photon spectrometer.

(100 ps). By setting the delay of this pulse train relative to the single-photon pulse train to precisely 200 ps, it is known that the bright coherent pulses are aligned with the same point of the RF waveform as the single photon pulses, and therefore will receive the same spectral shear. In this way it is possible to ensure the single photons are spectrally shifted by inspecting the spectrum of bright classical light.

6.3.2 Experimental set-up

The full experimental setup is depicted by Fig. 6.5. Single photons are produced using the optical set-up described in the Chapter 4, culminating in the KDP source. In this experiment, we use the spectrally broader of the two photons, with FWHM 12 nm. The broadband heralded photons are sent to the pulse shaper described in Chapter 5 to produce a range of wave packets to allow the reconstruction to be tested with a wide range of test pulse modes. To allow the photons to pass within the reflectivity window of the TRSPSs without the extrema of the spectrum being abruptly cut off, the pulse shaper also crops their spectrum by applying a Gaussian spectral intensity filter on the pulse with FWHM 7 nm. Our implementation of the EOSI uses a polarisation Mach-Zehnder (PMZ) configuration similar to the one used to produce spectral fringes in Chapter 4. This has several advantages over a path mode Mach-Zehnder or other interferometer designs: lower coupling losses, automatic spatial-mode matching, common-path stability, and a reduced need to account for internal spectral phase differences within the interferometer. One minor disadvantage is that the unmodulated pulse also passes through the modulator, making it susceptible to residual electro-optic effects. This could affect the relative shear Ω or otherwise distort the reference pulse and thus corrupt the extracted spectral phase, although this proved negligible in our demonstration. Several factors reduce the visibility of the interferogram: thermal fluctuations in the interferometer, the timing jitter of the RF signal with respect to the optical pulse train, the mixedness of the single-photon state arising from optical fluctuations in the pump and pulse shaper, and mixedness arising from imperfect separability of the two-photon state and the tracing over the state of the herald photon. Besides optical effects, the limited resolution caused by the point-spread function of the spectrometers also creates the appearance of reduced visibility.

The value of τ must be chosen such that the spectral fringe spacing is well below the sampling limit of the spectrometer (corresponding to $\tau \approx 27$ ps) to provide an interferogram with

good visibility, but large enough such that the interference term is clearly separable from the DC signal and that spectral fringes appear with sufficient density to extract the phase to high order. In the experiments, a time delay of $\tau \approx 5$ ps was chosen.

After passing through the pulse shaper, the signal photon is prepared by a half-wave plate, acting as the input of the PMZ, at 45° polarisation to the optical axis of the PM-fibre coupled EOM into which it is directed. The single photon is thus in a superposition of polarisation states, only one of which experiences a constant spectral translation. The pulses were then directed into a free-space path containing the BSC, which introduces a variable relative delay between the two polarisations. In practice the PM fibre, which is highly birefringent, and the modulator itself introduce more than enough delay to resolve the interference terms and the role of the calcite wedges is to easily set the spectral interference fringe spacing to below the sampling limit of the spectrometer. The two pulses are then rotated in polarisation by a final half-wave plate oriented at 22.5° to their polarisations and interfered at a polarizing beam splitter (closing the PMZI), with the resulting spectral interference pattern resolved on the TRSPS.

6.4 Calibrating the interferometer

To reconstruct the spectral phase, it is necessary to have precise knowledge of the birefringent time delay τ, which must be known to much higher accuracy than the chirp-induced effective delay $\Omega\phi_2$ for accurate reconstruction, and the spectral shear Ω. The value of Ω can be chosen and measured by sending classical light of the modulated and unmodulated polarisations into the interferometer and resolving the spectrum. However, the value of τ is more challenging to determine and much more important to the accuracy of the reconstruction. The error of the value of τ that would lead to errors in the reconstructed phase comparable to the typical values one would wish to measure is on the order of several hundred femtoseconds, out of an absolute

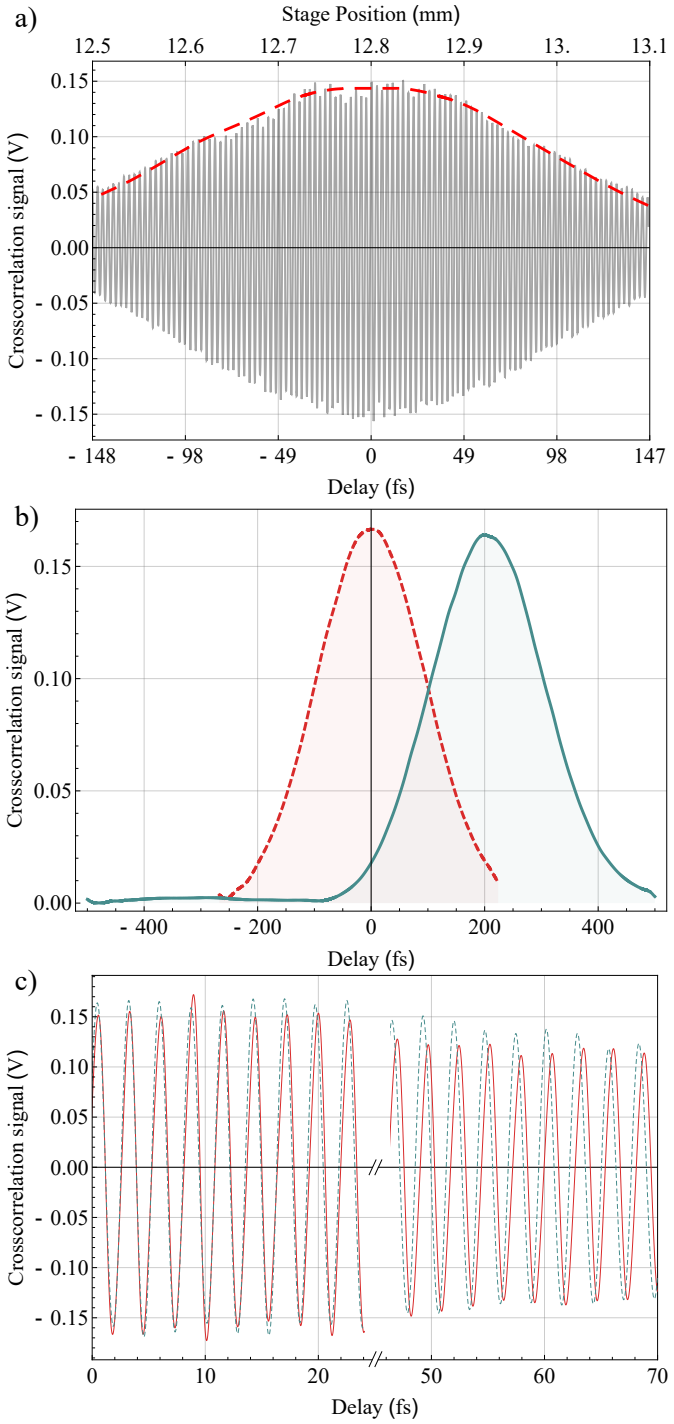


Figure 6.6: a) Temporal cross-correlation pattern of unsheared classical wavepackets with the calibrated time axis; dashed: envelope of the cross-correlations obtained by Hilbert transform. b) Comparison of the envelope of the cross-correlation pattern for an unsheared (dashed) and sheared (plain) classical wavepacket, showing a delay introduced by the group velocity change of approximately 200 fs. c) Superposition of carrier-wave fringes showing difference in frequency caused by the spectral shear Ω.

value of approximately 5 ps. It is therefore not possible to perform direct time-of-flight measurements of τ to satisfactory accuracy with a conventional photodiode. Attempts to calculate the value of τ theoretically are challenging due to the several processes within the modulator that contribute to the delay. The main contribution to τ is from the birefringence of the $LiNbO_3$ in the modulator, which is strongly temperature dependent. Furthermore, $LiNbO_3$ is a highly dispersive material, and so the difference in group velocity of the sheared and unsheared pulses and, again, the temperature dependence thereof, would need to be taken into account. One would also need to simulate how the group velocity of the sheared pulse varied as its spectrum was translated during its propagation through the modulator. We therefore used an interferometric means of directly measuring τ.

Calibration of τ with the calcite wedges is done by injecting bright classical pulses derived from the laser into the interferometer with the EOM switched off and measuring with a silicon photodiode the intensity at the output whilst scanning the position of the calcite wedges. This method only requires knowledge of the carrier frequency of the incident light to map the wedge position to delay. Firstly it is necessary to create a mapping of wedge position onto relative time delay introduced by the birefringence of the calcite. The interference signal at one output of the interferometer is given by:

$$I_{\text{out}} = \frac{1}{2}\int \mathrm{d}\omega\ I_0(\omega)\cos\left(\phi_{\text{rel}}(\omega)\right), \tag{6.18}$$

where $I_0(\omega)$ is the spectral intensity of the incident field and ϕ_{rel} is the relative spectral phase within the PMZI. With the EOM off, the relative phase $\phi_{\text{rel}}(\omega)$ only contains a linear term that corresponds to a global delay τ between the polarisations, and so it is possible to approximate the signal as:

$$I_{\text{out}}(\tau) = I_{\text{cc}}(\tau)\ \cos\left(\omega_0\tau\right), \tag{6.19}$$

where I_{cc} is the envelope of the cross-correlation and ω_0 is the carrier frequency of the pulse.

Note that unlike the intensity autocorrelation described in Chapter 2, this is only a field autocorrelation and hence is insensitive to the spectral phase. The pulse envelope is instead related to the spectrum of the pulse, and measurements similar to this are the basis of Fourier-transform spectroscopy [78]. I_{cc} contains all the delay from propagation through the EOM and the polarisation-maintaining fibre, and is also directly proportional to the length of calcite through which light travels. The latter allows control of the delay between the two polarisations. Hence, the position of the centre of the envelope gives the point of zero delay, while the fringe spacing gives the temporal delay as a function of wedge position, as shown by Fig. 6.6 a). To maximise overlap between the pulses in the two polarisations, this time-axis calibration would ideally be done with the EOM switched off. However, due to the aforementioned thermal effects on the refractive indices of the modulator, the axes can only be calibrated across the range of interest with the EOM being driven. Therefore, the phase of the RF relative to the optical pulse train was chosen such that the pulse sits at the extremum of the refractive index modulation. This leaves the center wavelength of the pulse unchanged, allowing extraction of the time delay by the method described above. Note that any change in fringe spacing due to mismatch of higher order spectral phase, such as dispersion, will only appear in the wings of the interferogram, and can be easily accounted for with Fourier analysis. This method then allows unambiguous calibration of the temporal delay caused by the calcite wedge.

With the axis calibration in hand it is then possible to extract the time delay τ of the interferometer. Since the pulse reconstruction experiment involves spectrally shearing one arm within the interferometer, this results in a change in the time delay τ between the two polarisations due to group delay dispersion. In this case, the cross-correlation signal is given by

$$I_{cc}(\tau) = I_{\mathrm{cc}}(\tau - \tau_0)\cos\left[(\omega_0 + \Omega/2)(\tau - \tau_0)\right], \tag{6.20}$$

where τ_0 is the contribution to the delay caused by group delay dispersion of the sheared pulse

as derived in Eq. 6.12. The interferogram measured when the EOM is shearing is then delayed by a constant value τ_0, and the difference in fringe spacing also allows measurement of the spectral shear. As shown in Fig. 6.6b), the zero-delay point is shifted by about 200 fs when maximum shear is applied on the EOM. The sign of this delay depends on the sign of the shear[1]. By defining the zero-delay point as the new reference, the stage position is then fully calibrated and the time delay τ between the two arms of the interferometer is fully characterised. The advantage of this calibration method is that it does not require any ultrafast detection: the sampling rate of the acquisition simply has to be sufficient to resolve temporal fringes created by the movement of the stage, which typically have a period on the order of a few kHz. It does however require phase stability, but this is obtained directly from the common-path polarisation interferometer. Finally, as depicted by Fig. 6.6 c), when the sheared and unsheared interferograms are superimposed, the difference in optical frequency due to the difference in wavelength can be clearly seen. Performing the scan multiple times and averaging the phase extracted from the Fourier analysis conclusively allows the extraction of the shear Ω. Though directly measuring the shear using a spectrometer is more robust, in the absence of a high-resolution conventional spectrometer the cross-correlation method allows a direct measurement at the output of the interferometer, taking into account every optical element.

6.5 Results

6.5.1 Data acquisition

The procedure for a typical experimental single-photon state characterisation is depicted by Fig. 6.2. An acquisition consists of accumulating a spectrogram at the output of the TRSPS over approximately 20 seconds (see Fig. 6.2 a). Heralded single photon count rates at the detection

[1] When shear is positive, i.e. the sheared pulse is blueshifted, the pulse is delayed in the interferometer, which is consistent with index progression in which n decreases when λ increases.

stage are typically around 120 Hz across the Bragg grating reflection window. An acquisition therefore consists of several thousand events, which was found to be a sufficiently large data set time for precise phase extraction given the final coincidence count rates. The visibility of the interference fringes is typically greater than 70% and is limited by phase instabilities within the interferometer and the resolution of the spectrometer. Performing the Fourier analysis detailed in Section 6.2 then allows extraction of the phase gradient θ shown in Fig. 6.2c from the sideband in the Fourier domain (Fig. 6.2b). The spectral phase information is finally obtained by following the algorithm from Section 6.2.2. Note that the spectral range over which the phase is reconstructed must be restricted to the region of the spectrum in which fringes are observed, since the extracted phase outside of this region is not recoverable- see the edge of Fig. 6.2 c).

To improve the reliability of the reconstruction, this procedure is repeated to produce multiple acquisitions, each consisting of 20 seconds of data, and the extracted phases are averaged. However, the individual interferograms themselves cannot generally be summed because long-term instabilities, such as slow temperature drifts, result in a slow shift of the global phase of the interference fringes and so reduce the contrast of the resultant interferogram. Interferograms with low contrast occasionally trigger instabilities in the reconstruction algorithm and a small proportion of low-contrast acquisitions yield values for the reconstructed phase lying substantially outside the main distribution. For this reason, interferograms that do not reach a threshold contrast of 50% are discarded and do not contribute to the final reconstruction.

6.5.2 Reconstruction of phase that is polynomial in frequency

The EOSI was tested with various spectral phase profiles imprinted on the pulse shaper to verify the fidelity of the reconstruction. In the absence of deliberately applied spectral phase, this technique recovers a spectral phase with a quadratic coefficient of 87000 ± 1000 fs^2 and a cubic of $(5 \pm 1) \cdot 10^5$ fs^3. This value is found to be in good agreement with the theoretically predicted spectral phase the single photons in our experiment receive from their generation

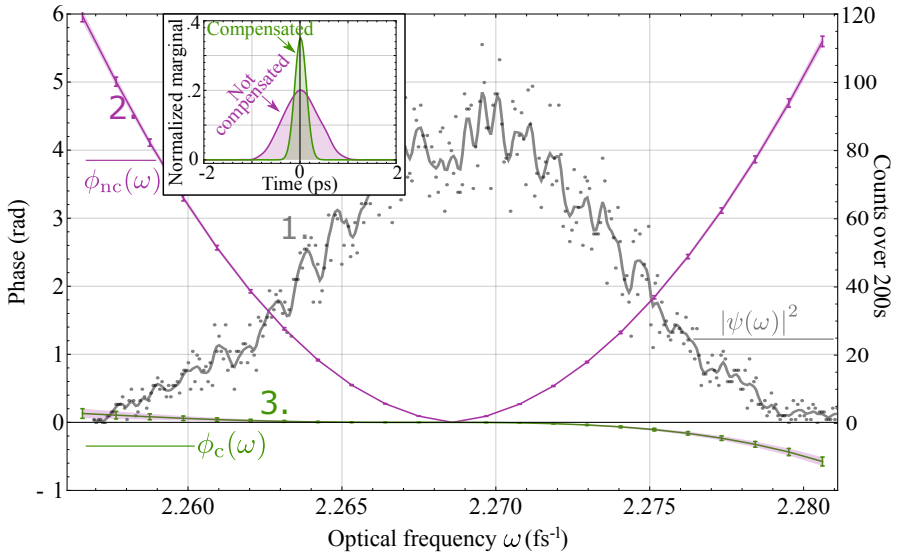


Figure 6.7: Reconstructed spectral phase of the compensated (green) and uncompensated (pink) pulses. The spectral amplitude is given in grey on the left axis. Reconstructed temporal intensity distributions given inset.

and propagation, taking into account the approximately 2.5 meters of polarisation-maintaining fibre, the KDP crystal, and the relative phase within the interferometer such as from the calcite wedges and EOM waveguide. This is referred to as the “uncompensated phase" and has a value of approximately 4000 fs^2.

This quadratic spectral phase is then removed by applying a compensating phase mask on the pulse shaper (see Fig. 6.7). The residual cubic component is not compensated. Similarly, additional phases are tested, such as excess cubic or quartic phase, with and without the compensation for the second-order phase. The phases that are extracted from the interference pattern are all shown on Fig. 6.8 for the different configurations of the pulse shaper, as well as the reconstructed phases. In the first case, without any applied phase on the shaper, we can see that the extracted phase gradient, $\theta(\omega, \Omega)$, is mostly linear and negative and the reconstructed phase itself is quadratic and positive. The difference in sign comes from the sign of the spectral

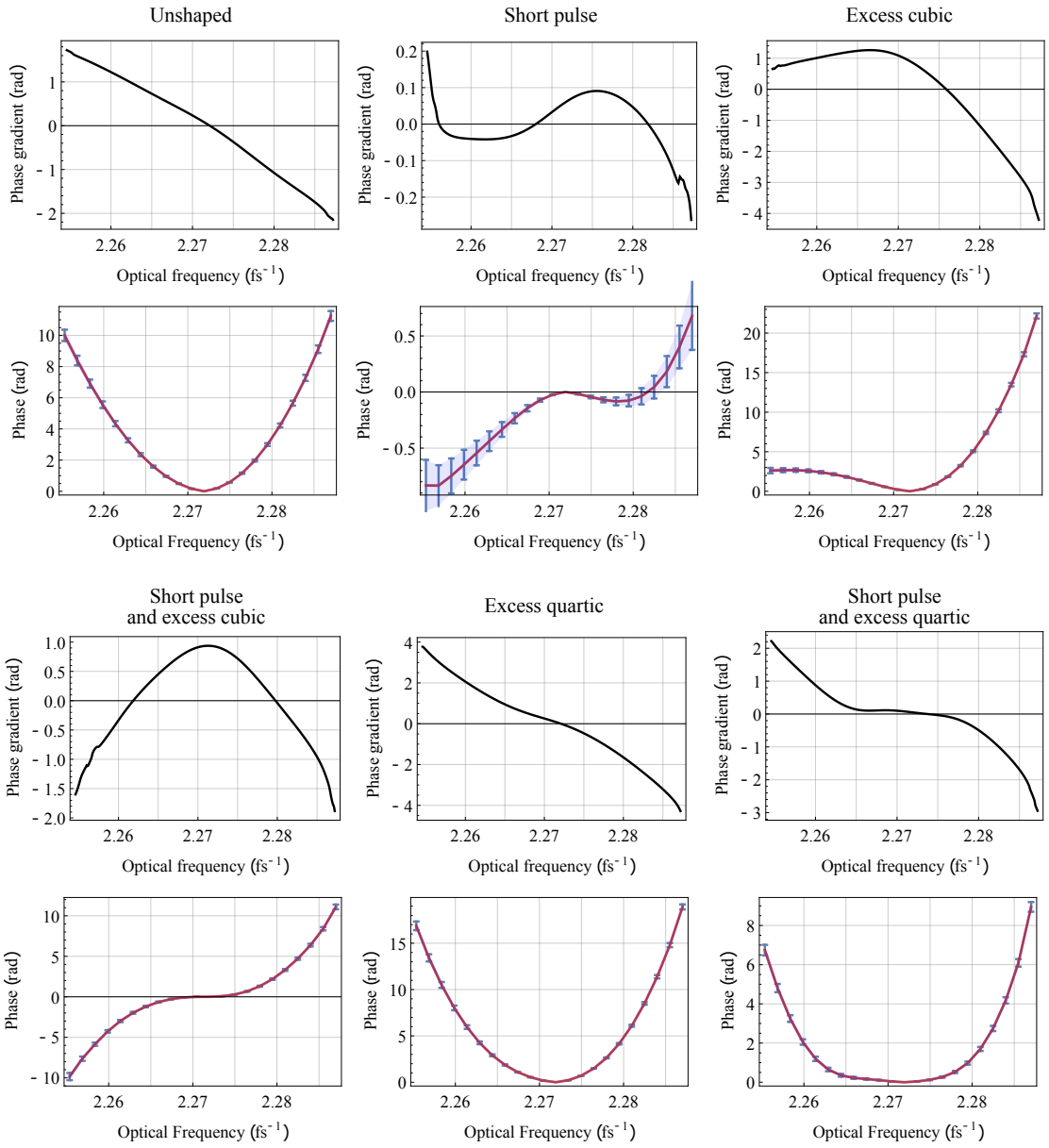


Figure 6.8: First and third rows: average of the extracted phase gradients corrected for delay; second (fourth) row: reconstructed phases from the first (third) row using the concatenation algorithm for a frequency shear $\Omega < 0$. Each pair of plots corresponds to a different phase profile written on the pulse shaper's mask. The error bars represent the standard deviation of the reconstructed phase from the distribution of 50-100 reconstructions.

shear, which was negative[2], and extracted phase can be approximated to the first order as the gradient of the real phase, hence a quadratic phase has a linear gradient. This trend can be verified in all the different phases that are imprinted on the pulse shaper. One can also verify that in the compensated case, the remaining phase is quite small in comparison to the large quadratic phase. A cubic component can be extracted, the value of which is found to be equal to that recovered in the uncompensated case, implying the expected additivity of the applied phase.

Polynomial phase profiles up to quartic spectral phase were imprinted on the ensemble of single photons by the pulse shaper, in every case with or without compensation of the quadratic part. In each case, it can be seen that the reconstruction is consistent with the phase applied on the shaper. The uncompensated cases always show a quadratic part around the same value (~ 90000 fs^2), which falls to zero in the compensated case, while the higher-order coefficients remain. The retrieved coefficient for cubic phase is $(2.5 \pm 0.3) \cdot 10^7$ fs^3 and $(2.0 \pm 1.0) \cdot 10^9$ fs^4 for quartic phase.

To further validate the calibration of the setup, we can compare the phase reconstruction to the known phase that was imprinted on the pulse shaper. This is achieved by computing the relative phase between the shaped and unshaped pulse and calculating the modulus of the mode overlap, $\left| \left\langle \tilde{\psi}_0 \middle| \tilde{\psi}_1 \right\rangle \right|$, where $\left| \tilde{\psi}_1 \right\rangle$ is the reconstructed state and $\left| \tilde{\psi}_0 \right\rangle$ is the state written on the pulse shaper. The results depicted by Fig. 6.9 show a good agreement between the reconstruction and the original phase. The discrepancy can be attributed to the inability of the pulse shaper to write phase with large high-order polynomial coefficients, since the phase is too steep on the edge of the spectrum, thus introducing errors. Indeed, it can be seen that the reconstruction for quartic phase is more unstable than the other cases, since such a phase shows very steep phase gradient close to the wings of the spectrum. However, it can still be reconstructed with high accuracy even in the uncompensated case where a large quadratic component is mixed. It is worth noting that both algorithms described in Sec. 6.2.2 can be

[2] I.e. a redshift, $\delta\lambda = 0.58$ nm

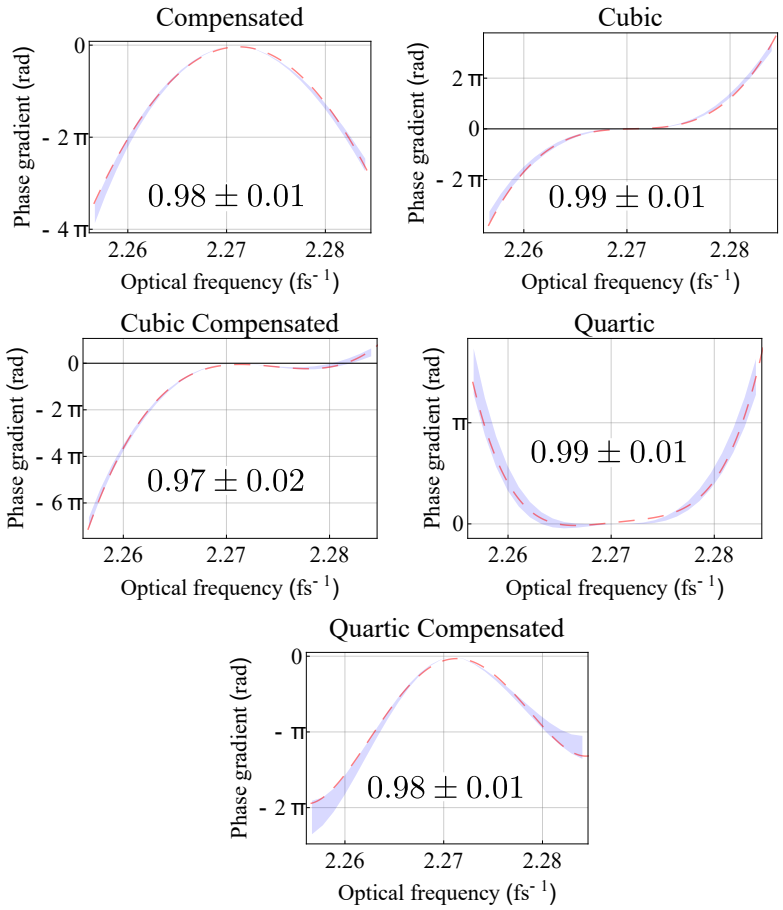


Figure 6.9: Comparison between the phase written on the pulse shaper (dashed) and the reconstructed phase (plain). The shaded area represents the standard deviation of the reconstruction, which is naturally larger the further from ω_0, where the phase is constrained. The inset numbers represent the fidelity of the reconstruction.

used to reconstruct polynomial phases, giving similar results. This shows that the setup and the algorithm are indeed able to reconstruct higher-order phase structures at the single-photon level.

6.5.3 Arbitrary phase reconstruction

A final set of measurements were achieved to test the reconstruction capabilities of the setup when the phase that is imprinted on the single photons may not be expanded on a finite polynomial basis. Two phase profiles were chosen, which resulted in similar spectral and temporal intensities, but actually formed two orthogonal modes. They are defined by a linear spectral phase proportional to $\pm|\omega-\omega_0|$, where the positive (negative) linear phase is labelled V-phase (Λ-phase). The effect of such a phase on the wavepacket is to delay or advance the long-wavelength part of the spectrum with respect to the short-wavelength part.

The value of the linear phase imprinted on the pulse shaper was ± 750 fs, and a reconstruction was made. Creating phase profiles of this sort, which present a non-continuous spatial derivative of the phase on the mask of the SLM, can introduce diffraction, resulting in a small hole in the spectrum at the non-analytic point. Similarly to the previous section, these phases were reconstructed with and without compensation of the dispersion. The extracted and reconstructed phases are shown in Fig. 6.10. The extracted phase gradients $\phi(\omega)-\phi(\omega+\Omega)$ closely resemble a step function where the steepness is determined by the value of the shear, and the value of the plateau reflect the amount of linear phase. Furthermore, we can clearly see an additional linear phase gradient in the uncompensated cases, showing again the presence of dispersion. The reconstructions show that the setup is able to easily distinguish the two phases. Moreover, a fit in the reconstruction gives an absolute linear phase of $+750\pm 25$ fs for the V-phase and -775 ± 50 fs for the Λ-phase, and the same quadratic phase found in the previous section for the uncompensated and compensated phases. The Λ-phase is more difficult to reconstruct compared to the previous phases due to the constraints put on the pulse shaper. Indeed, this phase has a steep negative slope, and compensating for dispersion adds an extra negative quadratic phase on the mask, resulting in additional wrapping.

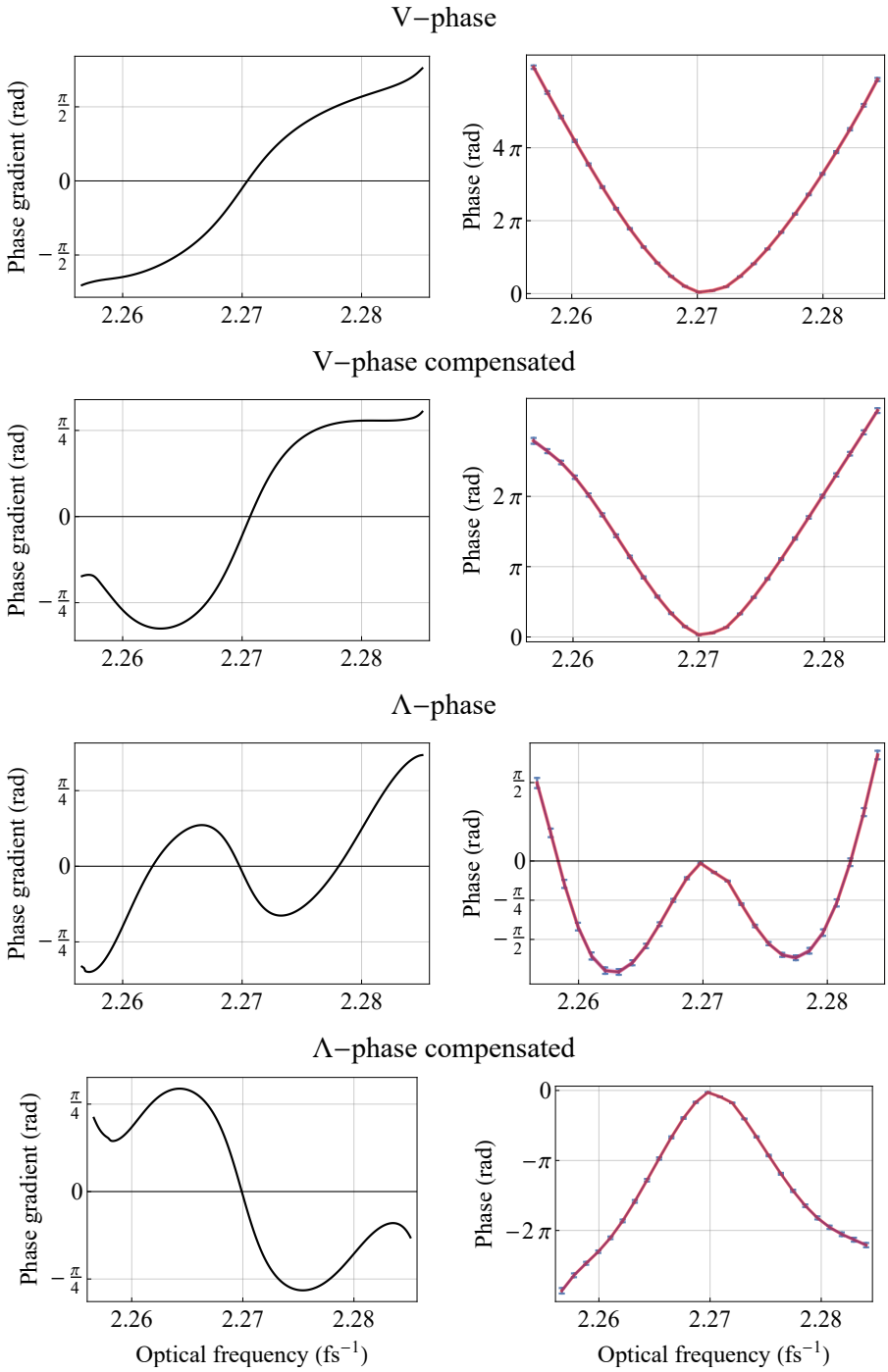


Figure 6.10: Left column: average of the extracted phase gradients corrected for delay; right column: reconstructed phases from the left column using the concatenation algorithm for a frequency shear $\Omega < 0$. The error bars represent the standard deviation. The error is zero at the center frequency since it is constrained by the algorithm. The left column approximately shows the derivative of the right one.

6.5.4 Time-frequency distributions

With the phase now reconstructed, it is possible to create time-frequency distributions to fully describe the spectral-temporal wave function of the single photon. Indeed, as it is the case with classical pulses, a complete description may be obtained by showing how the spectral parts are mapped in the time domain. Multiple ways to describe this distribution exist, and we choose the chronocyclic Wigner function defined in Chapter 3.

The chronocyclic Wigner function has the advantages that it provides a complete characterisation of the single-photon spectral-temporal density matrix, is normalised and real-valued everywhere, and the overlap of two states can be easily calculated from the overlap of the respective Wigner functions [58]. It is often referred to as a “quasiprobability distribution" since its marginals correspond to the probability distributions of measurement outcomes in those bases, although the function itself can locally take negative values. To compute this distribution, one needs the real spectral amplitude $|\tilde{\psi}(\omega)|$ in order to reconstruct the complete spectral wave function with the phase that was measured. In principle this can be directly measured during the acquisition by summing the two outputs of the interferometer, which removes the interference fringes, assuming equal efficiency detection at each output port of the interferometer. The result is quite close to the true spectrum for small values of the shear. It is also possible to independently measure the amplitude directly without sending pulses into the interferometer. The latter method was used here. The center frequency of the spectrum (i.e. the first moment of the distribution) is used as the experimental value of ω_0 throughout the algorithm, notably to constrain the center frequency of the phase concatenation and the fits. The time-frequency distributions for the polynomial and the arbitrary phases written with the pulse shaper are shown in Fig. 6.11.

Summing the distribution along one dimension yields either the temporal or the spectral marginals. As expected for polynomial phase, the temporal wave function of the uncompen-

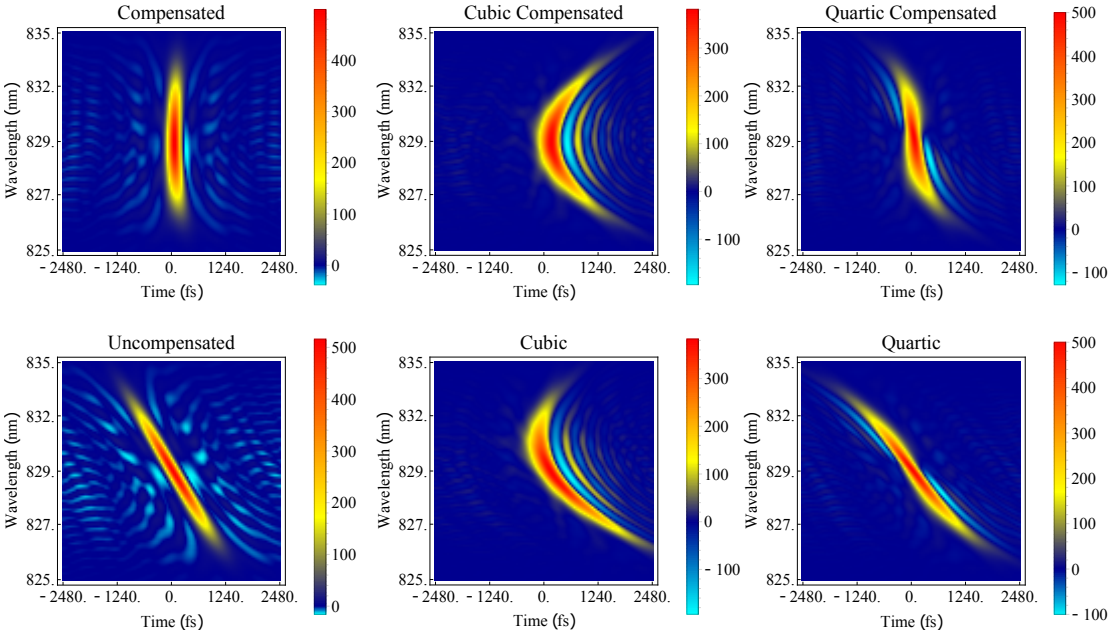


Figure 6.11: Chronocyclic Wigner function for the phases that were imprinted with the pulse shaper.

sated single photon is much broader than that of the compensated one, cubic phase creates replicas, and quartic phase creates a pedestal. In the case of the V-phase and Λ-phase, both marginals are similar, yet the two modes are orthogonal. Computing the overlap between these modes yield a value of 0.06 ± 0.01, while the overlap of their marginal temporal intensities is 0.95 ± 0.01 and the spectral overlap is unity.

6.6 Discussion

6.6.1 Characterisation of single-mode fields

We have thus far considered the reconstruction of the pulse mode occupied by a single photon excitation. However, this technique is not limited to single-photon pulses and can be used to reconstruct the pulse mode structure of a single mode field of arbitrary excitation. This arises

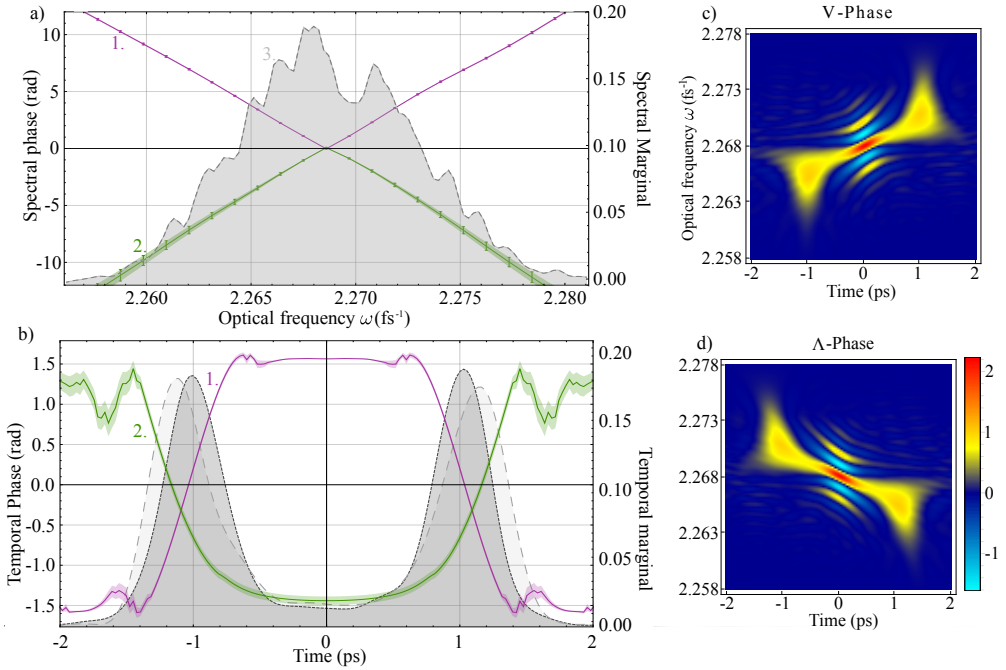


Figure 6.12: a) Reconstructed spectral phase profiles of pulses with applied V-phase (1. purple) and Λ-phase (2. green), with the single-photon spectrum shown in greyscale (3.). b) Reconstructed temporal phases for V-phase (1. purple) and Λ-phase (2. green), as well as the temporal profile, showing binodal temporal distribution. c) Chronocyclic Wigner functions of V-phase pulse and d) Λ-phase pulse.

from the fact that the approach presented here extracts the phase of the spectral mode from a measurement of the first-order field correlation function,

$$G^{(1)}(\omega,\omega') = \left\langle \hat{a}^{\dagger}(\omega')\hat{a}(\omega) \right\rangle, \tag{6.21}$$

where $\hat{a}^{\dagger}(\omega)$ and $\hat{a}(\omega)$ are photon creation and annihilation operators associated with the frequency mode ω and we drop the electric field amplitudes choosing to work with photon number instead. Considering a pulse mode $\psi(t)$, with $\tilde{\psi}(\omega) = \mathcal{FT}\{\psi(t)\}$, where $\tilde{\psi}(\omega)$ is the Fourier

transform of $\psi(t)$, a general state of the field is given by the density operator

$$\hat{\rho}_\psi = \sum_{m,n=0}^{\infty} \rho_{m,n} \left|m\right\rangle_\psi \, {}_\psi\!\left\langle n\right| , \tag{6.22}$$

where $\left|n\right\rangle_\psi$ is an n-photon state in the pulse mode $\psi(t)$, and $\rho_{m,n} = {}_\psi\!\left\langle m\right| \hat{\rho}_\psi \left|n\right\rangle_\psi$ is a matrix element of the density operator in the photon-number basis. In the remainder of this section we drop the pulse-mode label ψ on the states to simplify the notation. The first-order correlation function for the general single-mode state is given by the average photon number of the state, $\bar{n}$, multiplied by the product of the frequency-representation of the mode function and its complex conjugate evaluated at ω and ω'

$$G^{(1)}(\omega, \omega') = \bar{n}\tilde{\psi}(\omega)\tilde{\psi}^*(\omega'). \tag{6.23}$$

This can be seen by noting that the first-order correlation function for the single-mode state can be written as

$$G^{(1)}(\omega, \omega') = \sum_{k=0}^{\infty} \left\langle k\right| \hat{\rho}\hat{a}^\dagger(\omega')\hat{a}(\omega) \left|k\right\rangle , \tag{6.24}$$

where we use the fact that the state occupies a single field mode to simplify the ensemble average. Inserting the general expression for the state, Eq. (6.22), into the above expression gives

$$G^{(1)}(\omega, \omega') = \sum_{k,m,n=0}^{\infty} \rho_{m,n} \left\langle k|m\right\rangle \left\langle n\right| \hat{a}^\dagger(\omega')\hat{a}(\omega) \left|k\right\rangle . \tag{6.25}$$

To simplify this further, first note that $\hat{a}(\omega)\left|k\right\rangle = \sqrt{k}\tilde{\psi}(\omega)\left|k-1\right\rangle$, which arises from the commutation relations between creation and annihilation operators for a monochromatic mode, ω and pulse mode, $\psi(t)$, $[\hat{a}(\omega), \hat{a}_\psi^\dagger] = \tilde{\psi}(\omega)$ [66], where

$$\hat{a}_\psi^\dagger = \int \tilde{\psi}(\omega)\hat{a}^\dagger(\omega)\mathrm{d}\omega. \tag{6.26}$$

This relation allows the simplification of Eq. (6.25) to give

$$G^{(1)}(\omega,\omega') = \sum_{k,m,n=0}^{\infty} \rho_{m,n}\tilde{\psi}^*(\omega')\tilde{\psi}(\omega)\sqrt{nk}\delta_{n,k}\delta_{m,k}, \tag{6.27}$$

where we use the result

$$\langle n|\,\hat{a}^\dagger(\omega')\hat{a}(\omega)\,|k\rangle = \sqrt{nk}\tilde{\psi}^*(\omega')\tilde{\psi}(\omega)\langle n-1|k-1\rangle, \tag{6.28}$$

and the orthonormality of the single mode Fock states $\langle m|n\rangle = \delta_{m,n}$. Collapsing two of the sums down in Eq. (6.27) leads to the final result

$$G^{(1)}(\omega,\omega') = \tilde{\psi}^*(\omega')\tilde{\psi}(\omega)\sum_{k=0}^{\infty}\rho_{k,k}k = \bar{n}\tilde{\psi}(\omega)\tilde{\psi}^*(\omega'), \tag{6.29}$$

where the average photon number of the field is

$$\bar{n} = \sum_{k=0}^{\infty}\rho_{k,k}k, \tag{6.30}$$

and $p_k = \rho_{k,k}$ is the probability for the field to have a photon number of k. Thus we see that through measurement of the first-order field correlation function, which can be extracted for a single-mode field using the EOSI technique as in Eq. (6.4), one can determine the pulse structure for any single-mode field regardless of the photon number distribution. Indeed, one would not be able to distinguish between a single-photon source, an attenuated laser, or a weak thermal state of light if they all occupy the same temporal mode using the EOSI method. To distinguish between these sources, higher-order correlation functions must be measured, e.g. the second-order coherence function

$$g^{(2)}(\tau) = \frac{\langle\hat{a}^\dagger(0)\hat{a}^\dagger(\tau)\hat{a}(\tau)\hat{a}(0)\rangle}{\langle\hat{a}^\dagger(0)\hat{a}(0)\rangle\langle\hat{a}^\dagger(\tau)\hat{a}(\tau)\rangle}, \tag{6.31}$$

where $\hat{a}^\dagger(\tau)$ is the photon creation operator in a delta-function-like time bin at time τ. A single-photon state has $g^{(2)}(0) = 0$ indicating the source cannot emit more than one photon at any given instance, whereas a coherent state displays $g^{(2)}(0) = 1$ arising from the Poisson statistics of the photon number distribution of the state and a thermal state has $g^{(2)}(0) = 2$, which is often termed photon bunching [66]. A value of $g^{(2)}(0) \leq 1$ indicates the non-classical nature of the field, which cannot arise from a purely wave theory of light [66].

6.6.2 Mixed state reconstruction

The methods discussed thus far have been aimed at reconstruction of the pulse-mode state of pure single-photon sources, i.e. single-photon sources that emit photons into only one pulse mode. For sources that emit photons into a mixture of pulsed modes, we must generalise the state reconstruction process to enable characterisation of the full density operator $\hat{\rho}$. Note that this density operator, which describes the mode distribution of a single photon, should not be confused with that of the previous section, Eq. (6.22), which there describes the photon number distribution in a single-mode field. The problem of characterizing a mixed state single-photon source is similar to characterisation of a partially-coherent pulse train [79]. The result of a measurement with the EOSI is defined as the quantum counterpart of Eq. (6.2) as $S^{\pm}_{\Omega,\tau}(\omega) = \mathrm{Tr}\left[\hat{\rho}\hat{\Pi}^{\pm}_{\Omega,\tau}(\omega)\right]$, where $\left\{\hat{\Pi}^{\pm}_{\Omega,\tau}(\omega), \hat{\Pi}_{\mathrm{NC}}\right\}$ is the positive-operator valued measure (POVM) that describes the EOSI measurement. The measurement operators in this set are given by

$$\begin{aligned}\hat{\Pi}^{\pm}_{\Omega,\tau}(\omega) =& \frac{1}{4}\left(\hat{a}^\dagger(\omega)\hat{a}(\omega) + \hat{a}^\dagger(\omega+\Omega)\hat{a}(\omega+\Omega)\right) \\ &\pm \left(\hat{a}^\dagger(\omega)\hat{a}(\omega+\Omega)e^{i\omega\tau} + \hat{a}^\dagger(\omega+\Omega)\hat{a}(\omega)e^{-i\omega\tau}\right),\end{aligned} \tag{6.32}$$

where $\hat{a}^\dagger(\omega)$ ($\hat{a}(\omega)$) is the single-photon creation (annihilation) operator for frequency mode ω, and $\hat{\Pi}_{\mathrm{NC}}$ is the "no-click" measurement outcome.

For a pure single-photon state $|1\rangle_\psi$, in which the photon occupies the field mode, $\psi(t)$, it is

straightforward to show that this POVM results in measurement outcomes given by Eq. (6.2), equivalent to the following expression

$$\begin{aligned} S^{\pm}_{\Omega,\tau}(\omega) &= \frac{1}{4}\left[S(\omega)+S(\omega+\Omega)\right] \\ &\pm \frac{1}{2}\,\mathrm{Re}\left\{\tilde{\psi}(\omega)\tilde{\psi}^{*}(\omega+\Omega)e^{i\omega\tau}\right\}, \end{aligned} \tag{6.33}$$

where $S(\omega) = |\tilde{\psi}(\omega)|^2$ is the single-photon spectrum. For a mixed single-photon state with spectral density operator $\hat{\rho}$, by defining $\omega' = \omega + \Omega$ and scanning the shear, Ω, a 2-dimensional spectral interference pattern is obtained

$$\begin{aligned} I^{\pm}_{\tau}(\omega,\omega') =& \frac{1}{4}\left(\rho(\omega,\omega)+\rho(\omega',\omega')\right) \\ &\pm \frac{1}{2}\,\mathrm{Re}\left\{\rho(\omega,\omega')e^{i\omega\tau}\right\}, \end{aligned} \tag{6.34}$$

where $\rho(\omega,\omega') = \langle\omega|\,\hat{\rho}\,|\omega'\rangle$ is the single-photon spectral density matrix element, with $|\omega\rangle = |1\rangle_{\omega} = \hat{a}^{\dagger}(\omega)\,|\mathrm{vac}\rangle$ a single-photon state with frequency ω and $|\mathrm{vac}\rangle$ the vacuum state of the field. Hence, by scanning the spectral shift Ω, it is possible to measure the spectral density matrix elements $\rho(\omega,\omega')$ using 2D-Fourier analysis similar to the one presented in Chapter 5. Moreover, it may be easier to use the signal associated with the difference of the photodetection events at the outputs of the interferometer $I^{\mathrm{diff}}_{\tau}(\omega,\omega') = I^{+}_{\tau}(\omega,\omega') - I^{-}_{\tau}(\omega,\omega') = 2\,\mathrm{Re}\left\{\rho(\omega,\omega')e^{i\omega\tau}\right\}$, which directly samples the off-diagonal entries of the spectral density matrix assuming balanced beam splitters and detectors. Note that adding a $\pi/2$ phase shift in the interferometer yields an interference term $2\,\mathrm{Im}\left\{\rho(\omega,\omega')e^{i\omega\tau}\right\}$, which allows full reconstruction of the density matrix. Even though the full reconstruction would prove more difficult due to the increase in dimension and need to scan the spectral shift, it is still feasible with this method.

It is worth noting that this approach can only sample elements of the spectral density matrix within a band around the main diagonal of width 2Ω, determined by the range of spectral shear

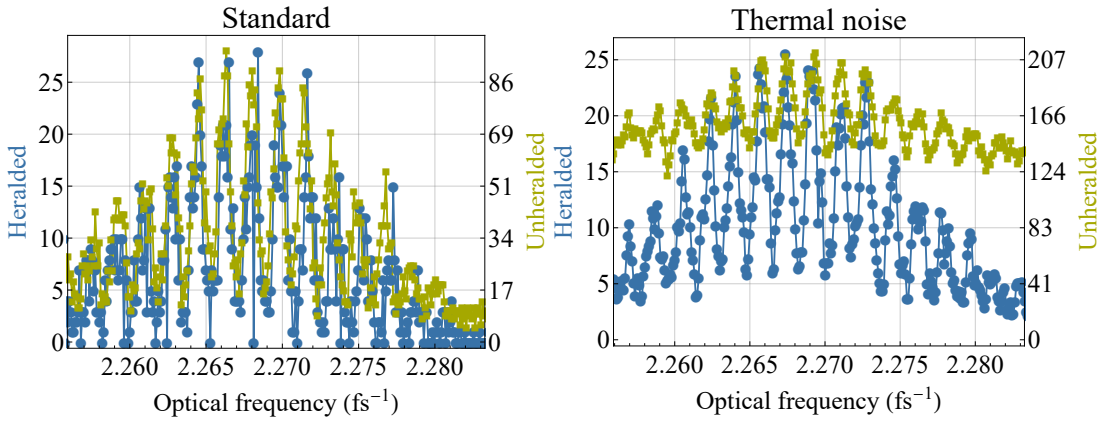


Figure 6.13: Comparaison between unheralded (green/square markers) and heralded (blue/round markers) spectrograms. Left: standard setup as presented throughout this article; Right: with added background noise.

values Ω accessible by the device. Full characterisation of an unknown state would require scanning the frequency shift over a range that is on the order of the spectral bandwidth. With the current capabilities outlined in this paper, a mixed state of approximately 0.5 nm bandwidth centered about a wavelength of 830 nm could in principle be reconstructed by scanning the spectral shear. As demonstrated in the previous chapter, however, for highly mixed states, elements far from the main diagonal of the spectral density matrix are suppressed.

6.6.3 Heralding

Another useful side of the experimental setup is the ability to herald spectrally-resolved single photons. Generally, heralding is a way of removing noise from the signal, such as electronic dark noise or thermal light. In the present case, the single photon source is specially engineered to yield a pure, non-entangled state. Consequently, the interferogram that one would obtain without heralding is quite similar to the heralded case, albeit with higher counts. Such a resemblance is depicted in Fig.6.13. We can see on this plot that the two cases are indeed quite similar and show a slight difference in contrast. The ratio of the number of counts shows a heralding

efficiency of $\sim 30\%$ which is limited mostly by the quantum efficiency of the detectors. However, it is worth stressing that the unheralded count rate is distributed between $\sim$ 200 Hz of dark detector noise and $\sim$ 300 Hz of actual single photons event. Consequently the unheralded interferogram does correspond to a mixed state, although in that case it merely results in a slight reduction of contrast that is not immediately visible. Since the dark-count background is mostly subtracted by Fourier filtering, applying the phase reconstruction algorithm on both plots would yield a similar result. That is again a direct consequence of source engineering that delivers a pure, non-entangled state.

It is however quite easy to think of situations in which heralding is mandatory. To illustrate, we replicated the previous interferogram measurement and added a source of spectrally incoherent background light, which can be easily obtained by increasing the exposure of the set-up to the laboratory lighting. In this situation, the unheralded case shows a clear difference from the heralded case, as shown by Fig.6.13. We can see that the thermal light diminishes dramatically the signal-to-noise, resulting in a large plateau in which the interference fringes are less visible. Such a drop in contrast leads to a much less stable reconstruction because of noisier fringe spacing. In that case, heralding allows projection in the single photon pure state while removing the large contribution from the thermal state. It worth noting that the example that is illustrated by Fig.6.13 is quite extreme, as the reduction in signal-to-noise inevitably increases the amount of accidental heralding events. There is however a clear increase in contrast due to heralding, and a more careful control over the heralding window can bring the accidental events down.

Finally, our setup can be extended to the analysis of frequency-entangled states whose joint spectrum may not be described by the product of the two single photon mode-functions. In that situation, if one were to characterise the mode of one photon by heralding with a bucket detector, as in the present work, this would result in a mixed state since the information about entanglement is lost. Although the foreknowledge of the intensity joint spectrum would bring

additional information, such a scheme would miss other parameters, such as spectral phase correlations between the two daughter photons. However, by performing a projective measurement on the hearalding photon, the signal photon is projected into a pure state, allowing full reconstruction. We will formalised and explore this extension in the next chapter.

6.6.4 Practical considerations

While the general scheme depicted by Fig. 6.1 is not particularly complex, the experimental implementation places some limitations on the input that EOSI can realistically characterise. Altogether, these constraints are in general much more lax for EOSI than those required by externally-referencing methods. Here, we detail these constraints, and discuss how to choose the proper settings for a given experimental setup.

The device presented here is based on a PMZ interferometric configuration, which requires an input with well-defined polarisation. Polarisation filtering may be employed to achieve this, but this incurs losses and precludes the device being used to explore polarisation-time/frequency correlations. To overcome these difficulties one could utilise a different interferometric scheme, such as a spatial-mode Mach-Zehnder interferometer. However, such an implementation would likely require active locking of the interferometer to perform the single-photon measurements.

A main building block of the EOSI is the high-resolution single-photon spectrometer described in Chapter 4. While modern detectors provide sufficient temporal resolution, the methods for obtaining large chirped pulses are still limited. It is not feasible to stretch pulses sufficiently in free space to enable frequency-to-time conversion, so a fibre setup is needed. In the near infrared, optical fibres show typical dispersion on the order of 100 ps/nm/km and propagation losses of more than 3 dB/km, rendering large chirp with fibre propagation impractical. CFBGs prove to be the most efficient way of achieving the dispersion needed by the setup, but typically act in reflection over a limited spectral region, which is mainly defined by the length of the fibre and the specified dispersion. Larger spectral windows and larger chirp parameters

could in principle be obtained by concatenating CFBG together. The association of the CFBG parameters and the timing jitter of the detectors then limit both the spectral range and the spectral resolution [69], thus requiring some *a priori* knowledge of the spectral range in which the test pulse lies.

The other main limitation comes from the EOM, with which the spectral shift is obtained. Various methods can be used to apply a high-power linear RF signal phase-locked to the pulse train. While we use frequency multiplication and a phase-lock loop, we note that it is possible to amplify the bandpass-filtered signal from a large bandwidth photodiode and use it as the RF-wave which is automatically locked to the pulse train [80]. As described by Eq. (6.17), the amplitude of the frequency shear is directly proportional to both the frequency and the amplitude of the RF wave. The amplitude is limited by the amplifiers and by the EOM itself, while the frequency is bounded by the temporal width of the linear region of the RF-wave. If the temporal duration of the pulse is too large compared to this linear region of the RF signal, the applied shear will no longer be constant across the pulse and thus introduce errors into the reconstruction. Therefore the device input must be a train of single photons with well-defined arrival times and it cannot be applied to continuous-wave single-photon sources. Such a problem could be tackled by replacing the sinusoidal RF wave by a serrodyne wave [81], which would not limit the temporal aperture of the device. The need for a large frequency shear is obvious from Eq.6.7, since it provides a larger amplitude of the phase gradient. It also needs to be larger than the resolution of the spectrometer. This parameter is however also bounded by the unknown state, as any phase structure smaller than the shear cannot be reconstructed. One could, in principle, concatenate several modulators (or multi-pass a single modulator) to increase the shear. However, this results in further insertion loss, timing jitter and dispersion that will adversely affect the calibration.

6.7 Chapter summary

This chapter describes a self-referencing technique to reconstruct the spectral-temporal state of a pulsed single photon. This method is applicable across a wide range of wavelengths and pulse characteristics, and is deterministic in that only technical losses prevent every photon entering the device from contributing to the final reconstruction. The method can be readily extended to the characterisation of mixed state single-photon sources and, in conjunction with correlation measurements, multi-photon systems. A key feature that distinguishes our approach from previous spectral-shearing interferometric methods for pulse reconstruction lies in the ability to perform spectrally-resolved measurements in coincidence with a trigger event. This enables pulse characterisation of conditionally prepared single-photon states [82], which could arise from a highly entangled biphoton state [83]. In its present design this device has wide applications in single-photon source and detector characterisation and quantum metrology.

Whilst phase-sensitive measurements at the single-photon level is certainly a useful capability in its own right, for quantum applications its implications truly becomes apparent when performed in conjuction with measurements on another system, especially one exhibiting non-local quantum correlations with the first. A spectro-temporally entangled biphoton is an example of such a system. In the next chapter, we explore how to utilise this technology for more diverse purposes, in particular the spectral-temporal characterisation of an entangled photon pair.

Chapter 7

Measuring a spectrally entangled photon pair

Contents

7.1 Introduction 162

7.2 The two-photon wave function 163

7.2.1 Schmidt decomposition 163

7.2.2 Local and nonlocal phase 164

7.3 Measurement principle 167

7.4 State preparation 168

7.4.1 Photon pair generation 168

7.4.2 Joint temporal distribution 170

7.4.3 Phase reconstruction 172

7.5 Experimental methods 175

7.5.1 Data acquisition and processing 175

7.5.2 Noise and stability 175

7.5.3 Spectral matching 176

7.6 Results 176

7.6.1 Unchirped pump 176
7.6.2 Chirped pump 178
7.6.3 Full complex joint amplitude reconstruction 178
7.7 Mixed state characterisation 182
7.8 Chapter summary 183

7.1 Introduction

So far, this thesis has been concerned with extracting the full time-frequency (TF) properties of single photons. In conjunction with coherence function measurements, the EOSI demonstrated in the previous chapter also suffices to characterise states of light that can be described by arbitrary nonzero photon number occupation of just one mode $\psi(\omega)$- that is, states of the form

$$|\Psi\rangle = \sum_n c_n \frac{(a_\psi^\dagger)^n}{\sqrt{n!}} |\text{vac}\rangle \,. \tag{7.1}$$

where $a_\psi^\dagger$ is the single-mode photon creation operator defined in Eq.3.94. However, many of the most interesting and useful applications of quantum light, including quantum key distribution [84, 17] and quantum-enhanced sensing [85] and communications [86], involve resources with manifest modal entanglement. The optical references used by these technologies must be well-characterised, and the detection stages of any such application must necessarily be sensitive to the nonclassical correlations that can exist between separate subsystems [87]. Additionally, it is these states that exhibit the most exotic behaviour characteristic of quantum mechanics, such as Bell inequality violation [53] and nonlocal dispersion cancellation [88]. A mechanism for determining the full quantum state of systems of two time-frequency entangled photons is therefore of profound fundamental interest to the scientific community, providing a platform for studying the evolution of high-dimensional quantum systems and probing the foundations

of quantum mechanics itself. However, until now performing full tomography on such complex quantum systems has confounded experimentalists except in certain special cases, such as with bandwidth-matched, frequency-degenerate photon pairs [54].

This chapter describes a technique to completely characterise the spectral-temporal wave function of an arbitrary broadband photon pair in a pure two-photon pulse mode state by extending the EOSI described previously. We demonstrate how a generalisation of this method may be used to fully characterise the spectral-temporal wave function of an entangled multi-photon system. We send one photon from a TF-entangled pair into the EOSI whilst spectrally resolving the other and recording the measurement outcomes in coincidence. By switching the measurements on the two photons and repeating, all TF information about a pure photon pair can be recovered. We also propose how to generalise this method further to enable TF characterisation of mixed states. This method remains fully self-referencing and introduces no constraints on the mode overlap between the two photons themselves.

7.2 The two-photon wave function

7.2.1 Schmidt decomposition

The pure two-photon TF state $|\Psi\rangle$ can be expressed in terms of the complex-valued joint spectral amplitude, or two-photon wave function, $f(\omega_1, \omega_2)$ according to Eq.3.101:

$$|\Psi\rangle = \int f(\omega_1, \omega_2) a^\dagger(\omega_1) b^\dagger(\omega_2) \mathrm{d}\omega_1 \mathrm{d}\omega_2 \, |\mathrm{vac}\rangle$$

$f(\omega_1, \omega_2)$ is related to the joint temporal amplitude $\tilde{f}(t_1, t_2)$ by a 2-dimensional Fourier transform. Since $f(\omega_1, \omega_2)$ is a function of two variables, it is possible to perform a Schmidt decom-

position on $f(\omega_1, \omega_2)$ [89]:

$$f(\omega_1, \omega_2) = \sum_{i=1}^{\infty} \lambda_i \psi_i(\omega_1) \chi_i(\omega_2) \tag{7.2}$$

where λ_i are the Schmidt coefficients and $\psi_i(\omega_1)$, $\chi_i(\omega_2)$ are the Schmidt modes for photons 1 and 2 respectively, introduced in Chapter 3. This represents $f(\omega_1, \omega_2)$ as a sum of straightforward products of normalised functions of just one of the photons' frequencies, $\psi_i(\omega_1)$ and $\chi_i(\omega_2)$, weighted by real coefficients λ_i. When $f(\omega_1, \omega_2)$ is separable, the corresponding $\psi_i(\omega_1)$ and $\chi_i(\omega_2)$ may be interpreted as the wave functions of the two photons and outcomes of local measurements on each photon are not correlated. Otherwise, the two photons are said to be entangled and measurements will exhibit nonclassical correlations. Values of the effective Schmidt rank K, defined in Eq. 3.104, greater than unity indicate spectral-temporal entanglement, with K corresponding to the effective number of modes of entanglement.

7.2.2 Local and nonlocal phase

As with the single-photon spectral mode $\tilde{\varepsilon}(\omega)$, the complex joint amplitude can be split into an amplitude and phase:

$$f(\omega_1, \omega_2) = |f(\omega_1, \omega_2)| e^{i\phi(\omega_1, \omega_2)} \tag{7.3}$$

The square modulus of the joint spectral amplitude $|f(\omega_1, \omega_2)|^2 = S(\omega_1, \omega_2)$ corresponds to the joint spectral intensity (JSI), which we have already seen how to measure in Chapter 4.

Full reconstruction of a pure biphoton state therefore requires only the extraction of the joint spectral phase $\phi(\omega_1, \omega_2)$. The spectral phase $\phi(\omega_1, \omega_2)$ may be expanded as a power series in frequency to second order about the central frequencies of the two photons ω_{c1} and

ω_{c2}, similarly to the single photon case in Chapter 6:

$$\begin{aligned}\phi(\tilde{\omega}_1,\tilde{\omega}_2) &= \phi_{00}+\phi_{10}\,\tilde{\omega}_1+\phi_{01}\,\tilde{\omega}_2 \\ &+ \phi_{20}\,\tilde{\omega}_1^2+\phi_{02}\,\tilde{\omega}_2^2+\phi_{11}\,\tilde{\omega}_1\tilde{\omega}_2+\ldots\end{aligned} \tag{7.4}$$

where we have shifted our frequency origin to the carrier frequencies, $\omega_1 = \omega_{c1} + \tilde{\omega}_1$, and $\omega_2 = \omega_{c2} + \tilde{\omega}_2$, and $\phi_{00} \equiv \phi(\omega_{c1}, \omega_{c2})$. Here, ϕ_{00} is the global carrier-envelope phase, which is the only term we will not be able to measure. Fortunately it is of limited physical significance for many-cycle pulses and hence we can neglect it in our experiments. All of the terms in the expansion of the joint spectral phase indexed with at least one zero are a function of only one of the two photon frequencies. These terms are known as the local phase. ϕ_{01} and ϕ_{10} are the local delays on each photon, whilst ϕ_{02} and ϕ_{20} are local chirps. These four quantities can be individually addressed by local operations on one photon or the other. Acting on the biphoton with arbitrary local spectral phase operations $\{\phi'_{n0}, \phi'_{0m}\}$ can be factored into the Schmidt decomposition:

$$\begin{aligned}\left(\prod_{[m,n]>0} e^{i\phi'_{n0}\tilde{\omega}_1^n} e^{i\phi'_{0m}\tilde{\omega}_2^m}\right) f(\omega_1,\omega_2) &= e^{i\phi_{00}}\left(\prod_{[m,n]>0} e^{i\phi'_{n0}\tilde{\omega}_1^n} e^{i\phi'_{0m}\tilde{\omega}_2^m}\right)\sum\nolimits_i \lambda_i\psi_i(\omega_1)\chi_i(\omega_2) \\ &= e^{i\phi_{00}}\sum\nolimits_i \lambda_i\left[\psi_i(\omega_1)\left(\prod_{n>0} e^{i\phi'_{n0}\tilde{\omega}_1^n}\right)\right]\left[\chi_i(\omega_2)\left(\prod_{m>0} e^{i\phi'_{0m}\tilde{\omega}_2^m}\right)\right].\end{aligned}$$

Since the Schmidt decomposition is unique up to a spectrally-independent phase term, the Schmidt number therefore depends only on the terms

$$|f(\omega_1,\omega_2)|\prod_{[m,n]>0} e^{i\phi_{nm}\tilde{\omega}_1^n\tilde{\omega}_2^m}. \tag{7.5}$$

We call the phase term in the Eq.7.5 the *nonlocal phase*. The Schmidt modes themselves, ψ_i and

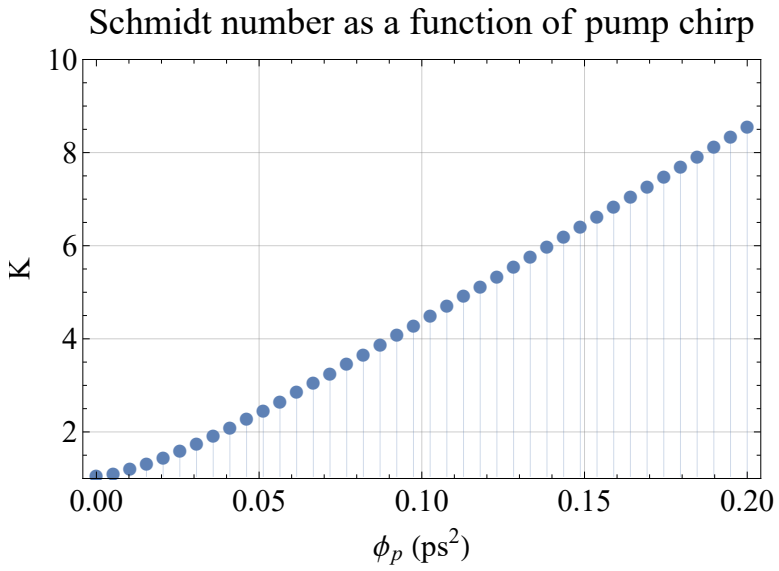


Figure 7.1: Scaling of effective Schmidt number with applied spectral phase on the pump ϕ_p.

χ_i, remain unaffected by local phase operations up to the local spectral phase in their photon. The ϕ_{11} coefficient in Eq.7.4 is the lowest-order term in the nonlocal phase of the photon pair and contributes to the entanglement. We can write its corresponding phase term as

$$\exp\{i\phi_{11}\tilde{\omega}_1\tilde{\omega}_2\} = \exp\{iT_2(\tilde{\omega}_1)\tilde{\omega}_2\} = \exp\{iT_1(\tilde{\omega}_2)\tilde{\omega}_1\}, \tag{7.6}$$

with $T_2(\omega_1) = \phi_{11}\tilde{\omega}_1$ and $T_1(\omega_2) = \phi_{11}\tilde{\omega}_2$. The nonlocal phase term may be thus interpreted as a time delay on either photon that varies with the frequency of the other, and so it creates correlations whereby the outcomes of spectral measurements on either photon are correlated with the arrival time of the other, and vice versa.

The approach we take here to determining the state of an entangled photon system involves sending one photon into a TRSPS (described in Chapter 4) and the other into the EOSI described in Chapter 6. The outcomes of these measurements are recorded in coincidence, and we will show that this suffices to measure the full wave function $f(\omega_1, \omega_2)$.

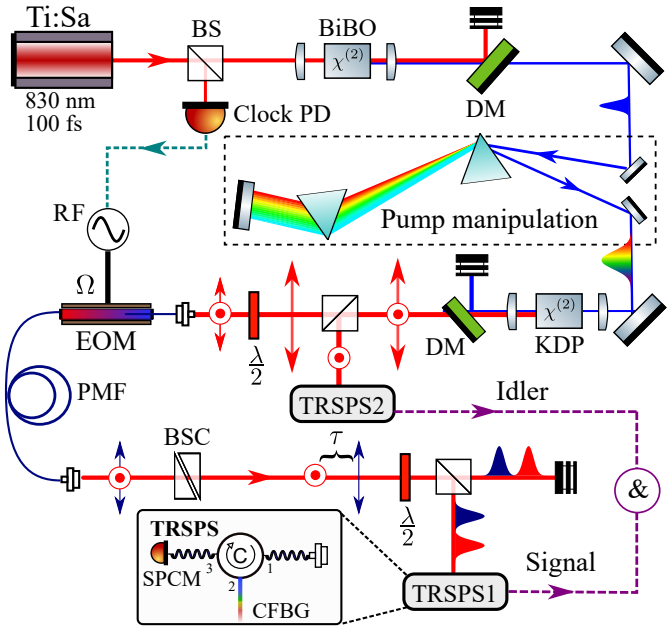


Figure 7.2: Experimental set-up. Frequency-doubled Ti:Sapph pulses are heavily dispersed in a prism stretcher. The stretched pulses pump the KDP crystal to generate a TF-entangled photon pair. One photon is then routed into a time-resolved single-photon spectrometer (TRSPS), whilst the other is routed into the EOSI. The outputs of the two spectrometers are recorded in coincidence.

7.3 Measurement principle

The experimental setup is illustrated in Fig. 7.2. This approach to measuring $f(\tilde{\omega}_1, \tilde{\omega}_2)$ relies on EOSI of one photon, projected into a spectrally pure state by spectrally-resolved projective measurement of its entangled partner.

The two photons are generated in orthogonal polarisations in the KDP source and are separated at a polarising beam splitter. The idler photon is immediately directed into a TRSPS [69] where it undergoes a spectral measurement. This projects its twin into a pure pulse mode conditioned on the outcome of the frequency measurement. The signal photon is sent into the EOSI. Although monitoring both outputs of the interferometer is possible and would reduce measurement times, it suffices to monitor a single output, where a spectral measurement is

recorded by a second TRSPS and logged in coincidence with the outcomes of the measurement for the idler photon. This is then repeated for many copies of the state until significant statistics are obtained. These data may then be represented as a two-dimensional histogram (Fig. 7.6), showing spectral interference fringes.

The joint spectral intensity of coincidence between the first photon (after its emergence from one port of the interferometer) and the second photon, or joint spectral interferogram, is then

$$S(\tilde{\omega}_1, \tilde{\omega}_2; \Omega) = \frac{1}{4} \{ S(\tilde{\omega}_1, \tilde{\omega}_2) + S(\tilde{\omega}_1 + \Omega, \tilde{\omega}_2) + 2\mathrm{Re}\left[f(\tilde{\omega}_1, \tilde{\omega}_2) f^*(\tilde{\omega}_1 + \Omega, \tilde{\omega}_2) e^{i\tilde{\omega}_1 \tau} \right] \},$$

The relative spectral phase can be extracted from the value of the final term, corresponding to spectral intereference fringes:

$$\phi(\tilde{\omega}_1 + \Omega, \tilde{\omega}_2) - \phi(\tilde{\omega}_1, \tilde{\omega}_2) = \mathrm{Arg}[f(\tilde{\omega}_1, \tilde{\omega}_2) f^*(\tilde{\omega}_1 + \Omega, \tilde{\omega}_2)].$$

7.4 State preparation

7.4.1 Photon pair generation

The first stage of this experiment is similar to that described in previous chapters. The Ti:Sapph oscillator described in Chapter 4 emits a train of pulses at 80 MHz repetition rate at 830 nm centre wavelength and 8 nm FWHM bandwidth. A pick-off from the primary beam is directed onto a fast photodiode to provide a global clock for the experiment. The primary pulse train is frequency-doubled in the BiBO crystal to generate a second-harmonic pump beam with central wavelength of 415 nm and average power of 550 mW.

To test our ability to measure the full two-photon state, it is necessary to modify the set-up

of the previous chapter to be able to selectively introduce nonlocal correlations. The full set-up is depicted in Fig. 7.2.

In the downconversion process, the complex joint amplitude of the biphoton depends on the pump spectral amplitude $\alpha(\omega_p) = \alpha(\omega_1 + \omega_2)$ according to

$$f(\tilde{\omega}_1, \tilde{\omega}_2) \propto |\alpha_p(\tilde{\omega}_1 + \tilde{\omega}_2)|\Phi(\tilde{\omega}_1, \tilde{\omega}_2)e^{i\phi_p(\tilde{\omega}_1+\tilde{\omega}_2)}e^{i\phi_{PDC}}, \tag{7.7}$$

where $\alpha_p(\tilde{\omega}_1 + \tilde{\omega}_2) = |\alpha_p(\tilde{\omega}_1 + \tilde{\omega}_2)|e^{i\phi_p(\tilde{\omega}_1+\tilde{\omega}_2)}$ is the complex spectral amplitude of the pump and $\phi_p(\tilde{\omega}_1+\tilde{\omega}_2)$ is the pump spectral phase evaluated at the point of downconversion, $\Phi(\tilde{\omega}_1, \tilde{\omega}_2)$ is the phase matching function of the nonlinear crystal and ϕ_{PDC} is a constant phase term acquired during the downconversion. This last term originates from the interaction between the pump and the non-linear medium, which is inherent to the SPDC process. Whilst it would be possible to control this term by inserting a dispersion compensation scheme on the pump beam, such as a prism or grating compressor [90], in our demonstration, this contribution was small and hence neglected.

The phase-matching function $\Phi(\tilde{\omega}_1, \tilde{\omega}_2)$ of the KDP photon pair source is engineered such that the joint spectral intensity $S(\tilde{\omega}_1, \tilde{w}_2) = |f(\tilde{\omega}_1, \tilde{\omega}_2)|^2$ is separable [52], verified by the JSI measurement in Fig. 4.8 and hence the spectral intensities of the two photons are not correlated. Whilst correlations in spectral amplitude are therefore more straightforward to observe, correlations in the spectral phase are more challenging. These can be introduced by modifying the joint spectral phase of the biphoton, which is achieved by pump manipulation.

The spectral phase of the pump at $\tilde{\omega}_p = \tilde{\omega}_1 + \tilde{\omega}_2$ may be expanded as follows:

$$\phi_p(\tilde{\omega}_1 + \tilde{\omega}_2) = \phi_{2p}(\tilde{\omega}_1 + \tilde{\omega}_2)^2 = \phi_{2p}\tilde{\omega}_1^2 + \phi_{2p}\tilde{\omega}_2^2 + 2\phi_{2p}\tilde{\omega}_1\tilde{\omega}_2 \tag{7.8}$$

where we have chose our time coordinates to remove any linear phase on the pump. Applying

a quadratic spectral phase ϕ_{2p} on the pump modifies the phase of the downconverted biphoton, with $\phi_{02} = \phi_{20} = \phi_{2p}/2$ and $\phi_{11} = \phi_{2p}$. By controlling this phase, we therefore also control the degree of entanglement, with K increasing monotonically with ϕ_{2p} (see. Fig. 7.1). Without modification, ϕ_{2p} is close to zero, with the pump beam having acquired only several thousand fs^2 of dispersion during propagation through the optics used in its generation and direction on the optical table.

To introduce a much larger chirp on the pump field a second highly dispersive beam path was set up along which the pump could be optionally directed using flip-mounted mirrors. In this path, the upconverted beam is sent into a prism stretcher consisting of two equilateral SF11 prisms of 25 mm side separated by approximately 30 cm, applying approximately 200,000 fs^2 of negative dispersion to the beam (see Fig. 7.2). The return beam is picked off with a cut mirror and is focused into the KDP crystal. Whilst introducing losses of around 65%, this beam path proved sufficiently wavelength-selective that there was no longer any need for a short-pass filter to remove the remaining infra-red in the beam, a component that introduced losses of approximately 20%. As a result, the overall power of the pump at the downconversion site was nearly 50% of that achievable in the unchirped case.

7.4.2 Joint temporal distribution

An interesting property of states of the form

$$f(\tilde{\omega}_1, \tilde{\omega}_2) = \varepsilon_{G1}(\tilde{\omega}_1)\varepsilon_{G2}(\tilde{\omega}_2)e^{i\phi_{11}\tilde{\omega}_1\tilde{\omega}_2}, \tag{7.9}$$

where $\varepsilon_{Gi}(\omega_i)$ are transform-limited Gaussian mode functions, is that the joint temporal distribution has the similar expression $\tilde{f}(t_1, t_2) = \tilde{\varepsilon}_{G1}(t_1)\tilde{\varepsilon}_{G1}(t_2)e^{i\alpha t_1 t_2}$, where α is a coefficient that depends on ϕ_{11} and on the spectral bandwidth of the single photons. Similarly to the case with joint spectral measurements, if one were to perform a joint time-of-flight measurement on

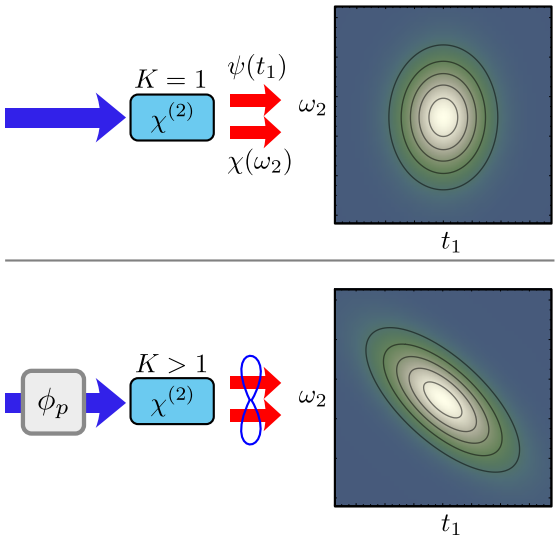


Figure 7.3: Schematic depicting the effect of pump's spectral phase on entanglement. SPDC in the non-linear medium results in a non-entangled state in both temporal and spectral domain (a). The same process with an additional spectral phase ϕ_p on the pump field results not only in a non-trivial entangled state in both domain, but entanglement also appears between the temporal and spectral mode-functions of the two daughter photons.

the state, no correlations would be visible since they are carried in the temporal phase. Remarkably, therefore, both joint-spectral and joint-temporal intensity measurements are uncorrelated, and entanglement of the form induced by the nonlocal spectral phase is therefore impossible to establish from such observations alone. By taking the Fourier transform of $f(\tilde{\omega}_1, \tilde{\omega}_2)$ along just one dimension, one obtains the spectral probability distribution of one photon as a function of the arrival time of the second (fig.7.4). In case of states of the form of Eq.7.9, with the transform taken over $\tilde{\omega}_1$, this time-frequency amplitude is given by $\tilde{\psi}(t_1 - \phi_p\tilde{\omega}_2) \cdot \chi(\tilde{\omega}_2)$.

In the event that there is additionally some local quadratic spectral phase on each photon, such that

$$f(\tilde{\omega}_1, \tilde{\omega}_2) = G_1(\tilde{\omega}_1)G_2(\tilde{\omega}_2)e^{i\phi_{20}\tilde{\omega}^2} \cdot e^{i\phi_{02}\tilde{\omega}_2^2} \cdot e^{i\phi_{11}\tilde{\omega}_1\tilde{\omega}_2}, \tag{7.10}$$

then there is some partial frequency-to-time mapping in the joint temporal distribution and a real cross-term appears, such that temporal intensity correlations become visible. This is apparent

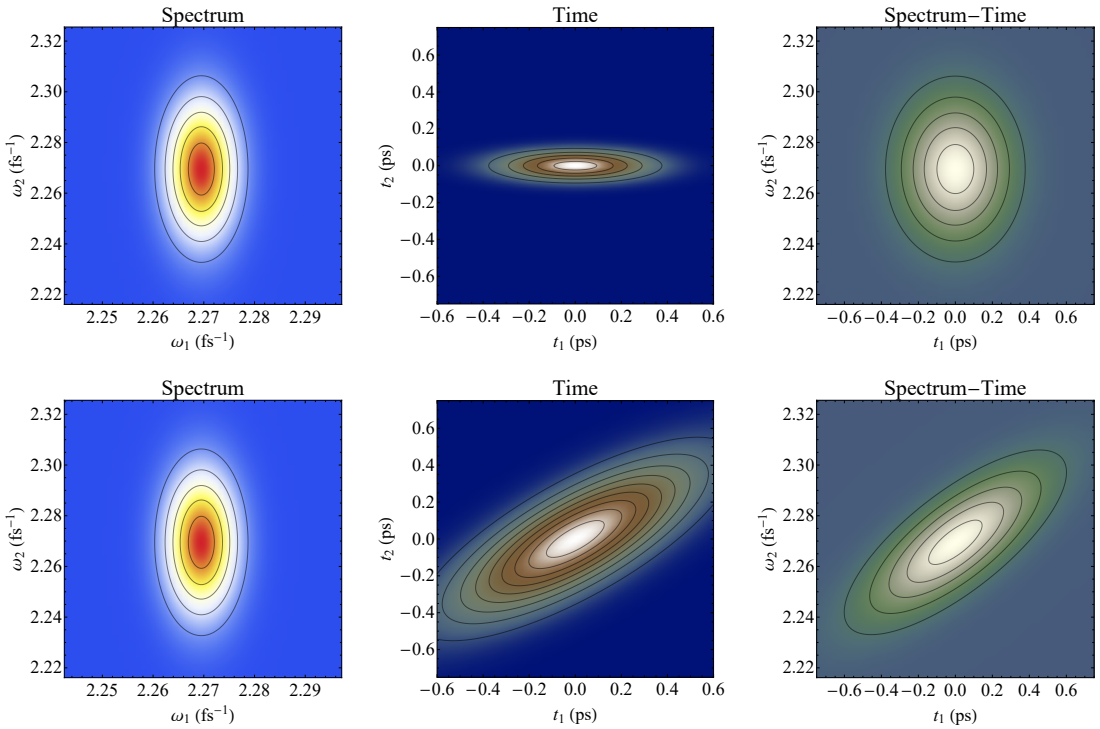


Figure 7.4: Joint spectral (left), joint temporal (centre) and spectral-temporal (right) intensity correlations in the unchirped-pump (top) and chirped pump (bottom) cases. Joint temporal intensity correlations become apparent only when both local and nonlocal spectral phase are present on the photon pair.

in the simulations in fig.7.4, where joint temporal intensity correlations emerge for the case $\phi_{20} = \phi_{02} = \phi_{11}/2$.

7.4.3 Phase reconstruction

The joint spectral phase of $f(\omega_1, \omega_2)$ is reconstructed using a multi-dimensional generalisation of the Fourier analysis methods common to spectral shearing interferometry as described in [47] and Chapter 6. The joint spectral interferogram $S_\Omega(\tilde{\omega}_1, \tilde{\omega}_2; \Omega)$ is Fourier transformed with respect to the frequency $\tilde{\omega}_1$ of the photon sent into the interferometer.

$$\begin{aligned}\mathcal{FT}_1\{S_\Omega(\tilde{\omega}_1,\tilde{\omega}_2;\Omega)\} &= \frac{1}{2}\overline{S}(T,\tilde{\omega}_2)(1+e^{iT\Omega}) \\ &+ \mathcal{FT}_1\{|f(\tilde{\omega}_1,\tilde{\omega}_2)f(\tilde{\omega}_1+\Omega,\tilde{\omega}_2)|e^{i\Delta\phi(\tilde{\omega}_1,\tilde{\omega}_2)}\} * \delta(T-\tau) \\ &+ \mathcal{FT}_1\{|f(\tilde{\omega}_1,\tilde{\omega}_2)f(\tilde{\omega}_1+\Omega,\tilde{\omega}_2)|e^{-i\Delta\phi(\tilde{\omega}_1,\tilde{\omega}_2)}\} * \delta(T+\tau),\end{aligned}$$

where $\mathcal{FT}_1$ denotes a Fourier transform with respect to the first variable, $*$ indicates a convolution, $\Delta\phi(\tilde{\omega}_1,\tilde{\omega}_2) = \phi(\tilde{\omega}_1,\tilde{\omega}_2) - \phi(\tilde{\omega}_1+\Omega,\tilde{\omega}_2)$ and $\overline{S}(T,\tilde{\omega}_2) \equiv \mathcal{FT}_1\left[S(\tilde{\omega}_1,\tilde{\omega}_2)\right]$. The latter two terms, which contain the phase information, correspond to peaks in the Fourier domain that are separated from the central peak by the added delay in the interferometer, τ. Since τ is chosen to be much larger than the temporal duration of the pulse and hence the width of $\overline{S}(T,\tilde{\omega}_2)$, these peaks can be isolated by Fourier-domain filtration. Inverse-Fourier transforming either peak and taking the argument of the resulting term provides the phase differential $\phi(\tilde{\omega}_1+\Omega,\tilde{\omega}_2) - \phi(\tilde{\omega}_1,\tilde{\omega}_2)$. These data may then be treated using the analyses described in Chapter 6 to extract the relative values of the phase $\phi(\tilde{\omega}_1,\tilde{\omega}_2)$ along lines of constant $\tilde{\omega}_2$. The reconstructed phase along some particular line of constant $\tilde{\omega}_2$ may be expanded

$$\begin{aligned}\Delta_1\phi(\tilde{\omega}_1,\tilde{\omega}_2) \equiv \phi(\tilde{\omega}_1,\tilde{\omega}_2) - \phi(0,\tilde{\omega}_2) &= \sum_{m>0}\left[\sum_n \tilde{\omega}_2^n\phi_{mn}\right]\tilde{\omega}_1^m \\ &= \sum_{m>0}\phi_m(\tilde{\omega}_2)\tilde{\omega}_1^m,\end{aligned} \tag{7.11}$$

where we have taken

$$\phi_m(\tilde{\omega}_2) = \left[\sum_n \tilde{\omega}_2^n\phi_{mn}\right]. \tag{7.12}$$

Because this extraction is based on relative values of the spectral phase along a line of constant $\tilde{\omega}_2$, the only unreconstructed part of the phase is just an additive term that is a function of $\tilde{\omega}_2$

only [1]

Since the coefficients $\phi_m(\tilde{\omega}_2)$ where $m > 0$ can then be measured for all $\tilde{\omega}_2$, they are each known as functions of $\tilde{\omega}_2$, and Eq.7.12 is simply the Taylor expansion of each coefficient $\phi_m(\tilde{\omega}_2)$ in terms of $\tilde{\omega}_2$. Hence, it is possible to reconstruct all terms in the expansion of the phase ϕ_{nm} such that $m > 0$, and this is sufficient to determine the nonlocal (correlated) phase. The remaining part of the phase, consisting of the terms ϕ_{0n} (for $n > 0$), can be determined by simply swapping the configuration round and repeating, such that photon 1 is spectrally resolved, and photon 2 is sent into the EOSI. This leaves only ϕ_{00}, the global phase which is typically unimportant. This prescripition entails some redundancy, since all nonlocal phase terms are measured twice and may be determined independently in either configuration.

In our experiment, only the second-order spectral phase terms ϕ_{02}, ϕ_{20} and ϕ_{11} are large enough to be measured, and hence we are only concerned with the terms in Eq.7.4. Spectrally-resolved detection of photon 2 projects photon 1 into a certain temporal mode, determining with what point on the linear slope of the RF waveform in the EOM (illustrated in Fig. 6.3) the pulse co-propagates. The pulse in the shearing arm of the interferometer thus acquires a phase that depends on its time of arrival into the EOSI, which is itself dependent on the outcome of the frequency measurement on the heralding photon. Hence the position of the fringes in $\tilde{\omega}_1$ are shifted in $\tilde{\omega}_2$ by an amount determined by the nonlocal phase ϕ_{11}. The contribution of this component to $\Delta_1\phi(\tilde{\omega}_1, \tilde{\omega}_2)$ is $\phi_{11}\Omega\tilde{\omega}_2$ - that is, the interference fringes along the $\tilde{\omega}_1$ direction - have a phase offset that is linear in $\tilde{\omega}_2$. It is this term that creates the tilted slant in the interference pattern in Fig.7.2.

[1] This is a 2D extension of how the single-photon EOSI is insensitive to the carrier-envelope phase. Across adjacent "slices" of the phase $\phi(\tilde{\omega}_1, \tilde{\omega}_2)$, the component of the phase that is independent of $\tilde{\omega}_1$, to which the EOSI is insensitive, may nonetheless still vary with $\tilde{\omega}_2$.

7.5 Experimental methods

7.5.1 Data acquisition and processing

Typical acquisition consists of running the TRSPSs in coincidence over a few hours at a typical rate of 15 spectrally-resolved coincidences per second, distributed on the $\tilde{\omega}_1, \tilde{\omega}_2$ space. These are binned into a 2D-histogram to produce the interferograms depicted by Fig. 7.6. A single acquisition is saved once it consisted of 5000 points, resulting in a new interferogram being generated approximately every 6 minutes. The phase reconstruction algorithm is then applied to all the individual interferograms from the long acquisition, consisting first of isolating one sideband in the Fourier domain and determining its intensity, or contrast of the interference fringes. This allows a quality control on the data set by determining if the contrast is beyond a certain threshold set to 40%. The selected datasets are each analysed by extracting the terms in the phase expansion as described in section 7.4.3. The results of the values of ϕ_{mn} from each interferogram are then averaged. The errors quoted are the standard deviations of these distributions of reconstructed values.

7.5.2 Noise and stability

The main source of noise in the experiment is attributed to phase drift in the interference fringes. For reconstruction to be possible, the absolute phase of the fringes must be stable over the data subset that is to be binned. If the phase drifts, the fringes wash away, rendering the reconstruction impossible. This is the reason why the long acquisition is divided into 5000-coincidence subsets, resulting in relatively low count densities but high fringe visibility. In practice, the relative phase between the arms of the EOSI does drift with time, due to several factors. The dominant effect is thermal variations in the EOM itself giving rise to a change in the index of refraction of the non-linear medium, which in turn can cause the phase to drift several radians over a typical timescale of around one hour. This effect was mitigated by carefully control-

ling the temperature variations of the EOM by attaching it with thermally conductive paste to a metallic heat sink with radiative fins. Another issue is the accuracy of the phase lock loop that is used to generate the 10 GHz RF-wave within the EOM. As a consequence of these factors, the phase drift, although minimized, was still present to the point that fringe visibility would be lost if one were to analyse an interferogram averaged over a few hours. Note that the acquisition time is also severely impacted by the poor quantum efficiency of our single-photon detectors ($\sim 10\%$ each), which compounds in coincidence. Much more efficient single-photon detectors with comparable timing resolution based on nanowires exist, and where possible we would recommend their use for a future implementation.

7.5.3 Spectral matching

In the unchirped-pump configuration, the spectral bandwidth of the pump was less when the pump was chirped. Due to the phase-matching conditions in KDP, the spectrum of the idler photon in particular is strongly dependent on the pump bandwidth, and hence in the chirped case the idler has considerably greater bandwidth than in the unchirped case. To facilitate direct comparison between the two cases, a pulse shaper was therefore used to carve a narrower bandwidth for the idler photon in the unchirped-pump measurement. The pulse shaper was fiber-coupled, adding additional dispersion to the single photons before the interferometer was open. Consequently, that phase was compensated by the pulse shaper, as described in Chapter 5.

7.6 Results

7.6.1 Unchirped pump

Initially, mode reconstruction was performed without chirping the pump, bypassing the prism compressor.

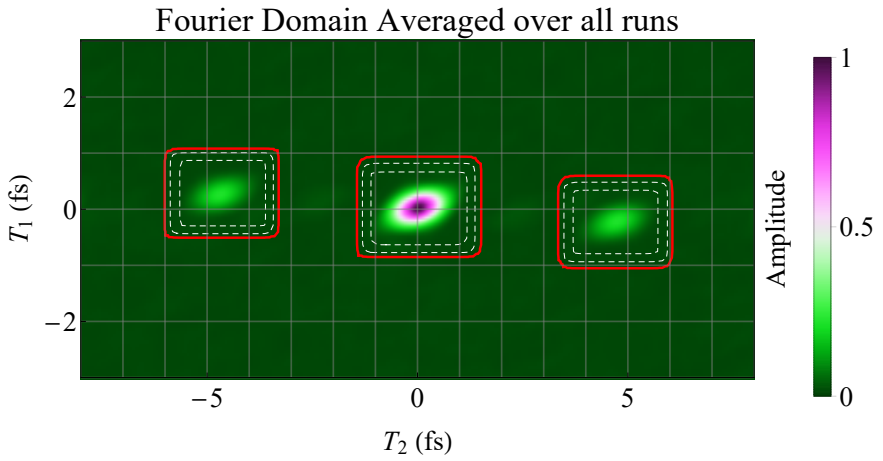


Figure 7.5: 2D Fourier transform of the measured joint spectral interferogram $S_\Omega(\tilde{\omega}_1, \tilde{\omega}_2; \Omega)$ in the case with a chirped pump. Note the displacement of the sidebands from the horizontal axis, indicating a diagonal slant on the spectral interference fringes associated with nonlocal phase correlations.

The spectral interference fringes depicted in Fig. 7.6, which have been filtered in the pseudo-temporal domain by considering only those terms contained within the bound regions of Fig. 7.5, are clearly not slanted as they are in the chirped pump case, pointing to the absence of phase correlations. Nonetheless, the experiment recovered a positive correlated phase ϕ_{11} of $(7.4 \pm 1) \cdot 10^3$ fs^2 from the first measurement (in which the narrowband signal photon was sent into the EOSI) and $(5.5 \pm 2) \cdot 10^3$ fs^2 for the second, where the broad idler photon was sent into the EOSI. While small, these values are statistically significant and can be attributed to the pump being slightly chirped or to correlations caused by the PDC crystal itself. Consideration of the total GDD of the elements in the optical path of the pump gave $\phi_{2p} \sim 3500$ fs^2, predicting $\phi_{11} \sim 7000$ fs^2, which is in strong agreement with the extracted values. The reconstructed spectral phase yielded the following coefficients: $(1.4 \pm 0.5) \cdot 10^4$ fs^2 for the signal and $(1.2 \pm 0.2) \cdot 10^4$ fs^2 for the idler, showing that the pulse shaper was close to compensating the large amount of dispersion caused by the meters of optical fibers leading to the interferometer through which the photons propagate.

7.6.2 Chirped pump

For a chirped pump, the position of the spectral interference fringes varies as a linear function of $\tilde{\omega}_2$, giving them a diagonal slant. Hence, the pattern is clearly not the product of its marginals, and so Eq.7.2 implies entanglement in the biphoton. The Fourier transform of the interferogram shows the two sidebands are each offset from the horizontal axes, suggesting the wave vector of the fringes has a component in the frequency of the heralding photon and hence pointing towards correlations in phase (Fig. 7.5). The measurement of the correlated phase ϕ_{11} for the signal photon EOSI yields a value of $(-1.61 \pm 0.08) \cdot 10^5$ fs^2 while the local quadratic spectral phase is estimated to $(-1.42 \pm 0.2) \cdot 10^5$ fs^2. The values are negative because the prism compressor adds anomalous dispersion to the pump beam which is passed to the daughter photons. The dispersion of the signal photon is less negative than the correlated phase because of local quadratic spectral phase added in the optical path after downconversion and remaining dispersion within the polarization interferometer, which was measured at $\sim 5 \cdot 10^3$ fs^2.

The signal and idler photon were then switched, with the idler photon injected into the EOSI and heralded by the spectrally-resolved signal photon. Fringes are then observed along the shorter bandwidth of the joint spectrum (see Fig.7.6), rendering the measurement of the slant less stable but that of the spacing more robust. Nevertheless, Fourier analysis retrieves the same values of ϕ_{11} at $(-1.45 \pm 0.2) \cdot 10^5$ fs^2 and of ϕ_{02} at $(-1.25 \pm 0.1) \cdot 10^5$ fs^2, consistent with the previous result within the theoretical model. No significant higher-order nonlocal spectral phase was observed.

7.6.3 Full complex joint amplitude reconstruction

Having measured the uncorrelated spectral phase of each photon as well as the nonlocal phase correlation with both an unchirped and chirped pump, it is now possible to reconstruct the full joint spectral amplitude $f(\omega_1, \omega_2) = |f(\omega_1, \omega_2)| e^{i\phi(\omega_1, \omega_2)}$. The reconstruction, depicted by

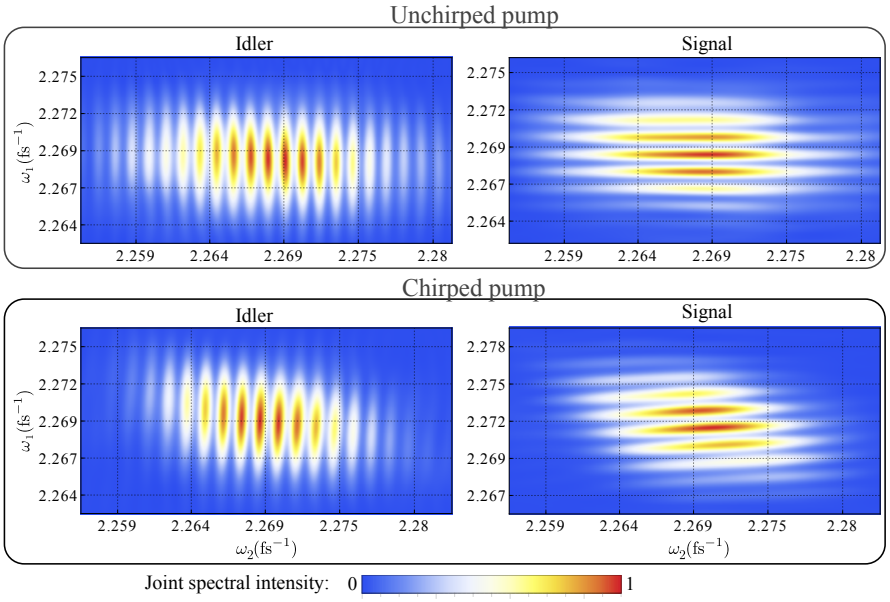


Figure 7.6: Fourier-filtered interferograms for the unchirped-pump (top) and chirped-pump (bottom) cases. Note the introduction of diagonal fringes in the chirped-pump case, indicating nonlocal spectral phase correlations.

Fig.7.7 (a,b), shows the amplitude of the probability distribution $|f(\tilde{\omega}_1, \tilde{\omega}_2)|^2$ of the two-photon state using contours overlaid on a heat-map that shows the phase $\mathrm{Arg}\,(f(\tilde{\omega}_1, \tilde{\omega}_2))$. This is represented for both the unchirped and chirped case. While the real amplitude $|f(\tilde{\omega}_1, \tilde{\omega}_2)|$ is indeed separable, the phase for a chirped pump is not flat and shows a saddle-like shape. Such a distribution is not possible with separable states, and reveals entanglement from spectral phase only.

Ultimately, this allows us to describe the entanglement of those states by performing a Schmidt decomposition on the two reconstructed states. The first 20 singular values or Schmidt coefficients squared, λ_i^2, are depicted by Fig.7.7 (c,d) for both cases, where the errors are the standard deviations of the distributions obtained from an ensemble of approximately 100 acquisitions. As a comparison, the modulus of the distributions were also diagonalised and their eigenspectrum is plotted on the same graphs (diamond markers). Note that the joint spectral

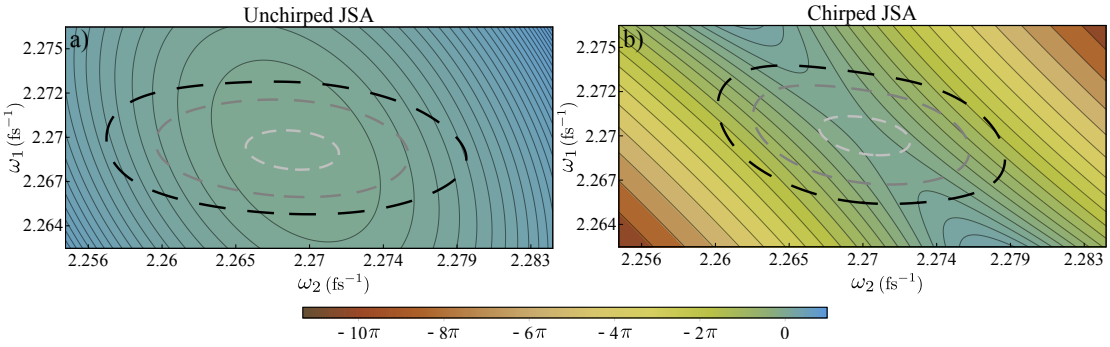


Figure 7.7: Left: Full phase-sensitive reconstruction of a two-photon joint spectral-temporal wave function for an unchirped (a) and a chirped (b) pump field. Background colour indicates the phase of the complex joint spectral amplitude $f(\tilde{\omega}_1, \tilde{\omega}_2)$ whilst the grayscale contours show lines of constant intensity $|f(\tilde{\omega}_1, \tilde{\omega}_2)|^2$.

intensities differ between both cases because in the chirped-pump case the prism compressor introduces considerable spatial-spectral coupling, which affects the spatial interaction within the SPDC crystal in a non-trivial manner. Even so, the spectral amplitude still remains largely uncorrelated, with a Schmidt number of just $K = 1.059$ under the assumption of flat phase, compared with $K = 1.016$ with the unchirped pump.

In the chirped pump case, this is greatly increased by the correlated phase, with the Schmidt number rising to $K = 5.0 \pm 0.5$. The singular values are distributed over a larger number of pairs of Schmidt modes and are represented in Fig.7.8 (c,d). For the unchirped case the joint spectral amplitude is approximately the product of its marginals, which give the dominant Schmidt mode-pair. In the chirped case, there are significant contributions from many pairs of Schmidt modes, which closely resemble the Hermite-Gauss modes.

Another way of visualising the spectral-temporal entanglement is by Fourier transforming the complex distributions to reconstruct joint-temporal intensity or spectral-temporal intensity distributions. The reconstructed distributions for the states measured here are shown in Fig.7.9. As expected, in the unchirped case (a-b), the two-photon state is separable and both the joint temporal intensity and the spectral-temporal intensity are uncorrelated. In the chirped case,

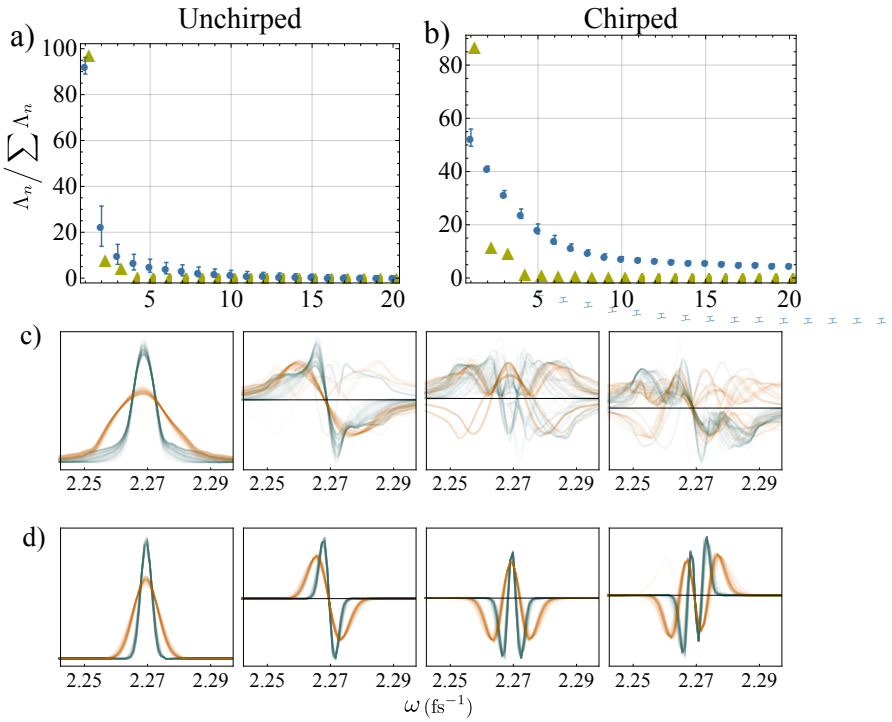


Figure 7.8: Top right (a,b): first 20 singular values of the decomposition of the complex joint amplitudes in teh chirped and unchirped cases. Diamonds markers represent the diagonalization of the modulus of the matrix, neglecting all phase effects. The error bars represent standard deviation. Bottom (c,d): overlay of the 4 first reconstructed Schmidt mode pairs for an unchirped (c) and a chirped (d) pump, plotted in the frequency domain. Blue (orange) represents spectral amplitude of the signal (idler). The higher Schmidt mode pairs in the unchirped case have low occupation and hence their reconstruction is subject to greater noise.

the spectral-temporal intensity (d) becomes correlated. As discussed in section 7.4.2, the joint temporal intensity (c) is also correlated, due to the presence of local quadratic spectral phase on both photons.

Note, however, that the sign of the correlation cannot change, and is therefore independent of the sign of the pump chirp. Note also that the temporal range over which the correlations in time-time or in time-frequency are observed is only several picoseconds, which would prove very challenging to measure with direct time-of-flight measurements using standard detectors. Our method instead takes advantage of interferometry to observe the effect of these temporal

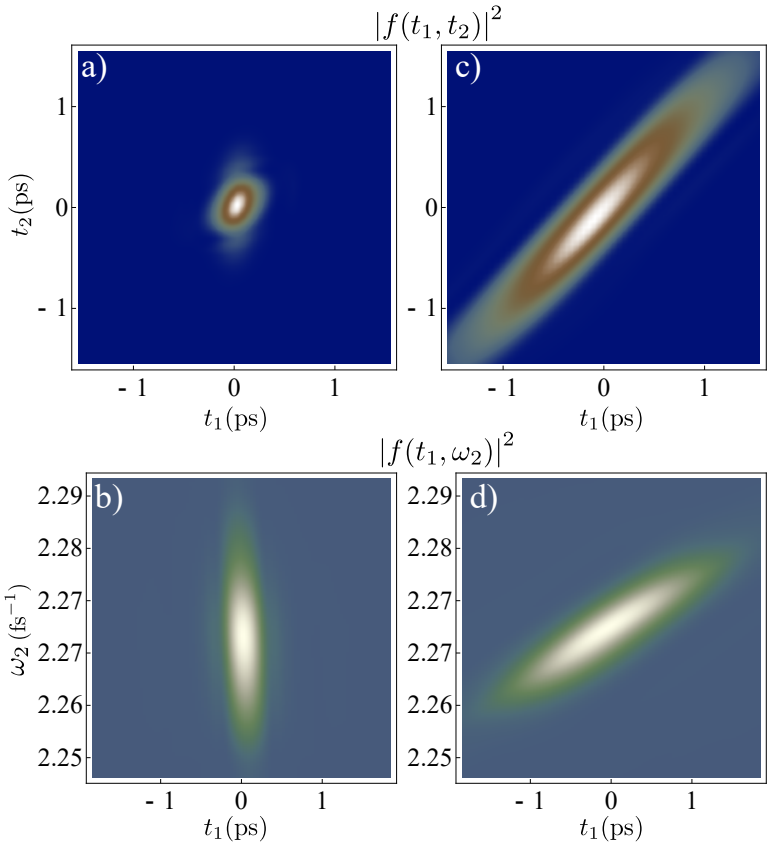


Figure 7.9: Reconstructed joint temporal intensity distributions (a,c) and temporal-spectral intensity distributions (b,d) for the unchirped (a,b) and chirped (c,d) cases.

correlations on the spectral phase, enabling us to infer the presence of short-duration temporal correlations which would likely be challenging to measure directly.

7.7 Mixed state characterisation

In the rest of this chapter, we have considered only the case where the biphoton is spectrally pure and hence is fully described by the complex joint amplitude $f(\tilde{\omega}_1, \tilde{\omega}_2)$. As a brief theoretical digression, we consider how this device could be used to characterise biphotons that are not known to be spectrally pure, and hence are described instead by the full two-photon spectral

density matrix

$$\rho = \int \rho(\tilde{\omega}_1, \tilde{\omega}_2, \tilde{\omega}_1', \tilde{\omega}_2') \left|\tilde{\omega}_1\right\rangle \left\langle\tilde{\omega}_1'\right| \otimes \left|\tilde{\omega}_2\right\rangle \left\langle\tilde{\omega}_2'\right| \mathrm{d}^4\tilde{\omega}, \tag{7.13}$$

where $\mathrm{d}^4\tilde{\omega} \equiv \mathrm{d}\tilde{\omega}_1\mathrm{d}\tilde{\omega}_1'\mathrm{d}\tilde{\omega}_2\mathrm{d}\tilde{\omega}_2'$. The measurement operator recovered from this measurement after Fourier filtering is

$$\hat{\Pi}(\tilde{\omega}_1, \tilde{\omega}_2, \Omega) = \left|\tilde{\omega}_1 + \Omega\right\rangle \left\langle\tilde{\omega}_1\right| \otimes \left|\tilde{\omega}_2\right\rangle \left\langle\tilde{\omega}_2\right| \tag{7.14}$$

where photon 1 is sent into the EOSI and photon 2 is spectrally resolved. Hence, if it is possible to repeat the measurement for controllable values of the spectral shear between some extremal values $\pm\Omega_m$, then it is possible to sample those elements of the spectral density matrix $\rho(\tilde{\omega}_1, \tilde{\omega}_2, \tilde{\omega}_1', \tilde{\omega}_2')$ where $\tilde{\omega}_2 = \tilde{\omega}_2'$ and $|\tilde{\omega}_1' - \tilde{\omega}_1| \leq \Omega_m$. By repeating in the other configuration, one could also obtain those elements where $\tilde{\omega}_1 = \tilde{\omega}_1'$ and $|\tilde{\omega}_2' - \tilde{\omega}_2| \leq \Omega_m$. However, in order to access all those values of the joint spectral density matrix where both $\tilde{\omega}_1 \neq \tilde{\omega}_1'$ and $\tilde{\omega}_2 \neq \tilde{\omega}_2'$, it would be necessary to simultaneously send both photons into independent EOSIs.

7.8 Chapter summary

In this chapter, we have extended the technique of EOSI introduced in Chapter 6 to demonstrate a highly flexible and reference-free method to measure the global wave function of a quantum system that exhibits multipartite entanglement across a high-dimensional basis. To the best of the author's knowledge, this work represents the first example of full quantum state tomography on a photon pair in asymmetric modes displaying high-dimensional bipartite entanglement across a continuous basis. This demonstration, where control of the parameters of the source was shown to have an elusive but powerful effect on the quantum properties of the output state, exemplifies the importance of a full characterisation scheme in understanding the physics of truly quantum optical systems. In doing so, it also provides a tool for studying and hence

controlling their behaviour.

With a powerful addition to our toolbox allowing us to fully characterise systems of spectrally entangled photons, we at last turn our attention to some of the potential applications of these physical systems. In the final experimental chapter of this thesis, we will explore how time-frequency entangled biphoton states, such as the ones studied in this chapter, can be applied practically in the spheres of measurement and communications to achieve an advantage over their classical counterparts.

Chapter 8

Entanglement-enhanced noise rejection

Contents

8.1 Introduction 186

8.2 Quantum metrology 186

8.3 Environmental noise reduction in parameter estimation 189

8.3.1 Environmental noise 189

8.3.2 The quantum Cramer-Rao bound 190

8.4 Demonstration 195

8.4.1 Experimental principle 195

8.4.2 Measurement stage 199

8.4.3 Experimental design 200

8.4.4 Results 202

8.4.5 Discussion 204

8.5 Chapter summary 205

8.1 Introduction

Given a source of broadband, spectrally-entangled photon pairs, the previous chapters have shown us how to fully characterise its output, and so placed us in a position to consider how such resources can be put to use. Whilst there are many paths we could go down at this juncture, in this chapter we choose to focus on the field of quantum metrology. This branch of quantum technology considers measurement protocols that, using non-classical probe preparation and detection of the probe system, surpass the limitations encountered when one is restricted to considering only classical resources[25].

This chapter explains how bipartite entanglement can be used to achieve a significant quantum enhancement of a phase measurement when the probing channel is afflicted by significant losses and background noise. It then describes an experiment that realises this by exploiting spectral-temporal entanglement between a transmitted probe photon and retained ancilla photon.

8.2 Quantum metrology

Much consideration has previously been given to quantum protocols that reduce noise that is intrinsic to the state, showing that nonclassical probe states achieve optical phase estimation beyond the shot-noise limited standard quantum limit [91]. In many real-world situations, however, the quantum states needed to realise these enhancements are difficult to produce, and the advantages are not robust in the presence of environmental considerations such as loss and background noise. Their potential is therefore restricted in scope, anticipating either greatly improved source or detector technology, near-perfect control over the environment, or special circumstances where high intensities introduce other adverse phenomena [2].

Rejection of extrinsic noise

Other treatments instead consider quantum enhancements in the common case where measurement precision is instead limited by *environmental* considerations such as loss and background noise. Many real-world measurements take place under conditions where loss of signal and the introduction of environmental noise are significant effects, and exploring quantum enhancements within this regime is a relatively new and evolving area of research. One such analysis is the quantum illumination (QI) protocol [92, 93], which determines the existence of a reflecting target by probing through lossy channels in the presence of background noise. QI is innately a loss-tolerant and noise-tolerant protocol, providing substantial enhancements even in the high-loss, high-noise limit. The principle of operation behind QI is improved discrimination against background noise using entanglement of the probe with a multimode "ancilla" system retained by the observer. Whilst environmental noise shows no correlations with the ancilla, any component of the original signal will still exhibit these tell-tale correlations, even long after signal degradation is so severe that the final state would fail any nonclassicality test. QI therefore exhibits thoroughly nonclassical enhancements for a broad and practically useful class of measurement problems.

Physical origin of enhancement

In this analysis, we compare protocols constrained only to using separable states to those where entangled resources are available. When considering only single-photon probes, the quantum advantage in discrimination against environmental noise can be most intuitively understood with the concepts of true- and false-positive detection events. The parameter of interest determines the amount of signal returned at the output of the measurement channel in certain detection modes, with the accuracy of the measurement therefore determined by the uncertainty in the number of counts in the detection mode that can be attributed to returned signal ("true

positives"). Background environmental noise in these modes ("false positives") cannot be distinguished from the signal, and so adds uncertainty to the true value of signal transmitted in the detection mode. A scheme that better rejects the false positives thus provides an advantage. This principle is illustrated in fig. 8.1.

In the unentangled case, the optimal scheme consists of sending the probe photon into the channel in one (known) mode of the d modes available. This photon will then be coupled into the detection modes at the output of the channel, in proportions determined by the parameter(s) of interest. By contrast, the entangled photon pair exists in a Hilbert space with dimension d^2. Here, we might choose a maximally entangled preparation and measurement basis[1]. For example, if $d = 2$, we might choose the Bell states, defined by

$$\begin{aligned} |\Phi\pm\rangle &= \frac{1}{\sqrt{2}} \left(|0\rangle_S |0\rangle_A \pm |1\rangle_S |1\rangle_A \right) \\ |\Psi\pm\rangle &= \frac{1}{\sqrt{2}} \left(|0\rangle_S |1\rangle_A \pm |1\rangle_S |0\rangle_A \right), \end{aligned} \tag{8.1}$$

where $|0\rangle$ and $|1\rangle$ denote the possible states of each of the pair of subsystems A (ancilla) and S (signal). We prepare our photon pair in, say, $|\Psi-\rangle$, and monitor with a projective measurement $|\Psi-\rangle\langle\Psi-|$. This consists of a joint measurement of the received and ancilla photon and amounts to monitoring only one of the d^2 modes whose populations contain information about the parameter of interest. Since we always retain the ancilla photon, the probability of a coincidence detection event is the probability of receiving a photon from the noisy channel in the detection mode(s). As there is no phase relationship between a background photon and the ancilla photon, the false detection events will be randomly and uniformly distributed across the whole d^2 -dimensional Hilbert space. The quantum speed-up thus derives from the fact that entanglement with an ancilla system distributes the background counts more diffusely over a much larger space such that fewer coincide with the detection modes, whilst the process being

[1] See section 3.3.7

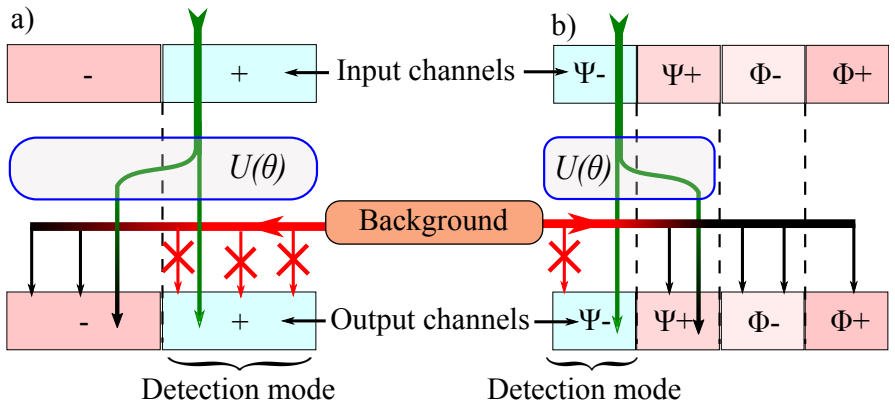


Figure 8.1: An operation $U(\theta)$ is probed with an optical state $|+\rangle$ (a) or $|\Psi-\rangle$ (b). $U(\theta)$ distributes the signal into the output modes depending on θ. A single output mode is monitored (blue). Background noise is randomly distributed across all output modes. Environmental noise entering the detection mode constitutes a false positive count (red crosses), which reduces the precision of the measurement. In the entangled case (b), background noise is still distributed randomly but since the Φ-subspace is irrelevant to the measurement and can be ignored, false positives in the detection mode occur less frequently relative to signal than the unentangled case (a) for a given probe system dimensionality d (here d=2).

probed only distributes the signal across a subset of this space. We therefore achieve a better ratio between true and false positives in the entangled case. Importantly, this is a coherent effect, so classically correlated states cannot reproduce it.

8.3 Environmental noise reduction in parameter estimation

8.3.1 Environmental noise

It has previously been established that entanglement between the probe and a retained ancilla gives rise to better discrimination between probes acted on by different operations [94]). Here we quantify this advantage in the case of a phase estimation problem. The target is illuminated with some probe (for example a single photon) in a quantum state $|\Xi\rangle\langle\Xi|$, a pure state on a space of dimension d. We suppose some portion of the signal is always reflected, and has been

acted on by some operator $U(\theta)$, such that the returned state is given by the density matrix

$$\hat{\rho} = (1-\eta)\hat{\rho}_N + \eta U(\theta)\left|\Xi\right\rangle\left\langle\Xi\right| U^{\dagger}(\theta). \tag{8.2}$$

Here $\hat{\rho}_N$ is a highly mixed density matrix corresponding to the background light, η is the intensity reflectivity, and $U(\theta)$ is a unitary operator whose action is dependent on the parameter θ, which is the target of the measurement. If we restrict our analysis to the single-photon subspace, then this noise model is general, since every photon at the output of the channel must either have originated as signal, or else must be background.

8.3.2 The quantum Cramer-Rao bound

The quantum Cramer-Rao bound [95] provides a measurement-independent lower bound on the variance σ_θ^2 in the estimated value of the parameter θ. It therefore yields the best possible precision attainable for a given probe state, optimised over all possible detection bases. The quantum Cramer-Rao bound, which is always saturable in the asymptotic limit $Q \to \infty$, where Q is the number of measurements, is expressed as

$$\sigma_\theta^2 \geq \frac{1}{QI_Q}, \tag{8.3}$$

where I_Q is the quantum Fisher information[96, 95]. This quantity expresses the maximum possible information about the target parameter that is attainable per measurement, for a given probe state. Here we calculate it using known results.

The quantum Fisher information is given by $I_Q = \mathrm{Tr}[\hat{\rho}' R_\rho^{-1}(\hat{\rho}')]$ [95, 96], where $\hat{\rho}' = \partial\hat{\rho}/\partial\theta$ is the derivative of $\hat{\rho}$ with respect to θ. Here $R_\rho^{-1}(A)$ is a superoperator[2] acting on an operator A such that

[2] A mapping of one set of operators onto another.

$$[R_\rho^{-1}(A)]_{mn} = \frac{A_{mn}}{\beta_m + \beta_n} \tag{8.4}$$

where $A_{mn} = \langle\phi_m| A |\phi_n\rangle$ for basis states $\{|\phi_n\rangle\}$ and close to $\theta = 0$,

$$\hat{\rho} = \sum_{n=1}^{d} \beta_n |\phi_n\rangle \langle\phi_n| . \tag{8.5}$$

We must therefore evaluate I_Q for the cases $\hat{\rho} = \hat{\rho}_S$, where $|\Xi\rangle$ is separable into probe and ancilla states, and $\hat{\rho} = \hat{\rho}_E$, where $|\Xi\rangle$ is an entangled state in the joint probe-ancilla space [96, 95]. This calculation necessarily requires some assumptions about the action of the unitary $U(\theta)$ on $|\Xi\rangle$ as well as the nature of the injected noise $\hat{\rho}_N$. To derive the quantitative relationship with the mode number, we consider an idealised case where the injected noise approximates a maximally mixed state $\hat{\rho}_N = \frac{1}{d}\sum_{n=1}^{d} |\phi_n\rangle \langle\phi_n| = \mathbb{1}/d$, where $\mathbb{1}$ is the identity operator. We choose the states $|\phi_i\rangle$ to be the eigenstates of $U(0)$[3]. Assuming variations in θ are small about zero, we take as an example a highly degenerate form for $U(\theta)$ with eigenvalues $|\phi_n\rangle$ such that:

$$U(\theta) |\phi_n\rangle = \begin{cases} e^{i\theta/2} |\phi_n\rangle , \approx (1 + i\theta/2) |\phi_n\rangle , & n \text{ odd} \\ e^{-i\theta/2} |\phi_n\rangle \approx (1 - i\theta/2) |\phi_n\rangle , & n \text{ even} \end{cases} \tag{8.6}$$

Separable case

Firstly, we consider the separable case, where the target is illuminated by an optimal probe state $|\Xi\rangle = |+\rangle$, where $|\pm\rangle = \frac{1}{\sqrt{2}}(|\phi_1\rangle \pm |\phi_2\rangle)$. The action of $U(\theta)$ on these states is given by

[3] We can choose basis freely since $\hat{\rho}_N$ has the same form in any basis, as it is proportional to the identity and so is invariant under unitary transformation.

$$\begin{aligned}\hat{U}(\theta)\left|\pm\right\rangle &= \frac{1}{\sqrt{2}}(e^{i\theta/2}\left|\phi_1\right\rangle \pm e^{-i\theta/2}\left|\phi_2\right\rangle) \\ &= \cos\frac{\theta}{2}\left|\pm\right\rangle \pm i\sin\frac{\theta}{2}\left|\mp\right\rangle \approx \left|\pm\right\rangle \pm \frac{i\theta}{2}\left|\mp\right\rangle, \end{aligned} \tag{8.7}$$

Referring back to Eq.8.2 and taking $\hat{\rho} = \hat{\rho}_S$, we see that at $\theta = 0$, the operator $\hat{\rho}_S$ can be written

$$\hat{\rho}_S = \beta_+ \left|+\right\rangle\left\langle+\right| + \beta_0(\mathbb{1} - \left|+\right\rangle\left\langle+\right|), \tag{8.8}$$

where

$$\beta_+ = \frac{1-\eta}{d} + \eta, \quad \beta_0 = \frac{1-\eta}{d}. \tag{8.9}$$

Differentiating Eq.8.2 with respect to θ and referring to Eq.8.7, we see

$$\begin{aligned}\hat{\rho}'_S &= \eta\left(\frac{\partial(U(\theta)\left|+\right\rangle)}{\partial\theta}\left\langle+\right| + \left|+\right\rangle\frac{\partial(\left\langle+\right|U(\theta))}{\partial\theta}\right) \\ &= \frac{-i\eta}{2}\left(\left|+\right\rangle\left\langle-\right| + \left|-\right\rangle\left\langle+\right|\right)\end{aligned} \tag{8.10}$$

Hence $\left\langle+\right|\hat{\rho}'\left|+\right\rangle = \left\langle-\right|\hat{\rho}'\left|-\right\rangle = 0$, and so

$$R^{-1}_{\hat{\rho}_S}(\hat{\rho}'_S) = \frac{\hat{\rho}'_S}{\beta_+ + \beta_0} = \frac{-i\eta d\left(\left|+\right\rangle\left\langle-\right| + \left|-\right\rangle\left\langle+\right|\right)}{2(1-\eta)+\eta d}. \tag{8.11}$$

And so we arrive at

$$\hat{\rho}'_S R^{-1}_{\hat{\rho}_S}(\hat{\rho}'_S) = \frac{\eta^2 d\left(\left|+\right\rangle\left\langle+\right| + \left|-\right\rangle\left\langle-\right|\right)}{4(1-\eta)+2\eta d}, \tag{8.12}$$

and finally

$$\boxed{I^S_Q = \mathrm{Tr}(\hat{\rho}' R^{-1}_\rho(\hat{\rho}')) = \frac{\eta^2 d}{4(1-\eta)+2\eta d}} \tag{8.13}$$

Entangled case

We then imagine that $|\Xi\rangle$ is instead drawn from a basis of maximally entangled states $|k,m\rangle = \frac{1}{\sqrt{d}}\sum_{j=1}^{d} e^{2i\pi jk/d}|\phi_j\rangle|\chi_{j+m}\rangle$, introduced in section 3.3.7. In this case Eq.8.2 changes to

$$\begin{aligned}\hat{\rho}_E &= (1-\eta)\hat{\rho}_{th}\otimes \mathrm{Tr}_S(|\Xi\rangle\langle\Xi|) + \eta U(\theta)|\Xi\rangle\langle\Xi|U^\dagger(\theta) \\ &= \frac{(1-\eta)}{d^2}I + \eta U(\theta)|k,m\rangle\langle k,m|U^\dagger(\theta)\end{aligned} \tag{8.14}$$

where Tr_S refers to the partial trace over the signal subsystem and the second equality follows from the fact that, since $|k,m\rangle$ is maximally entangled, $\mathrm{Tr}_S(|k,m\rangle\langle k,m|) = \mathbb{1}_A/d$, where $\mathbb{1}_A$ is the identity in the ancilla subsystem.

The action of $U(\theta)$ on $|k,m\rangle$ is as follows:

$$\begin{aligned}U(\theta)|k,m\rangle &= \frac{1}{\sqrt{d}}\sum_{j=1}^{d} e^{2i\pi jk/d}U(\theta)|\phi_j\rangle|\chi_{j+m}\rangle \\ &= \frac{1}{\sqrt{d}}\sum_{j\ \text{odd}}^{d} e^{-2i\pi jk/d+i\theta/2}|\phi_j\rangle|\chi_{j+m}\rangle + \frac{1}{\sqrt{d}}\sum_{j\ \text{even}}^{d} e^{-2i\pi jk/d-i\theta/2}|\phi_j\rangle|\chi_{j+m}\rangle\end{aligned} \tag{8.15}$$

Noting that

$$\left(\frac{1+e^{i\pi j}}{2}\right) = \begin{cases}1,\ j\ \text{even} \\ 0,\ j\ \text{odd}\end{cases} \quad \text{and} \quad \left(\frac{1-e^{i\pi j}}{2}\right) = \begin{cases}0,\ j\ \text{even} \\ 1,\ j\ \text{odd}\end{cases}, \tag{8.16}$$

we can write this as

$$
\begin{aligned}
U(\theta)\left|k,m\right\rangle &= \frac{1}{\sqrt{d}}\sum_{j=1}^{d} e^{2i\pi jk/d}\left[e^{-i\theta/2}\left(\frac{1+e^{i\pi j}}{2}\right)+e^{i\theta/2}\left(\frac{1-e^{i\pi j}}{2}\right)\right]\left|\phi_j\right\rangle\left|\chi_{j+m}\right\rangle . \\
&= \frac{1}{\sqrt{d}}\sum_{j=1}^{d}\left[\left(\frac{e^{i\theta/2}+e^{-i\theta/2}}{2}\right)e^{2i\pi jk/d}+\left(\frac{e^{i\theta/2}-e^{-i\theta/2}}{2}\right)e^{2i\pi j(k+d/2)/d}\right]\left|\phi_j\right\rangle\left|\chi_{j+m}\right\rangle \\
&= \left(\cos\frac{\theta}{2}\left|k,m\right\rangle + i\sin\frac{\theta}{2}\left|k+d/2,m\right\rangle\right) \\
&\approx \left(\left|k,m\right\rangle + \frac{i\theta}{2}\left|k+d/2,m\right\rangle\right). \qquad (8.17)
\end{aligned}
$$

This is the same form as Eq.8.7. We choose to illuminate with any of the states $|k,m\rangle$, say $|1,1\rangle$. The derivation of the quantum Fisher information then takes the same form as above, with $d \to d^2$, $|+\rangle \to |1,1\rangle$, $|-\rangle \to |1+d/2,1\rangle$. Hence the quantum Fisher information in the entangled case, I_Q^E, is given by

$$I_Q^E = \frac{d^2\eta^2}{4(1-\eta)+2\eta d^2} \qquad (8.18)$$

The quantum advantage factor I_Q^E/I_Q^S gives the proportional reduction in the number of measurements Q necessary to achieve a particular bound on σ_θ^2. This is given by

$$\boxed{\frac{I_Q^E}{I_Q^S} = \frac{d[2(1-\eta)+\eta d]}{2(1-\eta)+\eta d^2}} \qquad (8.19)$$

This quantity is plotted against the dimensionality d for various selected values of η in Fig. 8.2.

Eq.8.19 tells us that for $d >> 1/\eta$, $I_Q^E/I_Q^S \to 1$. The interpretation of this is that even in the unentangled case, the noise is so diffuse across the many modes that false positives are rare and entanglement makes little difference. However we can see from Fig. 8.2 that with high losses ($\eta \ll 1$) and intermediate values of d it is possible to achieve a substantial quantum speed-up. For $d \approx 500$ and $\eta \approx 10^{-5}$, achieving a certain bound on the precision of θ requires

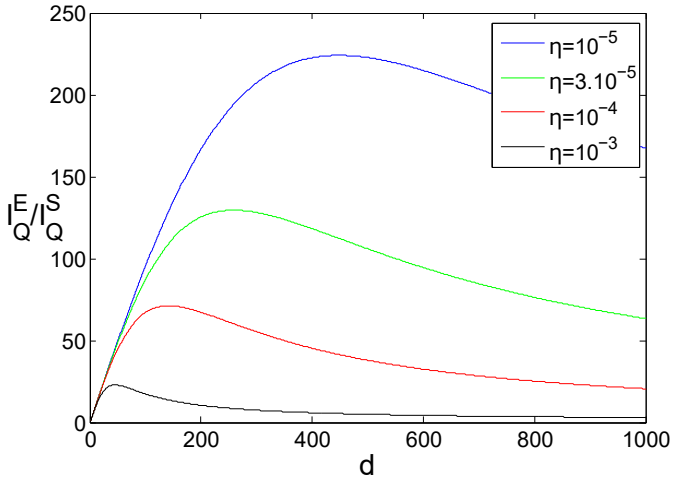


Figure 8.2: Quantum speed-up plotted against system dimensionality d, for selected values of the intensity reflectivity η.

over 200 times fewer measurements in the entangled case than classically.

8.4 Demonstration

8.4.1 Experimental principle

We demonstrate this advantage using spectral Bell states, a basis of maximally entangled $d = 2$ states. The physical platform used to realise this is a pair of frequency-entangled photons, with the roles of $|\phi_1\rangle$ and $|\phi_2\rangle$ occupied by different spectral modes $|R\rangle$ and $|B\rangle$. The parameter we seek to measure is the relative spectral phase between two quasi-monochromatic signals- a measurement performed classically using the well-known technique of multi-wavelength interferometry [97]. The probe consists of a single photon in a superposition of two occupied frequency modes ω_R and ω_B at separate frequencies, which acquires a relative spectral phase $\theta = (\omega_B - \omega_R)\tau$ as it propagates through a lossy, noisy channel, where τ is a controllable time delay in the path of the signal photon.

In the case of spectrally entangled single photons incident on a beam splitter, the interfer-

ence fringes in coincidence counts caused by varying their relative spectral phase in this manner is known as spatial quantum beating (SQB) [98]. We will show below that monitoring in coincidence in this manner is equivalent to monitoring the Bell-state detection mode $|\Psi-\rangle$. We measure these fringes in the presence of injected noise to illustrate the feasibility of the above measurement in the case where $d = 2$. In our demonstration, the injected noise takes the form of a coherent-state pulse delayed with respect to the signal by a unknown amount much larger than the coherence length of the single photons. We can therefore model it as an incoherent mixture of coherent states on the modes R and B (a phase-averaged coherent state). For ease of analysis, we will proceed with the assumption that the illumination of the target is constrained such that the average number of photons entering the channel per measurement cycle is much less than one. This allows us to restrict our analysis to the single-photon space and model the injected noise as a spectrally mixed single-photon state. We will also assume that the noise is dim enough that events containing only a single noise photon make the dominant contribution to the noise.

Separable comparison

For comparison, we first consider a hypothetical separable scheme, in which the target is illuminated with a coherent state on the two spectral modes R and B,

$$|\Xi\rangle = \hat{D}(\alpha)\,|0\rangle \tag{8.20}$$

where α is the coherent state parameter[4] and $\hat{D}(\alpha)$ is the vacuum displacement operator given by

$$\hat{D}(\alpha) = e^{\frac{-|\alpha|^2}{2}} \exp\{\frac{\alpha}{\sqrt{2}}(a_R^\dagger + a_B^\dagger)\}. \tag{8.21}$$

[4] See section 3.3.8

Collecting only the terms that are first order in α, we obtain

$$|\Xi\rangle \approx \left[1 + \frac{\alpha}{\sqrt{2}}(a_B^\dagger + a_R^\dagger)\right]|0\rangle \tag{8.22}$$

$$= |0\rangle + \alpha\,|+\rangle \tag{8.23}$$

with $|\pm\rangle \equiv \frac{1}{\sqrt{2}}(a_B^\dagger \pm a_R^\dagger)\,|\text{vac}\rangle$. The action of $\hat{U}(\theta)$ on these states is given by

$$\hat{U}(\theta)\,|\pm\rangle = \frac{1}{\sqrt{2}}(e^{i\theta/2}a_B^\dagger \pm e^{-i\theta/2}a_R^\dagger)\,|0\rangle \tag{8.24}$$

$$= \frac{1}{\sqrt{2}}\left(\cos\frac{\theta}{2}a_+^\dagger \pm i\sin\frac{\theta}{2}a_-^\dagger\right)|0\rangle$$

$$= \frac{1}{\sqrt{2}}\left(\cos\frac{\theta}{2}\,|\pm\rangle \pm i\sin\frac{\theta}{2}\,|\mp\rangle\right), \tag{8.25}$$

and we note the resemblence of this operation to Eq.8.7.

The overall density matrix of the channel is given by

$$\hat{\rho}_T = |\Xi\rangle\langle\Xi| \otimes \hat{\rho}_N \tag{8.26}$$

where $\hat{\rho}_N$ is the spectral phase-averaged noise density matrix given by

$$\hat{\rho}_N = \int \frac{d\phi}{2\pi}\hat{D}(\beta,\phi)\,|0\rangle\langle 0|\,\hat{D}^\dagger(\beta,\phi) \tag{8.27}$$

with $\hat{D}(\beta,\phi)$ defined on the injected noise modes b_B, b_R

$$\hat{D}(\beta,\phi) = e^{\frac{-|\beta|^2}{2}}\exp\{\frac{\beta}{\sqrt{2}}(b_R^\dagger + e^{i\phi}b_B^\dagger)\} \tag{8.28}$$

Applying the beamsplitter transformations on Eq.8.26 and post-selecting on single-photon events in the channel output mode to preserve the trace yields the spectral density matrix of the resul-

tant single photons at the output of the channel:

$$\hat{\rho}_S = s\hat{U}(\theta)\left|+\right\rangle\left\langle+\right|\hat{U}^\dagger(\theta) + \frac{(1-s)}{2}\mathbb{1}_2 \tag{8.29}$$

where where $\mathbb{1}_2/2$ is the maximally mixed state $\frac{1}{2}(\left|+\right\rangle\left\langle+\right| + \left|-\right\rangle\left\langle-\right|)$ and s is the proportion of returned signal,

$$s = \frac{\eta N_\alpha}{\eta N_\alpha + (1-\eta)N_\beta} \tag{8.30}$$

with N_α and N_β the average photon number in the signal and noise inputs respectively, with $N_\alpha \approx |\alpha|^2$ and $N_\beta \approx |\beta|^2$. We see that this is of the form of equation 8.2, and therefore obtain a bound on the Fisher information from Eq.8.13:

$$I_Q^S = \frac{s^2}{2} \tag{8.31}$$

We also note that, subject to the assumption that higher-order photon number terms will not make a significant contribution to the Fisher information, the higher photon number statistics of both the probe state and the noise are irrelevant.

Entangled case

We now compare this with a scheme based on entangled photon pairs. The downconversion source produces photon pairs in the symmetric anticorrelated Bell state $|\Psi+\rangle$, here given by

$$|\Psi+\rangle = \frac{1}{\sqrt{2}}\left(|R\rangle_S|B\rangle_A + |B\rangle_S|R\rangle_A\right), \tag{8.32}$$

where $|R\rangle$ and $|B\rangle$ denote the longer-wavelength and shorter-wavelength spectral modes respectively. These states are prepared post-selectively in the detection stage using spectral filtration and coincident detection at the output of a Hong-Ou-Mandel interferometer.

The action of $U(\theta)$ on this state is given by

$$\begin{aligned}\hat{U}_S(\theta)\left|\Psi+\right\rangle &= \frac{1}{\sqrt{2}}\left(e^{i\theta/2}\left|R\right\rangle_S\left|B\right\rangle_A + e^{-i\theta/2}\left|B\right\rangle_S\left|R\right\rangle_A\right)\\ &= \cos(\theta/2)\left|\Psi+\right\rangle - i\sin\theta/2\left|\Psi-\right\rangle,\end{aligned} \tag{8.33}$$

Varying the parameter θ by scanning the delay therefore gives rise to interference fringes in the number of coincidence counts. Following a similar analysis to that given above and postselecting on events where a photon pair arrives at the detection stage, the overall density matrix of the returned state is thus

$$\hat{\rho}_E = s\hat{U}(\theta)\left|\Psi+\right\rangle\left\langle\Psi+\right|\hat{U}^\dagger(\theta) + \frac{(1-s)}{4}\mathbb{1}_4, \tag{8.34}$$

with $\mathbb{1}_4/4$ the maximally mixed state in the space of the spectral Bell states. Substituting this into Eq.8.13 gives us an expression for the Fisher information:

$$I_Q^S = \frac{s^2}{1+s}, \tag{8.35}$$

and hence a quantum advantage of

$$\frac{I_Q^E}{I_Q^S} = \frac{2}{1+s}. \tag{8.36}$$

8.4.2 Measurement stage

The measurement that saturates the Cramer-Rao bound is projection onto the operator $\left|\Psi+\right\rangle\left\langle\Psi+\right| - \left|\Psi-\right\rangle\left\langle\Psi-\right|$; i.e. counting the difference between the number of pairs in the two Bell states whose occupations vary with θ, and thus determining at what point in the interference pattern Fig. 8.6 the system lies. The states $\left|\Phi\pm\right\rangle$ may be rejected as noise and need not be monitored, and the fact that half of the background light disappears into these modes is the origin

of the quantum enhancement. Bell-state detection is performed using spectrally filtered HOMI (see Fig.8.4). The two photons are interfered at a beam splitter, with the output modes of the beamsplitter being spectrally filtered at the two frequencies ω_R and ω_B, and monitored in coincidence. Spectral interference filters before the single-photon counting modules (SPCM) ensure that only the spectrally anticorrelated two-photon states, $|\Psi\pm\rangle$, are considered. Additionally, since in HOMI only the antisymmetric projection of the state contributes to coincidences (see Eq.5.9), a coincidence detection event corresponds to projection on the state $|\Psi-\rangle\langle\Psi-|$, hence monitoring only a single detection mode.

Whilst this is a sub-optimal measurement, in practice, the interference fringes in the $|+\rangle\langle+|$ mode precisely mirror those of the $|-\rangle\langle-|$ detection mode. Since $|\Psi\pm\rangle$ detection events contribute equal amounts of information to the measurement, the failure to monitor the $|\Psi+\rangle$ modes may be treated as a 50% loss of signal. It is nonetheless possible in principle to monitor both anticorrelated Bell states simultaneously using a linear optical network [99], although this would require a more complex experimental scheme.

We measure the SQB across the coherence length of the signal in the entangled case. The interferometric visibility of the SQB is simply the proportion of the channel output intensity corresponding to returned signal, s, and hence allows us to determine the Fisher information of the measurement around $\theta \approx \pi/2$. We first measure the fringes without any injected noise, and then repeat with introduced noise and loss in the signal mode.

8.4.3 Experimental design

The experimental set-up is illustrated by the schematic in Fig.8.4. We use a frequency-doubled Ti:Sapph set-up similar to the one described in Chapter 4. In this experiment, however, it is necessary to use an SPDC source that produces entangled photon pairs with spectral intensity correlations, so as not to illuminate the channel with the $|\Psi\pm\rangle$ states, which do not contribute any information to the measurement. We therefore pump a Type-II phase-matched SPDC source

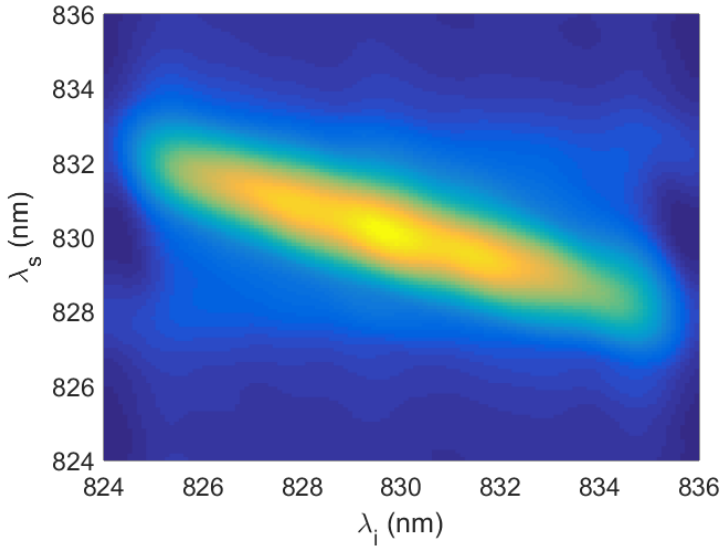


Figure 8.3: Joint spectral intensity of the BiBO downconversion source, showing spectral correlations.

in a second BiBO crystal, generating an orthogonally polarised photon pair with centre wavelengths at 830 nm and exhibiting correlations in frequency. This spectrum was then measured on the TRSPSs described in Chapter 4 (Fig.8.3). Noise is injected by sending attenuated coherent light derived from the laser through a large unknown time delay into the signal mode prior to the downconversion source. Light in the signal mode is delayed using a variable delay line built on a motor-actuated stage (Thorlabs) before being attenuated with a 6 dB absorptive neutral density filter. This was necessary to simulate the loss in the channel, so that the signal arm contained considerably fewer photons than the ancilla such that coincidence events could be reliably attributed to coincidences of an ancilla photon and a noise photon only[5]. The signal and idler modes are then coupled into fibre and interfere in a 50:50 fibre beam splitter. The outputs of this beam splitter are then coupled back into free space where they pass through separate spectral interference filters. One beam passes through an interference filter (Semrock)

[5]This is necessary in order to be consistent with the assumptions of the theoretical model, which does not account for losses in the ancilla arm or the inability to suppress noise-signal coincidences.

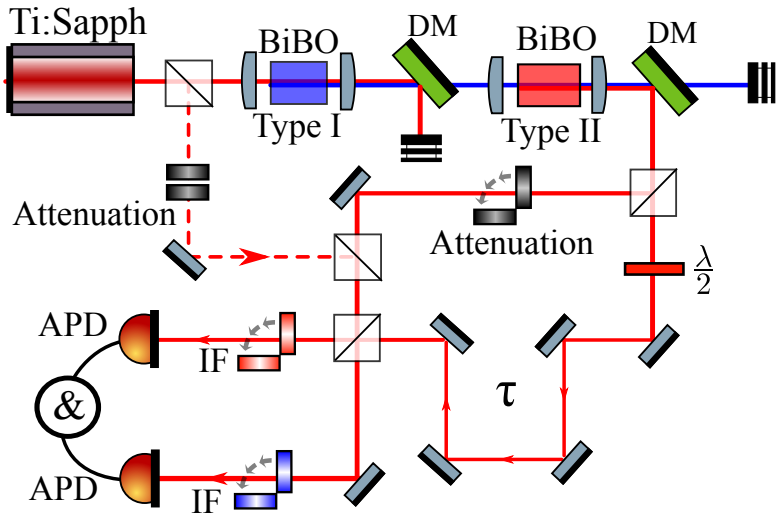


Figure 8.4: Experimental set-up. Frequency-correlated photon pairs are produced by an SPDC source pumped by frequency-doubled pulses from a Ti:Sapph laser. A controllable relative delay was introduced and weak coherent light was added at a low-reflectivity beam splitter as noise to one photon path. The photons were then interfered at a beamsplitter and the outputs spectrally filtered by interference filters (IF) prior to coincident detection by avalanche photodiodes (APD).

with centre wavelength 831.5 nm and FWHM bandwidth 0.5 nm, and the other through a second filter (Andover) with centre wavelength 828.5 nm and FWHM bandwidth of 1 nm. The two modes are again coupled into fibre where they are routed into the slow, high-efficiency SPCMs (PerkinElmer) and monitored in coincidence using a field-programmable gate array (FPGA). The zero-delay position was determined by removing the filters and centering at the minimum of a Hong-Ou-Mandel dip between the two photons, using the same procedure as described in Chapter 5. The filters were then replaced.

8.4.4 Results

In the case without noise and loss, ten 120-step acquisitions were taken across a range of -2 to 2 ps from the zero-delay point, with an acquisition time of 1 s per step. These acquisitions are shown in fig.8.6. These interference patterns exhibited a fringe visibiity of $V = 0.771 \pm$

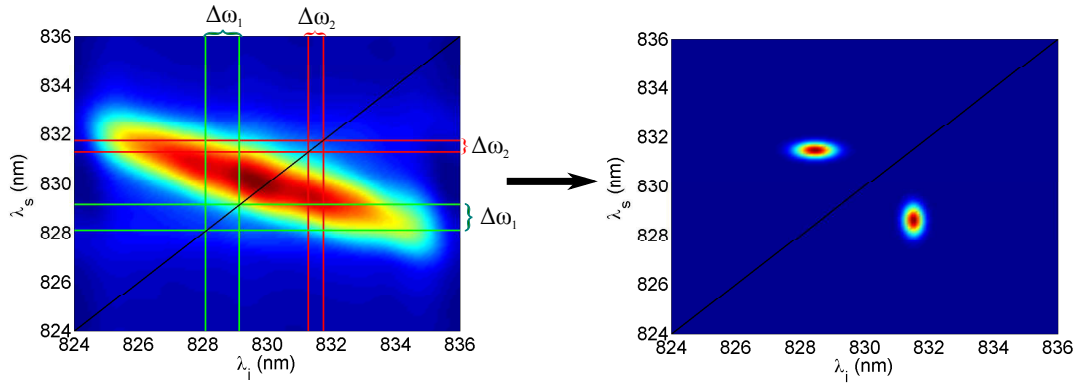


Figure 8.5: Procedure for post-selective preparation of $|\Psi+\rangle$ state. The green lines bound the transmission function of the B filter, whilst the red lines bound the transmission of the R filter. Only photon pairs generated in the off-diagonal bounding boxes register as coincidences, and hence the photon pair is post-selectively prepared in the anticorrelated $|\Psi-\rangle = (|R\rangle\,|B\rangle - |B\rangle\,|R\rangle)/\sqrt{2})$ state (right). Note the absence of amplitude in the correlated $|\Phi\pm\rangle = (|R\rangle\,|R\rangle \pm |B\rangle\,|B\rangle)/\sqrt{2})$ states.

0.011, which is consistent with the characterised mechanisms of contrast reduction, which are described in the Appendices.

The acquisition was repeated with a 6 dB attenuator inserted to the signal arm and classical light injected into the signal mode. In this case the fringes visibility dropped to $V = 0.671 \pm 0.015$. There are three contributions to this reduction in visibility: single photons from the injected noise coinciding with a signal photon (N_{sc}) or with an ancilla photon (N_{ac}), and coincidences originating from two noise photons (N_{cc}). Since the noise photons follow Poisson statistics and are not correlated with the signal or ancilla, the occurrence of these coincidences is equal to the product of the corresponding single-photon rates at the detectors $\{1,2\}$ $N_a^{1,2}$, $N_s^{1,2}$ and $N_c^{1,2}$. Each of these were determined by simply blocking the other two sources of light, and we thus obtained values of $N_{ac} = 1.8 \pm 0.1$ Hz, $N_{sc} = 0.2 \pm 0.01$ Hz and $N_{cc} = 0.43 \pm 0.02$ Hz. Hence, the dominant contribution came from coincidences between noise light and ancilla, and so the system is well-modelled by the analysis described above.

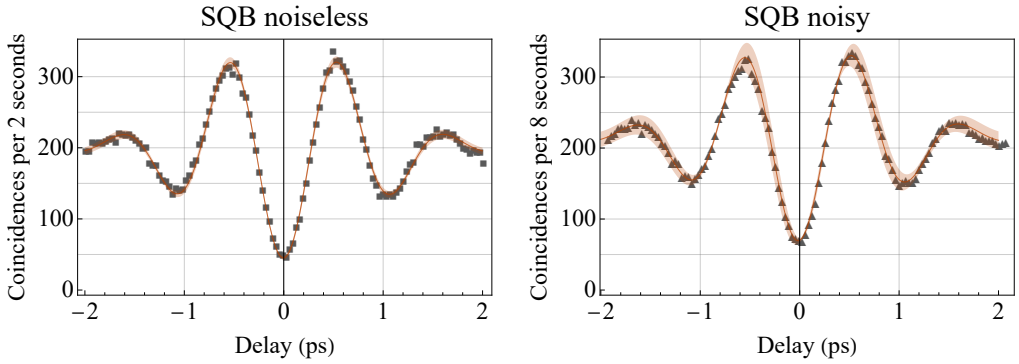


Figure 8.6: Spatial quantum beats in the absence of injected noise (left) and with an attenuated coherent state injected. The tan-coloured shading indicates the $1-\sigma$ error zone of the fitted curve.

8.4.5 Discussion

Let us place these results in context. In the classical comparison, the optimum probe state would be one of the states $|\pm\rangle$. In the absence of noise, measuring with a single detection projector, say $|+\rangle\langle+|$, would reveal interference fringes similar to the ones in Fig. 8.6. However, in the presence of environmental noise in a spectrally mixed state, half the background photons would register as false positives, as opposed to only a quarter in the entangled case. The addition of classical noise would therefore add another constant background of $N_{ac} = 1.8 \pm 0.1$ Hz, further reducing visibility. This case was simulated, with the visibility found to be 0.628 ± 0.016.

Further work could include an explicit demonstration of the separable comparison. This would require a separable photon pair source, such as the KDP source introduced in Chapter 4 and described in [52]. If one photon were prepared by pulse shaping in the state $|-\rangle$, then HOMI followed by coincident detection (*without* spectral filtering, since in the separable case this removes half of the signal) would project the signal photon into the state $|+\rangle$ with 50% efficiency. Such a comparison is illustrated in Fig. 8.7. However, due to experimental difficulties in preparing the separable state and the non-unit transmission efficiency of the filters used in

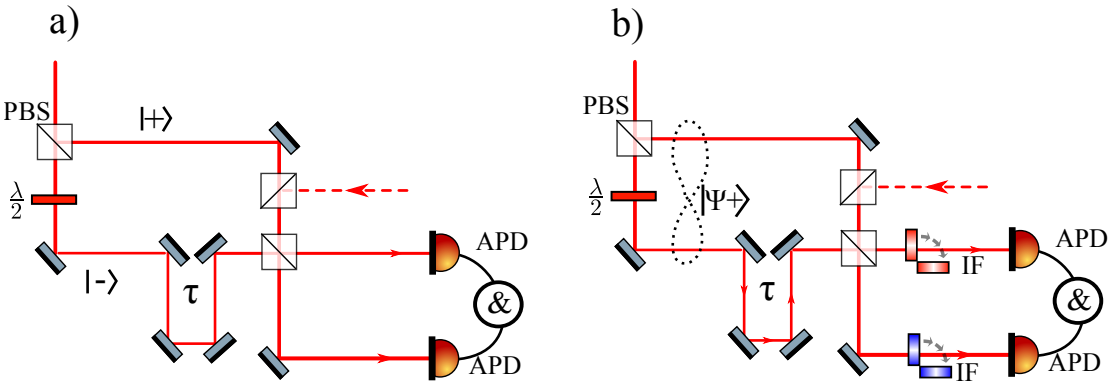


Figure 8.7: Like-for-like comparison of a separable (a) and entangled (b) implementations of spectral phase measurement in the presence of noise. a) Two photons in the states $|+\rangle$ and $|-\rangle$ undergo an unknown relative delay and are interfered in a Hong-Ou-Mandel interferometer in the presence of noise. A coincidence detection event projects the signal photon into the $|-\rangle\langle-|$ detection mode (with 50% probability). b) A photon pair is prepared in the spectral Bell state $|\Psi+\rangle$ and undergoes Hong-Ou-Mandel interference in the presence of noise. Unlike the classical case, spectrally-filtered detection may be employed to reject some of the classical noise, without reducing the signal.

the entangled case, such a like-for-like comparison is not presented here.

8.5 Chapter summary

This chapter shows theoretically how the advantage gained by entanglement-enhanced rejection of extrinsic noise extends to estimating a continuous parameter, deriving a result showing that a significant enhancement is accessible for large amounts of loss and noise. An interesting feature of the quantum-enhanced rejection of environmental noise is that the potential advantage becomes stronger at higher values of loss. This is in stark contrast with protocols designed to gain a quantum advantage in the presence of intrinsic noise, such as shot noise in an interferometer, in which even modest losses can rapidly neutralise quantum enhancements. On account of its intrinsic resistance to adverse environmental conditions, this principle holds the potential for an early real-world application of entanglement-enhanced technology to practical problems

in communications and metrology. Additionally, this advantage scales favourably with mode number, an auspicious observation in the context of the rapid improvements in time-frequency quantum optics such as those described earlier in this thesis.

Chapter 9

Conclusions and outlook

Contents

9.1 Summary 207

9.2 Outlook 209

9.2.1 Improvements 209

9.2.2 Implications 211

9.1 Summary

This thesis frames the important field of ultrafast quantum pulse characterisation in its scientific and technological context, and presents a toolbox of methods for measuring time-frequency states of quantum light with many applications including quantum enhanced precision sensing. Firstly, we demonstrate single-photon spectrometers based on dispersive time-to-frequency mapping. Unlike previous dispersive Fourier transform single-photon spectrometers, these devices use chirped fibre Bragg gratings to apply group delay dispersion, which extends the feasibility of this principle to wavelength regimes far from telecoms where losses in typical fibres would be prohibitive. These devices provided the means of spectrally-resolved detection used

throughout this thesis. We then realised the first of two methods to achieve full phase-sensitive reconstruction of the TF state of a single photon, by spectrally-resolved Hong-Ou-Mandel interference of the single photon pulse with an external reference. This approach has the advantage that it is able to reconstruct spectrally mixed states, but several drawbacks arising from the dependence on an external reference. Notably, the delay relative to the reference must be well characterised, and the region of the spectrum where the test pulse has significant spectral amplitude mus be known *a priori*.

To complement this approach, we develop and demonstrate a self-referenced method inspired by classical optics. This approach uses spectral shearing interferometry, with spectral shear applied deterministically with an electro-optic modulator. We used a pulse shaper to test this device with a wide range of test pulses, and we explain how this device can be generalised to characterise a mixed state.

We suggest that of the two methods for spectral-temporal quantum state characterisation, spectrally-resolved Hong-Ou-Mandel interference is most appropriate for spectrally mixed states with very low $g^{(2)}$ and well-characterised spectral support. On the other hand, the EOSI approach is best suited for quantum states of light described by single unknown spectral-temporal mode with arbitrary photon number occupation, which can subsequently be determined with coherence function measurements.

Building on the single-photon EOSI, we complete our toolbox by fully characterising the spectral-temporal wave function of a spectrally entangled photon pair. This provides a fully self-referencing approach to photon pair characterisation, and is suitable for a wide range of wavelengths, including to spectrally non-degenerate photon pairs. We demonstrate the effectiveness of this technique by performing a full reconstruction of both spectrally separable and spectrally entangled photon pairs, achieving good agreement with theoretical models.

Lastly, we present a new technique for using TF entangled photon pairs to realise quantum-enhanced precision measurement of a time delay in a quantum channel in the presence of en-

vironmental noise. This scheme is based on the entanglement-enhanced rejection of the background light and is well-suited to high-dimensional platforms such as TF states of light. Subject to the constraint of constant illumination of the channel, it can deliver a substantial quantum enhancement over a classical analogue, especially in the presence of large amounts of loss and noise in the channel. A simple experiment demonstrating the feasibility of such a measurement is presented.

9.2 Outlook

9.2.1 Improvements

One technological advance with profound implications for all the work reported here is the rapid progress in detector technology. Even over the course of the period in which these results were gathered, significant strides have been made in this field, such as in the continuing development of fast superconducting nanowire detectors [100]. These detectors combine high quantum efficiency with fast detection times, making them ideal for use in a time-resolved single photon spectrometer architecture such as that used throughout this thesis. This advantage compounds in coincidence and hence measurements based on intensity correlations such as those reported in Chapters 5 and 7 would experience pronounced improvements by incorporating this technology.

There are also a number of specific improvements that can be made to the individual experimental techniques reported here. Continuing progress in CFBG fabrication [101], combined with significant advances in detector technology, imply that in the future the time-resolved single-photon spectrometers can be brought to approach the Fourier transform limit on their resolution (which, for a periodic pulse train, suffices to fully characterise the spectral intensity). Additionally, these devices may become efficient enough that spectrally-resolved Hong-Ou-Mandel interference with an uncorrelated external reference becomes practical for the full

spectral-temporal characterisation of quantum light, include incoherent mixtures. The problem of background coincidences could be further suppressed by using a reference with sub-Poissonian photon number statistics.

The electro-optic spectral shearing interferometer demonstrated in this thesis already approaches characterisation speeds sufficient for real-time source feedback, with an interferogram of sufficient quality for phase extraction requiring only a few second of acquisition when using a photon source of typical brightness. This will only be improved further when combined with advances in detector technology. The obvious next step in developing this technique is to perform mixed-state characterisation by repeating the measurement across a range of spectral shears. Additionally, it has been suggested that the finite temporal aperture of the device, which is one of the main limitations on the range of pulses the device is able to characterise, can be extended arbitrarily by employing more complex RF waveforms for the driving signal of the EOM. In particular, a serrodyne or sawtooth waveform [81] would allow the near-continuous application of linear temporal phase, which would significantly ease restrictions on the maximum pulse duration or global delay that could be characterised by this device.

These improvements would carry forward into the two-photon wave function measurement. Partial characterisation of the density matrix for impure biphotons could be performed by scanning the shear. Additionally, the implementation of two EOSI devices operating in coincidence would allow for direct phase-sensitive reconstruction of a pure two-photon wave function without the need to reconfigure mid-measurement, whilst also opening the door to full characterisation of the density matrix of spectrally mixed biphotons. Going further, one could also imagine the EOSI being employed in conjunction with measurements on the spatial or polarisation state of a second subsystem to characterise hybrid-domain entanglement, or even an array of them being used to characterise multipartite entangled systems.

The theory underlying entanglement-enhanced rejection of environmental noise could be significantly improved by using a more generalised model for the incoherent processes afflicting

probe states. Such a general model is provided by Kraus' theorem [102], which states that any positive map $\Phi(\rho)$ of a quantum state can be expressed in terms of a set of matrices $\{B_k\}$ such that

$$\Phi(\rho) = \sum_k B_k \rho B_k^*, \tag{9.1}$$

where $\sum_k B_k B_k^* = 0$. Reframing the analysis in Chapter 8 to this representation would be highly insightful for generalising this advantage to multiphoton systems. Experimentally, the main obstacle is the need to perform a projective measurement on an entangled state at the output. It is not straightforward to see how to overcome this for implementations of dimensionality $d > 2$ until the development of efficient two-photon gates.

9.2.2 Implications

Full quantum state tomography has very general applications across all stages of quantum technology design. The development of the sources of nonclassical light, the processes used to manipulate them, and the final quantum information readout stage all require techniques to reconstruct the modes with which they interact.

One application for which this work is particularly well-suited is tuning optical sources with active feedback. The EOSI devices, in particular, are able to perform a full reconstruction on a timescale of minutes, which could be further improved with existing detector technology. This capability raises the prospect of being able to actively tune a source (for example, by controlling the pump properties, temperature, orientation etc.) and observe in near-real-time the effects of these adjustments. Active feedback could also be employed in mode-matching applications, where separate stages of a quantum network must be efficiently interfaced with one another.

Full state characterisation also plays a role in quantum process tomography, which is concerned with characterising an unknown quantum dynamical process. This consists of preparing an ensemble of quantum systems in a known state, allowing them to evolve under the unknown

process, and then performing a full state characterisation at the output. Characterisation techniques such as those developed here will therefore play a vital role in understanding and optimising the behaviour of future technologies, such as quantum memories, repeaters and gates. Similarly, understanding the response of detectors, the final crucial component in any quantum application, requires adequate characterisation of the spectral-temporal field modes with which they interact.

Spectral intensity measurements of quantum light, such as those described in Chapter 4, can also play a direct role in quantum technologies. Quantum key distribution is a protocol that allows two parties to exchange information with perfect security given their ability to communicate through a quantum channel and a verified, public, classical channel[103]. High-dimensionality quantum systems such as pulsed modes of light allow large amounts of information encoding per photon, enabling higher bit rates and greater security. However, a realisation of this requires high-dimensional spectrally-resolved measurement. A further requirement of quantum key distribution is the ability to encode and measure in at least two mutually-unbiased bases. The time-of-flight spectrometer architecture also permits this: by using a CFBG with negative rather than positive dispersion, the detector projects onto a basis of negatively-chirped pulses that is mutually unbiased with respect to the positively-chirped pulses[104].

Lastly, we note the profound implications of this work for precision measurement. Entangled quantum systems can be used as a resource for improving measurement precision, and as we have seen this is true in the presence of background noise. A surprising feature of this enhancement is that, in common with the related quantum illumination scheme but unlike many other quantum-enhanced measurement protocols, the advantage becomes more ever pronounced the worse the loss and noise becomes. It is therefore relevant to a broad and realistic class of measurement problems.

Appendix A

Path Integral formulation

Path integral

A very general principle in classical physics is that the equations of motion may be reformulated in terms of a “principle of least action", also known as Hamilton’s principle. This consists of finding a quantity S, known as the action, which depends variationally on the overall dynamics of the system and which is minimised over the dynamical path (variation of q and p with t) which obeys the classical equations of motion. In the case of the single electromagnetic field mode given above, the action is given by

$$S = \int \frac{1}{2}(p^2 - \omega^2 q^2) dV dt, \tag{A.1}$$

and it is possible to show that the trajectory that minimises this quantity is exactly the path the satisfies the Maxwell equations. In classical electromagnetism, this is the path which the system is dictated to follow, and at any given time the quantities q and p, and hence E and B, have specific and well-defined values. In other words, after some time t, the system will transition to the state that follows the path of least action with a probability of one.

The path integral formulation of quantum mechanics generalises this principle by asserting that the system does not follow a single path, but rather all possible paths. The system does not end its evolution in a single state with unit probability, but in all possible states, each with probabilities containing contributions from *all* the paths that lead there, *weighted by a phase term determined by the action of that path.* The resultant transition probability from an initial state q_i to some state q_f after time T is then simply

$$\langle q_f, T \,|\, q_i, 0 \rangle = \int_{q(0)=q_i}^{q(T)=q_f} e^{iS[q(t)]/\hbar} Dq(t), \tag{A.2}$$

where the integration is understood to be over an infinite number of variables $q(t)$ and $\hbar$ is Planck's constant.

In this formulation it is clear how classical physics is recovered from the quantum theory. Around the classical trajectory the action is stationary and so has little variational dependence on the path $q(t)$. These paths therefore all have similar phase, and hence contribute constructively to the overall transition probability. Around paths where the action is much greater than that of the classical path, however, variational dependence on $q(t)$ is much greater and so small deviations can vary the action by $\hbar$ or more. These terms are therefore rapidly oscillatory and destructively interfere. Hence, after some time t, the system is most likely to be observed having followed something close to the path of stationary action. In the limit where the observer is concerned with only large changes in action $\delta S >> \hbar$ this recovers Hamilton's principle, and with it classical electromagnetism, in accordance with the correspondence principle.

Whilst an analytic solution for Eq.A.2 does exist for the harmonic oscillator (systems with action of the form given in Eq.A.1), such calculations are usually lengthy. It is simpler to note that in the quantum generalisation, the canonical variables q and p do not have a specific value at any given time, and so it is no longer appropriate to denote them as normal scalars.

Appendix B

Loss of visibility analysis

This appendix discusses the various contributions to loss of visibility in the spatial quantum beats observed in Chapter 8. We identified three main contributions: two-photon-pair events, spectral imbalance in the filtered state, and asymmetry in the fibre beam splitter.

Two-pair event contribution to loss of visibility

The largest contribution to the loss of visibility arises from the instances when the downconversion source emits two photon pairs instead of one. Such events send four photons into the experiment, any two of which can contribute to a coincidence event at the output. There are therefore a very large number of terms in this expansion and the full calculation is too extensive to include here. However, we can simplify the calculation by making some approximations.

The output state at the downconversion source is given by

$$|\Psi\rangle \approx \exp\left(\int f(\omega_1,\omega_2)a_1^\dagger b_2^\dagger d^2\omega\right)|0\rangle\,. \tag{B.1}$$

Firstly, we must determine the amplitude of the quantity $f(\omega_1,\omega_2)$, which here is not normalised. An estimate can be obtained by considering the ratio of coincidences to single counts

at the output of the downconversion source. This method assumes that the spatial modes monitored by the detection apparatus are Schmidt modes of the downconversion source (otherwise there is a thermal contribution from unpartnered photons) and so only provides an upper bound on the downconversion probability. The probability of obtaining a coincidence, P_c, is given by $\int |t_a t_b f(\omega_1, \omega_2)|^2 d^2\omega$ and for a single count in mode i, $P_i = \int |t_i f(\omega_1, \omega_2)|^2 d^2\omega$, where t_i is the total transmission amplitude for the mode i (accounting for all sources of loss, including non-unit quantum efficiency of the detectors). The normalisation is then given by

$$\int |f(\omega_1, \omega_2)|^2 \mathrm{d}^2\omega = \frac{P_a P_b}{P_c}. \tag{B.2}$$

Using count rates of N_S = 1 MHz, N_I = 0.6 MHz and N_C = 0.125 MHz, and a repetition rate of 80 MHz, we obtained an estimate of $\int |f(\omega_1, \omega_2)|^2 d^2\omega \leq 0.06$.

We then consider the state $|\Psi\rangle$. Coincidences deriving from two-pair events will be represented in the expansion of this expression by terms in both of the detection modes c and d, at wavelengths transmitted by the filter. We proceed by modelling losses prior to the beam splitter in the usual fashion as beam splitter transformations,

$$\begin{aligned} a^\dagger &\rightarrow t_a a'^\dagger + r_a x^\dagger \\ b^\dagger &\rightarrow t_b b'^\dagger + r_b y^\dagger \end{aligned} \tag{B.3}$$

where $x^\dagger$ and $y^\dagger$ are unmonitored loss modes.

In our experiment, the losses in the signal mode are considerably greater than those in the idler mode and so form the largest contribution. For the sake of simplicity we will therefore neglect terms in t_a and assume that $r_a \approx 1$. This is equivalent to asserting that the dominant contribution to the false coincidences deriving from two-pair events will come from instances where the two photons in the ancilla arm survive to the detectors. We can thus represent the

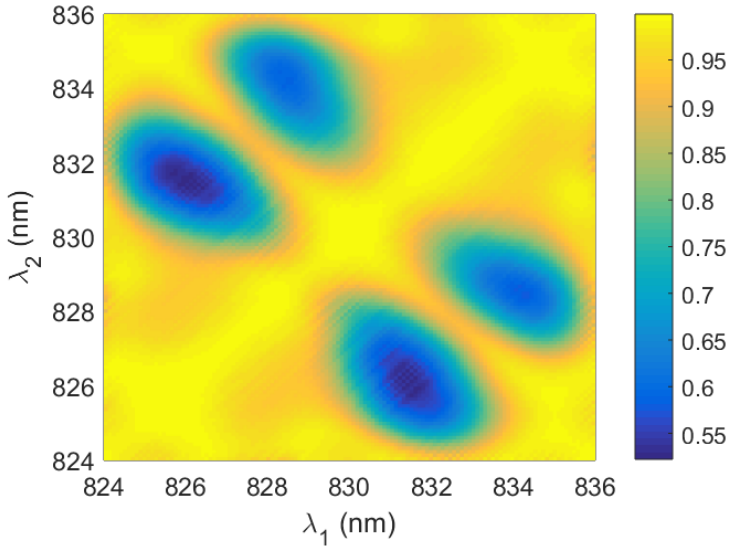


Figure B.1: Visibility of SQB as a function of filter centre wavelengths λ_1 and λ_2, with losses due to spectral imbalances in the transmitted state.

state as

$$|\Psi\rangle = \exp\left(\int f(\omega_1,\omega_2)x_1^\dagger(r_b y_2^\dagger + t_b b_2'^\dagger)\mathrm{d}^2\omega\right)|0\rangle \tag{B.4}$$

We then expand this to obtain the term that is quadratic in both $f(\omega_1,\omega_2)$ and $b'^\dagger$:

$$\int t_b^2 f(\omega_1,\omega_2)f(\omega_1',\omega_2')x_1^\dagger b_2'^\dagger x_{1'}^\dagger b_{2'}'^\dagger \mathrm{d}^4\omega\,|0\rangle \tag{B.5}$$

We then apply the beamsplitter transformation on the state, $b'^\dagger \rightarrow \frac{c^\dagger - d^\dagger}{\sqrt{2}}$ and collect terms in $c^\dagger d^\dagger$ to obtain the component $|\Psi'\rangle$ of the wave function that will contribute to the coincidence terms,

$$\begin{aligned}|\Psi'\rangle &= \int t_b^2 f(\omega_1,\omega_2)f(\omega_1',\omega_2')x_1^\dagger x_{1'}^\dagger c_2^\dagger d_{2'}^\dagger \mathrm{d}^4\omega\,|0\rangle \\ &\equiv \int t_b^2 f(\omega_1,\omega_2)f(\omega_1',\omega_2')x_1^\dagger x_{1'}^\dagger\,|\omega_2,\omega_{2'}\rangle\,\mathrm{d}^4\omega\end{aligned} \tag{B.6}$$

Finally, the probability of obtaining a coincidence due to this term is given by

$$P = \mathrm{Tr}_X \int \eta_c(\omega_c)\eta_d(\omega_d) \left\langle \Psi' \,\middle|\, \omega_c, \omega_d \right\rangle \left\langle \omega_c, \omega_d \,\middle|\, \Psi' \right\rangle \mathrm{d}^2\omega \tag{B.7}$$

where the trace is over the modes x and the filter intensity transmission functions are denoted by η. By substitution we can see that

$$P = |t_b|^4 \int \eta_c(\omega_c)\eta_d(\omega_d)|f(\omega_1, \omega_c)|^2|f(\omega_1', \omega_d)|^2\mathrm{d}^4\omega \tag{B.8}$$

Using the derived values of $|t_b|^2 = 0.25$, $f(\omega_1, \omega_2)$, and the measured values of the filter transmission, and accounting for sources of loss in the detection modes c and d themselves, we obtain a baseline contribution of approximately 20 Hz, or approximately a 10% reduction in visibility. We note that this term is independent of delay since both of the contributing photons come from the same input mode of the beam splitter, so there is no interference at play. This analysis is necessarily an approximatation: on the one hand, it neglects the effect of photons transmitted through the signal arm, but on the other hand uses an upper bound for the squeezing parameter by assuming the monitored modes are Schmidt modes of the downconversion source.

Spectrally imbalanced state

In order to achieve SQB, it is necessary to ensure that the two components of the entangled states, $|R\rangle_S |B\rangle_A$ and $|B\rangle_S |R\rangle_A$ have coefficients of approximately equal magnitude. The downconversion source was characterised by a joint-spectral measurement (fig.8.3) using time-of-flight spectrometers [OE], and this measurement was used to ensure the optimal placement of the filters. To verify this, we initially injected the signal and idler modes directly into the filtered paths R and B respectively (bypassing the beam splitter) and noted the coincidences. This measures the occupation of the mode $|R\rangle_S |B\rangle_A$. This was then repeated in the other

configuration and the filter positions were fine-tuned until equal numbers of coincidences were observed. We estimate the true coincidence rates were matched to within approximately 5%, with the residual error due to difficulties in measuring the precise count rates and configuration-dependent loss such as differences in compatibility between the fibres. In addition to this, some further loss of visibility is associated with asymmetry in the distribution of amplitude within the finite bandwidth of these two parts of the joint spectrum. A simulation of the dependence of the fringe visibility on filter placement based on the measured JSI and filter transmission functions is shown in fig.B.1. At our filter positions, we estimated this effect accounts for approximately another 5% reduction of fringe contrast.

Beam splitter asymmetry

A further contribution to the loss of visibility is asymmetry in the beam splitter. At the zero delay point, the state arriving at the beam splitter is given by equation 8.32. Applying the beam splitter transformation on this state (allowing for unequal amplitude reflectivity r and transmissivity t, where $|r|^2 + |t|^2 = 1$) gives the term that leads to coincidences is $\frac{(r^2-t^2)}{\sqrt{2}} c_R^\dagger d_B^\dagger$. The coefficient of this term at the fringe maximum is $1/\sqrt{2}$ and is not affected by the asymmetry. The effect of beam splitter asymmetry is therefore to raise the minimum of the fringes by an amount $|r^2 - t^2|^2 I_{\text{max}}$, where I_{max} is the maximum intensity, which gives a loss of visibility of approximately $2|r^2 - t^2|^2$. The beam splitter was measured to have an intensity splitting of $|r|^2 = 0.55 \pm 0.01$, $|t|^2 = 0.45 \pm 0.01$, and so the loss of visibility associated with beam splitter asymmetry is therefore approximately $2 \times 0.1^2 = 0.02$.

Multiphoton probes

This analysis is restricted to the case where terms with more than one photon at the output of the channel make a negligible contribution to the Fisher information. Here we briefly discuss

the effect of considering higher photon number terms.

In general, considering more photon number states increases the effective dimensionality of the probe. In the original QI, it was shown [105] that the use of weak coherent light for the probe state achieves better error-probability than illumination with a single photon, subject to the condition of the same average number of photons being sent into the signal channel. This can be explained by considering that the coherent state spans a wider Hilbert space that includes multi-photon terms, allowing a precise phase to be defined. This phase is then used as an additonal discriminator between true reflected signal and background light, which has a random phase. The full treatment for the QI problem using Gaussian states was provided Tan et al. [93], showing a factor of 4 improvement in the error-probability exponent over a classical protocol. Subsequent work (e.g. [106]) shows that this factor can be greatly improved using more exotic, non-Gaussian photon-number entangled states such as photon-subtracted two-mode squeezed states. The simplified noise model given in Eq.8.2, where the signal state is entirely lost and substituted for by a background term, is not physically realistic for probe states with more than one photon where loss does not completely erase the information in the signal. A more realistic description of loss in this case is exemplified in, for example, [107]. Nonetheless, since the physical origin of the quantum enhancement in the lossy/noisy parameter estimation problem is the same as the QI hypothesis testing problem, it stands to reason that an appreciable quantum enhancement is still accessible in the multi-photon regime.

Bibliography

[1] A. Einstein, B. Podolsky, and N. Rosen. Can quantum-mechanical description of physical reality be considered complete? *Phys. Rev.*, 47:777–780, May 1935. 5

[2] LIGO collaboration. Enhanced sensitivity of the LIGO gravitational wave detector by using squeezed states of light. *Nature Photon.*, 7:613–619, 2013. 7, 9, 14, 186

[3] P. A. Franken, A. E. Hill, C. W. Peters, and G. Weinreich. Generation of optical harmonics. *Phys. Rev. Lett.*, 7:118–119, Aug 1961. 8

[4] David C. Burnham and Donald L. Weinberg. Observation of simultaneity in parametric production of optical photon pairs. *Phys. Rev. Lett.*, 25:84–87, Jul 1970. 8

[5] Paul G. Kwiat, Klaus Mattle, Harald Weinfurter, Anton Zeilinger, Alexander V. Sergienko, and Yanhua Shih. New high-intensity source of polarization-entangled photon pairs. *Phys. Rev. Lett.*, 75:4337–4341, Dec 1995. 8, 16

[6] Hiroki Takesue and Kyo Inoue. Generation of polarization-entangled photon pairs and violation of bell's inequality using spontaneous four-wave mixing in a fiber loop. *Phys. Rev. A*, 70:031802, Sep 2004. 8, 16

[7] Robert H Hadfield. Single-photon detectors for optical quantum information applications. *Nature photonics*, 3(12):696, 2009. 8, 17

[8] Matthew D Eisaman, JMAPS Fan, Alan Migdall, and Sergey V Polyakov. Invited review article: Single-photon sources and detectors. *Review of scientific instruments*, 82(7):071101, 2011. 8, 17

[9] Rafał Demkowicz-Dobrzański, Jan Kołodyński, and Mădălin Gută. The elusive Heisenberg limit in quantum-enhanced metrology. 14

[10] Brahim Lamine, Claude Fabre, and Nicolas Treps. Quantum improvement of time transfer between remote clocks. *Phys. Rev. Lett.*, 101:123601, 2008. 14

[11] Peter C Humphreys, W Steven Kolthammer, Joshua Nunn, Marco Barbieri, Animesh Datta, and Ian A Walmsley. Continuous-variable quantum computing in optical time-frequency modes using quantum memories. *Phys. Rev. Lett.*, 113:130502, 2014. 14

[12] B Brecht, Dileep V Reddy, Ch Silberhorn, and MG Raymer. Photon temporal modes: a complete framework for quantum information science. *Physical Review X*, 5(4):041017, 2015. 14, 15

[13] Pieter Kok, William J Munro, Kae Nemoto, Timothy C Ralph, Jonathan P Dowling, and Gerard J Milburn. Linear optical quantum computing with photonic qubits. *Reviews of Modern Physics*, 79(1):135, 2007. 14

[14] Justin B Spring, Benjamin J Metcalf, Peter C Humphreys, W Steven Kolthammer, Xian-Min Jin, Marco Barbieri, Animesh Datta, Nicholas Thomas-Peter, Nathan K Langford, Dmytro Kundys, et al. Boson sampling on a photonic chip. *Science*, page 1231692, 2012. 14

[15] YM Hao, GW Lin, Keyu Xia, XM Lin, YP Niu, and SQ Gong. Quantum controlled-phase-flip gate between a flying optical photon and a rydberg atomic ensemble. *Scientific reports*, 5:10005, 2015. 14

[16] Tian Zhong, Hongchao Zhou, Robert D Horansky, Catherine Lee, Varun B Verma, Adriana E Lita, Alessandro Restelli, Joshua C Bienfang, Richard P Mirin, Thomas Gerrits, S. W. Nam, Francesco Marsili, Matthew Shaw, Zheshen Zhang, Ligong Wang, Dirk Englund, Gregory Wornell, J. H. Shapiro, and Franco N. C. Wong. Photon-efficient quantum key distribution using time–energy entanglement with high-dimensional encoding. *New J. Phys.*, 17:022002, 2015. 14

[17] J. Nunn, L. J. Wright, C. Söller, L. Zhang, I. A. Walmsley, and B. J. Smith. Large-alphabet time-frequency entangled quantum key distribution by means of time-to-frequency conversion. *Opt. Express*, 21(13):15959–15973, Jul 2013. 14, 162

[18] Charles H Bennett, Peter W Shor, John A Smolin, and Ashish V Thapliyal. Entanglement-Assisted Capacity of a Quantum Channel and the Reverse Shannon Theorem. 2002. 14

[19] David E Spence, P Np Kean, and Wilson Sibbett. 60-fsec pulse generation from a self-mode-locked ti: sapphire laser. *Optics letters*, 16(1):42–44, 1991. 15

[20] Andrew M Weiner. Femtosecond pulse shaping using spatial light modulators. *Review of scientific instruments*, 71(5):1929–1960, 2000. 15, 108

[21] M. Hentschel, R. Kienberger, Ch Spielmann, G. A. Reider, and et al. Attosecond metrology. *Nature*, 414(6863):509–13, Nov 29 2001. Copyright - Copyright Macmillan Journals Ltd. Nov 29, 2001; Last updated - 2013-01-28; CODEN - NATUAS. 15

[22] Steven T Cundiff and Shaul Mukamel. Optical multidimensional coherent spectroscopy. *Phys. Today*, 66(7):44, 2013. 15

[23] Andrew M. Weiner. Ultrafast optical pulse shaping: A tutorial review. *Optics Communications*, 284(15):3669–3692, jul 2011. 15, 110

[24] Jonathan Roslund, Renné Medeiros De Araujo, Shifeng Jiang, Claude Fabre, and Nicolas Treps. Wavelength-multiplexed quantum networks with ultrafast frequency combs. *Nature Photonics*, 8(2):109, 2014. 15

[25] Vittorio Giovannetti, Seth Lloyd, and Lorenzo Maccone. Advances in quantum metrology. *Nature photonics*, 5(4):222, 2011. 15, 186

[26] Alexander R Dixon, ZL Yuan, JF Dynes, AW Sharpe, and AJ Shields. Continuous operation of high bit rate quantum key distribution. *Applied Physics Letters*, 96(16):161102, 2010. 15

[27] H Jeff Kimble. The quantum internet. *Nature*, 453(7198):1023, 2008. 17

[28] S. R. Huisman, Nitin Jain, S. A. Babichev, Frank Vewinger, A. N. Zhang, S. H. Youn, and A. I. Lvovsky. Instant single-photon fock state tomography. *Opt. Lett.*, 34(18):2739–2741, Sep 2009. 17

[29] Kevin Zielnicki et al. Joint spectral characterization of photon-pair sources. *Journal of Modern Optics*, 0(0):1–20, 2018. 20, 31, 80

[30] Yoon-Ho Kim and Warren P. Grice. Measurement of the spectral properties of the two-photon state generated via type ii spontaneous parametric downconversion. *Opt. Lett.*, 30(8):908–910, Apr 2005. 20, 31, 88

[31] Wojciech Wasilewski, Piotr Wasylczyk, Piotr Kolenderski, Konrad Banaszek, and Czesław Radzewicz. Joint spectrum of photon pairs measured by coincidence fourier spectroscopy. *Opt. Lett.*, 31(8):1130–1132, 2006. 20, 31

[32] F Zappa, S Tisa, A Tosi, and S Cova. Principles and features of single-photon avalanche diode arrays. *Sensor. Actuat. A: Phys.*, 140:103–112, 2007. 21, 88

[33] Y. C. Tong, L. Y. Chan, and H. K. Tsang. Fibre dispersion or pulse spectrum measurement using a sampling oscilloscope. *Electron. Lett.*, 33:983–985, 1997. 21, 84, 88

[34] Keisuke Goda and Bahram Jalali. Dispersive Fourier transformation for fast continuous single-shot measurements. *Nature Photon.*, 7:102–112, 2013. 21, 84, 88

[35] Malte Avenhaus, A. Eckstein, P. J. Mosley, and C. Silberhorn. Fiber-assisted single-photon spectrograph. *Opt. Lett.*, 34(18):2873–2875, Sep 2009. 21, 88

[36] P. S. Kuo, T. Gerrits, V. B. Verma, and S. W. Nam. Spectral correlation and interference in non-degenerate photon pairs at telecom wavelengths. *Opt. Lett.*, 41, 2016. 21, 85, 88

[37] E. Poem, T. Hiemstra, A. Eckstein, X.-M. Jin, and I. A. Walmsley. Free-space spectro-temporal and spatio-temporal conversion for pulsed light. *Opt. Lett.*, 41(18):4328–4331, 2016. 21

[38] Kent D Irwin and Gene C Hilton. Transition-edge sensors. In *Cryogenic particle detection*, pages 63–150. Springer, 2005. 22

[39] Markus Allgaier, Vahid Ansari, Christof Eigner, Viktor Quiring, Raimund Ricken, John Matthew Donohue, Thomas Czerniuk, Marc Aßmann, Manfred Bayer, Benjamin Brecht, et al. Streak camera imaging of single photons at telecom wavelength. *Applied Physics Letters*, 112(3):031110, 2018. 23

[40] Rick Trebino, Kenneth W DeLong, David N Fittinghoff, John N Sweetser, Marco A Krumbügel, Bruce A Richman, and Daniel J Kane. Measuring ultrashort laser pulses in the time-frequency domain using frequency-resolved optical gating. *Review of Scientific Instruments*, 68(9):3277–3295, 1997. 25

[41] Andreas Eckstein, Benjamin Brecht, and Christine Silberhorn. A quantum pulse gate based on spectrally engineered sum frequency generation. *Opt. Express*, 19(15):13770–13778, Jul 2011. 26

[42] Jean-Philippe W. MacLean, John M. Donohue, and Kevin J. Resch. Direct characterization of ultrafast energy-time entangled photon pairs. *Phys. Rev. Lett.*, 120:053601, Jan 2018. 26, 32

[43] Eleftherios Goulielmakis, Matthias Uiberacker, Reinhard Kienberger, Andrius Baltuska, Vladislav Yakovlev, Armin Scrinzi, Th Westerwalbesloh, U Kleineberg, Ulrich Heinzmann, Markus Drescher, et al. Direct measurement of light waves. *Science*, 305(5688):1267–1269, 2004. 26

[44] Wojciech Wasilewski, Piotr Kolenderski, and Robert Frankowski. Spectral density matrix of a single photon measured. *Physical review letters*, 99(12):123601, 2007. 26, 103, 111

[45] Constantina Polycarpou, KN Cassemiro, G Venturi, A Zavatta, and M Bellini. Adaptive detection of arbitrarily shaped ultrashort quantum light states. *Physical review letters*, 109(5):053602, 2012. 27

[46] Zhongzhong Qin, Adarsh S Prasad, Travis Brannan, Andrew MacRae, A Lezama, and AI Lvovsky. Complete temporal characterization of a single photon. *Light: Science & Applications*, 4(6):e298, 2015. 27

[47] I.A. Walmsley and C. Dorrer. Characterization of ultrashort electromagnetic pulses. *Advances in Optics and Photonics*, 1:308–437, 2009. 28, 123, 129, 172

[48] Christophe Dorrer and Ian A Walmsley. Accuracy criterion for ultrashort pulse characterization techniques: application to spectral phase interferometry for direct electric field reconstruction. *JOSA B*, 19(5):1019–1029, 2002. 28, 123, 129

[49] Christophe Dorrer and Inuk Kang. Highly sensitive direct characterization of femtosecond pulses by electro-optic spectral shearing interferometry. *Optics letters*, 28(6):477–479, 2003. 29, 122

[50] Bin Fang, Offir Cohen, Marco Liscidini, John E. Sipe, and Virginia O. Lorenz. Fast and highly resolved capture of the joint spectral density of photon pairs. *Optica*, 1(5):281–284, Nov 2014. 31

[51] Iman Jizan, Bryn Bell, L. G. Helt, Alvaro Casas Bedoya, Chunle Xiong, and Benjamin J. Eggleton. Phase-sensitive tomography of the joint spectral amplitude of photon pair sources. *Opt. Lett.*, 41(20):4803–4806, Oct 2016. 31

[52] Peter J. Mosley, Jeff S. Lundeen, Brian J. Smith, Piotr Wasylczyk, Alfred B. U'Ren, Christine Silberhorn, and Ian A. Walmsley. Heralded generation of ultrafast single photons in pure quantum states. *Phys. Rev. Lett.*, 100:133601, Apr 2008. 31, 87, 169, 204

[53] W. Tittel, J. Brendel, B. Gisin, T. Herzog, H. Zbinden, and N. Gisin. Experimental demonstration of quantum correlations over more than 10 km. *Phys. Rev. A*, 57:3229–3232, May 1998. 32, 162

[54] Peng Chen, Chi Shu, Xianxin Guo, M. M. T. Loy, and Shengwang Du. Measuring the biphoton temporal wave function with polarization-dependent and time-resolved two-photon interference. *Phys. Rev. Lett.*, 114:010401, Jan 2015. 32, 163

[55] A. I. Lvovsky and M. G. Raymer. Continuous-variable optical quantum-state tomography. *Rev. Mod. Phys.*, 81:299–332, Mar 2009. 32

[56] *Introduction to Optics*. Pearson Education, 2008. 39

[57] R Simon, ECG Sudarshan, and N Mukunda. Gaussian pure states in quantum mechanics and the symplectic group. *Physical Review A*, 37(8):3028, 1988. 53

[58] J. Paye. The Chronocyclic Representation of Ultrashort Light Pulses. *IEEE Journal of Quantum Electronics*, 28(10):2262–2273, 1992. 53, 148

[59] Christopher Gerry and Peter Knight. *Introductory Quantum Optics*. Cambridge University Press, 2004. 58

[60] L. Mandel. Configuration-space photon number operators in quantum optics. *Phys. Rev.*, 144:1071–1077, Apr 1966. 66

[61] Artur Ekert and Peter L. Knight. Entangled quantum systems and the schmidt decomposition. *American Journal of Physics*, 63(5):415–423, 1995. 70

[62] Roy J Glauber. The quantum theory of optical coherence. *Physical Review*, 130(6):2529, 1963. 80

[63] José Azaña and Miguel A Muriel. Real-time optical spectrum analysis based on the time-space duality in chirped fiber gratings. *IEEE J. Quant. Electron.*, 36:517–526, 2000. 84, 88

[64] Vıctor Torres-Company, Jesús Lancis, and Pedro Andrés. Space–time analogies in optics. *Prog. Opt.*, 56:1, 2011. 84

[65] P Moseley et al. *New J. Phys.*, 10:093011, 2008. 87

[66] Rodney Loudon. *The Quantum Theory of Light*. Oxford University Press, 2000. 87, 151, 153

[67] Mark Beck. Comparing measurements of g (2)(0) performed with different coincidence detection techniques. *JOSA B*, 24(12):2972–2978, 2007. 87

[68] M. A. Muriel, J. Azaña, and A. Carballar. Real-time Fourier transformer based on fiber gratings. *Opt. Lett.*, 24:1–3, 1999. 88

[69] A.O.C. Davis, P. Saulnier, M. Karpiński, and B.J. Smith. Pulsed single-photon spectrometer by frequency-to-time mapping using chirped fiber bragg gratings. *Optics Express*, 25:12804, 2017. 88, 158, 167

[70] C. K. Hong, Z. Y. Ou, and L. Mandel. Measurement of subpicosecond time intervals between two photons by interference. *Phys. Rev. Lett.*, 59:2044–2046, Nov 1987. 102

[71] Victor Wong and Ian A. Walmsley. Analysis of ultrashort pulse-shape measurement using linear interferometers. *Opt. Lett.*, 19(4):287–289, Feb 1994. 109

[72] C. Dorrer, E.M. Kosik, and I.A. Walmsley. *Optics Letters*, 27:548–550, 2002. 123

[73] C. Dorrer, E.M. Kosik, and I.A. Walmsley. *Applied Physics B.*, 74:s209–s217, 2014. 123

[74] C. Dorrer and J. Bromage. *Optics Letters*, 35, 2010. 129, 133

[75] Laura J Wright, Michał Karpiński, Christoph Söller, and Brian J Smith. Spectral shearing of quantum light pulses by electro-optic phase modulation. *Physical review letters*, 118(2):023601, 2017. 130, 131, 133

[76] Michał Karpiński, Michał Jachura, Laura J Wright, and Brian J Smith. Bandwidth manipulation of quantum light by an electro-optic time lens. *Nature Photonics*, 11(1):53, 2017. 131

[77] C. Dorrer. *Optics Express*, 16:6567–6578, 2008. 132

[78] James W Brault. Fourier transform spectroscopy. In *High Resolution in Astronomy, Fifteenth Advanced Course of the Swiss Society of Astronomy and Astrophysics. Edited by AO Benz, M. Huber, and M. Mayer. Sauverny, Switzerland: Geneva Observatory, 1985, p. 3-61*, pages 3–61, 1985. 139

[79] Charles Bourassin-Bouchet and M-E Couprie. Partially coherent ultrafast spectrography. *Nature communications*, 6:6465, 2015. 153

[80] J. D. McKinney, D. E. Leaird, and A. M. Weiner. Millimeter-wave arbitrary waveform generation with a direct space-to-time pulse shaper. *Optics letters*, 27(15):1345–1347, 2002. 158

[81] Leonard M Johnson and Ch H Cox. Serrodyne optical frequency translation with high sideband suppression. *Journal of lightwave technology*, 6(1):109–112, 1988. 158, 210

[82] Vahid Ansari, Emanuele Roccia, Matteo Santandrea, Mahnaz Doostdar, Christof Eigner, Laura Padberg, Ilaria Gianani, Marco Sbroscia, John M Donohue, Luca Mancino, et al. Heralded generation of high-purity ultrashort single photons in programmable temporal shapes. *Optics express*, 26(3):2764–2774, 2018. 159

[83] Vahid Ansari, John M Donohue, Markus Allgaier, Linda Sansoni, Benjamin Brecht, Jonathan Roslund, Nicolas Treps, Georg Harder, and Christine Silberhorn. Tomography and purification of the temporal-mode structure of quantum light. *arXiv preprint arXiv:1607.03001*, 2016. 159

[84] W. Tittel, J. Brendel, H. Zbinden, and N. Gisin. Quantum cryptography using entangled photons in energy-time bell states. *Phys. Rev. Lett.*, 84:4737–4740, May 2000. 162

[85] M. G. Raymer, Andrew H. Marcus, Julia R. Widom, and Dashiell L. P. Vitullo. Entangled photon-pair two-dimensional fluorescence spectroscopy (epp-2dfs). *The Journal of Physical Chemistry B*, 117(49):15559–15575, 2013. PMID: 24047447. 162

[86] Charles H. Bennett, Peter W. Shor, John A. Smolin, and Ashish V. Thapliyal. Entanglement-assisted classical capacity of noisy quantum channels. *Phys. Rev. Lett.*, 83:3081–3084, Oct 1999. 162

[87] Anthony Martin, Thiago Guerreiro, Alexey Tiranov, Sébastien Designolle, Florian Fröwis, Nicolas Brunner, Marcus Huber, and Nicolas Gisin. Quantifying photonic high-dimensional entanglement. *Phys. Rev. Lett.*, 118:110501, Mar 2017. 162

[88] JD Franson. Nonlocal cancellation of dispersion. *Physical Review A*, 45(5):3126, 1992. 162

[89] Asher Peres. *Quantum theory: concepts and methods*, volume 57. Springer Science & Business Media, 2006. 164

[90] OE Martinez, JP Gordon, and RL Fork. Negative group-velocity dispersion using refraction. *JOSA A*, 1(10):1003–1006, 1984. 169

[91] B. C. Sanders and G. J. Milburn. Optimal quantum measurements for phase estimation. *Phys. Rev. Lett.*, 75:2944–2947, Oct 1995. 186

[92] S. Lloyd. *Science*, 321:1463–1465, 2008. 187

[93] S. Tan et al. *Phys. Rev. Lett.*, 101:1–4, 2008. 187, 220

[94] M. Piani and J. Watrous. *Phys. Rev. Lett*, 102:250501, 2009. 189

[95] P. Jian. *Quantum limits in range-finding measurements with optical frequency combs*. 2014. 190, 191

[96] M. Braunstein and C.M. Caves. *Phys. Rev. Lett.*, 72, 1994. 190, 191

[97] K Meiners-Hagen, R Schödel, F Pollinger, and A Abou-Zeid. Multi-wavelength interferometry for length measurements using diode lasers. *Measurement Science Review*, 9(1):16–26, 2009. 195

[98] ZY Ou and L Mandel. Observation of spatial quantum beating with separated photodetectors. *Physical review letters*, 61(1):54, 1988. 196

[99] S. Lee and H. Joeng. *Proceedings of the First International Workshop on ECS and Its Application to QIS*, pages 41–46, 2013. 200

[100] Eric A Dauler, Matthew E Grein, Andrew J Kerman, Francesco Marsili, Shigehito Miki, Sae Woo Nam, Matthew D Shaw, Hirotaka Terai, Varun B Verma, and Taro Yamashita. Review of superconducting nanowire single-photon detector system design options and demonstrated performance. *Optical Engineering*, 53(8):081907, 2014. 209

[101] John Canning. Fibre gratings and devices for sensors and lasers. *Laser Photon. Rev.*, 2:275–289, 2008. 209

[102] K Kraus. General state changes in quantum theory. *Annals of Physics*, 64(2):311 – 335, 1971. 211

[103] C. H. Bennett and G. Brassard. Quantum cryptography: Public key distribution and coin tossing. *Proceedings of IEEE International Conference on Computers, Systems and Signal Processing*, 175:8, 1984. 212

[104] Jacob Mower, Zheshen Zhang, Pierre Desjardins, Catherine Lee, Jeffrey H. Shapiro, and Dirk Englund. High-dimensional quantum key distribution using dispersive optics. *Phys. Rev. A*, 87:062322, Jun 2013. 212

[105] J. Shapiro and S. Lloyd. *New Journal of Physics*, 11:1–6, 2009. 220

[106] S. Zhang et al. *Physical Review A*, 062309:1–6, 2014. 220

[107] Liang Xian-Ting. Classical Information Capacities of Some Single Qubit Quantum Noisy Channels. *Communications in Theoretical Physics*, 39(5):537–542, may 2003. 220